STRUCTURE OF JUPITER'S DAYSIDE MIDDLE MAGNETOSPHERE

by

Mark R. Sands

B.S., University of Arizona
(1978)
M.S., University of Arizona
(1981)

SUBMITTED IN PARTIAL FULFILLMENT
OF THE REQUIREMENTS OF THE
DEGREE OF

DOCTOR OF PHILOSOPHY
IN NUCLEAR ENGINEERING

at the

MASSACHUSETTS INSTITUTE OF TECHNOLOGY

June 1987

© Massachusetts Institute of Technology 1987

Signature of Author _____
Department of Nuclear Engineering
May 8, 1987

Certified by _____
Ralph L. McNutt Jr.
Thesis Supervisor

Certified by _____
Kim Molvig
Reader

Accepted by _____
Allan F. Henry
Chairman, Department Committee on Graduate Students

STRUCTURE OF JUPITER'S DAYSIDE MIDDLE MAGNETOSPHERE

by

Mark R. Sands

Submitted to the Department of Nuclear Engineering on May 8, 1987, in partial fulfillment of the requirements for the Degree of Doctor of Philosophy in Applied Plasma Physics.

THESIS ABSTRACT

Plasma data obtained by the Plasma Science (PLS) experiment onboard the Voyager 1 and 2 spacecraft during their encounter with Jupiter, was analyzed. The main goal was to determine plasma bulk flow velocities inside Jupiter's magnetosphere which could then be used as a means of validating (or invalidating) existing theories governing the dynamics of the system. For a magnetized body (a planet in our case) imersed in an ocean of supersonic plasma, a collisionless bow shock is set up (analogous to collisional shocks in fluid dynamics) in front of the planet. Behind this shock boundary is a region called the magnetosheath. In this region the "shocked" solar wind is turbulent and is deflected around the planet. The inner "edge" of this boundary is called the magnetopause. Inside the magnetopause, where plasma is within the "sphere" of influence of the planet's magnetic field, is the region known as the magnetosphere. At the magnetopause, the solar wind ram pressure balances the sum of the magnetic and particle pressure within the magnetosphere of the planet.

Using an interactive non-linear least squares fitting routine, plasma velocities were obtained assuming the ion distribution function to be a convected isotropic Maxwellian. To check the effect of temperature anisotropies on the analysis, a model was developed to simulate the current detected by the PLS experiment, assuming the ion distribution to be a convected bimaxwellian. It was found that the magnetospheric plasma was well approximated by a Maxwellian distribution.

With the plasma velocities as a data base, it was shown that radially outward plasma transport cannot be due to the negative magnetic anomaly seen on the surface of Jupiter. A magnetic anomaly is defined as a deviation of the surface magnetic field from that expected from the best fit displaced dipole (negative anomaly implies a depressed magnetic field region). The plasma outflow is not enhanced in the range of longitude containing the anomaly, as predicted by this model, in fact the flow is seen to be radially inward, not outward, during one of the traversals of this longitude sector.

For a physical system in equilbrium, the sum total of all forces acting on it must be zero. Using a currently accepted magnetic field model of Jupiter, the inwardly directed Lorentz force is seen to be much larger than the sum of the outwardly directed centrifugal and pressure gradient forces. By calculating the radius of curvature and using the field-aligned flow obtained through the analysis, the contribution to the inertial force, due to magnetic field line curvature, was calculated. It was found that this added term in the stress balance could not account for the excess Lorentz force (i.e., the outward inertial and pressure gradient forces still cannot balance the inward Lorentz force).

Thesis Supervisor: Ralph L. McNutt Jr.
Title: Associate Professor of Physics

ACKNOWLEDGMENT

I would like to express my gratitude to Ralph, who I consider to be a good thesis advisor. During the past four years, he has always been available to talk to when needed, even if he didn't have the time. Whether Ralph knows it or not, some of his exacting research style has rubbed off on me (which I consider to be a good thing).

My thanks also go out to Pam Milligan, who has given me assistance far above and beyond the call of duty. Besides always helping me with countless computer problems, she single handedly typed Chapter 2 of this thesis (a task I thought humanly impossible, but for which I will be eternally grateful).

To Joan Quigley I also give my thanks, her assistance, especially with the Goddard computing system has been much appreciated. Lord only knows what would have happened before, during, and after the Uranus encounter if she was not here making sure data was accessible, and knowing how to access it.

Anne Bowes receives a special Thank You for all her time and patience, both of which I always seemed to demand of her. On the fear of sounding sentimental, I will always be greatful for the kindness and support she has always shown me.

Let me say thanks to everyone in the plasma group, at the Center for Space Research, for putting up with me during these past four years, especially during the writing of this thesis and during The Truck adventure. May the Incense of George go with you all!

I cannot possibly fully express my gratitude to Candace for her support. She has been there ready to help, in any way possible, 30 hours a day. I will forever be greatful for the confidence she had in me.

Lastly, but most importantly, I want to say how proud I am to be one of five children of Richard and Frances Sands. They have been the immovable object in this world of irresistable forces. I only hope I can make them half as proud of me, as I am of them.

TABLE OF CONTENTS

Abstract 2

Acknowledgment 3

Chapter 1. Introduction 9

Chapter 2. Plasma Science Experiment 23

2.1. General Description 23

2.2. Current Calculation 27

Chapter 3. Data Analysis 74

3.1. Introduction 74

3.2. Analysis Technique 78

3.3. Maxwellian Fits 84

3.4. Bimaxwellian Fits 116

Chapter 4. Results 125

4.1. Magnetospheric Convection 125

4.2. Stress Balance 141

Chapter 5. Conclusion 147

5.1. Summary of Results 147

5.2. Questions and Recommendations 149

Appendix A. PLS Modulator Stepping 151

Appendix B. LABBI Source Code 163

Appendix C. Sample Input Listing for MJSANL 173

Appendix D. Table of Data for Stress Balance 189

Appendix E. Determination of Errors 192

Appendix F. References 195

LIST OF FIGURES

Figure 1.1-1. Cartoon of the Jovian Magnetosphere 11

Figure 1.1-2. Ion Temperature vs. Distance 13

Figure 1.1-3. Ion Charge Density vs. Distance 14

Figure 1.1-4. Plasma Data 20

Figure 1.1-5. Schematic View of Plasma Sheet 21

Figure 2.1-1. Plasma Science Experiment 24

Figure 2.1-2. Cross-sectional View of a Faraday Cup 26

Figure 2.2-1. Definition of Shift Vector 31

Figure 2.2-2. Potential Across the Grids 33

Figure 2.2-3. Plot of Cup Sensitive Area 35

Figure 2.2-4. Plot of Sensitive Area Approximation 37

Figure 2.2-5. A Plot of $\phi(Z)$ and its Approximate Form 46

Figure 2.2-6. Currents Produced with LABBI (Maxwellian Case) 62

Figure 2.2-7. Currents Produced with ABSO (Maxwellian Case) 63

Figure 2.2-8. LABBI Results (Bimaxwellian Case) 64

Figure 2.2-9. PMODEL Results (Bimaxwellian Case) 65

Figure 2.2-10. LABBI Results (Bimaxwellian Case) 67

Figure 2.2-11. PMODEL Results (Bimaxwellian Case) 68

Figure 2.2.12. LABBI Results (Bimaxwellian Case) 69

Figure 2.2-13. PMODEL Results (Bimaxwellian Case) 70

Figure 2.2-14. LABBI Results (Bimaxwellian Case) 72

Figure 2.2-15. PMODEL Results (Bimaxwellian Case) 73

Figure 3.1-1. Voyager 1 Trajectory Plot 76

Figure 3.1-2. Plot of Ion Mass and Charge Density vs. Time 77

Figure 3.2-1. Flow Chart of MJSANL 80

Figure 3.3-1. Fractional Current Difference vs. Position 85
Figure 3.3-2. Sample Cold Spectrum 87
Figure 3.3-3. Sample Hot Spectrum 88
Figure 3.3-4. Simulation of Spectrum in Fig. 3.3-2 89
Figure 3.3-5. Simulation of Spectrum in Fig. 3.3-3 91
Figure 3.3-6. Plasma Velocity and Magnetic Field vs. Distance 102
Figure 3.3-7. Field-aligned Flow vs. Non-azimuthal flow 104
Figure 3.3-8. Field-aligned/Non-azimuthal Flow vs. Distance 105
Figure 3.3-9. Cold Spectrum at 62 1027 UT 107
Figure 3.3-10. Simulation of Spectrum at 62 1027 UT 109
Figure 3.3-11. Spectrum Obtained During PLOMAN 2 112
Figure 3.3-12. Simulation of Main Sensor of Spectrum in Fig. 3.3-11 113
Figure 3.3-13. Simulation of D-Cup of Spectrum in Fig. 3.3-11 114
Figure 3.3-14. Spectrum From Outbound Trajectory 117
Figure 3.3-15. Simulation of Outbound Spectrum in Fig. 3.3-14 118
Figure 3.4-1. Bimaxwellian Analysis of Spectrum in Fig. 3.3-2 120
Figure 3.4-2. Spectrum From Voyager 2 Encounter with Jupiter 122
Figure 3.4-3. Maxwellian Simulation of Spectrum in Fig. 3.4-2 123
Figure 3.4-4. Bimaxwellian Simulation of Spectrum in Fig. 3.4-2 124
Figure 4.1-1. Convection Flow Pattern Mapped onto Planet's Surface 127
Figure 4.1-2. Convection Flow Pattern Mapped into Equatorial Plane 128
Figure 4.1-3. Magnetosphere/Ionosphere Current System 130
Figure 4.1-4. Plasma Rotational Motion Mapped onto Planet's Surface 131
Figure 4.1-5. Superposition of Convective and Rotational Motion 132
Figure 4.1-6. Plasma Flow when Rotation Dominates over Convection 134
Figure 4.1-7. Flux Tube Geometry for Magnetic Anomaly Model 135
Figure 4.1-8. Corotating Convection Current System 137

Figure 4.1-9. Plasma Flow Associated with Corotating Convection 138

Figure 4.2-1. Geometry Associated with Stress Balance 144

Figure 4.2-2. Ratio of Curvature/Centrifugal Force vs. Distance 145

LIST OF TABLES

Table 3.3-1. Plasma Velocities from Analysis 92

Table 3.3-2. Spectral Data 94

Table 3.3-3. **B** and **V** in Tilted Dipole Coordinates 97

Table 3.3-4. Field-aligned and Cross-field Flows in Dipole Coordinates 100

Table 3.3-5. Plasma Velocities (Assumed Azimuthal) 110

Table 3.3-6. Plasma Velocities During PLOMAN 2 115

Table 4.1-1. Radial Velocities: Observed vs. Predicted 140

Table D.1. Data used to Calculate Fig. 4.2-2 190

CHAPTER 1

INTRODUCTION

As its Roman name implies, Jupiter is the "king" of planets. Jupiter is the largest planet in the solar system, and with a radius of 71,398 km ($\equiv 1\ R_J$), over 11 Earths could be placed side by side inside the planet. Another distinguishing feature of Jupiter is its magnetic field. In 1954, *Burke and Franklin* [1955] discovered radio emissions from Jupiter at 22.2 MHz. These emissions were right circularly polarized, and suggested that Jupiter had a magnetic field which was influencing the radio propagation. Although it is not the only planet with a magnetic field, the magnitude of the field is by far the largest among the planets: over 10 gauss at the poles (as compared to ~0.3 gauss at Earth). The magnetic axis is tilted ~9.6° to the spin axis (as compared to ~12° at Earth), with a sense opposite to that of the Earth; the north magnetic pole is in the northern hemisphere, while for Earth, it is in the southern hemisphere.

The rotation period of Jupiter is approximately 9 hours 55 minutes, and is the shortest of all the planets. Coupling this with Jupiter's size produces a centrifugal force at the visible cloud deck which causes the substantial equatorial bulge (the polar radius is 7% smaller than the equatorial radius). *Brice and Ioannidis* [1970] noted that the distance from the spin axis at which the components of centrifugal force and gravitational force would balance along dipole magnetic field lines, would be ~2 R_J. they concluded that any Jovian magnetosphere would, therefore, be dominated by rotational effects. Because Jupiter is a rapid rotator with a large magnetic field, it can be likened to a pulsar [*Kennel and Coroniti*, 1975], and this alone makes Jupiter worthy of study. In Chapter 1 a review of relevant observations of the Jovian magnetosphere is given. These observations result from the *in situ* measurements made by the Pioneer 10 and 11 and Voyager 1 and 2 spacecraft, during their respective encounters with Jupiter. Also, a brief review is given of some of the theoretical models which these observations inspired.

Chapter 2 describes the Plasma Science experiment flown on the Voyager 1 and 2 spacecraft. A model (i.e., analysis routine) to simulate currents detected by the instrument, assuming a convected bimaxwellian ion distribution function, is described. Lastly, a comparison of this analysis routine against two other benchmarked analysis routines is made.

The results of a detailed plasma data analysis of the low energy plasma population is presented in Chapter 3. Besides describing the analysis technique, plasma bulk flow velocities are presented along with a description of the input conditions used to obtain them.

Chapter 4 discusses the implications which the bulk plasma flow (presented in the tables in Chapter 3) has, on the currently accepted dynamical picture of the Jovian magnetosphere. Implications of the bulk flow pattern on existing theories of plasma flow are addressed. Finally, some ways of extending this work are presented.

For a magnetized body (a planet in our case) imersed in an ocean of supersonic plasma, a collisionless bow shock is set up (analogous to collisional shocks in fluid dynamics) in front of the planet. Behind this shock boundary is a region called the magnetosheath. In this region the "shocked" solar wind is turbulent and is deflected around the planet. The inner "edge" of this boundary is called the magnetopause. Inside the magnetopause, where plasma is within the "sphere" of influence of the planet's magnetic field, is the region known as the magnetosphere. At the magnetopause, the solar wind ram pressure balances the sum of the magnetic and particle pressure within the magnetosphere of the planet. Of the planets known to have magnetic fields, Jupiter has the largest magnetosphere. If "reflective paint" was poured over the Jovian magnetosphere so it could be seen from Earth, its face-on orientation would appear to be four times the size of the full moon. Figure 1.1-1 depicts the canonical cartoon of the Jovian magnetosphere.

A planet's magnetosphere can be divided into two halves, the dayside and the nightside. Jupiter's magnetosphere is further subdivided into three regions; an inner, middle, and outer magnetosphere. The inner magnetosphere extends from the ionosphere to about 6 R_J, the outer magnetosphere extends from approximately 40 R_J to the magnetopause, and everything in

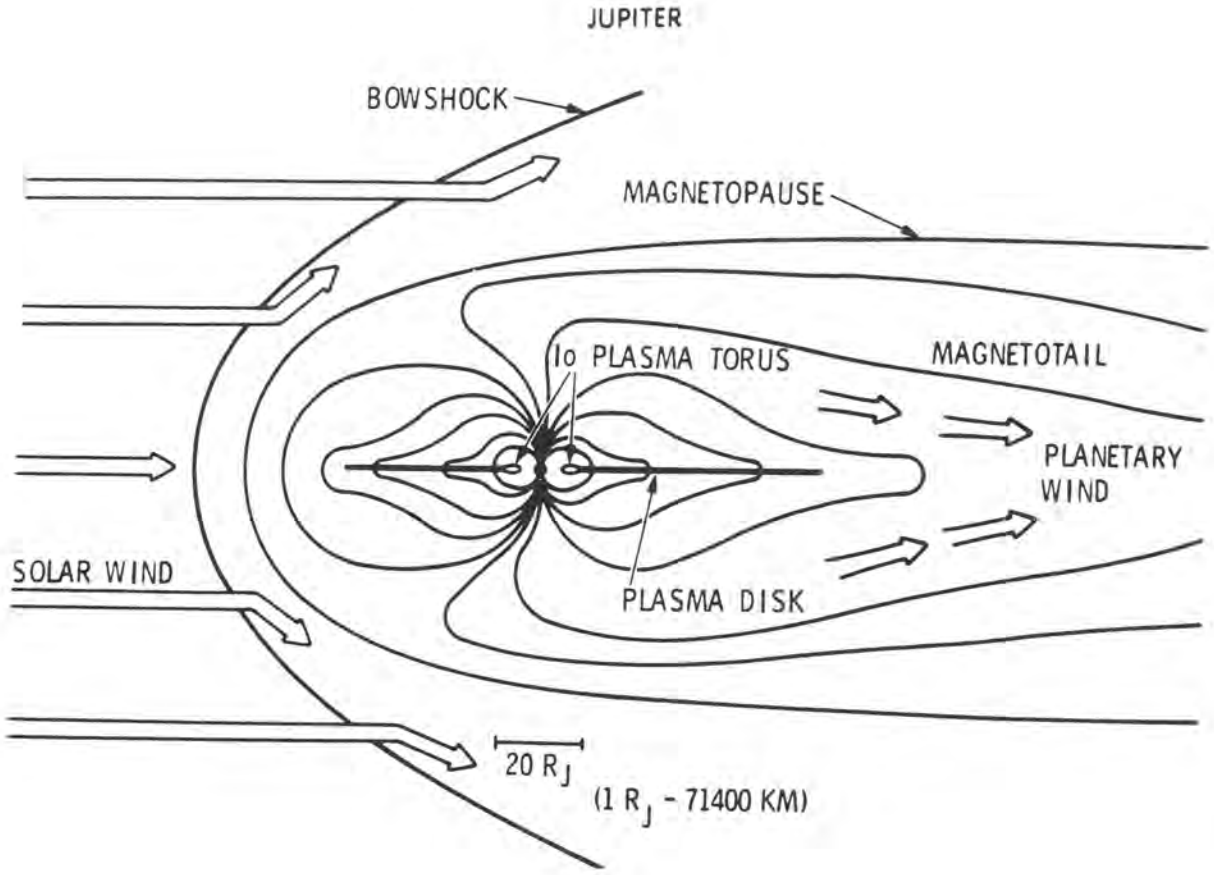

Figure 1.1-1. Cartoon depicting the Jovian magnetosphere.

between is termed the middle magnetosphere.

The dominant feature of the inner magnetosphere is the dense plasma torus associated with the satellite Io (Io is 5.95 R_J from the center of Jupiter). Ground-based optical observations gave the first clues of this feature associated with Io. Emission lines of neutral sodium [*Brown and Chaffee*, 1974] and ionized sulfer [*Kupo et. al.*, 1976], were detected in the region near Io and its orbit. Assuming local thermodynamic equilibrium, *Brown* [1976] speculated that the observations were consistant with a plasma cloud of density $\sim 10^3 - 10^4$ cm^{-3} and temperature $\sim 10^4 - 10^5$ $°K$. These observations were confirmed and greatly extended during the Voyager 1 flyby on March 5, 1979. The Io torus was found to consist of two regions, a cold (inner) region and a warm (outer) region [*Bridge et. al.*, 1979]. During the encounter, *in situ* plasma measurements showed that the outer portion of the torus extended from about 5.5 R_J to approximately 7.5 R_J. This region has a scale height (or half thickness) of ~1.5 R_J and consists mainly of warm (~40 eV) sulfer and oxygen ions [*Bridge et. al.*, 1979] and cooler electrons (about 5 eV), with a smaller population of hot (on the order of 1 keV) electrons [*Scudder et. al.*, 1981]. The inner torus was observed from closest approach (4.89 R_J) to 5.5 R_J. Here, the scale height thickness is about 0.2 R_J and consists mainly of cold (less than 1 eV) positive ions such as S^+, O^+, S^{2+}, S^{3+}, O^{2+}, and Na^+ [*Bagenal and Sullivan*, 1981]. Features of both torus regions are shown in Figures 1.1-2 and 1.1-3. A radial profile of ion temperature, determined from positive ion fits to spectra (the terms "fit" and "spectra" are defined in Chapter 2), is given in Fig. 1.1-2. Transition from the warm to the cold torus can be seen as a sudden, sharp gradient in temperature just inside of 6 R_J. Fig. 1.1-3 shows the corresponding charge density measurements, showing a similar gradient in going from the warm to the cold torus. Both figures show the corresponding position of the spacecraft with respect to the magnetic dipole equatorial plane. The region of the Io torus and current sheet (discussed later in this chapter) is also shown.

Ions rotate rigidly with Jupiter as the $\mathbf{E} \times \mathbf{B}$ drift in the corotational electric field imposed by the highly conducting, rotating ionosphere. Ions diffuse away from the Io source region under the influence of the centrifugal force, which aids outward but inhibits inward transport

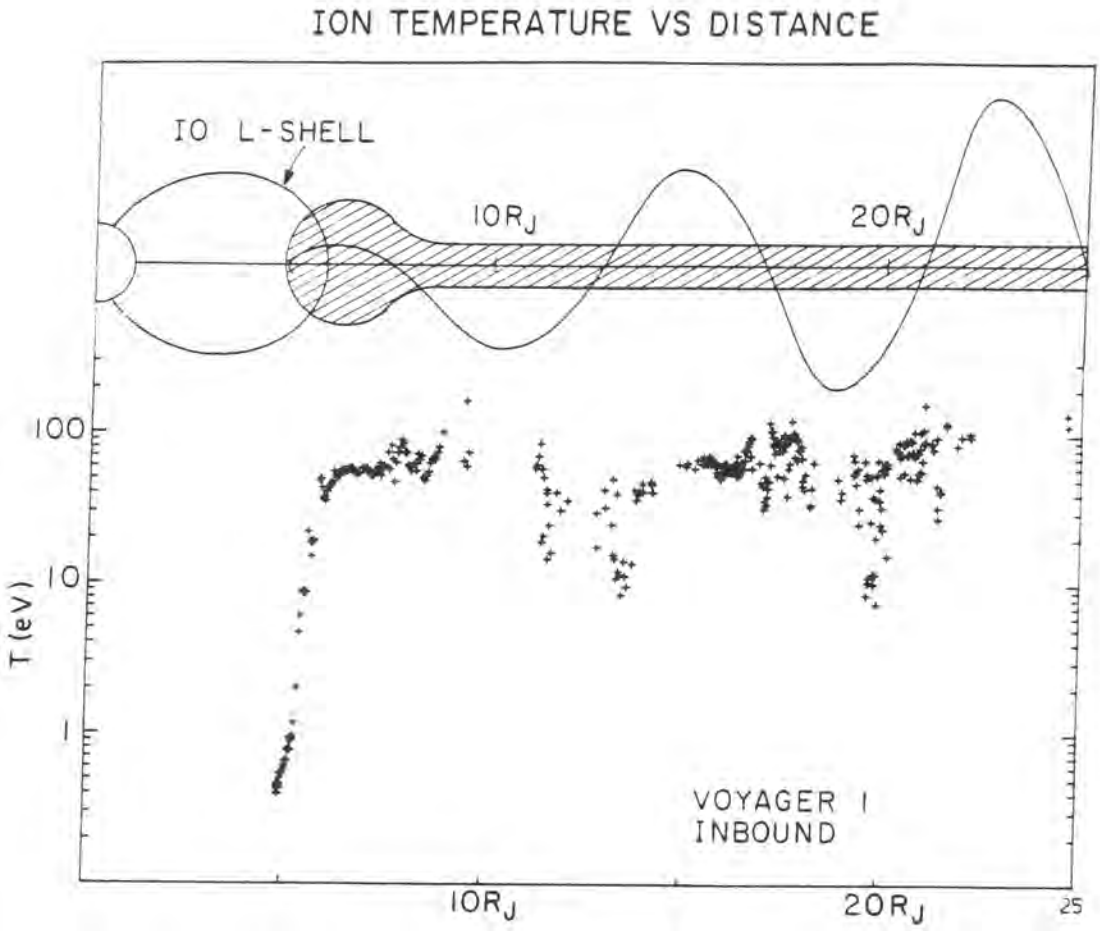

Figure 1.1-2. Bottom half of the figure shows the radial profile of the positive ion temperature, corresponding to the spacecraft position. Top half of the figure depicts the current sheet and Io torus (buldge) by the hatched region. The squiggly line represents the distance of the spacecraft from the magnetic dipole equatorial plane during the inbound portion of the Voyager 1 enocunter.

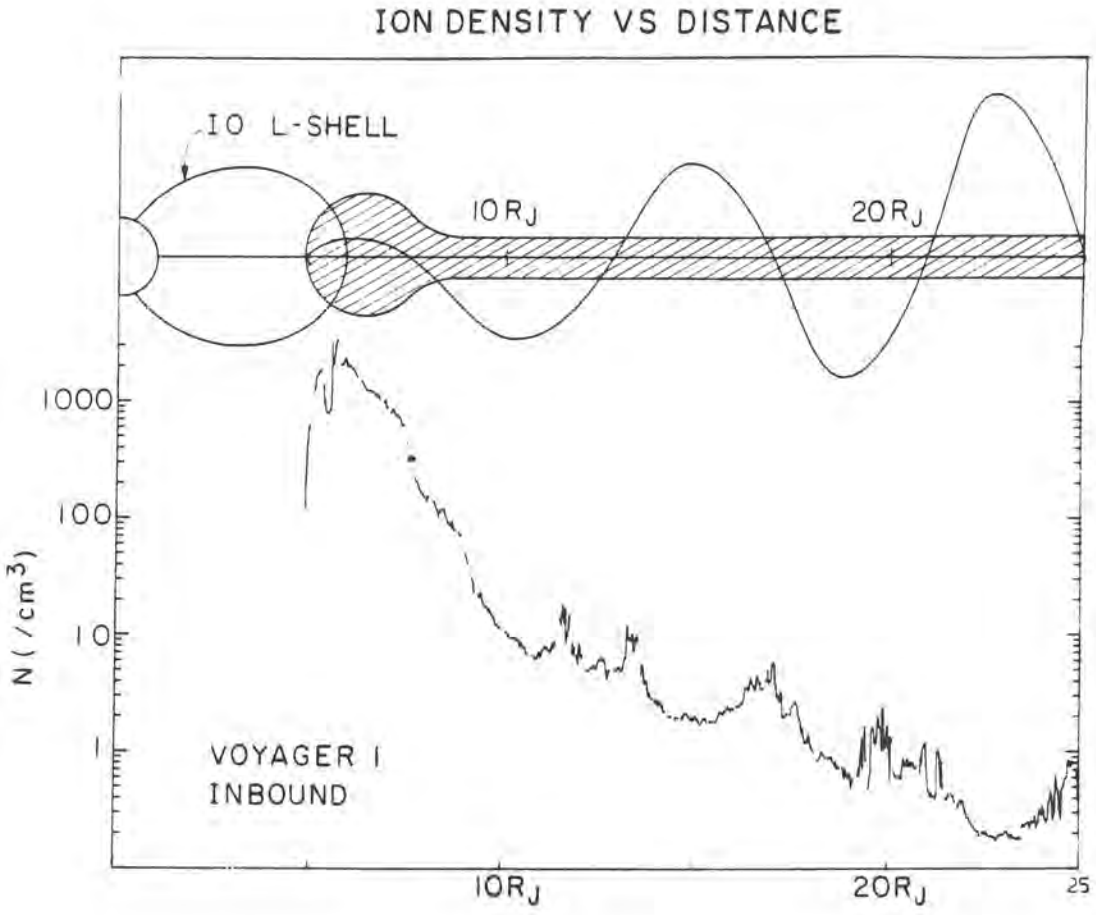

Figure 1.1-3. Estimates of the total charge density of positive ions for the Voyager 1 encounter.

[*Richardson et. al.*, 1980; *Siscoe and Summers*, 1981]. For this reason, the density outside the orbit of Io remains high over a larger radial distance while the density drops off dramatically inside of Io. Similarly, the temperature remains high over a larger radial distance, outside of Io, because the plasma does not have time to cool by radiation. But, the inward diffusion of plasma is slow, allowing the plasma time to cool by radiation, thus collapsing to the centrifugal equator. Since cooling rate is proportional to plasma density, once cooling starts, a positive feedback mechanism is set up. As temperature decreases, the density at the equator increases, causing a further increase in the cooling rate.

Many investigators have developed detailed models of plasma transport, but problems remain. *Richardson and Siscoe* [1983] attempted to model the large gradients in both temperature and density, inside of Io, using diffusion models. However, they were not able to simultaneously reproduce the profiles. Other models invoke inward motion of near empty flux tubes to replace outward-moving flux tubes carrying Iogenic plasma [*Summers and Siscoe*, 1985; *Pontius et. al.*, 1986]. Using data from the Voyager plasma science experiment, *Richardson and McNutt* [1987] have shown that density fluctuations of more than 10% over distance scales of a few Jovian radii do not occur, ruling out interchange modes.

The dayside outer magnetosphere is much different in appearance than the inner region. From Pioneer observations *Smith et. al.* [1975] described this region of the magnetosphere as having an irregular magnetic field but showing a persistent southward component, indicating closed magnetic field lines. A major portion of this field is produced by currents inside the magnetosphere, termed the current sheet (discussed later in this chapter), rather than by the planetary field [*Smith et. al.*, 1978]. The relative contribution of the planetary dipole field to the field near the magnetopause becomes more significant as the solar wind ram pressure increases, ranging from about 20% at 100 R_J to over 40% at 50 R_J [*Acuna et. al.*, 1983].

Organized plasma sheet structure, seen in the middle magnetosphere, vanishes in the dayside outer magnetosphere. There are occasional appearances of cold, dense regions of electrons and ions which, in appearance, are similar to the "spikey" structure seen in the plasma

sheet associated with the middle magnetosphere [*Belcher*, 1983]. However, these sitings occur randomly and are not near any expected crossings of the magnetic equator. Overall, the plasma characteristics in the dayside outer magnetosphere seem to be disordered and turbulent.

Between the inner and outer magnetosphere, is a region referred to as the middle magnetosphere. In this region, *Melrose* [1966] and *Gledhill* [1967] expected the magnetosphere to be flattened. They both argued that the magnetospheric plasma would be dominated by rotational effects, and expected the magnetosphere to corotate with Jupiter. If the neutral atmosphere viscosity and the ionosphere conductivity are large enough, the magnetic field in the magnetosphere will be "rigidly" coupled to the planet. The plasma velocity will then be given by

$$\mathbf{V} = \boldsymbol{\Omega} \times \mathbf{r}$$

where $\boldsymbol{\Omega}$ is the planetary angular velocity and $\mathbf{r}$ is radial position. The magnetosphere is then said to "rigidly corotate" or "corotate" with the planet [*Davis*, 1947; *Davis*, 1948; *Hones and Bergeson*, 1965]. However, there is also the possibility that a magnetosphere might exhibit differential rotation, an idea investigated by *Vlasov and Khakimov* [1964], in looking at the radiation belts around Earth.

One of the initial results of the Pioneer 10 (P10) encounter was the discovery of a 10 hour particle flux modulation which researchers attributed to the confinement of energetic particles near the magnetic equatorial plane. This confinement region was believed to oscillate above and below the rotational equatorial plane [*Van Allen et. al.*, 1974a; *Simpson et. al.*, 1974; *Trainor et. al.*, 1974; *Fillius and McIlwain*, 1974]. After a more detailed analysis of their data, *Van Allan et. al.* [1974] concluded that Jupiter had a thin disk-like magnetosphere. They adopted the term magnetodisk, after a suggestion by William Dixon. Their observations indicated that to first order this magnetodisk could be represented as a thin, tilted, rigid disk attached to the planet. Because of this rotating disk (*i.e.* current sheet), a perturbation field is set up, which, when added to the planetary dipole field, creates a magnetic field which varies more slowly than r^{-3} [*Smith et. al.*, 1974]. The result is a radially distended magnetic field.

It was hypothesized that the cause for this current sheet was due to a thermal plasma (E < 10 keV), corotating with Jupiter in force balance: gravitational, pressure gradient, magnetic, and centrifugal [*Van Allen et. al.*, 1974; *Smith et. al.*, 1974]. This supposed plasma population could not be directly verified by the plasma instrument onboard the P10 or P11 spacecraft since the electrostatic analyzers used were not adequately shielded [*Frank et al.*, 1976]. Indeed, much of the thermal plasma population escaped verification until being detected by the Plasma Science (PLS) experiment onboard the Voyager 1 and 2 spacecraft, during the encounters with Jupiter [*Bridge et. al.*, 1979a; *Bridge et. al.*, 1979b]. Assuming the plasma source to be the Galilean satellites, Io in particular, and not the ionosphere, *Hill and Michel* [1976] estimated the current sheet to have a centrifugal scale height of $1 - 2\ R_J$ thickness. They found that the scale height was independent of the distance from Jupiter. Assuming the plasma pressure in the current sheet to be comparable to, or larger than, the corotational energy density, and using the current sheet field model of *Goertz et al.* [1976], *Goertz* [1976] obtained a current sheet with half thickness $\sim 2\ R_J$. Using the same field model, *Goldstein* [1977] calculated isobars and isodensity lines, assuming corotation and a constant or radially decreasing plasma pressure in the equatorial plane. He confirmed the existance of the plasma sheet by showing the maxima of pressure and density to lie in the equatorial plane.

Smith et. al. [1975] found that Jupiter's magnetic field did not lie in meridional planes, but instead had a spiral structure. *Van Allen et. al.* [1974] found from particle anisotropies that the current sheet did not rigidly corotate with Jupiter, and was later confirmed by *McDonald et. al.* [1979] after analyzing energetic proton (from 0.2 – 20 MeV) data obtained by P10 and P11. The explanation of this observation was put forward by *Northrop et. al.* [1974]. Breakdown of corotation, which implies an azimuthal distortion of the magnetic field from a meridional plane, could be accounted for by allowing the feet of the field lines to slip. As long as the ionosphere is not a perfect conductor, a point exists where the torque exerted on the ionosphere, by the magnetic field, is too great to maintain corotation. Out to some distance, the required torque to maintain corotation can be maintained by the ionosphere. However, further out, the torque exerted by the field lines due to the outwardly diffusing plasma, is too great and the feet of the

field lines will slip in the ionosphere, causing a breakdown in corotation. *Hill* [1979] showed that corotation breaks down significantly (azimuthal velocity is roughly three fourths its corotational value) at distances greater than ~ 20 R_J. Outside 20 R_J, the azimuthal velocity becomes almost constant at ~200 km/sec [*Eviatar et. al.*, 1986; *McNutt et. al.*, 1979]. A detailed formulation of the magnetosphere-ionosphere interaction, with application to the terrestrial magnetosphere, is given by *Vasyliunas* [1970]; Jovian magnetosphere is treated by *Hill* [1979].

Besides a breakdown in corotation, plasma streaming along magnetic field lines was also seen in the middle magnetosphere [*Van Allen et. al.*, 1974; *McDonald et. al.*, 1979; *Northrop et. al.*, 1979]. In looking at the energetic proton (0.2 – 20 MeV) data from P10 and P11, *McDonald et. al.* [1979], found large anisotropies which were due not only to corotation effects but also to field-aligned streaming. There was also a much smaller anisotropy due to spatial gradients in particle intensity. A detailed analysis of 1.8 – 2.15 MeV proton data taken by P10, was performed by *Northrop et. al.* [1979]. In one case, they assumed the ion distribution function, f_0, was isotropic, allowed no field-aligned flow, and assumed the electric field to be due entirely to corotation. In a second case, f_0 was allowed to be anisotropic, and finally, in a third case, f_0 was again assumed isotropic, but parallel flow was allowed. The only case which was able to account for most of the anisotropy was that which assumed parallel flow. The other cases required density gradients which were orders of magnitude too large (and sometimes in the wrong direction), while almost no gradient was needed if parallel flow was allowed. Both this analysis and the analysis done by *McDonald et. al.* [1979], suggested that at least a part of this field-aligned flow might, in fact, be directed away from the magnetic equator.

After the Jupiter flybys with the Voyager 1 and 2 spacecraft, plasma flow in the dayside middle magnetosphere was better understood. Initial results from both encounters reconfirmed that the plasma moved primarily in the corotational (azimuthal), direction but did not rigidly corotate with the planet [*Bridge et. al.*, 1979a; *Bridge et. al.*, 1979b]. It was later shown that breakdown of rigid corotation occured at distances greater than approximately 10 R_J [*McNutt et. al.*, 1979; *Belcher et. al.*, 1980]. These observations were consistent with inferred ionospheric

conductivities and plasma production rates at Io [*Hill*, 1979].

Belcher and McNutt [1980] and *McNutt et. al.* [1981], showed qualitatively that plasma flowed away from the magnetic equator on the dayside and toward the equator on the nightside. This confirmed what *Northrop et. al.* [1979] and *McDonald et. al.* [1979] had alluded to.

The observation of a plasma sheet both north and south of the current sheet was reported by *McNutt et. al.* [1981]. Enhanced plasma density along with relative enhancement of heavy ions with respect to protons, and decreased temperature identify the plasma sheet. The bifurcation is clearly seen in Fig. 1.1-4, a plot of current versus energy-per-charge, over a 4 hour period. Each line is a spectrum obtained by the Plasma Science experiment (see Chapter 2 for a description of how the experiment operates). The crossing of the magnetic equator occured at about 0000 UT (Universal Time) while the two density enhancements identify the plasma sheet crossings. This suggests that the plasma sheet may be in a dynamic state of motion relative to the current sheet. Physically, this motion is thought to be due to the solar wind compression of the magnetosphere [*McNutt et. al.*, 1981; *Belcher and McNutt*, 1980]. A schematic view of this dynamic plasma sheet is given in Fig. 1.1-5. Plasma is accelerated from midnight to noon and decelerated from noon to midnight, with the corresponding velocity away from the magnetic equator on the dayside and toward the equator on the nightside. The sheet is therefore thinnest near dawn and thickest near dusk. Even though the sheet is in motion, there is no net transport of plasma, implying a time stationary structure. The most serious objection to his model is the question of whether the solar wind interaction can actually produce such effects deep into the magnetosphere.

Ever since P10 and P11, investigators have known that Jupiter's magnetosphere undergoes large scale compression due to the solar wind. After the Pioneer 10 encounter *Smith et. al.* [1975] remarked that changes in size by factors of two in the dimensions of the magnetosphere were common. This came after observing that Pioneer 10 went through several bow shock and magnetosphere crossings (three inbound and three outbound). Again, after the Pioneer 11 encounter, investigators observed several crossings beginning at ~100 R_J and ending with the

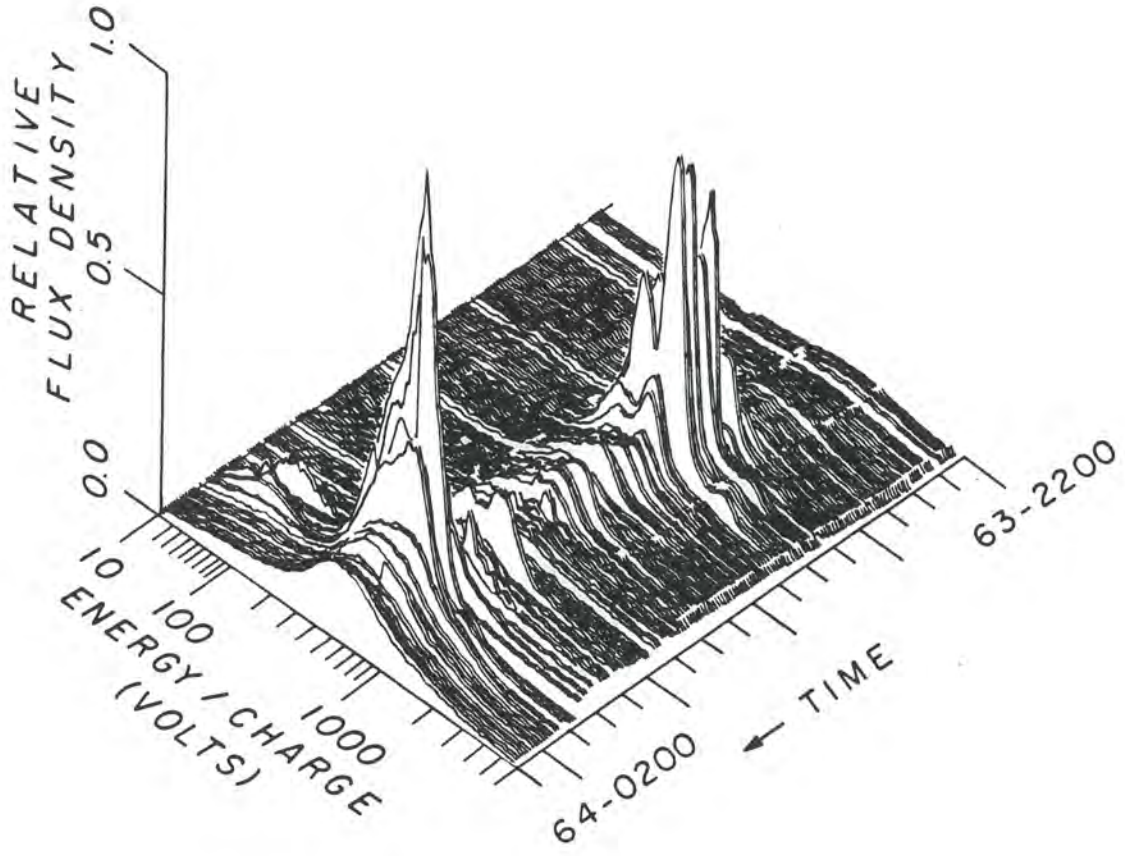

Figure 1.1-4. A plot of the relative flux density as measured by the side sensor of the Plasma Science experiment between 2200 UT on day 63 (March 4) and 0200 UT on day 64, 1979. Reprinted from *McNutt et. al.*, [1981].

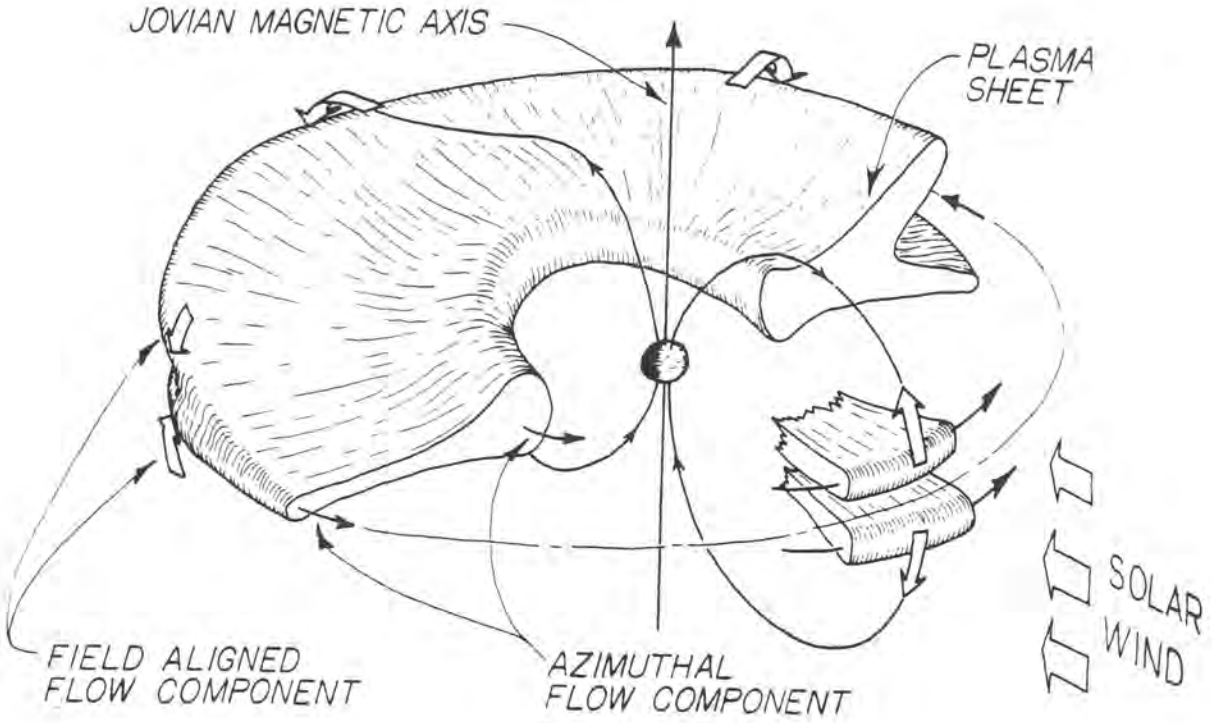

Figure 1.1-5. A schematic of the dynamic plasma sheet. Reprinted from *McNutt et. al.*, [1981].

final entry into the magnetosphere at ~50 R_J [*Wolfe et. al.*, 1974a; *Smith et. al.*, 1974a; *Mihalov et. al.*, 1975]. These encounters gave the first evidence that Jupiter's magnetosphere was much more compressible than Earth's. Enhancement in compressibility is due to the fact that, beyond the inner magnetosphere, the magnetic field is mostly due to the current sheet [*Smith et. al.*, 1978]. After the Voyager 1 encounter, *Bridge et. al.* [1979a] noted several bow shock and magnetosphere crossings, between ~86 R_J and ~47 R_J. Voyager 2 detected a large compression of the Jovian magnetosphere, by solar wind, after noting the initial entry at ~99 R_J and the final entry at ~62 R_J [*Bridge et. al.*, 1979b]. From these observations it is easy to see that the large scale compressions (and subsequent expansions) make the Jovian magnetosphere a very dynamic system.

CHAPTER 2

PLASMA SCIENCE EXPERIMENT

2.1. General Description

The Plasma Science (PLS) experiment on the Voyager 1 and Voyager 2 spacecraft consists of two plasma detectors (see Fig. 2.1-1). One detector, the main sensor, is made up of three modulated-grid Faraday cups, the A, B, and C cups, while the side sensor, or D-cup, consists of one modulated-grid Faraday cup. The symmetry axis of the main sensor is parallel to the axis of the high gain antenna on the spacecraft and thus points toward the earth, except for short periods of time during spacecraft maneuvers. The normals of these three cups are tilted 20° to the symmetry axis and are equally spaced at 120° in azimuth about the axis. The D-cup normal is − 88° to the symmetry axis and is located 167° in azimuth from the A-cup normal. Looking down onto the PLS experiment, the three cups forming the main sensor are labeled A, B, and C in a clockwise sense.

Currents due to positive ions are measured by all four cups in the energy-per-charge range of 10 - 5950 V. In addition, the side sensor measures currents due to electrons over the same energy-per-charge range. The energy range is covered by a set of discrete, contiguous voltage windows which, to first order, are spaced logarithmically. While measuring positive ions, there are two instrument modes which can be utilized. A low resolution mode (L-mode) breaks up the energy range into 16 voltage windows, each with an energy-per-charge resolution ($\Delta E/E$), of ~29%; a high resolution mode (M-mode) has 128 voltage windows, each with an energy-per-charge resolution of ~3.6%. As a result the L-mode has a better signal-to-noise ratio but poorer spectral resolution than the M-mode. The channel numbers and corresponding voltage range for both the L and M-modes are listed in Appendix A. During much of the mission cruise phase, as well as the encounters with Jupiter and Saturn, the integration time per channel (the time during which current into each channel is sampled) is 210 milliseconds with an additional 30

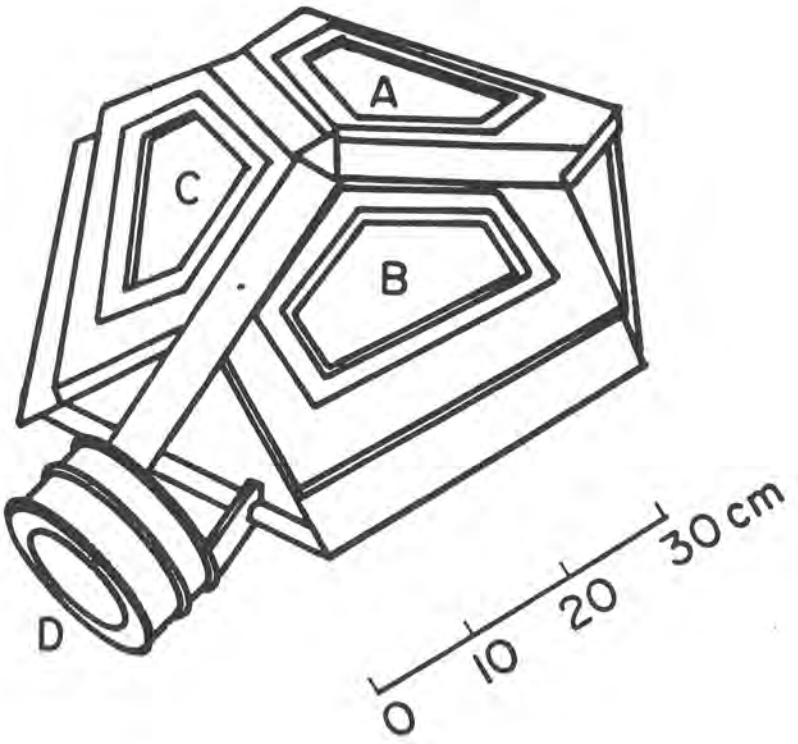

Figure 2.1-1. A drawing of the Plasma Science (PLS) experiment. The main sensor consists of the A, B, and C-cups while the D-cup makes up the side sensor.

milliseconds required to switch voltage levels. A complete L-mode then takes 3.84 seconds to acquire, while a complete M-mode measurement takes 30.72 seconds. Each measurement sequence lasts 96 seconds in which currents from only 72 energy channels of the M-mode are telemetered to Earth. Thus, to obtain a complete M-mode spectral set at Earth, two measurement sequences, or 192 seconds are required. The convention adopted here for analysis of M-modes involves producing one entire set of M-mode spectra (from all four cups) every 192 seconds by combining channnels 1 - 56 from one measurement sequence with channels 57 - 128 from the subsequent sequence.

A schematic cross-sectional view of one of the modulated grid Faraday cups is shown in Fig. 2.1-2. In the positive-ion mode the modulator grids are given a positive potential while the shield grids remains at ground. As the detector steps through the energy range (16 steps for L-modes, 128 steps for M-modes), the positive potential applied to the modulator grids is alternated at 400 Hz between the values listed in Appendix A. The suppressor grid is set to -95 volts (in the positive ion mode) to prevent the escape of secondary electrons produced at the collector plate, which would add to the observed positive ion current. In the figure the viewing angle is also shown, where the full view angle defines the range of particle trajectories such that every particle passing through the aperture hits the collector. The partial view angle is the range of particle trajectories such that only some of the particles passing through the aperture hit the collector. The "primary" field of view of the main sensor is defined as the region common to all three full view cones and is approximately a cone of half-angle 45°. Similarly, the "secondary" field of view is defined as the region common to all three partial view cones, having a cone of half-angle 90°.

The major difference between the main sensor cups and the side sensor cup is the shape of the aperture and collector plate. While the three cups comprising the main sensor are shaped like home plate, in baseball, the D-cup is circular. This introduces important differences, noted in the next section, in calculating the current measured in each cup, assuming a convected bimaxwellian ion distribution. For a more detailed description of the PLS experiment, see *Bridge et. al.*, [1977].

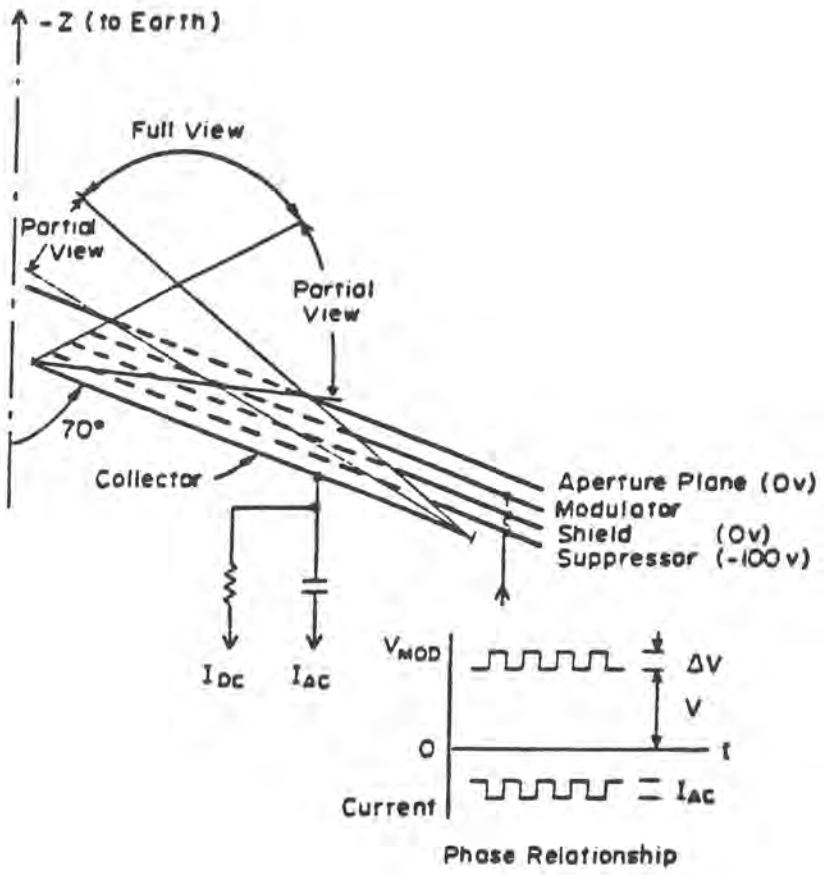

Figure 2.1-2. Cross-sectional schematic view of the grid structure for one of the three cups of the main sensor. Only a single shield and modulator grid are shown (the sensor actually has six shield grids and three modulator grids). Reprinted from *Bridge et. al.*, [1977].

2.2. Current Calculation

Once received, data from the PLS experiment during the Voyager 1 and 2 encounters with Jupiter can be analyzed to determine compositive, density, velocity, and other properties of the plasma. Analysis of the data consists of trying to duplicate the currents measured by the PLS experiment with currents calculated by the analysis routine given assumed plasma properties. This analysis routine, called MJSANL, allows the user to choose a model for the calculated currents and then proceeds through a non-linear least squares fitting routine to try and match calculated currents with measured currents. The parameters which are to be varied, (the fit parmeters) in matching the currents, define the plasma distribution functions. Because the current models are complicated functions of the fit parameters, linear least squares fitting techniques cannot be used, i.e., the currents cannot be expanded in terms of functions which are linear in the fit parameters. Hence a non-linear least squares fitting routine is used. MJSANL uses a method known as the gradient-expansion, or Marquardt, algorithm. For more detail on the gradient-expansion algorithm, see Chapter 3, or *Bevington* [1969].

Even though many spectra can be analyzed assuming the plasma distribution functions are convected Maxwellians, there are spectra which cannot be duplicated (i.e., fit) using simple Maxwellian distributions. For example, by assuming ion distributions to be Maxwellian, temperature (pressure) anisotropies cannot be taken into account. To investigate the possibility of temperature anisotropies, the next logical step is to use a code which allows the use of a convected bimaxwellian ion distribution function. However, the only code which had been capable of simulating a non-maxwellian distribution, called PMODEL, is very CPU intensive and expensive to run. For this reason a more efficient analysis routine which can calculate the current for each energy channel, assuming the distribution function $f(\mathrm{x}, \mathrm{v}, t)$ to be a convected bimaxwellian (with the convected maxwellian as a special case), was developed. The rest of this chapter deals with the details of the faster algorithm. A listing of the corresponding computer code is given in Appendix B.

Current measured by the PLS experiment, for a given energy-per-charge channel, k, is given by the relation

$$I_k(\mathbf{x}, t) = I_k^*(\mathbf{x}, t) - I_{k+1}^*(\mathbf{x}, t) \tag{2.2.1}$$

where $I_k^*(\mathbf{x}, t)$ and $I_{k+1}^*(\mathbf{x}, t)$ are the total currents measured by the instrument (at location $\mathbf{x}$ and time t) due to positive ions with velocities greater than the threshold velocities for channels k and $k+1$, respectively. These threshold velocities are defined by.

$$v_k \equiv \left[\frac{2eZ_i^*\phi_k}{A_i m_p}\right]^{1/2} \tag{2.2.2}$$

with e and m_p being the proton charge and mass, respectively. For ionic species i, the mass number and charge state are denoted by A_i and Z_i^*, respectively. The set of contiguous potentials, provided by the modulator grid to select the energy-per-charge channels is $\left\{\phi_k\right\}_{k=1}^{N+1}$ where N is 16 for the L-mode, and 128 for the M-mode. Thus, the current measured for the kth channel is principally due to particles with velocities which fall into the velocity window of width Δv_k, where

$$\Delta v_k = v_{k+1} - v_k \tag{2.2.3}$$

although there is also a "feedthrough" contribution (discussed below).

The total measured currents making up the terms on the right hand side of Eq. 2.2.1 are given by

$$I_k^*(\mathbf{x}, t) = Z^* e \int_{-\infty}^{\infty}\int_{-\infty}^{\infty}\int_{v_k}^{\infty} d\mathbf{v}\ (\mathbf{v}\cdot\hat{\mathbf{n}})\ f(\mathbf{x}, \mathbf{v}, t)\ R(\mathbf{v}, v_k) \tag{2.2.4}$$

where $\hat{\mathbf{n}}$ is a unit vector in the direction normal to the PLS cup being considered. Thus

$$I_k^*(\mathbf{x}, t) = Z^* e \int_{-\infty}^{\infty} dv_x \int_{-\infty}^{\infty} dv_y \int_{v_k}^{\infty} dv_z\ v_z\ f(\mathbf{x}, \mathbf{v}, t)\ R(\mathbf{v}, v_k) \tag{2.2.5}$$

where $f(\mathbf{x}, \mathbf{v}, t)$ is the ion distribution function and $R(\mathbf{v}, \mathbf{v}_k)$ is defined as the instrument response function.

The response function is analyzed in great detail by Barnett [*Barnett*, 1984; *Barnett and Olbert*, 1986], therefore only a brief description will be given here. Symbolically, $R(\mathbf{v}, \mathbf{v}_k)$ can be written as a product of two terms,

$$R(\mathbf{v}, \mathbf{v}_k) = T(\mathbf{v}, \mathbf{v}_k)\, A(\mathbf{v}, \mathbf{v}_k) \tag{2.2.6}$$

where $T(\mathbf{v}, \mathbf{v}_k)$ is defined as the transparency function and $A(\mathbf{v}, \mathbf{v}_k)$ the "sensitive" area of the collector.

Consider a single grid composed of two sets of coplanar perpendicular wires. The transparency of this grid is defined as the probability of an incident particle passing, unobstructed, through the grid plane. Since each cup of the main sensor has 9 such grids, $T(\mathbf{v}, \mathbf{v}_k)$ is a product of the nine associated probabilities; the side sensor has 6 grids, hence, six such probabilities. This final probability can be approximated in terms of four gaussians for the main sensor cups,

$$T(\mathbf{v}, \mathbf{v}_k) \equiv T_0 \sum_{i,j=1}^{2} c_i\, c_j \exp\left[- a_i \left[\frac{\mathrm{v}_x}{\mathrm{v}_z}\right]^2 - a_j \left[\frac{\mathrm{v}_y}{\mathrm{v}_z}\right]^2 \right] \tag{2.2.7}$$

where a_i, a_j, c_i, and c_j are functions of $(\mathrm{v}_x/\mathrm{v}_k)^2$ and $(\mathrm{v}_x/\mathrm{v}_s)^2$ and whose values have been determined numerically and are stored in tabular form [*Barnett*, 1984]. The subscript s refers to the suppressor grid and v_s is defined in a manner analogous to v_k

$$\mathrm{v}_s \equiv \left[\frac{2\, Z_i^* e\, \phi_s}{A_i\, m_p}\right]^{1/2} \tag{2.2.8}$$

where ϕ_s is the potential on the suppressor grid. T_0 is the value of the transparency function at normal incidence, where $T_0 = 0.65$ for the main sensor and $T_0 = 0.68$ for the side sensor.

The sensitive area is defined to be the area overlap of the collector with the projected image of the aperture onto the collector. Depending on the angle of incidence of the particle, the projected image of the aperture onto the collector will shift. This shift vector, $\mathbf{s}^*(v, v_k, v_s)$, is then defined as the displacement of the aperture image from a perpendicular projection of the aperture into the plane of the collector (see Fig. 2.2-1). The sensitive area of the main sensor can be written as a product of two terms

$$A(v, v_k) = A_0 A_x\left[\frac{s_x^*(v_k, v_s)}{h}\right] A_y\left[\frac{s_x^*(v_k, v_s)}{h}, \frac{s_y^*(v_k, v_s)}{h}\right] \tag{2.2.9}$$

At normal incidence, the sensitive area is equal to the aperture area, A_0. The product of the transparency function and sensitive area, at normal incidence, is defined as the effective area, where $A_0T_0 = 67.3\ \text{cm}^2$ for each of the three cups making up the main sensor and $A_0T_0 = 56.2\ \text{cm}^2$ for the side sensor. $A_x(s_x^*/h)$ is the x component of the sensitive area due to a shift in the v_x direction, while $A_y(s_x^*/h, s_y^*/h)$ is the y component of the sensitive area due to a shift in both the v_x and v_y direction. The dependence of A_y on both v_x and v_y is due to the geometry of the instrument. The depth of the sensor is given by h.

From the equation of motion, the x and y components of the shift vector, i.e., s_x^* and s_y^* respectively, can be calculated. Using the conservation of energy and the assumption that the electrostatic fields are entirely in the z-direction, one obtains

$$\begin{aligned} s_x^* &\equiv x = v_x\, t \\ s_y^* &\equiv y = v_y\, t \end{aligned} \tag{2.2.10}$$

where t is the transit time of the particle from the aperture to the collector plate,

$$t \equiv \int_0^t dt' = \int_0^h \frac{dz}{\left[v_z^2 - \dfrac{2Z^* e\phi(z)}{Am_p}\right]^{1/2}} \tag{2.2.11}$$

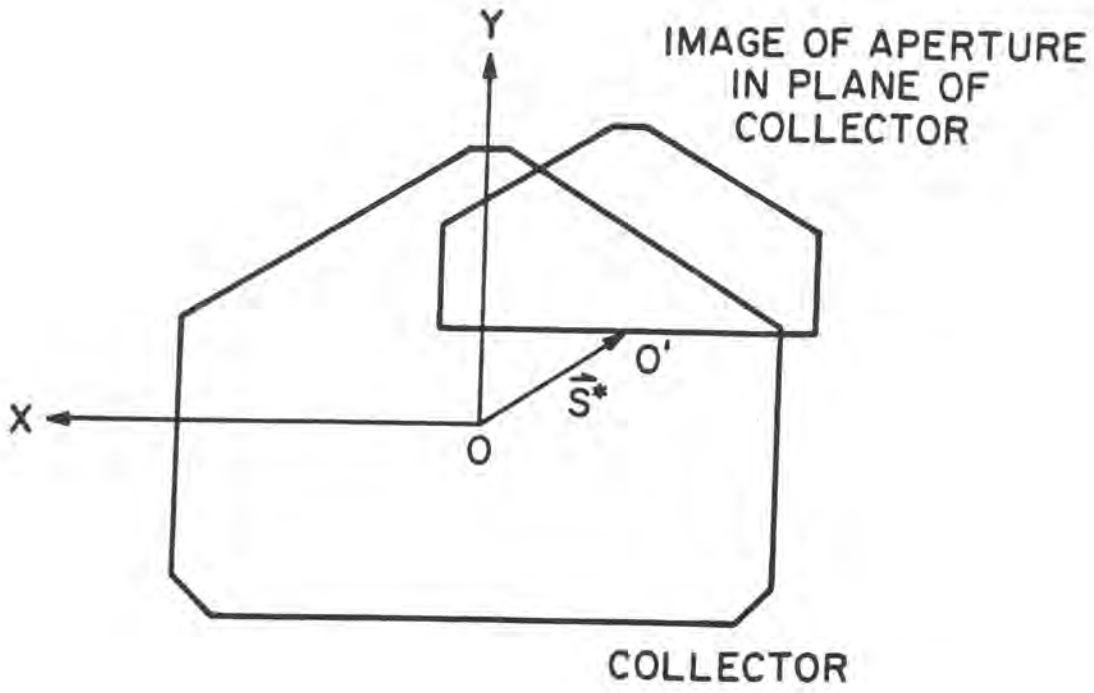

DEFINITION OF SHIFT VECTOR

Figure 2.2-1. Outline of the collector of one of the main sensor cups, with the image of the aperture in the collector plane superposed on it. The shift vector $\vec{s}^*$, lies in the collector plane and points from the position directly beneath the center of the long side of the aperture to the corresponing point on the image of the aperture in the incident beam. The $\hat{z}$ direction points into the cup for cup coordinates. Reprinted from *Barnett and Olbert*, [1986].

Substituting the following expressions for $\phi(z)$, see Fig. 2.2-2, into Eq. (2.2.11), *Barnett* [1984] obtains t for the main sensor:

$$\phi(z) = \begin{cases} \dfrac{z}{.762}\,\phi_k & 0 < z < .762 \\ \phi_k & .762 < z < 1.143 \\ \dfrac{1.905 - z}{.762}\,\phi_k & 1.143 < z < 1.905 \\ 0 & 1.905 < z < 2.286 \\ \dfrac{z - 2.286}{.414}\,\phi_s & 2.286 < z < 2.700 \\ \dfrac{3.089 - z}{.389}\,\phi_s & 2.700 < z < 3.089 \\ 0 & 3.089 < z < 4.100 \end{cases} \tag{2.2.12}$$

and solving for t, Eq. 2.2.10 becomes

$$s_x^* = s(v_k\,,\, v_s)\left[\frac{v_x}{v_z}\right] h \tag{2.2.13}$$

$$s_y^* = s(v_k\,,\, v_s)\left[\frac{v_y}{v_z}\right] h \tag{2.2.14}$$

where $s(v_k\,,v_s)$, the shift function, is, for the main sensor cups, given by

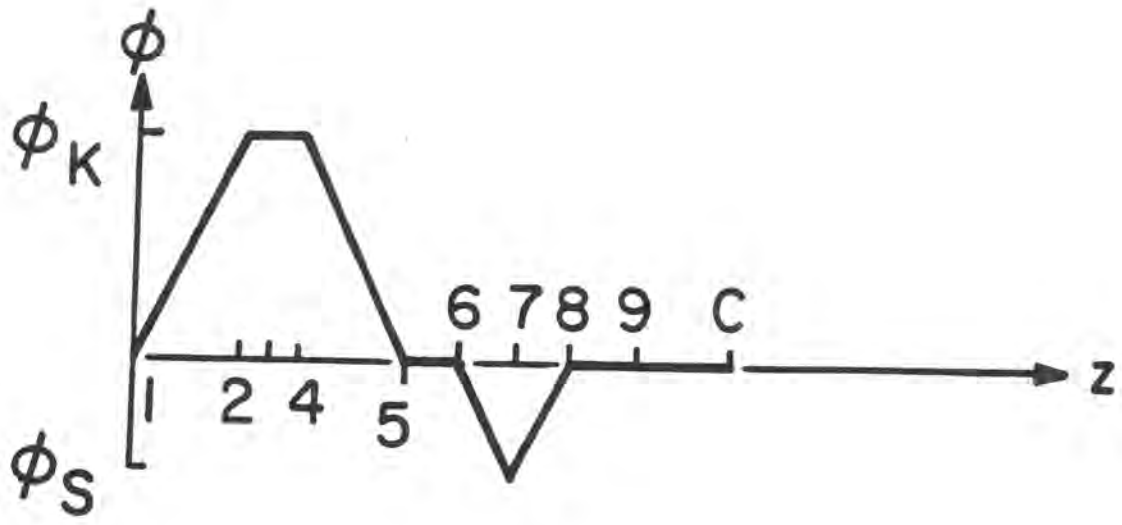

Figure 2.2-2. Model potential vs. z for a main sensor cup of the PLS. The numbered tick marks correspond to the grid locations, and c corresponds to the collector. Reprinted from *Barnett and Olbert*, [1986].

$$s(v_k, v_s) \equiv .743 \left\{ \frac{1-\left[1-\left[\frac{v_k}{v_z}\right]^2\right]^{1/2}}{\left[\frac{v_k}{v_z}\right]^2} \right\} + .093 \left[\frac{1}{1-\left[\frac{v_k}{v_z}\right]^2} \right]^{1/2}$$

$$+ .392 \left\{ \frac{\left[1+\left[\frac{v_s}{v_z}\right]^2\right]^{1/2} - 1}{\left[\frac{v_s}{v_z}\right]^2} \right\} + .340 \qquad (2.2.15)$$

Assuming the potential is a linear function of the distance between any two neighboring grids, z, is a good approximation since all that is neglected are the fringing fields. Fringing fields are important only near the edge of the grids, thus any particle whose trajectory would bring it near the grid edge would tend to miss the collector anyway due to cup transparency. The expression for the shift function for the side sensor, $s(v_k, v_s)$ found from a calculation similar to that given above, is

$$s(v_k, v_s) \equiv .720 \left\{ \frac{1-\left[1-\left[\frac{v_k}{v_z}\right]^2\right]^{1/2}}{\left[\frac{v_k}{v_z}\right]^2} \right\} + .290 \left\{ \frac{\left[1+\left[\frac{v_s}{v_z}\right]^2\right]^{1/2} - 1}{\left[\frac{v_s}{v_z}\right]^2} \right\} + .495$$

(2.2.16)

The sensitive area is now fully defined, and Fig. 2.2-3 shows $A(s^*)$ plotted as a function of s_y^*/h, with s_x^*/h as a parameter. However, the exact expression of $A(s^*)$ is not very tractable and an approximate representation is used, namely

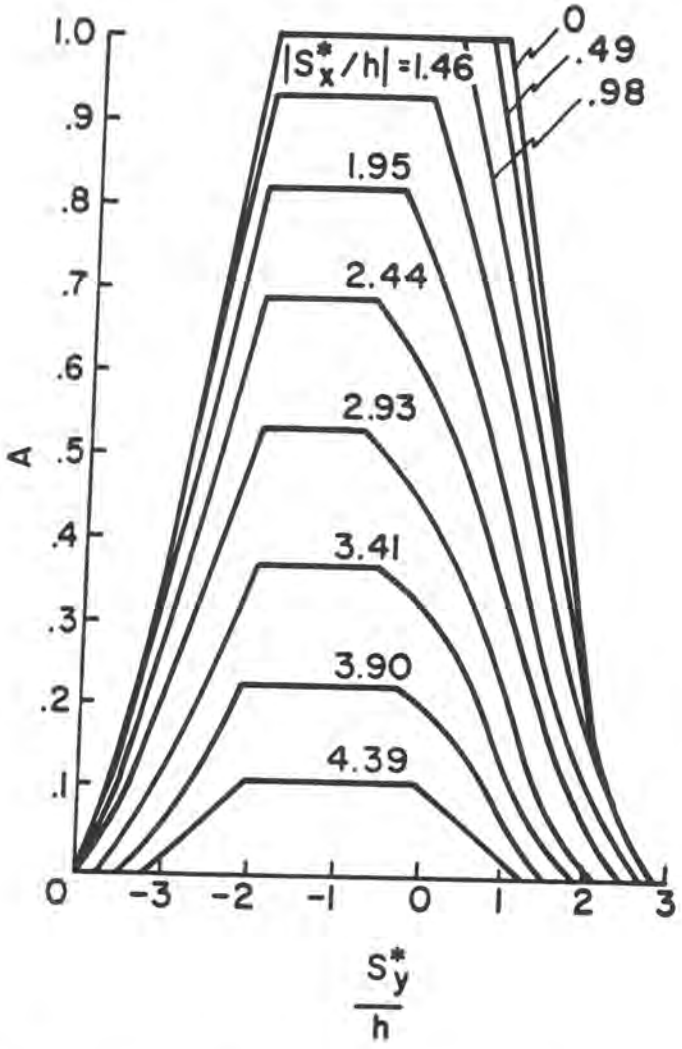

Figure 2.2-3. Main sensor sensitive area as a function of s_y^*/h with s_x^*/h as a parameter. Reprinted from *Barnett and Olbert*, [1986].

$$A_x\left[\frac{s_x^*}{h}\right] = \begin{cases} \dfrac{\frac{s_x^*}{h} + X_{r'}}{X_{r'} - X_r} & X_{l'} < \dfrac{s_x^*}{h} < X_l \\ 1 & X_l < \dfrac{s_x^*}{h} < X_r \\ \dfrac{X_{r'} - \frac{s_x^*}{h}}{X_{r'} - X_r} & X_r < \dfrac{s_x^*}{h} < X_{r'} \\ 0 & \textit{otherwise} \end{cases} \tag{2.2.17}$$

$$A_y\left[\frac{s_x^*}{h}, \frac{s_y^*}{h}\right] = \begin{cases} \dfrac{\frac{s_y^*}{h} - Y_{d'}}{Y_d - Y_{d'}} & Y_{d'} < \dfrac{s_y^*}{h} < Y_d \\ 1 & Y_d < \dfrac{s_y^*}{h} < Y_u\left[\dfrac{s_x^*}{h}\right] \\ \dfrac{\frac{s_y^*}{h} - Y_{u'}\left[\frac{s_x^*}{h}\right]}{Y_u\left[\frac{s_x^*}{h}\right] - Y_{u'}\left[\frac{s_x^*}{h}\right]} & Y_u\left[\dfrac{s_x^*}{h}\right] < \dfrac{s_y^*}{h} < Y_{u'}\left[\dfrac{s_x^*}{h}\right] \\ 0 & \textit{otherwise} \end{cases}$$

where $A(\mathbf{s}^*)$ is then given by Eq. 2.2.9 and $-X_{r'} = X_{l'}$ while $-X_r = X_l$. This new representation of the sensitive area is shown in Fig. 2.2-4. The values of X_r, $X_{r'}$, Y_d, $Y_{d'}$, $Y_u(s_x^*/h)$, and $Y_{u'}(s_x^*/h)$ are given below and were chosen such that the volume of the solid generated by the approximate expression of $A(\mathbf{s}^*)$, as given by Eq. 2.2.17, would match as closely as possible the

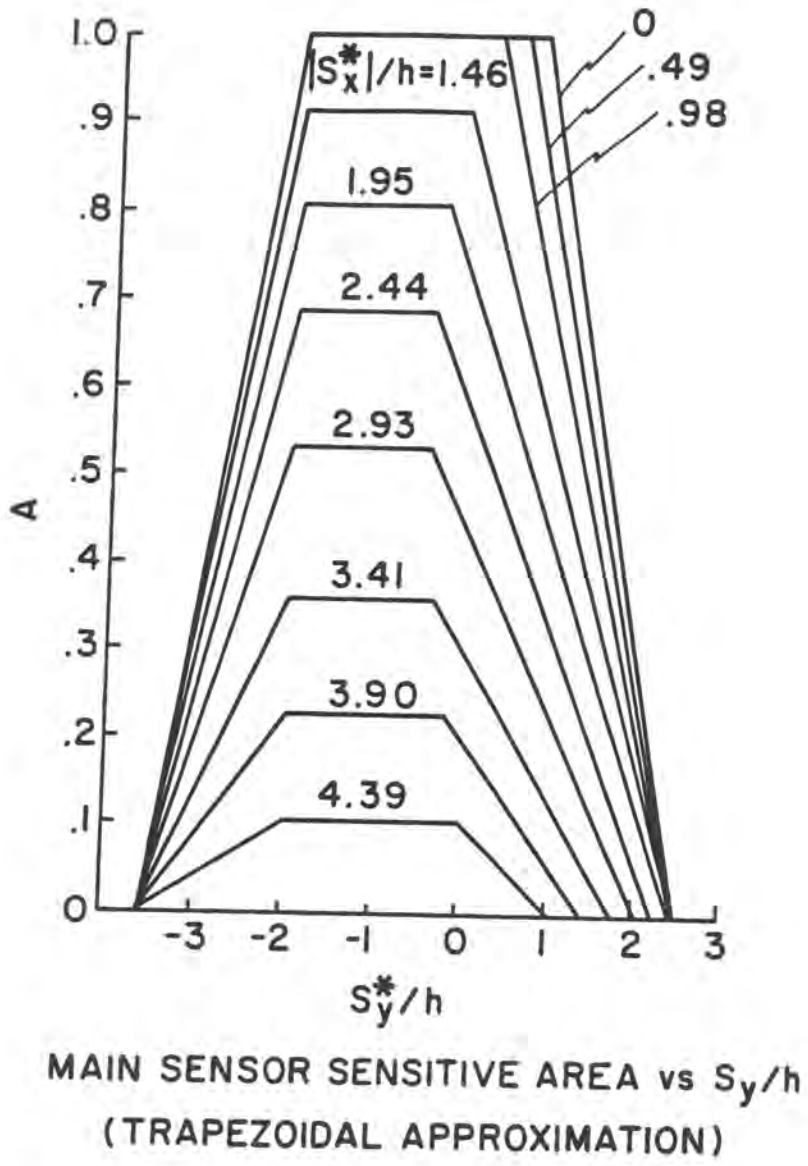

Figure 2.2-4. Main sensor sensitive area vs. s_y^*/h using the approximate form of $A(s^*)$ (i.e., using Eq. 2.2.17 for $A(s^*)$). Reprinted from *Barnett and Olbert*, [1986].

volume of the solid generated by the exact expression of $A(s^*)$ [*Barnett*, 1984].

$$X_r \equiv 1.10$$

$$X_{r'} \equiv 4.94$$

$$Y_d \equiv -2.02$$

$$Y_{d'} \equiv -3.62$$

$$Y_u \equiv \frac{.762 \cos\left[1.018\left[\frac{s_x^*}{h}\right] + .247\right]}{1 + .25\left[\frac{s_x^*}{h}\right]} \tag{2.2.18}$$

$$Y_{u'} \equiv 2.5 - .125\left[\left[\frac{s_x^*}{h}\right] - 1\right]^2$$

Substituting Eq. 2.2.6 into Eq. 2.2.5 gives for the expression of the total current,

$$I_k^*(\mathbf{x}, t) = Z^* e \int_{-\infty}^{\infty} dv_x \int_{-\infty}^{\infty} dv_y \int_{v_k}^{\infty} dv_z \, v_z f(\mathbf{x}, \mathbf{v}, t) \, T(\mathbf{v}, v_k) \, A(\mathbf{v}, v_k) \tag{2.2.19}$$

where $T(\mathbf{v}, v_k)$ is given by Eq. 2.2.7 and $A(\mathbf{v}, v_k)$ is given by Eq. 2.2.9 with $A_x(s_x^*/h)$ and $A_y(s_x^*/h, s_y^*/h)$ given, in turn, by the expressions in Eq. 2.2.17.

To completely specify the currents $I_k^*(\mathbf{x}, t)$, we must finally specify an analytic form of the distribution function of the ions, $f(\mathbf{x}, \mathbf{v}, t)$. Eq. 2.2.19 has been explicitly evaluated using two different ion distributions: a convected isotropic Maxwellian distribution and a convected bimaxwellian distribution. The case of a convected isotropic Maxwellian distribution was covered by *Barnett* [1984]. The bimaxwellian case is discussed below.

In general, a bimaxwellian distribution function can be written in the following form (see, e.g., *Rossi and Olbert* [1970]),

$$f(\mathbf{x}, \mathbf{v}, t) = \frac{n}{\pi^{3/2} w_{\|} w_{\perp}^2} \exp\left\{ - \frac{|\mathbf{v} - \mathbf{u}|^2}{w_{\perp}^2} - \left[\frac{1}{w_{\|}^2} - \frac{1}{w_{\perp}^2} \right] |(\mathbf{v} - \mathbf{u}) \cdot \hat{\mathbf{b}}|^2 \right\} \tag{2.2.20}$$

where,

$\mathbf{v} \equiv$ particle velocity

$n(\mathbf{x}, t) \equiv$ ion number density

$w_{\|}(\mathbf{x}, t) \equiv$ ion parallel thermal speed

$w_{\perp}(\mathbf{x}, t) \equiv$ ion perpendicular thermal speed

$\mathbf{u}(\mathbf{x}, t) \equiv$ ion bulk velocity

$\hat{\mathbf{b}}(\mathbf{x}, t) \equiv$ magnetic field unit vector

Substituting this expression for $f(\mathbf{x}, \mathbf{v}, t)$ into Eq. 2.2.19, making use of Eqs. 2.2.7 and 2.2.9 for $T(\mathrm{v}, \mathrm{v}_k)$ and $A(\mathbf{v}, \mathrm{v}_k)$ respectively, and rearranging terms, yields for $I_k^*(\mathbf{x}, t)$,

$$I_k^*(\mathbf{x}, t) = \sum_{i,j=1}^{2} B_{ij}(\mathbf{x}, t) \int_{\mathrm{v}_k}^{\infty} d\mathrm{v}_z \, \mathrm{v}_z \, I_3(\mathrm{v}_z) \int_{-\infty}^{\infty} d\mathrm{v}_x \, I_1(\mathrm{v}_x, \mathrm{v}_z) \int_{-\infty}^{\infty} d\mathrm{v}_y \, I_2(\mathbf{v}) \tag{2.2.21}$$

with

$$B_{ij}(\mathbf{x},t) \equiv \frac{Z^* e n T_0 A_0}{\pi^{3/2} w_{\|} w_{\perp}^2} \, c_i \, c_j \exp\left\{ - \left[\frac{u^2}{w_{\perp}^2} + \left[\frac{1}{w_{\|}^2} - \frac{1}{w_{\perp}^2} \right] (\mathbf{u} \cdot \hat{\mathbf{b}})^2 \right] \right\}$$

$$I_1(v_x, v_z) \equiv \exp\left\{ - v_x^2 \left[\frac{1}{w_\perp^2} + \left[\frac{1}{w_\parallel^2} - \frac{1}{w_\perp^2} \right] b_x^2 + \frac{a_i}{v_z^2} \right] + 2v_x \left[\frac{u_x}{w_\perp^2} - \left[\frac{1}{w_\parallel^2} - \frac{1}{w_\perp^2} \right] b_x \left[v_z b_z - \mathbf{u} \cdot \hat{\mathbf{b}} \right] \right] \right\} A_x \tag{2.2.22}$$

$$I_2(v) \equiv \exp\left\{ - v_y^2 \left[\frac{1}{w_\perp^2} + \left[\frac{1}{w_\parallel^2} - \frac{1}{w_\perp^2} \right] b_y^2 + \frac{a_j}{v_z^2} \right] + 2v_y \left[\frac{u_y}{w_\perp^2} - \left[\frac{1}{w_\parallel^2} - \frac{1}{w_\perp^2} \right] b_y \left[v_x b_x + v_z b_z - \mathbf{u} \cdot \hat{\mathbf{b}} \right] \right] \right\} A_y$$

$$I_3(v_z) \equiv \exp\left\{ -v_z^2 \left[\frac{1}{w_\perp^2} + \left[\frac{1}{w_\parallel^2} - \frac{1}{w_\perp^2} \right] b_z^2 \right] + 2v_z \left[\frac{u_z}{w_\perp^2} + \left[\frac{1}{w_\parallel^2} - \frac{1}{w_\perp^2} \right] b_z \left(\mathbf{u} \cdot \hat{\mathbf{b}} \right) \right] \right\}$$

By making a change of variable for each of the transverse velocity integrals and defining new variables,

$$X \equiv \left[\frac{v_x}{v_z} \right] s \quad , \quad Y \equiv \left[\frac{v_y}{v_x} \right] s \tag{2.2.23}$$

Eq. 2.2.21 takes on the final working form,

$$I_k^* = \frac{1}{s^2} \sum_{i,j=1}^{2} B_{ij} \int_{v_k}^{\infty} dv_z \, v_z^3 \, I_z \int_{-\infty}^{\infty} dX \, I_x(X) \int_{-\infty}^{\infty} dY \, I_y(X, Y) \tag{2.2.24}$$

Where s is the shift function and X and Y are defined as s_x^*/h and s_y^*/h, respectively (cf., Eqs. 2.2.13 and 2.2.14). In terms of these variables we also have

$$I_x(X) \equiv \exp\left(-\beta_x X^2 + 2\gamma_x X\right) A_x$$

$$I_y(X, Y) \equiv \exp\left[-\beta_y Y^2 + 2\gamma_y(X) Y\right] A_y$$

$$I_z \equiv \exp\left(-\beta_z v_z^2 + 2\gamma_z v_z\right)$$

with

$$\beta_x \equiv \left[\frac{v_z}{s}\right]^2 \left[\frac{1}{w_\perp^2} + \left[\frac{1}{w_\parallel^2} - \frac{1}{w_\perp^2}\right] b_x^2 + \frac{a_i}{v_z^2}\right]$$

$$\beta_y \equiv \left[\frac{v_z}{s}\right]^2 \left[\frac{1}{w_\perp^2} + \left[\frac{1}{w_\parallel^2} - \frac{1}{w_\perp^2}\right] b_y^2 + \frac{a_j}{v_z^2}\right]$$

$$\beta_z \equiv \frac{1}{w_\perp^2} + \left[\frac{1}{w_\parallel^2} - \frac{1}{w_\perp^2}\right] b_z^2$$

(2.2.25)

$$\gamma_x \equiv \left[\frac{v_z}{s}\right] \left\{\frac{u_x}{w_\perp^2} - \left[\frac{1}{w_\parallel^2} - \frac{1}{w_\perp^2}\right] b_x \left[v_z b_z - (\mathbf{u} \cdot \hat{\mathbf{b}})\right]\right\}$$

$$\gamma_y(X) \equiv \left[\frac{v_z}{s}\right] \left\{\frac{u_y}{w_\perp^2} - \left[\frac{1}{w_\parallel^2} - \frac{1}{w_\perp^2}\right] b_y \left[\left[\frac{X v_z}{s}\right] b_x + v_z b_z - (\mathbf{u} \cdot \hat{\mathbf{b}})\right]\right\}$$

$$\gamma_z \equiv \frac{u_z}{w_\perp^2} + \left[\frac{1}{w_\parallel^2} - \frac{1}{w_\perp^2}\right] b_z \, (\mathbf{u} \cdot \hat{\mathbf{b}})$$

A non-zero temperature anisotropy shows up via the expression $\left[\frac{1}{w_{\parallel}^2} - \frac{1}{w_{\perp}^2}\right]$. This expression can dominate terms in the expressions which contain it. As discussed later in this chapter, this temperature anisotropy factor greatly increases the mathematical complexity required to evaluate the model currents. This occurs because γ_y has an X dependence which adds considerable analytical complexity over the Maxwellian case.

Since there is an X dependence in the integrand of the Y integral, we evaluate the latter integral first. Looking only at the Y integral in Eq. 2.2.24, and completing the square in the exponential term in I_y, we obtain

$$K(X) \equiv \int_{-\infty}^{\infty} dY\, I_y(X, Y) = \frac{1}{\beta_y^{1/2}} \exp\left[\frac{\gamma_y^2(X)}{\beta_y}\right] \int_{-\infty}^{\infty} dZ\, A_y\, e^{-Z^2} \tag{2.2.26}$$

where

$$Z \equiv \beta_y^{1/2}\left[Y - \frac{\gamma_y(X)}{\beta_y}\right] \tag{2.2.27}$$

and A_y, as defined by Eq. 2.2.17, has Y (i.e. s_y^*/h) replaced by $\frac{1}{\beta_y^{1/2}}\left[Z + \frac{\gamma_y(X)}{\beta_y^{1/2}}\right]$ from Eq. 2.2.27. Substituting Eq. 2.2.17 for A_y into the integrand of Eq. 2.2.26 and integrating, gives

$$K(X) = \frac{1}{2}\left[\frac{\pi}{\beta_y}\right]^{1/2} \exp\left[\frac{\gamma_y{}^2(X)}{\beta_y}\right]\left[\frac{\phi(Z_{u'}) - \phi(Z_u)}{Z_{u'} - Z_u} - \frac{\phi(Z_{d'}) - \phi(Z_d)}{Z_{d'} - Z_d}\right] \tag{2.2.28}$$

with

$$\phi(Z) \equiv Z\, erf\,(Z) + \frac{1}{\sqrt{\pi}}\, e^{-Z^2} \tag{2.2.29}$$

and *erf*(*Z*) being the error function, viz.

$$erf(Z) \equiv \frac{2}{\sqrt{\pi}} \int_0^Z e^{-t^2}\, dt$$

The subscripts on Z refer to which value of Y, as defined in Eq. 2.2.18, was used in Eq. 2.2.27.

Before performing the X integral, a little background must be provided to understand the reason for selecting the particular solution technique used. The integral of interest is

$$G(v_z) \equiv \frac{1}{2} \left[\frac{\pi}{\beta_y}\right]^{1/2} \int_{-\infty}^{\infty} dX\, A_x \left[\frac{\phi(Z_{u'}) - \phi(Z_u)}{Z_{u'} - Z_u} - \frac{\phi(Z_{d'}) - \phi(Z_d)}{Z_{d'} - Z_d}\right] \qquad (2.2.30)$$

$$\times \exp\left[-\beta_x X^2 + 2\gamma_x X + \frac{\gamma_y^2(X)}{\beta_y}\right]$$

with $Z_{u'}$, Z_u, and γ_y all having X dependences. As the integral stands now, it cannot be evaluated in terms of analytical functions. Approximations must be made to simplify the integrand so the integral can be evaluated analytically.

In the case of a Maxwellian ion distribution function, the term inside the square brackets in Eq. 2.2.30, is a slowly varying function of X. For this reason, Eq. 2.2.30 can be expanded in a Taylor series and an average value of X defined (Mean Value Theorem, see *Barnett* [1984]). Let,

$$L(X) \equiv \left[\frac{\phi(Z_{u'}) - \phi(Z_u)}{Z_{u'} - Z_u} - \frac{\phi(Z_{d'}) - \phi(Z_d)}{Z_{d'} - Z_d}\right] \qquad (2.2.31)$$

Expanding yields

$$L(X) = L(\bar{X}) + \frac{X - \bar{X}}{2!} L'(\bar{X}) + \cdots$$

and we substitute this into Eq. 2.2.30, to obtain

$$G(v_z) \equiv \frac{1}{2}\left[\frac{\pi}{\beta_y}\right]^{1/2}\left\{ L(\bar{X})\int_{-\infty}^{\infty} dX\, A_x \exp\left[-\beta_x X^2 + 2\gamma_x X + \frac{\gamma_y^2}{\beta_y}\right] \right.$$
$$+ \left[\int_{-\infty}^{\infty} dX\, X\, A_x \exp\left[-\beta_x X^2 + 2\gamma_x X + \frac{\gamma_y^2}{\beta_y}\right]\right.$$
$$\left.\left. - \bar{X}\int_{-\infty}^{\infty} dX\, A_x \exp\left[-\beta_x X^2 + 2\gamma_x X + \frac{\gamma_y^2}{\beta_y}\right]\right] \frac{1}{2} L'(\bar{X}) \right\}$$

By defining $\bar{X}$ in the following way

$$\bar{X} \equiv \frac{\displaystyle\int_{-\infty}^{\infty} dX\, X\, A_x \exp\left[-\beta_x X^2 + 2\gamma_x X + \frac{\gamma_y^2(X)}{\beta_y}\right]}{\displaystyle\int_{-\infty}^{\infty} dX\, A_x \exp\left[-\beta_x X^2 + 2\gamma_x X + \frac{\gamma_y^2(X)}{\beta_y}\right]} \qquad (2.2.32)$$

the expression for the X integral is accurate to second order

$$G(v_z) \approx \frac{1}{2}\left[\frac{\pi}{\beta_y}\right]^{1/2} L(\bar{X})\int_{-\infty}^{\infty} dX\, A_x \exp\left[-\beta_x X^2 + 2\gamma_x X + \frac{\gamma_y^2}{\beta_y}\right]$$

where $L(X)$ is given by Eq. 2.2.31 and $\bar{X}$ given by Eq. 2.2.32. With this procedure, the transverse integrals (over v_y and v_x) can be performed analytically, leaving only the v_z integral to be done numerically.

This same procedure will not work to the same order of accuracy in the bimaxwellian case. The problem lies in the assumption that the expression in Eq. 2.2.31 is a slowly varying function of its argument. For the bimaxwellian situation, Z, which is a function of γ_y, has a term

like $\left[\frac{1}{w_{\|}^2} - \frac{1}{w_{\perp}^2}\right] X$, not found in the Maxwellian case. This added term can go through large, rapid changes as the analysis code searches parameter space for the best fit to the data. As a result, Eq. 2.2.31 can change quickly and an "average" value of X can no longer be well defined.

To circumvent this problem, the function $\phi(Z)$ was fit to a set of elementary functions. These functions, combined with the rest of the integrand, can then be integrated analytically. The empirical relation for $\phi(Z)$ is

$$\phi(Z) \approx |Z| + \frac{1}{\sqrt{\pi}} e^{-Z^2} + |Z| \left[c_1 e^{-a_1 Z^2} + c_2 e^{-a_2 Z^2}\right] \tag{2.2.33}$$

where,

$$a_1 = 1.3$$

$$a_2 = 7.0$$

$$c_1 = -.6$$

$$c_2 = -.3$$

with a maximum error of ~0.2% occurring in the interval $Z = 0.0$ to $Z = 2.5$. A plot of $\phi(Z)$ along with its approximation, Eq. 2.2.33, is given in Fig. 2.2-5. The first two terms in Eq. 2.2.33 were obtained by considering the two limiting cases of the exact expression of $\phi(Z)$, Eq. 2.2.29. In the case of $Z \to \pm\infty$, $\phi(Z) \to |Z|$, and when $Z \to 0$, $\phi(Z) \to \frac{1}{\sqrt{\pi}} e^{-Z^2}$. The last two terms are simply a combination of the first two with parameters chosen to minimize the error between the exact expression of $\phi(Z)$ and its empirical representation, Eq. 2.2.33.

Using Eq. 2.2.33 for $\phi(Z)$, Eq. 2.2.30 can now be integrated. By completing the square of the argument of the exponential, Eq. 2.2.30 becomes

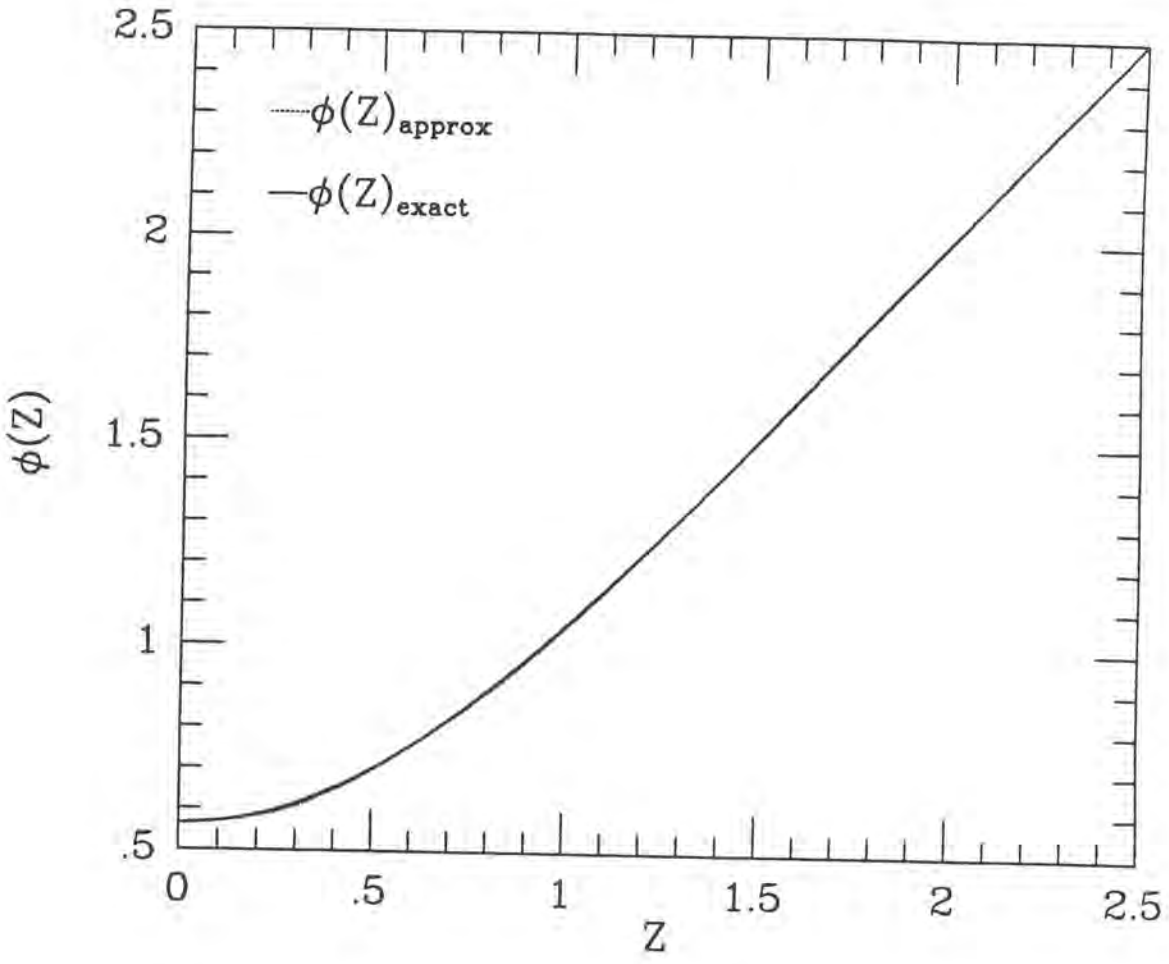

Figure 2.2-5. A plot of $\phi(Z)$ (i.e., Eq. 2.2.29) and its empirical approximation (Eq. 2.2.33).

$$G(v_z) = \frac{1}{2}\left[\frac{\pi}{\beta_y}\right]^{1/2} \exp(\delta + \frac{\gamma^2}{\beta}) \int_{-\infty}^{\infty} dX\, A_x\, L(X) \exp\left[-\beta(X - \frac{\gamma}{\beta})^2\right] \qquad (2.2.34)$$

with

$$\delta \equiv \frac{\left\{\left[\frac{u_y}{w_\perp^2} - \left[\frac{1}{w_\parallel^2} - \frac{1}{w_\perp^2}\right] b_y \left[v_z b_z - (\mathbf{u}\cdot\hat{\mathbf{b}})\right]\right]\right\}^2}{\left[\frac{1}{w_\perp^2} + \left[\frac{1}{w_\parallel^2} - \frac{1}{w_\perp^2}\right] b_y^2 + \frac{a_j}{v_z^2}\right]}$$

$$\beta \equiv \left[\frac{v_z}{s}\right]^2 \left\{\left[\frac{1}{w_\perp^2} + \left[\frac{1}{w_\parallel^2} - \frac{1}{w_\perp^2}\right] b_x^2 + \frac{a_i}{v_z^2}\right] - \frac{\left[\left[\frac{1}{w_\parallel^2} - \frac{1}{w_\perp^2}\right] b_y b_x\right]^2}{\left[\frac{1}{w_\perp^2} + \left[\frac{1}{w_\parallel^2} - \frac{1}{w_\perp^2}\right] b_y^2 + \frac{a_j}{v_z^2}\right]}\right\}$$

$$\gamma \equiv \left[\frac{v_z}{s}\right]\left\{\frac{u_x}{w_\perp^2} - \left[\frac{1}{w_\parallel^2} - \frac{1}{w_\perp^2}\right] b_x \left[v_z b_z - (\mathbf{u}\cdot\hat{\mathbf{b}})\right]\right.$$

$$\left. - \left[\frac{1}{w_\parallel^2} - \frac{1}{w_\perp^2}\right] b_y b_x \frac{\left\{\left[\frac{u_y}{w_\perp^2} - \left[\frac{1}{w_\parallel^2} - \frac{1}{w_\perp^2}\right] b_y \left[v_z b_z - (\mathbf{u}\cdot\hat{\mathbf{b}})\right]\right]\right\}}{\left[\frac{1}{w_\perp^2} + \left[\frac{1}{w_\parallel^2} - \frac{1}{w_\perp^2}\right] b_y^2 + \frac{a_j}{v_z^2}\right]}\right\}$$

and with A_x and $L(X)$ given by Eqs. 2.2.17 and 2.2.31, respectively. Since the X dependence in Y_u and $Y_{u'}$ (i.e., Z_u and $Z_{u'}$) is weak, it is neglected and the integration in Eq. 2.2.34 can be performed. The values used for Y_u and $Y_{u'}$ resulted from a weighted average using A_x for the weighting function, and are $Y_u = 0.048$ and $Y_{u'} = 2.29$ [*McNutt and Olbert*, private communication].

Since $\phi(Z)$ is a function of $|Z|$, there are several cases for the integral in Eq.2.2.34. In general Z can be written in the form

$$Z = \alpha + \sigma X$$

where α and σ are defined via

$$\alpha \equiv \beta_y^{1/2} \left\{ Y - \frac{\left[\frac{v_z}{s}\right]\left[\frac{u_y}{w_\perp^2} - \left[\frac{1}{w_\parallel^2} - \frac{1}{w_\perp^2}\right] b_y \left[v_z b_z - (\mathbf{u}\cdot\hat{\mathbf{b}})\right]\right]}{\beta_y} \right\}$$

$$\sigma \equiv \frac{1}{\beta_y^{1/2}} \left[\left[\frac{v_z}{s}\right]^2 \left[\frac{1}{w_\parallel^2} - \frac{1}{w_\perp^2}\right] b_y b_x\right]$$

For the case where $\sigma > 0$,

$$Z > 0 \quad when \quad X > -\frac{\alpha}{\sigma}$$
$$Z < 0 \quad when \quad X < -\frac{\alpha}{\sigma}$$

If $\sigma < 0$, the inequalities are reversed

$$Z > 0 \quad when \quad X < \frac{\alpha}{|\sigma|}$$
$$Z < 0 \quad when \quad X > \frac{\alpha}{|\sigma|}$$

Also, since A_x takes on five different expressions throughout the range of integration, there are ten possible results for the integral of Eq. 2.2.34. Which of these ten expressions is used depends on where Z changes sign and on the sign of σ. For the case where $\sigma > 0$, the following inequalities determine which of the five possible expressions is to be used for the integral:

(A) $\quad P_c < \xi_{l'}$

(B) $\quad \xi_{l'} < P_c < \xi_l$

(C) $\quad \xi_l < P_c < \xi_r$

(D) $\quad \xi_r < P_c < \xi_{r'}$

(E) $\quad \xi_{r'} < P_c$

where P_c is the critical point, defined as that point where Z changes sign, and ξ represents a generalized variable of integration. The subscripts correspond to the endpoints of each of the ranges over which the various forms of A_x are used.

Since $L(X)$ contains only sums and differences of the function $\phi(Z)$, one needs only perform the following integral (cf., Eq 2.2.34)

$$g(v_z) \equiv \frac{1}{2}\left[\frac{\pi}{\beta_y}\right]^{1/2} \exp(\delta + \frac{\gamma^2}{\beta}) \int_{-\infty}^{\infty} dX\, A_x\, \phi[\, Z(X)\,] \exp\left[-\beta(X - \frac{\gamma}{\beta})^2\right] \tag{2.2.35}$$

Substituting in Eq. 2.2.33 for $\phi(Z)$, four integrals must be performed. These integrals are summarized below:

$$g_1(v_z) = \frac{1}{2}\left[\frac{\pi}{\beta_y}\right]^{1/2} \exp(\delta + \frac{\gamma^2}{\beta}) \int_{-\infty}^{\infty} dX\, A_x\, |Z(X)| \exp\left[-\beta(X - \frac{\gamma}{\beta})^2\right]$$

$$g_2(v_z) = \frac{1}{2}\left[\frac{\pi}{\beta_y}\right]^{1/2} \frac{1}{\sqrt{\pi}} \exp(\delta + \frac{\gamma^2}{\beta}) \int_{-\infty}^{\infty} dX\, A_x\, e^{-Z^2(X)} \exp\left[-\beta(X - \frac{\gamma}{\beta})^2\right]$$

$$g_3(v_z) = \frac{1}{2}\left[\frac{\pi}{\beta_y}\right]^{1/2} B \exp(\delta + \frac{\gamma^2}{\beta}) \int_{-\infty}^{\infty} dX\, A_x\, |Z(X)|\, e^{-KZ^2(X)} \exp\left[-\beta(X - \frac{\gamma}{\beta})^2\right]$$

(2.2.36)

where,

$$B = c_1 \text{ or } c_2$$

$$K = a_1 \text{ or } a_2$$

The first integral is

$$g_1(v_z) = \frac{1}{2}\left[\frac{\pi}{\beta_y}\right]^{1/2} \exp(\delta + \frac{\gamma^2}{\beta}) \int_{-\infty}^{\infty} dX\, A_x\, |Z(x)| \exp\left[-\beta(X - \frac{\gamma}{\beta})^2\right]$$

Performing a change of variables, define

$$\hat{Z} \equiv \beta^{1/2}(X - \frac{\gamma}{\beta})$$

then $|Z| = \left|\alpha + \sigma\left[\frac{\hat{Z}}{\beta^{1/2}} + \frac{\gamma}{\beta}\right]\right|$, and the generalized variable of integration, ξ, becomes $\hat{Z}$. Using the five inequalities previously mentioned, the results are,

Case (A) $\quad P_c < \hat{Z}_f$

For this situation, $|Z| \rightarrow +Z$ throughout the range of integration,

$$g_1^A(v_z) = \frac{1}{2}\left[\frac{\pi}{\beta_y}\right]^{1/2}\left[\frac{1}{\hat{Z}_{f'} - \hat{Z}_r}\right]\frac{\sqrt{\pi}}{2}\frac{1}{\beta^{1/2}}\exp(\delta + \frac{\gamma^2}{\beta})\left\{\frac{1}{2}\frac{\sigma}{\beta^{1/2}}\left[erf(\hat{Z}_l)\right.\right.$$

$$\left.\left. + erf(\hat{Z}_r) - erf(\hat{Z}_f) - erf(\hat{Z}_{f'})\right] + (\alpha + \frac{\sigma\gamma}{\beta})\left[\phi(\hat{Z}_f) + \phi(\hat{Z}_{f'}) - \phi(\hat{Z}_l) - \phi(\hat{Z}_r)\right]\right\} \tag{2.2.37}$$

Case (B) $\quad \hat{Z}_f < P_c < \hat{Z}_l$

For this integral, the sign of Z changes in the interval of integration, that is

$$\int_{\hat{Z}_f}^{\hat{Z}_l} d\hat{Z}\,|Z|\,A_x\,e^{-\hat{Z}^2} = -\int_{\hat{Z}_f}^{P_c} d\hat{Z}\,Z\,A_x\,e^{-\hat{Z}^2} + \int_{P_c}^{\hat{Z}_l} d\hat{Z}\,Z\,A_x\,e^{-\hat{Z}^2}$$

One obtains,

$$g_1^B(v_z) = \frac{1}{2}\left[\frac{\pi}{\beta_y}\right]^{1/2}\left[\frac{1}{\hat{Z}_{f'} - \hat{Z}_r}\right]\frac{\sqrt{\pi}}{2}\frac{1}{\beta^{1/2}}\exp(\delta + \frac{\gamma^2}{\beta})\left\{\frac{1}{2}\frac{\sigma}{\beta^{1/2}}\right.$$

$$\times\left[erf(\hat{Z}_{f'}) + erf(\hat{Z}_l) + erf(\hat{Z}_r) - erf(\hat{Z}_{r'}) - 2erf(P_c) + \frac{4}{\sqrt{\pi}}(P_c - \hat{Z}_f)\,e^{-P_c^2}\right]$$

$$\left. + (\alpha + \frac{\sigma\gamma}{\beta})\left[\phi(\hat{Z}_{r'}) - \phi(\hat{Z}_{f'}) - \phi(\hat{Z}_l) - \phi(\hat{Z}_r) + 2\left[\hat{Z}_f\,erf(P_c) + \frac{1}{\sqrt{\pi}}\,e^{-P_c^2}\right]\right]\right\} \tag{2.2.38}$$

Case (C) $\quad \hat{Z}_l < P_c < \hat{Z}_r$

Since the point, within the range of the integral, at which Z changes sign has increased, a larger portion of the integral has a sign change, and we must break up the integral as follows;

$$\int_{\hat{Z}_{r'}}^{\hat{Z}_{l'}}(\ ) = -\int_{\hat{Z}_{r'}}^{\hat{Z}_l}(\ ) - \int_{\hat{Z}_l}^{P_c}(\ ) + \int_{P_c}^{\hat{Z}_r}(\ ) + \int_{\hat{Z}_r}^{\hat{Z}_{r'}}(\ )$$

Performing these integrals yields the following results

$$g_1^C(v_z) = \frac{1}{2}\left[\frac{\pi}{\beta_y}\right]^{1/2}\left[\frac{1}{\hat{Z}_{r'} - \hat{Z}_r}\right]\frac{\sqrt{\pi}}{2}\frac{1}{\beta^{1/2}}\exp(\delta + \frac{\gamma^2}{\beta})\left\{\frac{1}{2}\frac{\sigma}{\beta^{1/2}}\right.$$
$$\times\left[erf(\hat{Z}_{l'}) + erf(\hat{Z}_r) - erf(\hat{Z}_l) - erf(\hat{Z}_{r'}) + \frac{4}{\sqrt{\pi}}(\hat{Z}_r - \hat{Z}_r)\,e^{-P_c^2}\right]$$
$$\left. + (\alpha + \frac{\sigma\gamma}{\beta})\left[\phi(\hat{Z}_l) + \phi(\hat{Z}_{r'}) - \phi(\hat{Z}_{l'}) - \phi(\hat{Z}_r) - 2(\hat{Z}_{r'} - \hat{Z}_r)\,erf(P_c)\right]\right\} \tag{2.2.39}$$

Case (D) $\quad \hat{Z}_r < P_c < \hat{Z}_{r'}$

The integral now becomes

$$\int_{\hat{Z}_{r'}}^{\hat{Z}_{l'}}(\ ) = -\int_{\hat{Z}_{r'}}^{\hat{Z}_l}(\ ) - \int_{\hat{Z}_l}^{\hat{Z}_r}(\ ) - \int_{\hat{Z}_r}^{P_c}(\ ) + \int_{P_c}^{\hat{Z}_{r'}}(\ )$$

and the result is

$$g_1^D(v_z) = \frac{1}{2}\left[\frac{\pi}{\beta_y}\right]^{1/2}\left[\frac{1}{\hat{Z}_{r'} - \hat{Z}_r}\right]\frac{\sqrt{\pi}}{2}\frac{1}{\beta^{1/2}}\exp(\delta + \frac{\gamma^2}{\beta})\left\{\frac{1}{2}\frac{\sigma}{\beta^{1/2}}\right.$$

$$\times\left[erf(\hat{Z}_{l'}) - erf(\hat{Z}_l) - erf(\hat{Z}_r) - erf(\hat{Z}_{r'}) + 2erf(P_c) + \frac{4}{\sqrt{\pi}}(\hat{Z}_r - P_c)\,e^{-P_c^2}\right]$$

$$\left. + (\alpha + \frac{\sigma\gamma}{\beta})\left[\phi(\hat{Z}_l) + \phi(\hat{Z}_r) + \phi(\hat{Z}_{r'}) - \phi(\hat{Z}_{l'}) - 2\left[\hat{Z}_{r'}\,erf(P_c) + \frac{1}{\sqrt{\pi}}\,e^{-P_c^2}\right]\right]\right\} \tag{2.2.40}$$

Case (E) $\quad \hat{Z}_{r'} < P_c$

For this situation, $|Z| \rightarrow -Z$ over the full range of integration. Thus, the result will be the negative of the expression for Case (A).

$$g_1^E(v_z) = -g_1^A(v_z) \tag{2.2.41}$$

The second general integral to be evaluated is

$$g_2(v_z) = \frac{1}{2}\left[\frac{\pi}{\beta_y}\right]^{1/2}\frac{1}{\sqrt{\pi}}\exp(\delta + \frac{\gamma^2}{\beta})\int_{-\infty}^{\infty} dX\, A_x(X)\exp\left[-\beta\,(X - \frac{\gamma}{\beta})^2 - Z^2(X)\right]$$

Using the fact that $Z = \alpha + \sigma X$, one can complete the square of the argument of the exponential. Redefining the general variable of integration, $\xi = Z^*$, $g_2(v_z)$ may be rewritten as

$$g_2(v_z) = \frac{1}{2}\left[\frac{\pi}{\beta_y}\right]^{1/2}\frac{1}{\sqrt{\pi}}\,\frac{1}{\psi^{1/2}}\exp(\rho^2\psi + \delta - \alpha^2)\int_{-\infty}^{\infty} dZ^*\, A_x\left[\frac{Z^*}{\psi^{1/2}} + \rho\right]e^{-Z^{*2}} \tag{2.2.42}$$

where,

$$Z^* \equiv \psi^{1/2}(X - \rho)$$

$$\psi \equiv \beta + \sigma^2$$

$$\rho \equiv \frac{\gamma - \alpha\sigma}{\beta + \sigma^2} = \frac{\gamma - \alpha\sigma}{\psi}$$

Note that this integral is independent of $|Z|$, thus, the result is

$$g_2^A(v_z) = g_2^B(v_z) = g_2^C(v_z) = g_2^D(v_z) = g_2^E(v_z) =$$

$$\frac{1}{2}\left[\frac{\pi}{\beta_y}\right]^{1/2} \frac{1}{2}\frac{1}{\psi^{1/2}} \left[\frac{1}{\hat{Z}_{r'} - \hat{Z}_r}\right] \exp(\rho^2\psi + \delta - \alpha^2) \left[\phi(Z_r^*) + \phi(Z_{r'}^*) - \phi(Z_l^*) - \phi(Z_r^*)\right] \tag{2.2.43}$$

For the third general integral

$$g_3(v_z) = \frac{1}{2}\left[\frac{\pi}{\beta_y}\right]^{1/2} B \exp(\delta + \frac{\gamma^2}{\beta}) \int_{-\infty}^{\infty} dX\, A_x(X)\, |Z(X)| \exp\left[-\beta\,(X - \frac{\gamma}{\beta})^2 - KZ^2(X)\right]$$

Following the same procedure as for $g_2(v_z)$, $g_3(v_z)$ becomes

$$g_3(v_z) = \frac{1}{2}\left[\frac{\pi}{\beta_y}\right]^{1/2} \frac{B}{\psi^{1/2}} \exp(\rho^2\psi + \delta - K\alpha^2) \tag{2.2.44}$$

$$\times \int_{-\infty}^{\infty} dZ^*\, A_x\left[\frac{Z^*}{\psi^{1/2}} + \rho\right] \left|\alpha + \sigma\left[\frac{Z^*}{\psi^{1/2}} + \rho\right]\right| e^{-Z^{*2}}$$

This form is identical to the form $g_1(v_z)$. The results will then be the same; only the variable names are different. Explicitly, the expressions are

$$g_3^A(v_z) = \frac{1}{2}\left[\frac{\pi}{\beta_y}\right]^{1/2} \sum_{i=1}^{2} \frac{\sqrt{\pi}}{2}\left[\frac{1}{Z_{r'}^* - Z_r^*}\right]_i \frac{B_i}{\psi_i^{1/2}} \exp(\rho_i^2\psi_i + \delta - K_i\alpha^2)$$

$$\times \left\{\frac{1}{2}\,\frac{\sigma}{\psi_i^{1/2}}\left[erf(Z_l^*) + erf(Z_r^*) - erf(Z_{l'}^*) - erf(Z_{r'}^*)\right]_i\right.$$

$$\left. + (\alpha + \sigma\rho_i)\left[\phi(Z_{l'}^*) + \phi(Z_{r'}^*) - \phi(Z_l^*) - \phi(Z_r^*)\right]_i\right\} \qquad (2.2.45)$$

$$g_3^B(v_z) = \frac{1}{2}\left[\frac{\pi}{\beta_y}\right]^{1/2} \sum_{i=1}^{2} \frac{\sqrt{\pi}}{2}\left[\frac{1}{Z_{r'}^* - Z_r^*}\right]_i \frac{B_i}{\psi_i^{1/2}} \exp(\rho_i^2\psi_i + \delta - K_i\alpha^2) \left\{\frac{1}{2}\,\frac{\sigma}{\psi_i^{1/2}}\right.$$

$$\times \left[erf(Z_{l'}^*) + erf(Z_l^*) + erf(Z_r^*) - erf(Z_{r'}^*) - 2erf(P_c) + \frac{4}{\sqrt{\pi}}\,(P_c - Z_{l'}^*)\,e^{-P_c^2}\right]_i$$

$$\left. + (\alpha + \sigma\rho_i)\left[\phi(Z_{r'}^*) - \phi(Z_{l'}^*) - \phi(Z_l^*) - \phi(Z_r^*) + 2\left[Z_{l'}^*\,erf(P_c) + \frac{1}{\sqrt{\pi}}e^{-P_c^2}\right]\right]_i\right\}$$

(2.2.46)

$$g_3^C(v_z) = \frac{1}{2}\left[\frac{\pi}{\beta_y}\right]^{1/2} \sum_{i=1}^{2} \frac{\sqrt{\pi}}{2}\left[\frac{1}{Z_{r'}^* - Z_r^*}\right]_i \frac{B_i}{\psi_i^{1/2}} \exp(\rho_i^2\psi_i + \delta - K_i\alpha^2)$$

$$\times \left\{\frac{1}{2}\,\frac{\sigma}{\psi_i^{1/2}}\left[erf(Z_{l'}^*) + erf(Z_r^*) - erf(Z_l^*) - erf(Z_{r'}^*) + \frac{4}{\sqrt{\pi}}\,(Z_{r'}^* - Z_r^*)\,e^{-P_c^2}\right]_i\right.$$

$$\left. + (\alpha + \sigma\rho_i)\left[\phi(Z_l^*) + \phi(Z_{r'}^*) - \phi(Z_{l'}^*) - \phi(Z_r^*) - 2(Z_{r'}^* - Z_r^*)\,erf(P_c)\right]_i\right\}$$

(2.2.47)

$$g_3^D(v_z) = \frac{1}{2}\left[\frac{\pi}{\beta_y}\right]^{1/2} \sum_{i=1}^{2} \frac{\sqrt{\pi}}{2}\left[\frac{1}{Z_{r'}^* - Z_r^*}\right]_i \frac{B_i}{\psi_i^{1/2}} \exp(\rho_i^2\psi_i^2 + \delta - K_i\alpha^2)\left\{\frac{1}{2}\frac{\sigma}{\psi_i^{1/2}}\right.$$

$$\times\left\{\left[\left[erf(Z_{l'}^*) - erf(Z_l^*) - erf(Z_r^*) - erf(Z_{r'}^*) + 2erf(P_c) + \frac{4}{\sqrt{\pi}}(Z_{r'}^* - P_c)\, e^{-P_c^2}\right]\right]_i\right.$$

$$\left.\left. + (\alpha + \sigma\rho_i)\left[\left[\phi(Z_l^*) + \phi(Z_r^*) + \phi(Z_{r'}^*) - \phi(Z_{l'}^*) - 2\left[Z_{r'}^*\, erf(P_c) + \frac{1}{\sqrt{\pi}}e^{-P_c^2}\right]\right]\right]_i\right\} \tag{2.2.48}$$

$$g_3^E(v_z) = -g_3^A(v_z) \tag{2.2.49}$$

The summation is a reminder that there are actually two integrals being performed simultaneously. Recall that B_i and K_i refer to the parameters c_i and a_i, respectively, which are used in the empirical fit to the function $\phi(Z)$, Eq. 2.2.33. Also, in this case

$$Z_i^* \equiv \psi_i^{1/2}\,(X - \rho_i)$$

$$\psi_i \equiv \beta + K_i\,\sigma^2$$

$$\rho_i \equiv \frac{\gamma - K_i\,\alpha\sigma}{\beta + K_i\,\sigma^2} = \frac{\gamma - K_i\,\alpha\sigma}{\psi_i}$$

These variables differ from their counterparts used in evaluating $g_2(v_z)$ in that they are all dependent on the parameter K_i.

Eqs. 2.2.37 – 2.2.41, 2.2.43, and 2.2.45 – 2.2.49 have been derived assuming $\sigma > 0$; for the case $\sigma < 0$ the results are basically the same. For $\sigma < 0$ Eqs. 2.2.37 – 2.2.41 and 2.2.45 – 2.2.49 have a sign change for the entire expression. Only Eq. 2.2.43 remains unchanged since it is not a function of $|Z|$.

Collecting results, we list the ten possible results of evaluating Eq. 2.2.35 for cases (A) through (E), as defined above.

Case (A) $P_c < \xi_{sr}$:

$$g(v_z) = \begin{cases} g_1^A(v_z) + g_2^A(v_z) + g_3^A(v_z) & , \ \sigma > 0 \\ -g_1^A(v_z) + g_2^A(v_z) - g_3^A(v_z) & , \ \sigma < 0 \end{cases} \tag{2.2.50}$$

where $g_1^A(v_z)$, $g_2^A(v_z)$, and $g_3^A(v_z)$ are given by Eqs. 2.2.37, 2.2.43, and 2.2.45, respectively.

Case (B) $\xi_{sr} < P_c < \xi_{sl}$:

$$g(v_z) = \begin{cases} g_1^B(v_z) + g_2^B(v_z) + g_3^B(v_z) & , \ \sigma > 0 \\ -g_1^B(v_z) + g_2^B(v_z) - g_3^B(v_z) & , \ \sigma < 0 \end{cases} \tag{2.2.51}$$

where $g_1^B(v_z)$, $g_2^B(v_z)$, and and $g_3^B(v_z)$ are given by Eqs. 2.2.38, 2.2.43, and 2.2.46, respectively.

Case (C) $\xi_{sl} < P_c < \xi_{sr}$:

$$g(v_z) = \begin{cases} g_1^C(v_z) + g_2^C(v_z) + g_3^C(v_z) & , \ \sigma > 0 \\ -g_1^C(v_z) + g_2^C(v_z) - g_3^C(v_z) & , \ \sigma < 0 \end{cases} \tag{2.2.52}$$

where $g_1^C(v_z)$, $g_2^C(v_z)$, and $g_3^C(v_z)$ are given by Eqs. 2.2.39, 2.2.43, and 2.2.47, respectively.

Case (D) $\xi_{sr} < P_c < \xi_{sr'}$:

$$g(v_z) = \begin{cases} g_1^D(v_z) + g_2^D(v_z) + g_3^D(v_z) & , \ \sigma > 0 \\ -g_1^D(v_z) + g_2^D(v_z) - g_3^D(v_z) & , \ \sigma < 0 \end{cases} \tag{2.2.53}$$

where $g_1^D(v_z)$, $g_2^D(v_z)$, and $g_3^D(v_z)$ are given by Eqs. 2.2.40, 2.2.43, and 2.2.48, respectively.

Case (E) $\quad \xi_{r'} < P_c$:

$$g(v_z) = \begin{cases} g_1^E(v_z) + g_2^E(v_z) + g_3^E(v_z) & , \ \sigma > 0 \\ -g_1^E(v_z) + g_2^E(v_z) - g_3^E(v_z) & , \ \sigma < 0 \end{cases} \tag{2.2.54}$$

where $g_1^E(v_z)$, $g_2^E(v_z)$, and $g_3^E(v_z)$ are given by Eqs. 2.2.41, 2.2.43, and 2.2.49, respectively.

Using Eqs. 2.2.50 – 2.2.54, $G(v_z)$, as given by Eq. 2.2.34, can be determined under any of the ten conditions enumerated above and can be written as

$$G(v_z) = \frac{g_{u'}(v_z) - g_u(v_z)}{Z_{u'} - Z_u} - \frac{g_{d'}(v_z) - g_d(v_z)}{Z_{d'} - Z_d} \tag{2.2.55}$$

The subscripts on the g functions indicate which Y is being used (Eq. 2.2.18). Total current, given by Eq. 2.2.24, may then be written as

$$I_k^* = \frac{1}{s^2} \sum_{i,j=1}^{2} B_{ij} \int_{v_k}^{\infty} dv_z \, v_z^3 \, G(v_z) \, I_z \tag{2.2.56}$$

or, explicitly

$$I_k^* = \frac{1}{s^2} \sum_{i,j=1}^{2} B_{ij} \int_{v_k}^{\infty} dv_z \, v_z^3 \left[\frac{g_{u'}(v_z) - g_u(v_z)}{Z_{u'} - Z_u} - \frac{g_{d'}(v_z) - g_d(v_z)}{Z_{d'} - Z_d} \right] \tag{2.2.57}$$

$$\times \exp \left\{ -v_z^2 \left[\frac{1}{w_\perp^2} + \left[\frac{1}{w_\parallel^2} - \frac{1}{w_\perp^2} \right] b_z^2 \right] + 2v_z \left[\frac{u_z}{w_\perp^2} + \left[\frac{1}{w_\parallel^2} - \frac{1}{w_\perp^2} \right] b_z \, (\mathbf{u} \cdot \hat{\mathbf{b}}) \right] \right\}$$

The final integration over v_z, in Eq. 2.2.57, must be done numerically. The integrand is so convoluted that no analytical solution is possible unless many assumptions are made which

would result in a serious limitation of the usefulness of the analysis. Once $I_k^*(\mathbf{x},t)$ is found numerically, the current due to a given set of plasma parameters which would be measured in any given channel k, $I_k(\mathbf{x},t)$, can be calculated using Eq. 2.2.1.

The technique described above was chosen with the goal of calculating the current, in any given energy-per-charge channel, for the cups comprising the main sensor. To determine the current seen by the side sensor, or D-cup, a modification must be made. Since the side sensor has a circular aperture and collector, the response function is a function of $\sqrt{v_x^2 + v_y^2}$ and not of v_x and v_y separately as are the A, B, and C-cups. This ignores the geometry of the grid wires; however, the alignment of the grid wires is significant only for very supersonic flows into the side sensor [*Barnett*, 1984]. To apply the solution technique outlined in this chapter to the D-cup, an "equivalent" aperture and collector plate must be defined for the D-cup. This is done by taking the area of the D-cup aperture and defining an equivalent square aperture with the same area. This has the added advantage that Y_u and $Y_{u'}$ no longer have an X, i.e. v_x, dependence as did the cups of the main sensor (see Eq. 2.2.18).

This new bimaxwellian simulation code, called LABBI, was tested for accuracy by comparing the computed currents with those computed by two other simulation routines. For the case of the ion distribution function being a convected isotropic Maxwellian, currents computed by LABBI were compared against those computed with ABSO. The ABSO package was written by *Barnett* [1984] to compute the instrument response to a convected, isotropic Maxwellian distribution (the algorithm used was described above). Bimaxwellian simulations were compared with the output of the code PMODEL. This code evaluates the current (Eq. 2.2.1) for (arbitrary) distribution functions $f(\mathbf{x}, \mathbf{v}, t)$ specified in the rest frame of the plasma. The code was written by V. M. Vasyliunas and performs the triple integral of Eq. 2.2.4 numerically. The inherent problems of long computational time and numerical errors in PMODEL were primary motivations for producing the semi-analytic expressions given above.

The input plasma parameters for these cases are approximately the parameters for the O^+ peak in the spectrum obtained by Voyager 1 at Jupiter at 2323 UT (Universal Time) on day 63

(March 4) in 1979. These are:

$$
\begin{aligned}
A &= 16 \\
Z^* &= 1 \\
n &= 8.7\ \mathrm{cm}^{-3} \\
w &= 14.5\ \mathrm{km/sec} \\
u_x &= -115.281\ \mathrm{km/sec} \\
u_y &= -56.061\ \mathrm{km/sec} \\
u_z &= 34.5\ \mathrm{km/sec} \\
B_x &= 77.275\ \gamma \\
B_y &= -88.675\ \gamma \\
B_z &= -38.011\ \gamma
\end{aligned}
$$

Where $1\gamma \equiv 10^{-9}\ T$ and the thermal speed given is for the convected isotropic Maxwellian case. When comparing LABBI currents against those calculated with PMODEL, the thermal speed is broken up into parallel and perpendicular (with respect to the magnetic field) components, and these are then varied. The parameters chosen here represent a worst case because both the plasma velocity and magnetic field are oblique to the instrument.

Before discussing the results of the comparisons, we define the term "feedthrough", which is important in the discussion of the results. In the case of a convected isotropic Maxwellian, let the reduced distribution function (i.e., the transverse velocity integrals have been expicitly performed) be

$$f(\mathrm{v}_z) = \frac{n}{w\sqrt{\pi}}\, e^{-(\mathrm{v}_z - u_z)^2/w^2} \tag{2.2.58}$$

and the reduced, but unnormalized, response function for channel k be $R_k(\mathrm{v}_z)$; then Eq. 2.2.4 becomes

$$I_k^* = Z^* e \int_{\mathrm{v}_t}^{\infty} \mathrm{v}_z\, f(\mathrm{v}_z)\, R_k(\mathrm{v}_z)\, d\mathrm{v}_z \tag{2.2.59}$$

If the subtraction in Eq. 2.2.1 is performed before doing the numerical integration, the current

for channel k can be written as

$$I_k = Z^* e \int_{v_k}^{v_{k+1}} v_z f(v_z)\, R_k(v_z)\, dv_z + Z^* e \int_{v_{k+1}}^{\infty} v_z f(v_z) \left[R_k(v_z) - R_{k+1}(v_z) \right] dv_z \tag{2.2.60}$$

The first term on the right hand side of Eq. 2.2.60 represents the direct contribution to I_k, while the second term represents the feedthrough contribution. In the case of supersonic plasma flow into the sensors, the second term is negligible and leads to the approximately differential response of the instrument [*Bridge et. al.*, 1977]. Note the Eq. 2.2.60 immediately shows the origin of the feedthrough current by letting $f(v_z) \rightarrow n\delta(v_z - u_z)$.

For the Maxwellian case, comparison of currents produced with LABBI and those with ABSO show excellent agreement (see Figures 2.2-6 and 2.2-7). The maximum error in the currents in all the cups occurs in the D-cup and is less than 2%. The error occurs only in the feedthrough portion of the spectrum. At the peak, the currents calculated by the two routines are identical to four significant figures. Difference in the currents is due to the fact that LABBI uses the circular-to-square aperture modification mentioned above, while ABSO assumes a circular aperture [*Barnett*, 1984].

In the bimaxwellian case, comparison of LABBI and PMODEL is not as simple as for the Maxwellian case. The main problem stems from the fact that the integration step size used by PMODEL is an input variable. A step size which is reasonable for one choice of $w_{\parallel}$ and $w_{\perp}$ need not be (and usually is not) small enough for some other choice of $w_{\parallel}$ and $w_{\perp}$. Unfortunately, the computational time required by PMODEL increases approximately as the square of the number of velocity intervals used in numerically performing each of the velocity integrals, RSTEP [*R. L. McNutt, Jr.*, private communication, 1986]. Four cases representing various values of parallel and perpendicular thermal speeds are shown, with a discussion of each.

For the first case, we have taken $w_{\parallel} = 2.0$ km/sec , $w_{\perp} = 14.5$ km/sec and RSTEP = 7; the results are shown in Figures 2.2-8 and 2.2-9. The currents calculated were also printed in

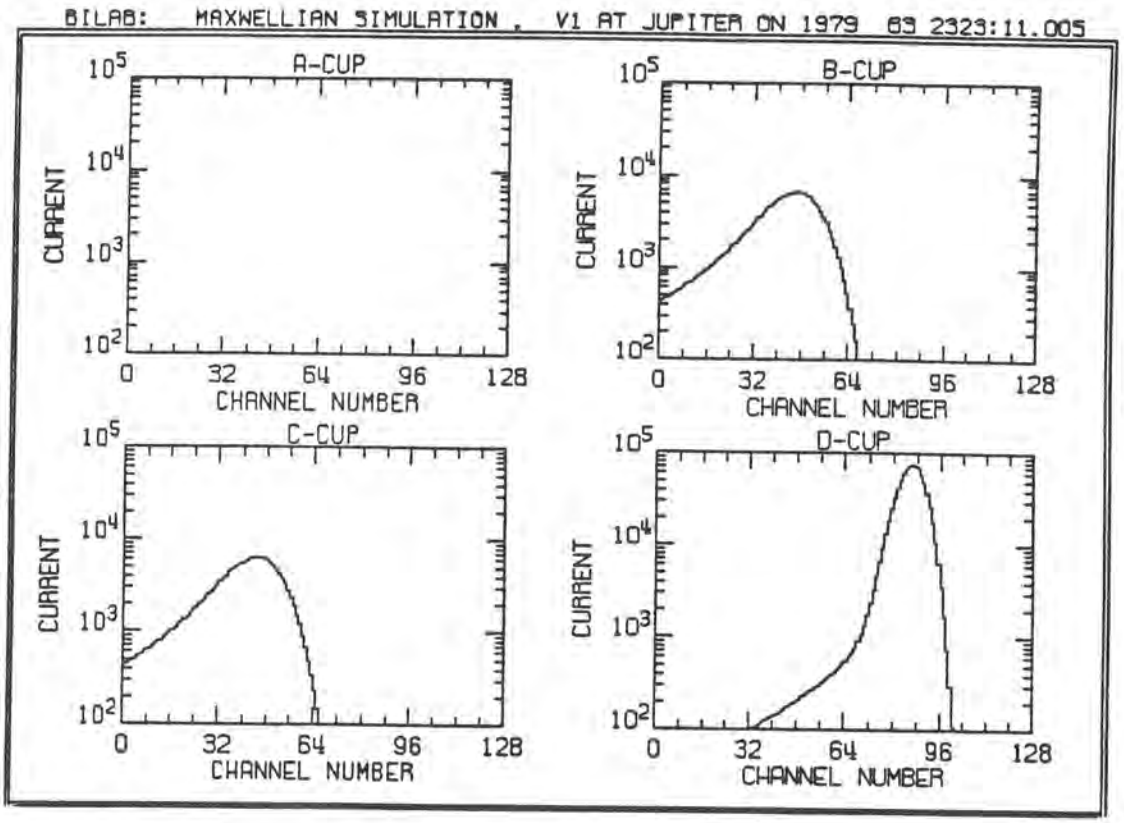

Figure 2.2-6. Simulated currents using LABBI. The input plasma parameters approximately represent the parameters for the O^+ peak from the spectrum at 2323 UT on day 63. The positive ion distribution function is assumed to be Maxwellian.

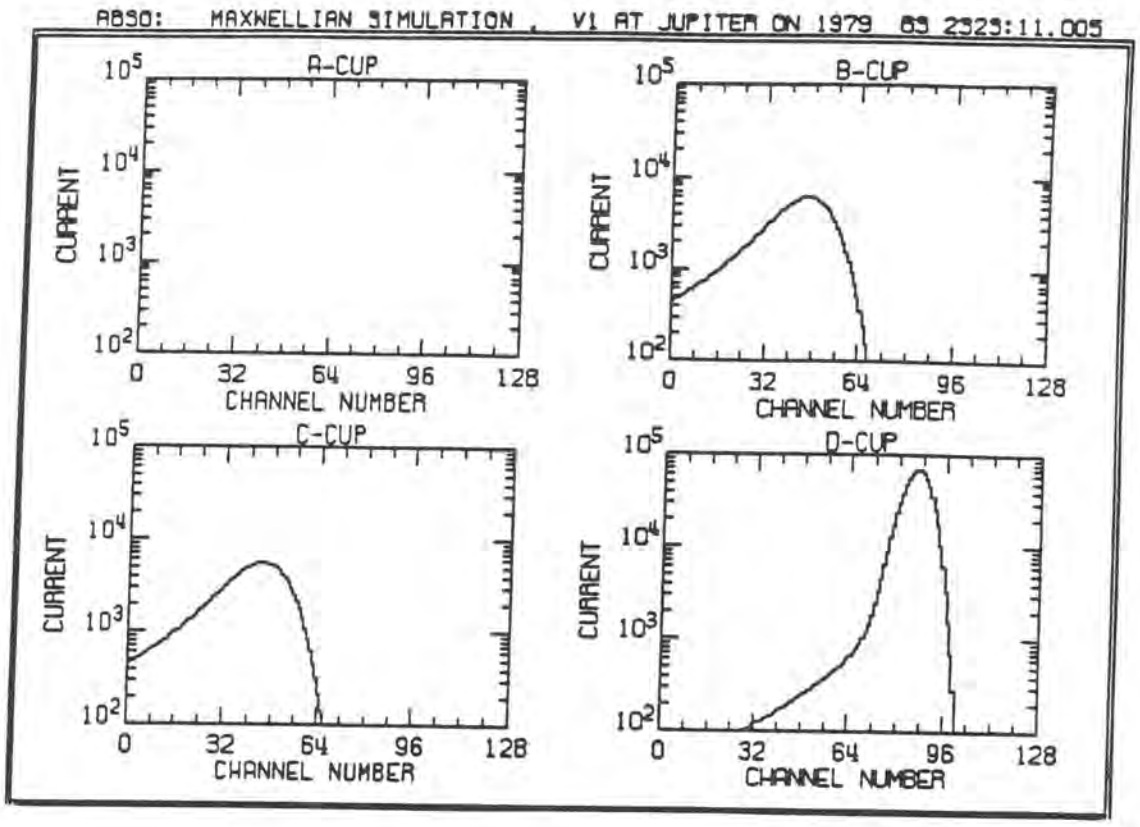

Figure 2.2-7. Simulated currents using ABSO. The input plasma parameters are the same as those for Fig. 2.2-6.

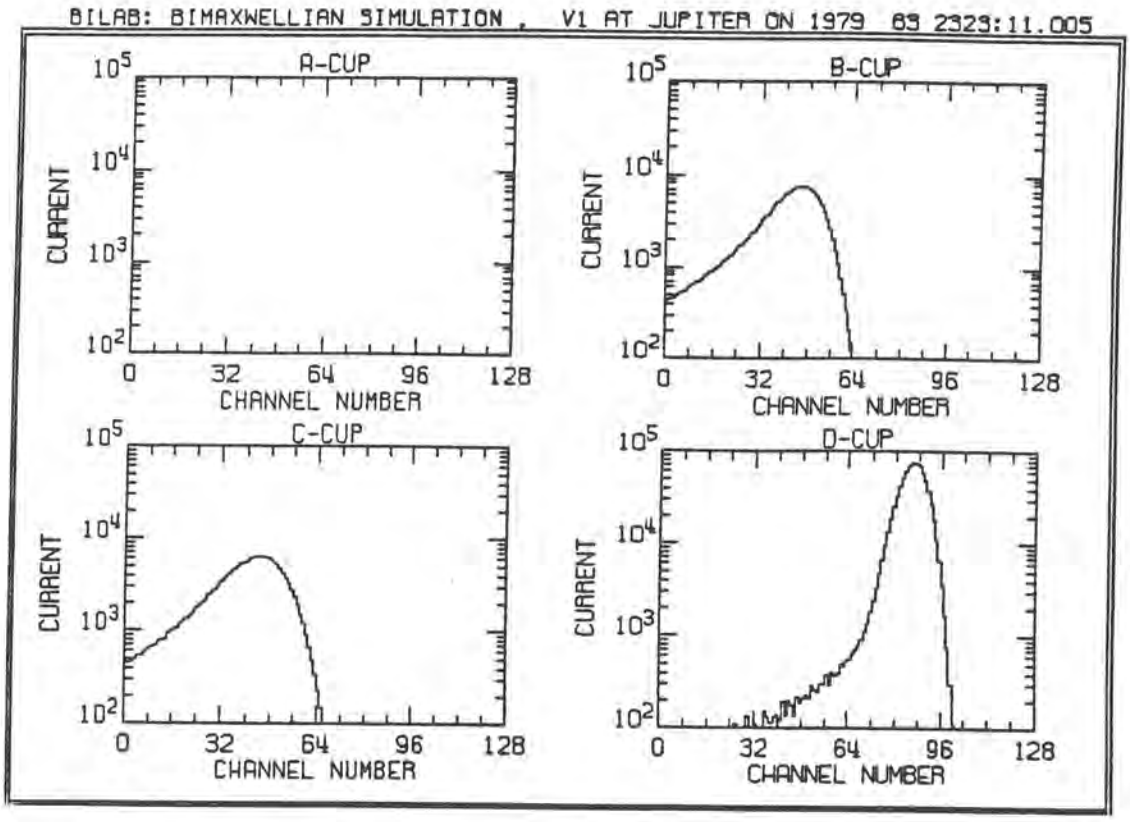

Figure 2.2-8. Simulated currents using LABBI, with a bimaxwellian positive ion distribution function. For this case, $w_{\parallel} = 2.0$ km/sec and $w_{\perp} = 14.5$ km/sec.

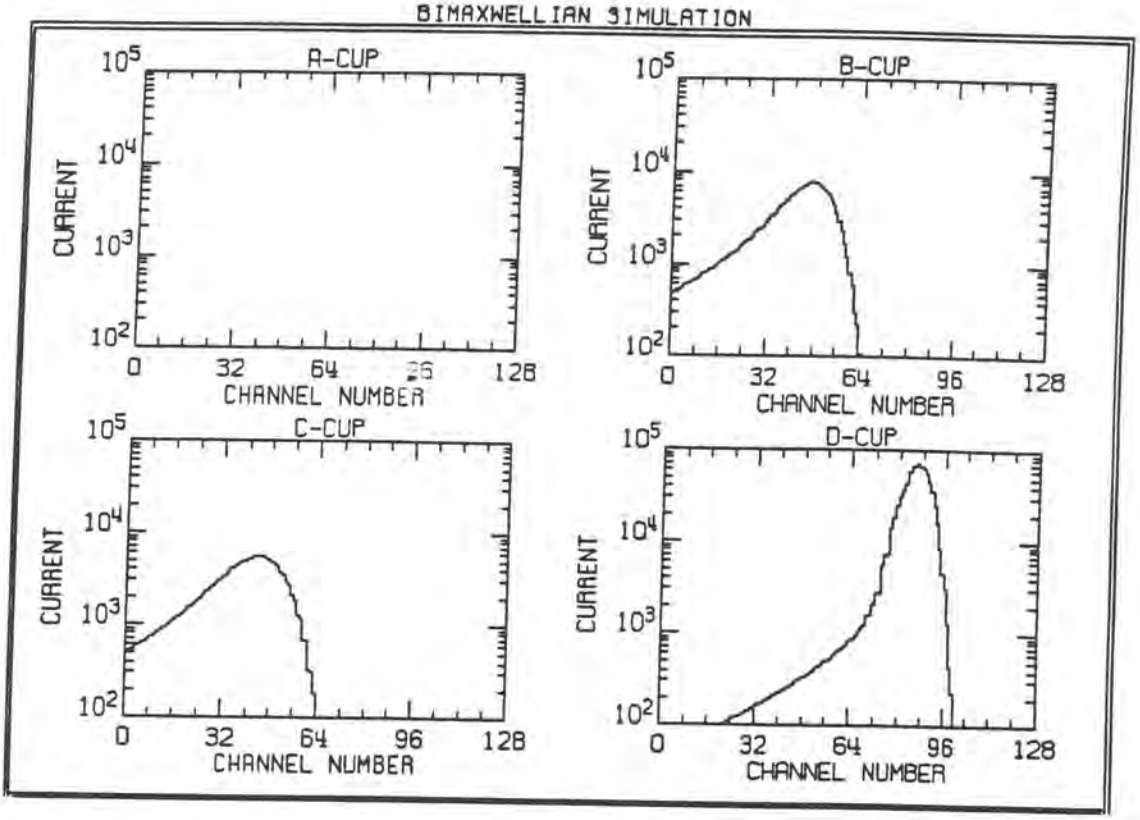

Figure 2.2-9. Simulated currents using PMODEL. The thermal speeds used are the same as those listed in Fig. 2.2-8, and the number of velocity steps used was RSTEP = 7.

tabular form so errors could be calculated. The maximum errors occured in the feedthrough portion (low energy tail) of the spectrum of currents. The maximum error of ~16% occurs in the first channel of the B-cup. At the channel corresponding to the maximum current (ion peak), the errors were quite small, < ~ 6 % in the main sensor and < 1 % in the D-cup.

In looking at Fig. 2.2-8 it is obvious that LABBI has trouble calculating the feedthrough portion of the current in the D-cup. However, in this region the peak has already decreased by about 2.5 orders of magnitude. Hence, this will not greatly affect the results of a fit to data exhibiting several ion peaks because the peaks due to other ions are also at least an order of magnitude larger than this feedthrough current. Figure 2.2-9 indicates that the integration step size used in PMODEL is marginal; the peaks have a rough appearance indicative of a step size which is too large. For this case the execution time is ~4 CPU minutes for LABBI and ~3 CPU minutes for PMODEL.

In the second case $w_{\|} = 7.25$ km/sec , $w_{\perp} = 14.5$ km/sec, and RSTEP = 10 (minimum required step size to insure accuracy); the results are shown in Figures 2.2-10 and 2.2-11. Again the maximum errors occured in the feedthrough portion of the spectrum and an error of ~16% was incurred in the first channel of the B-cup. Errors in the peak channels were < ~6% in the main sensor and ~9% in the side sensor. The error calculated for the D-cup is artifically high because the current calculated in that channel by PMODEL (see Fig. 2.2-11) is anomalously large. The spike, seen in the peak channel, gets smaller and smaller as RSTEP is increased. However, the running time gets prohibitively long as RSTEP increases. Increasing RSTEP from 10 to 15 increases the runtime from ~5 CPU minutes to over 20 CPU minutes, respectively (using the IBM 3081 at the Goddard Space Flight Center in Maryland). The feedthrough is handled much better by LABBI in this case (see Fig. 2.2-10), although the current is still lower then that calculated by PMODEL.

Next, the anisotropy is reversed; $w_{\|} = 14.5$ km/sec , $w_{\perp} = 7.25$ km/sec, and RSTEP = 20. The results shown in Figures 2.2-12 and 2.2-13 indicate errors that are larger throughout the whole spectrum. A maximum error of ~28% occurs in the D-cup, in the feedthrough portion of

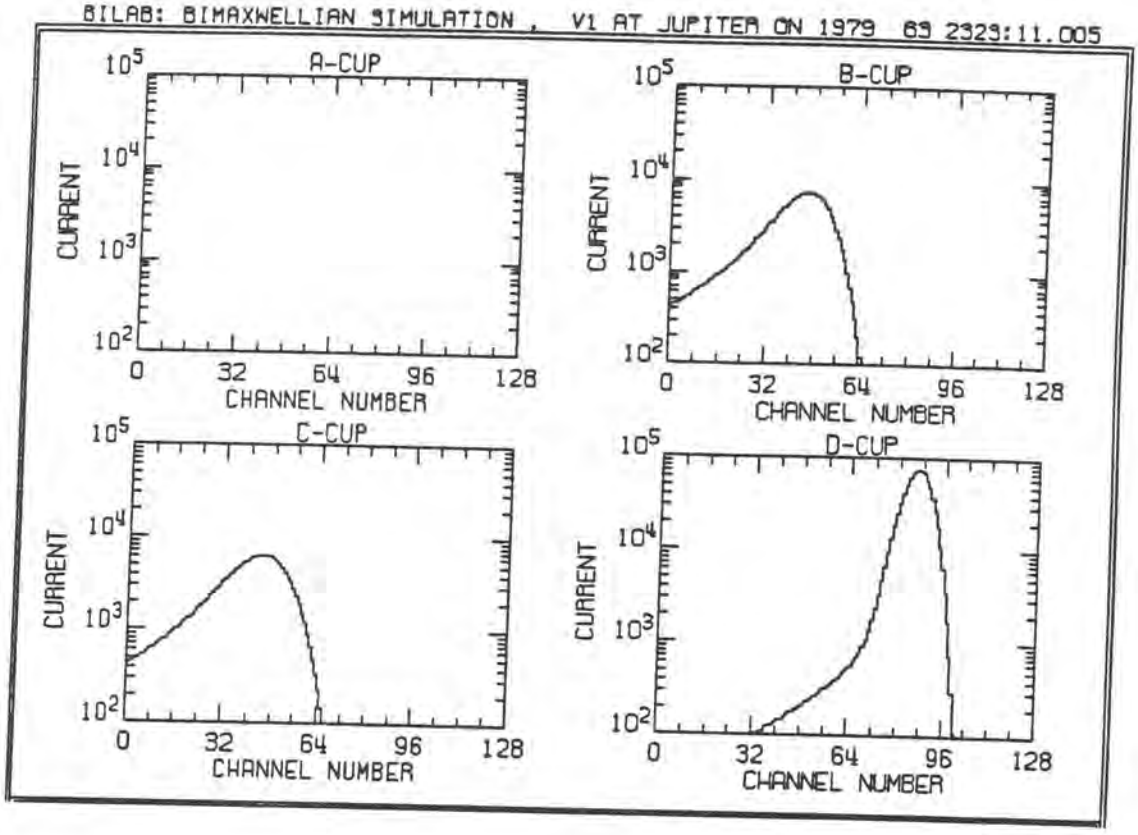

Figure 2.2-10. Simulated currents using LABBI. The thermal speeds used were $w_{\parallel} = 7.25$ km/sec and $w_{\perp} = 14.5$ km/sec.

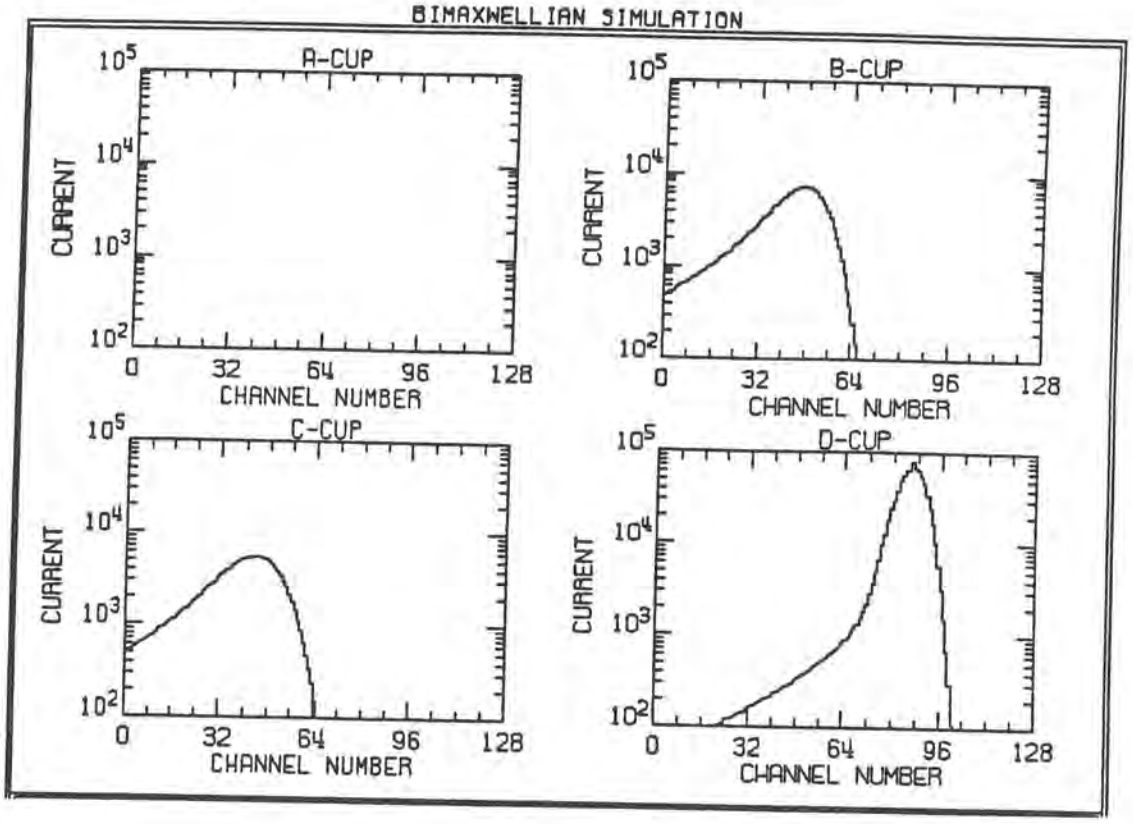

Figure 2.2-11. Simulated currents using PMODEL. The thermal speeds used are the same as those listed in Fig. 2.2-10, and the number of velocity steps used was RSTEP = 10.

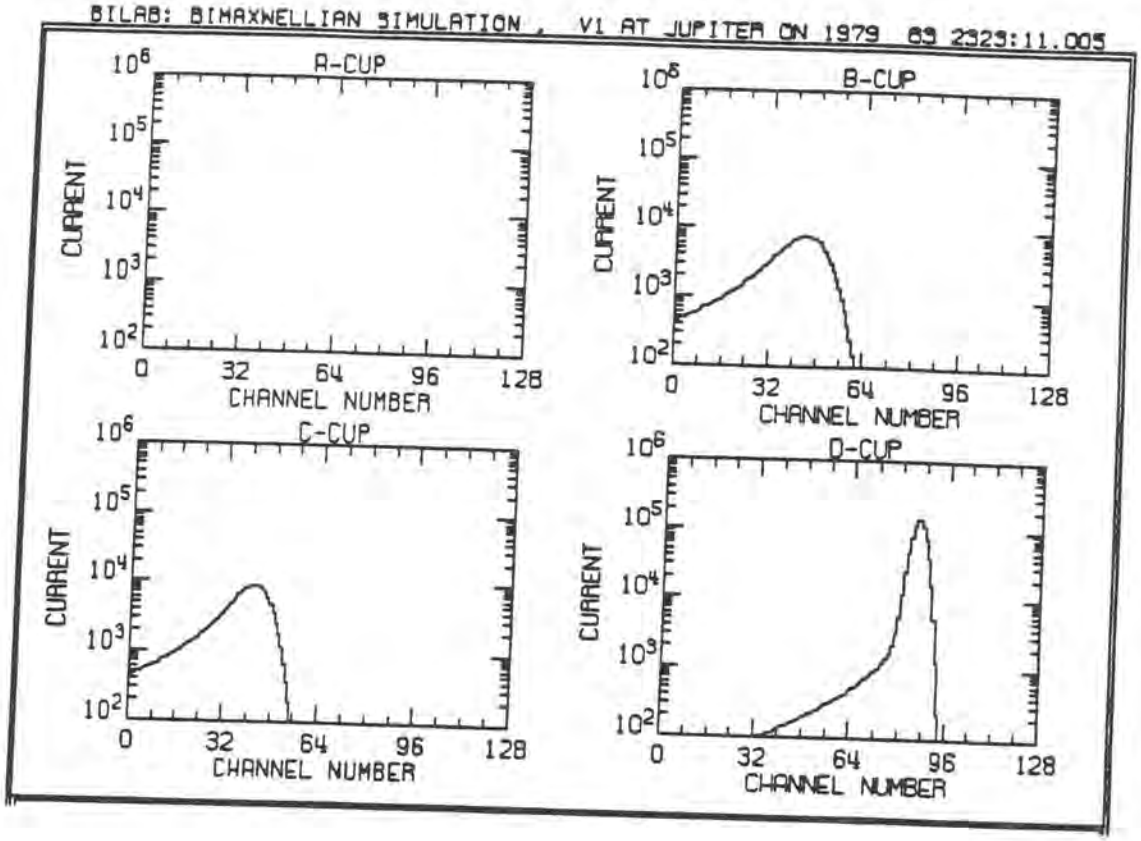

Figure 2.2-12. Simulated currents using LABBI. The thermal speeds used were $w_{\parallel} = 14.5$ km/sec and $w_{\perp} = 7.25$ km/sec. Note that the anisotropy is reversed from that of the previous figures ($w_{\parallel}$ is now larger than $w_{\perp}$).

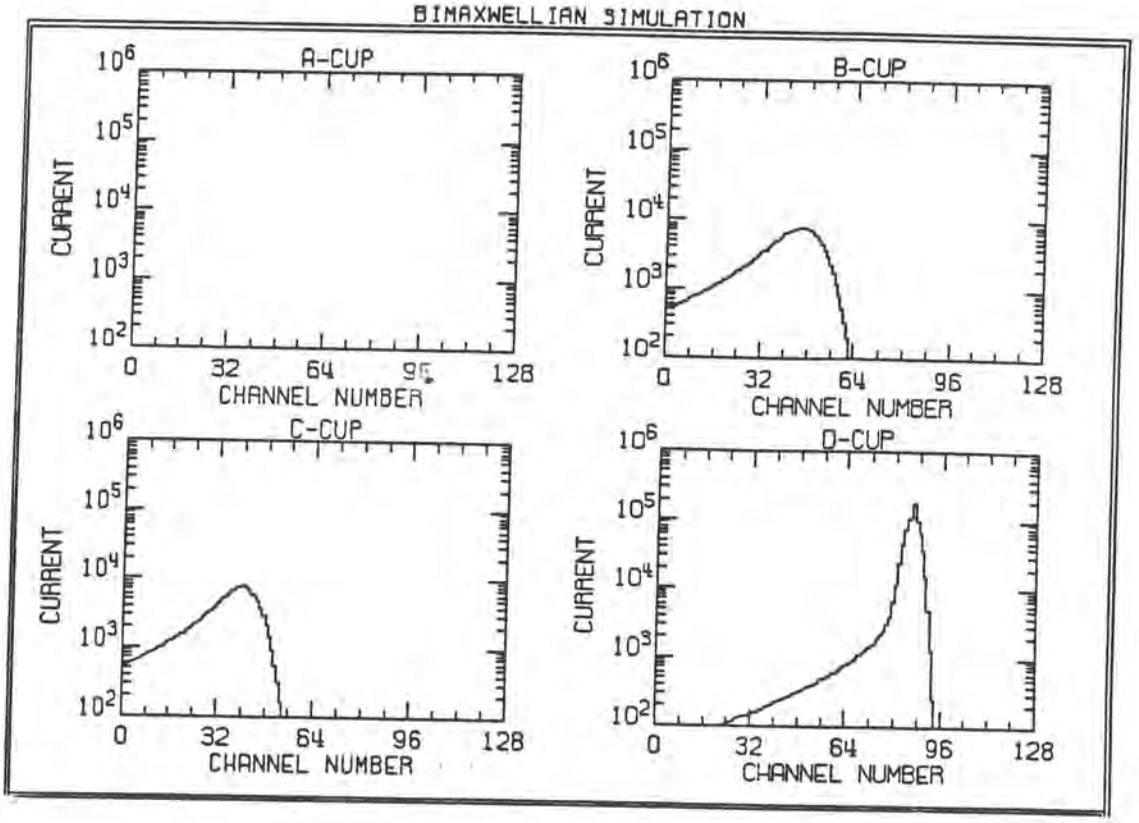

Figure 2.2-13. Simulated currents using PMODEL. The thermal speeds used are the same as those listed in Fig. 2.2-12, and the number of velocity steps used was RSTEP = 20.

the spectrum. The current in this region is once again too low, as compared with PMODEL. For the main sensor, the error associated with the peak channel is < ~7%, while the D-cup peak channel has an error of about 24%. However, as in the previous case, the peak current calculated by PMODEL, for the D-cup, is high due to numerical errors associated with the finite integration step size. As RSTEP is increased to 20, this current spike in the peak channel (see Fig. 2.2-13) decreases. Runing PMODEL at a RSTEP = 20 produced an execution time in excess of 30 CPU minutes, so another simulation with an even larger value of RSTEP was not performed.

As a final case $w_\perp$ was decreased even further; parameters used were $w_\parallel$ = 14.5 km/sec , $w_\perp$ = 2.0 km/sec, and RSTEP = 15. The results shown in Figures 2.2-14 and 2.2-15. In this case, the width of the distribution function approaches the energy-per-charge resolution of the instrument. In this extreme case, LABBI exhibits numerical problems (see Fig. 2.2-14), so errors associated with this run were not calculated. The value of RSTEP must also be increased since PMODEL also exhibits numerical problems (see Fig. 2.2-15). In particular, there seems to be a second peak forming in the B-cup, which is not physical, and the peak current in the D-cup is probably high.

To summerize, the currents calculated by LABBI are in excellent agreement with ABSO, when assuming a Maxwellian distribution, and in good agreement with PMODEL, when assuming a bimaxwellian distribution. Although the currents calculated in the feedthrough region are somewhat low compared to PMODEL, the difference in not enough to significantly affect fits to the data (such fits are considered in the next chapter).

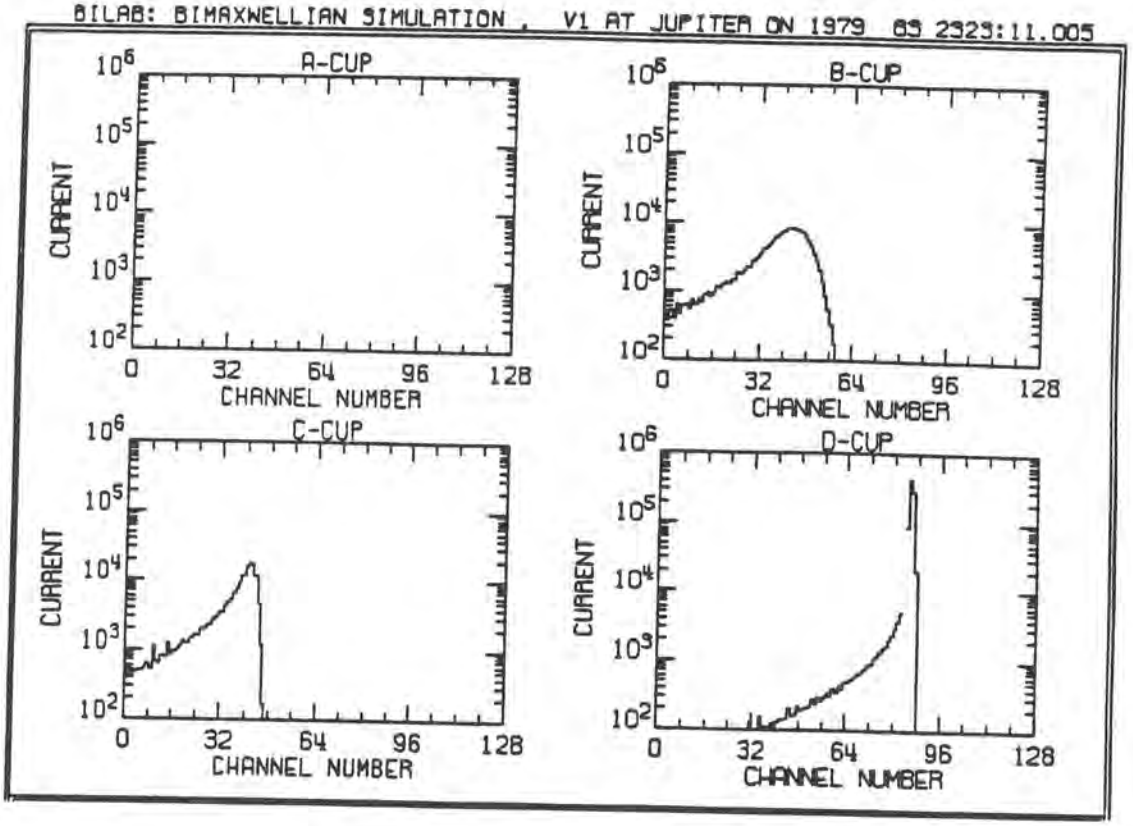

Figure 2.2-14. Simulated currents using LABBI. the thermal speeds used were $w_{\parallel} = 14.5$ km/sec and $w_{\perp} = 2.0$ km/sec.

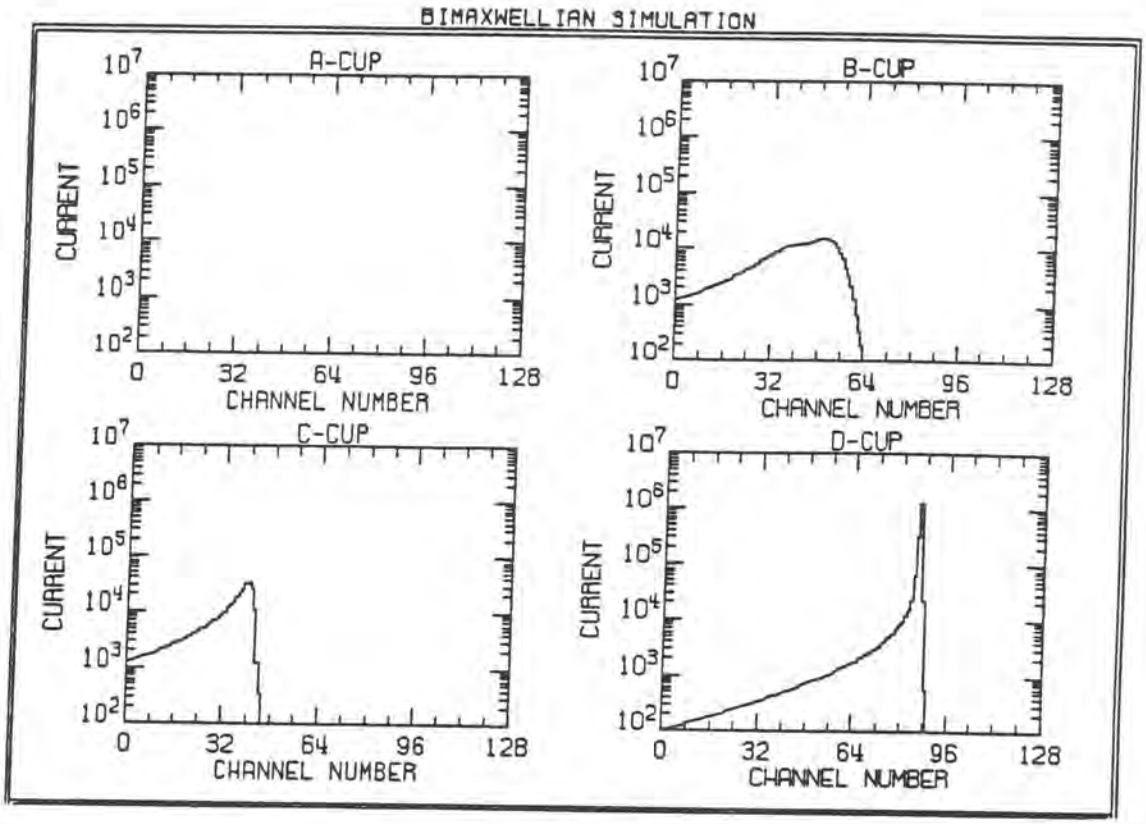

Figure 2.2-15. Simulated currents using PMODEL. The thermal speeds used are the same as those listed in Fig. 2.2-14, and the number of velocity steps used was RSTEP = 15.

CHAPTER 3

DATA ANALYSIS

3.1. Introduction

All the data analyzed for this thesis comes from the encounter of Jupiter by the Voyager 1 spacecraft. Most of the positive ion spectra obtained by Voyager 2 during the Jupiter encounter are "hot" and more difficult to analyze in detail. The term "hot" ("cold") here refers to the ratio of the component of bulk plasma velocity into a cup, V, to the ion thermal speed, w. This ratio is equivalent to an effective Mach number, M, of the particular ion species, where $M \equiv | V | / w$. A spectrum is considered "hot" when the thermal velocity is large enough to yield a Mach number roughly less than five. In this case, the individual ion peaks making up a spectrum begin to overlap each other and, if the spectrum is hot enough, only one large broad peak is present. Such data cannot be analyzed uniquely. However, if $M > 5$ the individual ion peaks are distinguishable and unique plasma parameters can be determined. It has been suggested that the spectra were hotter during the Voyager 2 encounter because the magnetosphere underwent compression due to an increase in solar wind ram pressure [*McNutt et. al.*, 1987]. Even though Voyager 1 obtained many spectra which were too hot to analyze, many spectra were cold and therefore analyzable. The largest region of cold spectra was found in Jupiter's middle magnetosphere, the region between ~8 R_J and ~50 R_J.

Because of spacecraft orientation, data sent back during the outbound portion of the encounter cannot be easily interpreted. On the inbound leg of the trajectory, azimuthal flow is seen primarily by the D cup, with any non-azimuthal flow picked up by the B and C cups. Outbound, the spacecraft was oriented such that the D cup pointed northward of the equatorial plane and the symmetry axis of the main sensor pointed Earthward. Analysis of spectra for well-determined plasma parameters has been limited to Jupiter's dayside, middle magnetosphere. The trajectory of Voyager 1 as projected onto the Jovian equatorial plane is

shown in Figure 3.1-1. Both axes represent distance from the center of Jupiter in units of Jovian radii. The arrow labeled S is the projection of the symmetry axis of the main sensor onto the equatorial plane, and the arrow labeled D represents the projection of the D cup axis. Tick marks are shown every 12 hours; the day of year is also given. Orbits of the four Galilean satellites are represented by circles.

Voyager passed through the magnetic equator twice every rotation period (~10 hours) due to the tilt of the magnetic axis to the spin axis (9.6°). To first order, crossings of the magnetic equator corresponds to passes through the plasma sheet. This connection is made clear in Figure 3.1-2 where ion mass and charge densities are plotted versus time with arrows indicating times of magnetic equator crossings [*McNutt et. al.*, 1981]. These crossings line up with enhancements in mass and charge density. A "wiggle" plot of the spacecraft trajectory, during the same time period, is shown above the density plot. If the spacecraft trajectory is projected into a magnetic meridional plane, (the plane that contains the Jupiter-sun line and is perpendicular to the magnetic equatorial plane) one obtains a "wiggle" plot. The analysis of spectra across several magnetic equatorial crossings has resulted in a fascinating picture of the plasma sheet on Jupiter's dayside.

To organize the data three coordinate systems are employed: System III (SIII), Jovicentric Cylindrical, and Tilted Dipole Cylindrical coordinates. The SIII coordinate system is a non-inertial system which corotates with the planet. It is a Jovicentric system with the z-axis parallel to the spin axis, the x-axis passing through the Prime Meridian (an arbitrarily chosen 0° longitude defined as the point beneath the observer at some predefined time using a determined Jovian rotation period), and the y-axis defined so as to complete the right-handed coordinate system. Latitude is measured in the conventional sense, longitude however, is the angle measured positive *westward* from the Prime Meridian. There are two versions of the coordinate system, SIII(1957) and SIII(1965). The SIII(1957) coordinate system rotation rate is determined from the rotation of the Jovian decimeter and decameter radio sources [*Mead*, 1974]. The SIII(1965) coordinate system also uses the rotation of the Jovian radio sources but it includes the 3°/yr of drift in longitude in SIII(1957) detected after years of additional measurements.

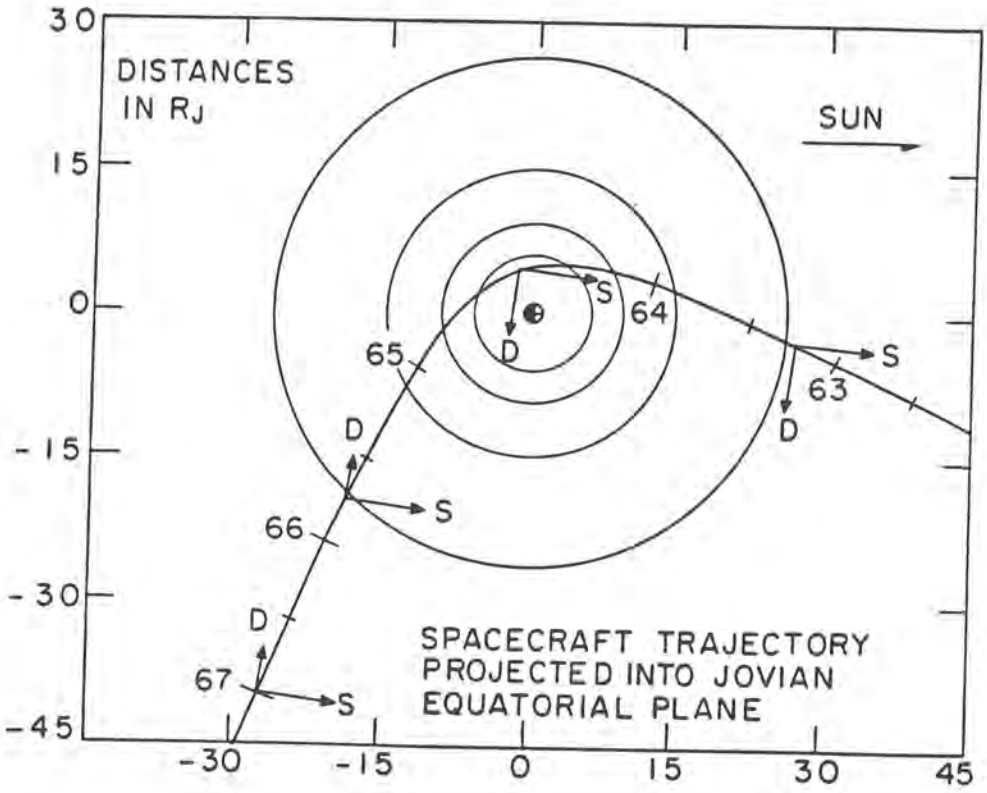

Figure 3.1-1. Voyager 1 trajectory projected onto the Jovian equatorial plane. The arrow labeled *S* is the projection of the symmetry axis of the main sensor onto the equatorial plane. The projection of the D-cup axis is the arrow labeled *D*. Reprinted from *McNutt et. al.*, [1981].

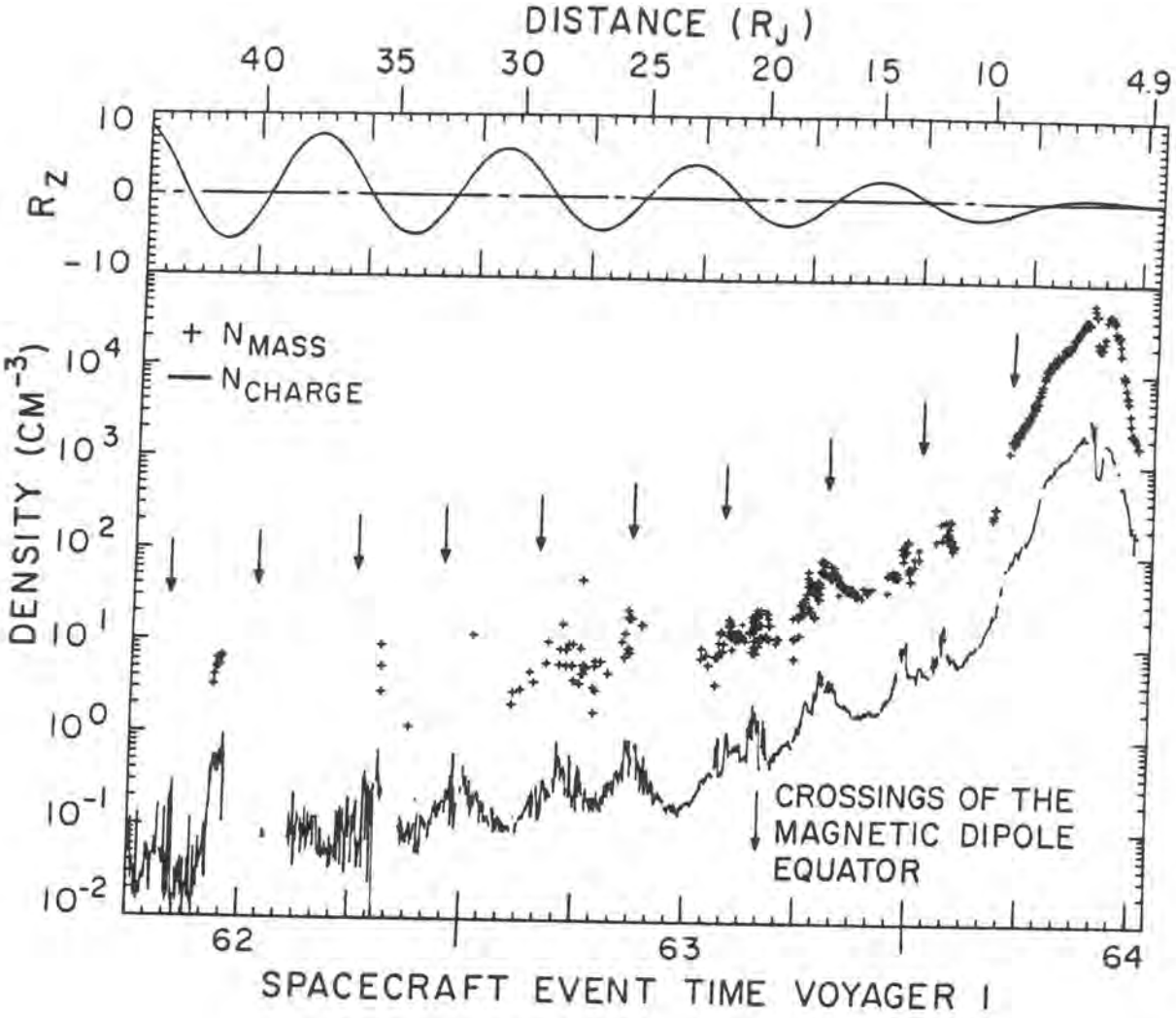

Figure 3.1-2. Estimates of the total mass and charge densities of positive ions, in units of amu cm^{-3}, respectively. A "wiggle" diagram of the spacecraft trajectory is shown in the top panel. Note how density enhancements occur near crossings of the magnetic equator (arrows indicate magnetic equator crossings). Reprinted from *McNutt et. al.*, [1981].

This thesis will use only the latter version, *i.e.* SIII(1965). The exact System III(1965) period is $9^h55^m29^s.711 \pm 0^s.04$ [*Devine*, 1976].

The Jovicentric cylindrical coordinate system is an inertial system where the z-axis is parallel to Jupiter's rotation axis while the x-axis is in the plane formed by the z-axis and the direction to the sun, lying in the same hemisphere as the sun. The y-axis completes the right-handed system.

The tilted dipole (O_4 model) coordinate system, is a Jovicentric system based upon the magnetic field model of *Acuna and Ness* [1976a,c]. The z-axis is parallel to the dipole moment while the x-axis intersects the System III Prime Meridian. The y-axis completes the right-handed system.

3.2. Analysis Technique

As mentioned earlier, the PLS experiment measures, and transmits back to earth, data consisting of positive ion, and electron, current as a function of energy-per-charge. To analyze this data an interactive analysis program was developed. This interactive analysis package, called MJSANL (Mariner Jupiter Saturn ANaLysis), is composed of two major components, a non-linear least squares fitting package [*Bevington*, 1969], and the actual analysis (current calculating) routine. Most of these routines assume the ion distribution function to be a convected isotropic maxewllian. Of these routines, the main difference between them is execution time. For example, the analysis routine with the longest execution time, called ABSO, analyzes both L and M-mode spectra and uses the full instrument response function in calculating currents for Maxwellian ion distribution functions (e.g., Eqs. 2.2.4, 2.2.6, 2.2.7, 2.2.9, and 2.2.17). The analysis routine with the shortest execution time is XJC, which also analyzes L and M-mode spectra. XJC uses one major simplifying assumption, the finite aperture infinite collector approximation; every particle entering the aperture is assumed to impinge on the collector and, therefore, "seen" by the instrument. Using this assumption, $R(v, v_k) = 1.0$, the integrals over the transverse velocities for calculating the current, see Eq. 2.2.5, are straight forward and can be written in terms of elementary functions. By using this

approximation, execution time is reduced by about 20 times that for ABSO.

When making assumtions, there is a certain range over which the approximation is good. For the case of XJC, as long as the ion species are cold ($M > 5$) and the flow is directly into the cups, the finite aperture, infinite collector approximation is valid (as is the case when Voyager is in interplanetary space, the solar wind flows directly into the main sensor [*Bridge et. al.*, 1977]). When the ions are not cold and the flow direction into the sensor is oblique ($\geq 45°$) the full response function must be used to correctly unfold the ion properties from the response. This is because oblique flows and/or hot ions imply that some of the ions entering the aperture will not be collected (due to geometry effects and modulation of the transparency function) and thus the response function, $R(v, v_k)$, is no longer unity. Once inside a planetary magnetosphere, the situation which is almost always present is the latter. The analysis performed for this thesis was done using ABSO (full response and convected isotropic Maxwellian distribution function) and LABBI (full response and convected bimaxwellian distribution function [see below]).

The remaining analysis routines are more flexible in that they do not assume the ion distribution function to be a convected Maxwellian. One routine, called PMODEL, allows the user to specify the distribution function in the plasma rest frame. However, this code is very expensive to run as it performs all three integrals in Eq. 2.2.4 numerically. The other analysis code, LABBI, uses a convected bimaxwellian for the ion distribution function (see Chapter 2). This routine was also used in this thesis to check for temperature anisotropies and determine the effect of anisotropies on plasma bulk flows.

A flow chart of MJSANL is shown in Figure 3.2-1. To perform the analysis with MJSANL several parameters must be input. Input parameters include: time of spectrum, desired analysis routine, number and type of ion species, fit parameters (described below) to be used, energy-per-charge channels, of each cup, used in the analysis, and initial values of density, thermal speed, and bulk velocity, for each ion species (a sample input listing is included in Appendix C). With this information MJSANL calculates "synthesized" currents, compares these with the actual currents measured and determines the error associated with each fit

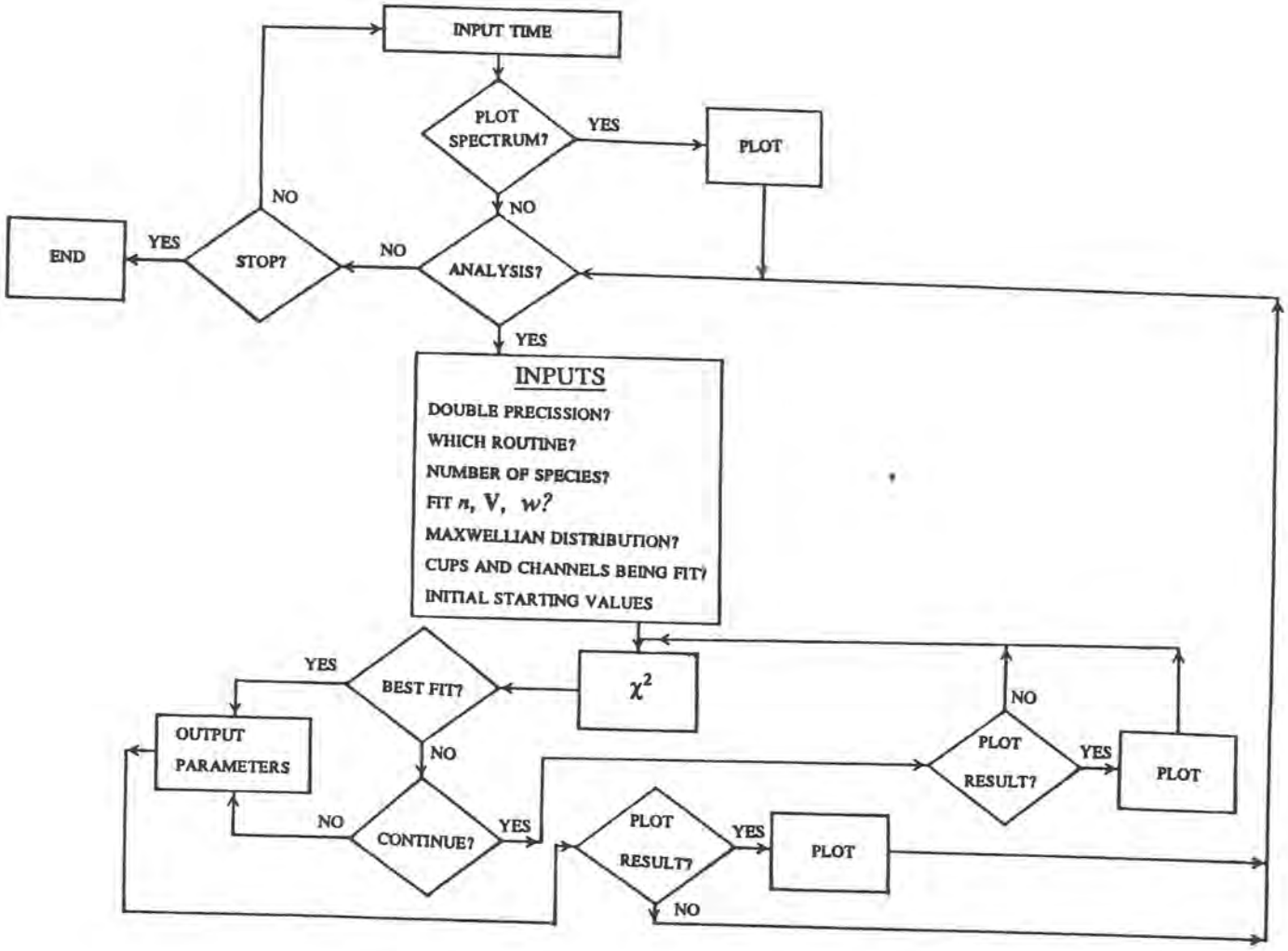

Figure 3.2-1. Flow chart of MJSANL; an interactive non-linear least squares fitting routine used to analyze plasma spectral data.

parameter. During each iteration of MJSANL, a small increment is added to the fit parameter with the currents then being recalculated. This enables the routine to determine a derivative for that fit parameter which in turn is used to calculate an error associated with the value of that variable. Using these errors, corrections to densities, temperatures, and bulk flow components (i.e., the fit parameters) are recalculated. These new values of the fit parameters are then used to perform another iteration; obtaining a new set of simulated currents. The analysis routine uses the difference between the *in situ* measured currents and the calculated currents to determine a χ^2 for the current fit. This χ^2 represents the "goodness" of the fit to the actual data (described below). If χ^2 is too large (i.e., fit not very good), another iteration can be performed. This iterative process can be continued until a satisfactory fit is obtained (when χ^2 reaches a minimum), at which time the densities, bulk velocity, and thermal speeds of the species are printed out and the resulting currents can be plotted for comparison with the actual measured currents.

To determine χ^2, an non-linear least squares fitting technique must be used. Linear methods are restricted to functions which are linear in the coefficients a_i,

$$y(x) = a_0 + \sum_{i=1}^{n} a_i X_i(x) \tag{3.2.1}$$

Because the expression for current (Eq. 2.2.4) cannot be cast into the above form, a non-linear least squares fitting algorithm is utilized. Like the linear least squares fitting technique, a measure of the "goodness" of fit, χ^2, is defined as

$$\chi^2 = \sum_{i=1}^{n} \left\{ \frac{1}{\sigma_i^2} \left[y_i - y(x_i) \right]^2 \right\} \tag{3.2.2}$$

where σ_i are the uncertainties in the data points y_i. The optimum values of the a_i are obtained by minimizing χ^2 with respect to each of the parameters simultaneously. This amounts to searching n-dimensional parameter space to find the appropriate minimum value of χ^2. The problem which arises is, for an arbitrary function there are many local minima of χ^2, and finding the main minimum can be difficult.

A non-linear least squares fitting technique developed by *Marquardt* [1963] is used in the analysis code. This technique is referred to as the gradient-expansion algorithm and combines the best features of two other methods; the gradient search method and the method of linearizing the fitting function. Before describing how the Marquardt method works, a brief description of the other two methods will be given (see *Bevington*, [1969]).

If the variation of χ^2 with each parameter, a_i, is "fairly" independent of the optimizing of χ^2 with the other parameters, then the optimum values of each parameter can be found by minimizing χ^2 with respect to each parameter seperately. However, when the variations of χ^2 with each parameter is not independent this method will converge slowly to the minimum.

In the gradient search method, all the parameters, a_i, are incremented simultaneously by the amount δa_i, with the relative magnitudes, γ_i, adjusted so that the resultant direction of travel, in parameter space, is along the gradient of χ^2. The increment size, δa_i is defined as

$$\delta a_i = -\gamma_i \Delta a_i \tag{3.2.3}$$

where Δa_i is the step size and γ_i is given by

$$\gamma_i = \frac{\dfrac{\partial \chi^2}{\partial b_i}}{\sqrt{\displaystyle\sum_{k=1}^{n} \left[\frac{\partial \chi^2}{\partial b_k}\right]^2}} \tag{3.2.4}$$

and can also be thought of as a dimensionless gradient with a magnitude of unity. The b_i are dimensionless normalization parameters given by

$$b_i = \frac{a_i}{\Delta a_i} \tag{3.2.5}$$

A major drawback of using this method alone is its inability to home in on the minimum of χ^2 once it starts getting close to the minimum. This is because evaluating the derivative of χ^2,

$$(\nabla \chi^2)_i = \frac{\partial \chi^2}{\partial a_i} \approx \frac{\chi^2(a_i + f\,\Delta a_i) - \chi^2(a_i)}{f\,\Delta a_i} \tag{3.2.6}$$

consists of taking the difference between two nearly equal numbers (this difference is zero at the minimum of χ^2). Trying to perform such an operation numerically always results in roundoff errors which leads to a breakdown of the numerical scheme being used. The fraction f symbolizes the fact that a_i should be changed by less than Δa_i when determining the derivative.

The method of linearizing the fitting function $y(x)$, consists of expanding $y(x)$ in terms of the parameters a_i and then using linear least squares to determine the optimum value for the parameter increments δa_i. Expanding $y(x)$ to first order in a Taylor series

$$y(x) \approx y_0(x) + \sum_{i=1}^{n} \left[\frac{\partial y_0(x)}{\partial a_i} \, \delta a_i \right] \tag{3.2.7}$$

results in a function which is linear in δa_i, allowing the method of linear least squares to be used.

$$\chi^2 = \sum_j \frac{1}{\sigma_j^2} \left\{ y_j - y_0(x_j) - \sum_{i=1}^{n} \left[\frac{\partial y_0(x_j)}{\partial a_i} \, \delta a_i \right] \right\}^2 \tag{3.2.8}$$

Following this, χ^2 is minimized with respect to each parameter increment δa_i by setting the derivatives equal to zero. This scheme converges quite rapidly to the point of minimum χ^2 from points nearby. However, it may not approach the minimum with any accuracy from a point outside the region where the χ^2 hypersurface is approximately parabolic (see *Bevington*, [1969] for details).

By combining the method of linearizing the fitting function, which is good for the region near a minimum of χ^2, with the gradient search method, which works well in the region far from a minimum, another algorithm can be developed which has good convergence properties in all χ^2 hyperspace. The fusion of these two techniques is then the gradient-expansion (Marquardt) method. Details of the derivations of these algorithms are presented by *Bevington* [1969].

3.3. Maxwellian Fits

Using the analysis code MJSANL, outlined in the previous section, spectra obtained during the Voyager 1 flyby of Jupiter's dayside magnetosphere were analyzed. As discussed in Chapter 2, the currents calculated by the analysis code are given by

$$I_k(\mathbf{x}, t) = I_k^*(\mathbf{x}, t) - I_{k+1}^*(\mathbf{x}, t) \tag{3.3.1}$$

where,

$$I_k^*(\mathbf{x}, t) = Z^* e \int_{-\infty}^{\infty}\int_{-\infty}^{\infty}\int_{v_k}^{\infty} d\mathbf{v}\ (\mathbf{v}\cdot\hat{\mathbf{n}})\, f(\mathbf{x}, \mathbf{v}, t)\, R(\mathbf{v}, v_k) \tag{3.3.2}$$

$I_k(\mathbf{x}, t)$ can be evaluated for general $f(\mathbf{x}, \mathbf{v}, t)$ by using PMODEL. In practice the spectra are well approximated by assuming the various ion species are described by isotropic, Maxwellian distributions [*Sands and McNutt*, 1986; *Sands*, 1984]. We also consider the case of bimaxwellians to study the effect of temperature anisotropies on the determination of bulk plasma flows. In this case the expression for $I_k^*(\mathbf{x}, t)$ is reduced to a single quadrature in Chapter 2.

An indication of plasma flow can be found from considering the total particle flux into the various PLS cups. Looking at the currents measured in the B and C cups, one sees that the current levels are not the same. In Figure 3.3-1 the fractional difference in these currents (left vertical scale) is plotted against position of the spacecraft in tilted dipole coordinates. The distance above and below the magnetic equator is given by R_Z while the distance indicated at the top of the plot is the radial distance from the dipole axis, both measured in terms of R_J. Superimposed on this plot is the trajectory of Voyager 1, projected onto a magnetic meridional plane. Local time (defined such that the plane which contains the Jupiter-sun line is 1200, increasing in a counter-clockwise sense when looking down from the northern hemisphere) is shown on the bottom scale and universal time is given on the top scale. If one assumes the ion distribution functions to be convected Maxwellians, these differences in flux densities can only be accounted for by a non-azimuthal bulk plasma flow. However, these differences could also

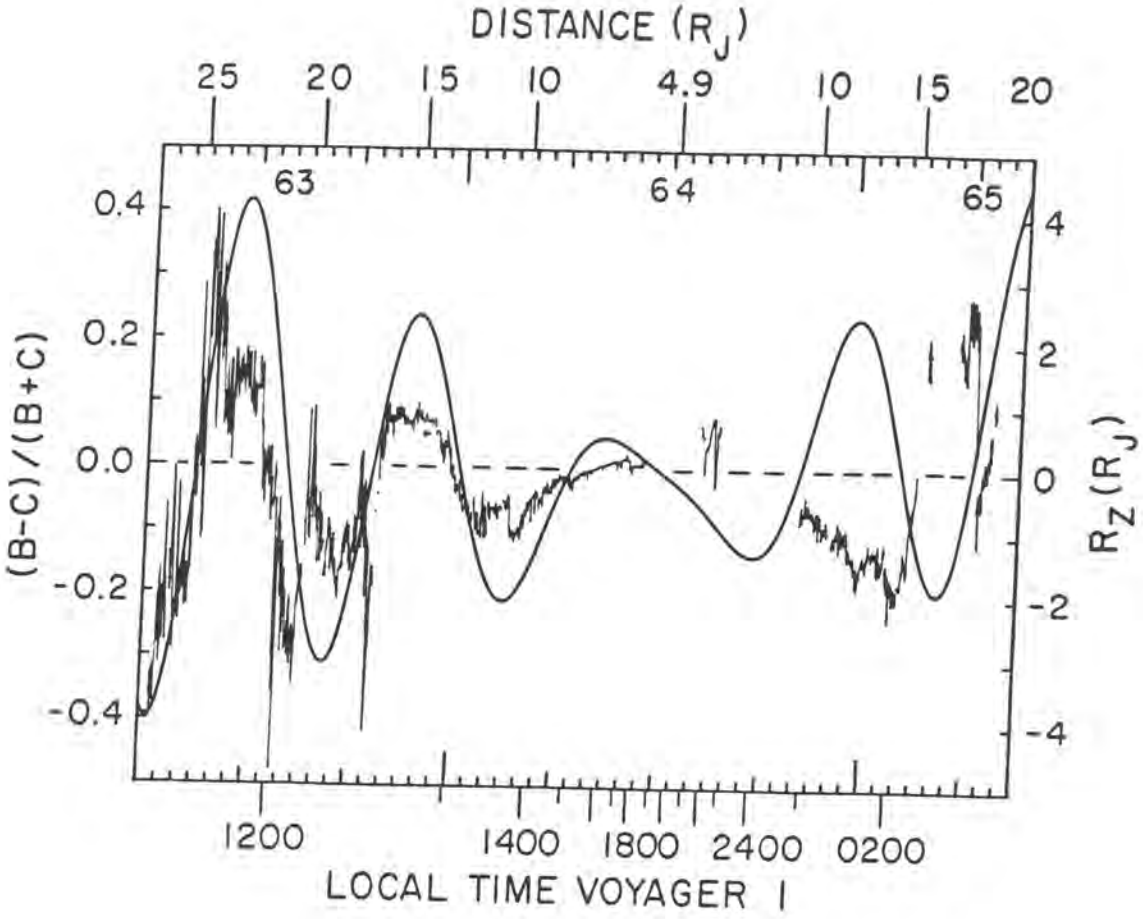

Figure 3.3-1. Plot of the difference between the B and C-cup flux densities divided by their sum, during the Voyager 1 encounter with Jupiter. The same pattern persists during the Voyager 2 encounter half a year later.

be due to non-Maxwellian features (this possibility will be discussed later in the chapter).

Using the analysis code MJSANL, outlined in the previous section, spectra obtained during the Voyager 1 flyby of Jupiter's dayside magnetosphere were analyzed. In every set of spectra analyzed it was assumed that the ion distribution function could be represented as a convected, isotropic Maxwellian. The analysis of the plasma data was sometimes straight forward, like the spectrum in Figure 3.3-2, and sometimes difficult, like the spectrum in Figure 3.3-3.

The spectrum shown in Figure 3.3-2 was obtained by Voyager 1 on March 4 at 23 hours 23 minutes UT (i.e., 1979 63 2323). The spacecraft was approximately 13.5 R_J from the dipole axis and 1.06 R_J above the magnetic equater. The four cups, A, B, C, and D, refer to the four sensors of the PLS experiment. Currents are measured in units of femptoamps (10^{-15} amps = 1 femptoamp) on the vertical axis while channel number, on the horizontal axis, refers to the energy-per-charge channels ranging from 10 - 5950 V on a scale which is logarithmic to first order.

The spectrum is quite cold, the peaks representing the heavy positive ions can be picked out as well as the proton peak. There are five arrows which point out and identify the various peaks in the figure. As input to MJSANL, five positive ion species were used (H^+, O^{+2}, S^{+3}, O^+ (S^{+2}), and S^+) and V_R , V_ϕ , V_z , and the five ion densities were fit parameters. The proton thermal speed was also a fit parameter, with the other four ion thermal speeds determined from the proton thermal speed, assuming a common temperature. Results of this fit are shown in Figure 3.3-4. All the peaks in the D-cup were fit quite well as were the lower energy channels in the B and C cups. The signal seen in the upper channels is due to a hot ion background. This background ion population was not fit for two reasons, first it does not affect the velocity calculation and secondly, it is very hard numerically to take this hot ion background into account. Results of this analysis gave a bulk plasma flow of $V = -4.5\hat{e}_R + 139.7\hat{e}_\phi + 16.7\hat{e}_z$ km/sec.

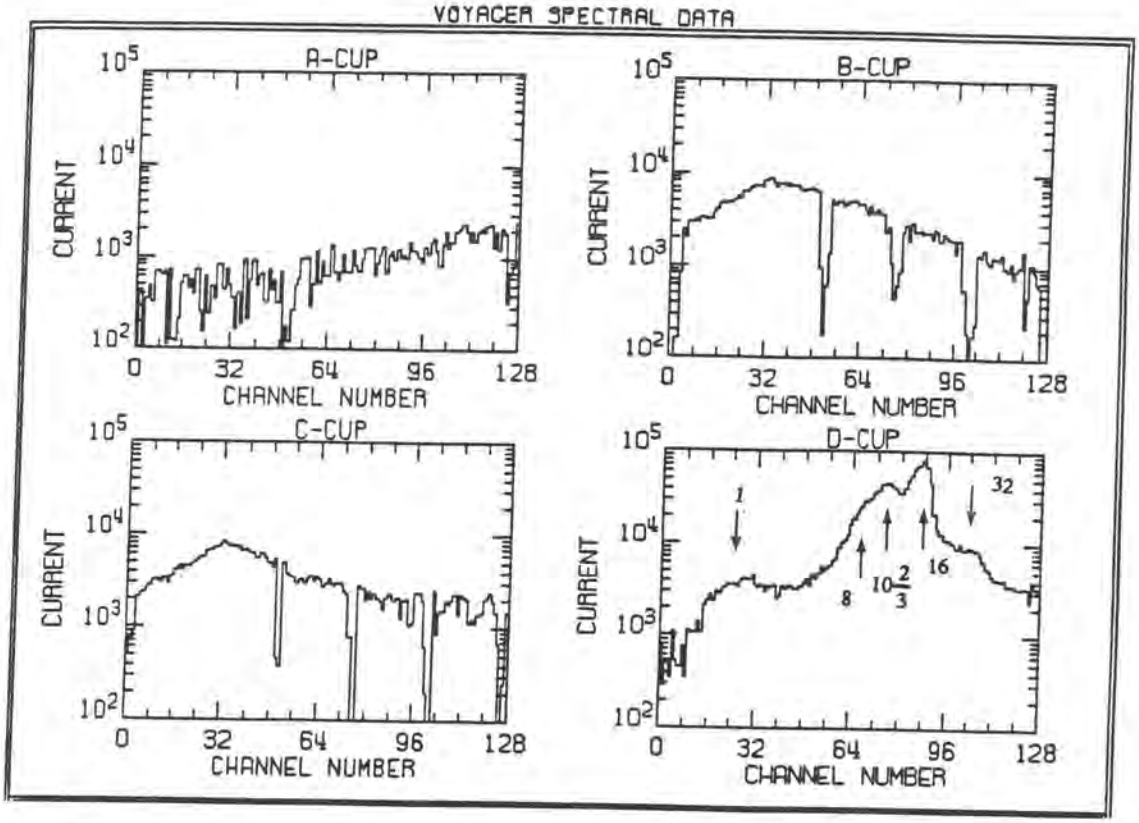

Figure 3.3-2. Example of a "cold" spectrum. All the ion peaks are well resolved allowing an easy determination of plasma parameters. The five arrows point out and identify the various peaks.

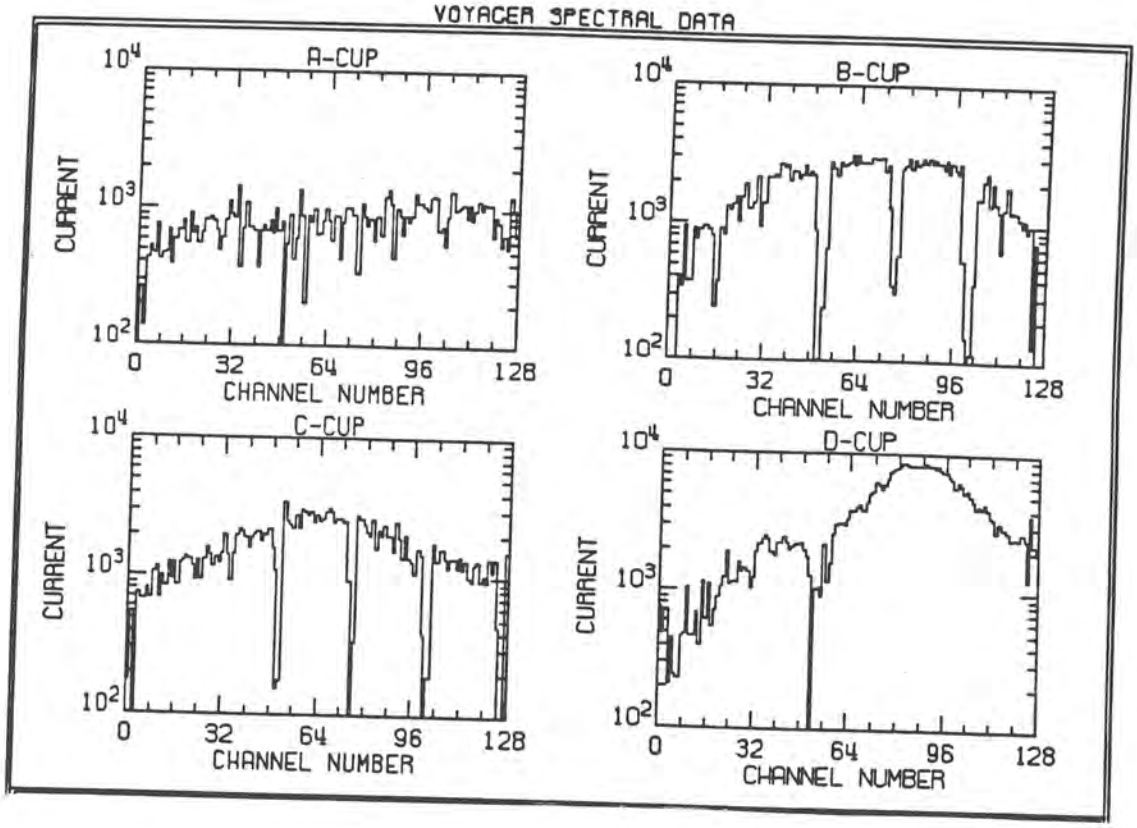

Figure 3.3-3. Example of a "hot" spectrum. All the heavy ion peaks are smeared together into one large broad peak. The proton peak can be identified by the arrow in the D-cup. Plasma parameters cannot be easily calculated since there are no individual heavy ion peaks for the analysis routine to work with.

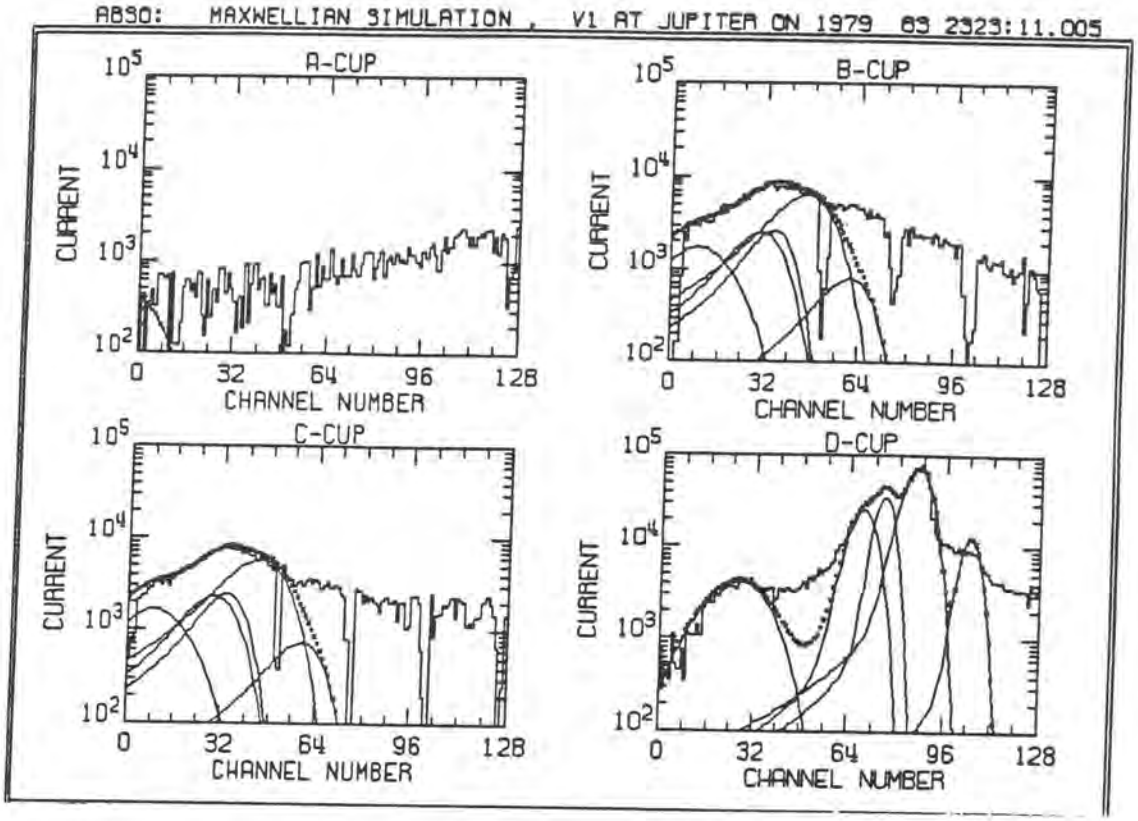

Figure 3.3-4. Currents calculated for the spectrum of Fig. 3.3-2. The simulated currents are superposed on the spectral data for easy comparison. Calculated currents due to each ion species is shown

A typical "worse" case spectrum looks like Figure 3.3-3. This spectrum was obtained when Voyager was at a cylindrical radial distance of 14 R_J from Jupiter and 1.9 R_J above the magnetic equator, on day 63 (March 4) at 2236 UT. The ions are very hot causing all the heavy ion peaks to "smear" together into one large broad peak (the proton peak can be identified in the D-cup by the arrow). Sharp "drop-outs" in the spectrum are due to interference from another experiment. These do not cause any problem however, since the channels containing the "drop-outs" can be removed from the analysis.

Six ion species were used in the analysis (H^+, O^{+3}, O^{+2}, S^{+3}, O^+, and S^+), with the three velocity components, all six densities, and the proton and O^{+3} ion thermal speeds as the fit parameters. The proton temperature was assumed different from the temperature of the heavy ions. In effect, we have assumed that the protons and heavy ions have not had time to come to a thermodynamic equilibrium. With the spectrum as hot as it is, this is probably an acceptable approximation (assuming an isothermal case gives a poor representation to the data). Figure 3.3-5 shows the result of the analysis of this spectrum. Figure 3.3-5. Simulation of Spectrum in Fig. 3.3-3 Overall, the simulation was not bad. Most noticeable was the inability to simulate the upper channels in the three cups of the main sensor. However, the current signal in those channels is due to a hot ion background, which, although it changes the total ion density, does not affect the plasma bulk velocity determination. The simulated current in the B and C-cups is a little high in the low channels, but again the velocity should not be greatly affected. The analysis did a good job in simulating the current in the D-cup, only the very highest energy-per-charge channels could not be reproduced (a hot ion background would fit those channels). The plasma bulk velocity was determined to be $\mathbf{V} = -15.9\hat{\mathbf{e}}_R + 167.6\hat{\mathbf{e}}_\phi + 28.4\hat{\mathbf{e}}_z$.

A listing of each spectral set analyzed is presented in Tables 3.3-1 and 3.3-2. In Table 3.3-1, the time and mode of each spectral set, along with its corresponding plasma bulk flow velocity (obtained from the analysis) is listed. The velocities are given in Jovicentric cylindrical coordinates and have units of km/sec. Besides the time and mode of each spectral set, Table 3.3-2 lists the corresponding position of the spacecraft in System III(1965) latitude and longitude, its position in tilted dipole coordinates (radial distance from the magnetic dipole axis

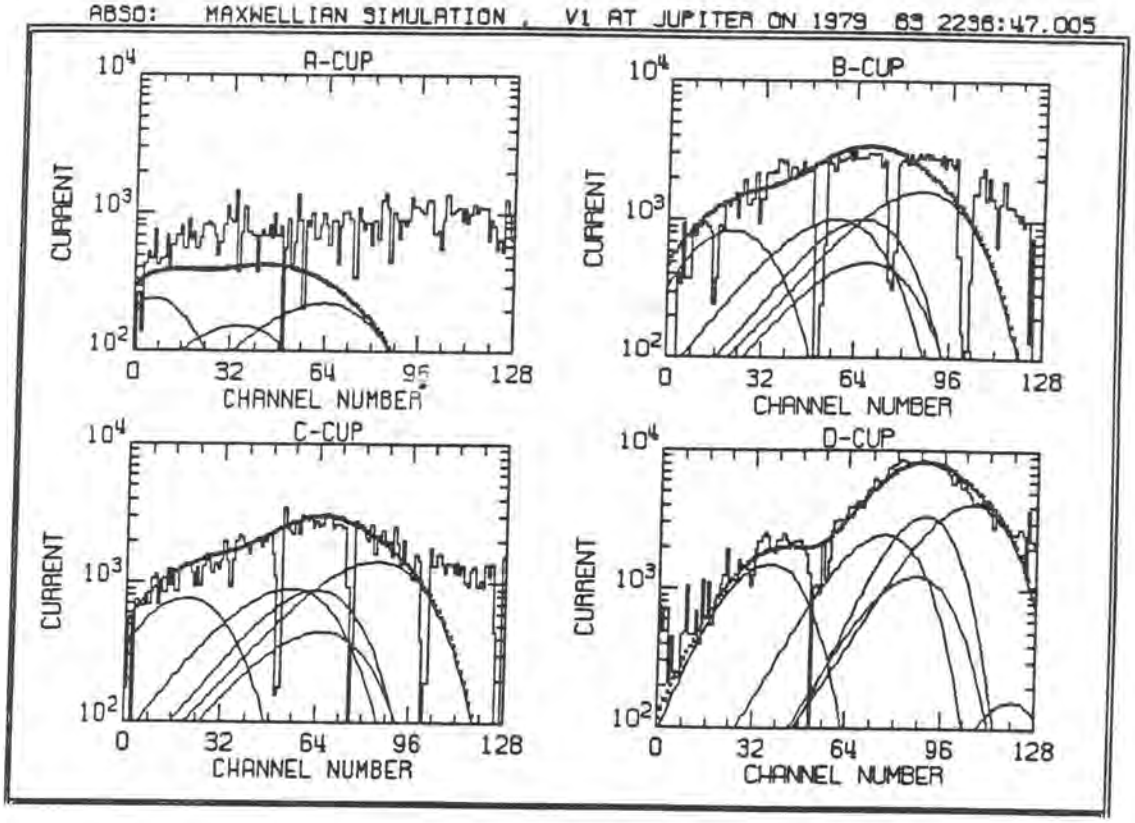

Figure 3.3-5. Currents calculated for the spectrum of Fig. 3.3-3. The simulated currents are superposed on the spectral data for easy comparison. Calculated currents due to each ion species is shown

Table 3.3-1. PLASMA VELOCITIES FROM ANALYSIS

TIME/MODE	V_R (km/sec)	V_ϕ (km/sec)	V_z (km/sec)
063 0841:00/L	-41.525 ± 4.733	237.901 ± 2.173	-23.249 ± 14.969
1527:24/L	-18.123 ± 2.775	205.589 ± 1.786	-37.568 ± 13.157
1535:24/L	-8.394 ± 1.621	202.730 ± 1.436	-25.000 ± 11.300
1738:36/L	-29.729 ± 4.945	202.486 ± 7.942	-1.038 ± 3.573
1755:11/M	-2.652 ± 1.078	201.968 ± 0.780	5.668 ± 2.089
1819:11/M	6.842 ± 1.605	206.782 ± 0.785	4.027 ± 1.183
1827:11/M	16.752 ± 1.920	199.854 ± 0.660	5.773 ± 1.192
1844:47/M	13.208 ± 0.974	196.779 ± 0.618	4.320 ± 1.390
1903:59/M	12.641 ± 3.079	196.999 ± 0.766	-6.180 ± 1.271
1913:35/M	1.625 ± 0.392	183.728 ± 0.468	4.350 ± 0.952
1933:48/L	5.758 ± 1.276	197.419 ± 3.136	33.575 ± 5.416
1934:23/M	2.901 ± 0.493	187.821 ± 0.886	46.306 ± 3.995
1950:23/M	-0.202 ± 0.049	179.648 ± 1.395	50.666 ± 3.482
1956:47/M	9.816 ± 0.715	179.579 ± 0.766	45.427 ± 2.496
2011:11/M	-5.216 ± 0.438	181.341 ± 0.844	50.992 ± 2.362
2033:35/M	-18.271 ± 0.876	181.311 ± 1.147	47.419 ± 2.645
2103:59/M	-17.415 ± 1.352	181.488 ± 3.335	45.279 ± 2.999
2148:47/M	-18.590 ± 1.566	172.734 ± 3.155	33.379 ± 6.081
2223:24/L	-6.643 ± 1.103	156.614 ± 1.883	29.810 ± 3.466
2233:35/M	-14.244 ± 0.954	156.819 ± 1.830	25.387 ± 2.495
2236:12/M	-15.915 ± 1.148	167.645 ± 3.561	28.436 ± 2.830
2244:47/M	-19.194 ± 0.828	171.766 ± 1.358	21.333 ± 2.881
2255:59/M	-19.622 ± 0.819	156.772 ± 1.291	18.834 ± 2.746
2308:47/M	-12.987 ± 1.379	144.775 ± 1.486	21.710 ± 3.929
2311:59/M	-8.247 ± 0.748	144.000 ± 0.602	21.606 ± 2.336
2323:11/M	-3.965 ± 0.327	139.390 ± 0.148	15.120 ± 0.629
2324:47/M	-5.727 ± 0.013	137.986 ± 0.008	18.793 ± 0.032

Table 3.3-1. PLASMA VELOCITIES FROM ANALYSIS (continued)

TIME/MODE	V_R (km/sec)	V_ϕ (km/sec)	V_z (km/sec)
063 2326:23/M	-11.560 ± 0.285	140.904 ± 0.177	22.082 ± 0.766
2327:59/M	-14.879 ± 0.350	136.540 ± 0.257	24.207 ± 0.943
2329:35/M	-14.822 ± 0.368	136.217 ± 0.277	23.356 ± 0.989
2331:11/M	-9.460 ± 0.250	139.216 ± 0.129	17.106 ± 0.629
2332:47/M	-3.480 ± 0.287	137.195 ± 0.250	15.440 ± 1.082
2334:23/M	-3.109 ± 0.351	135.300 ± 0.373	17.873 ± 1.633
2335:59/M	-5.731 ± 0.249	136.483 ± 0.182	22.537 ± 0.815
2337:35/M	-6.268 ± 0.277	136.689 ± 0.184	21.855 ± 0.790
2339:11/M	-13.259 ± 0.333	139.456 ± 0.243	17.914 ± 0.854
2340:47/M	-7.172 ± 0.287	142.482 ± 0.137	9.293 ± 0.873
	-6.728 ± 0.112	142.211 ± 0.153	13.742 ± 0.324
064 0025:00/L	-9.234 ± 0.204	124.056 ± 0.195	4.717 ± 0.697
0045:48/L	-14.812 ± 0.341	141.812 ± 0.205	7.582 ± 0.766
	-15.344 ± 0.523	146.934 ± 0.119	4.917 ± 0.802
0111:24/L	-7.376 ± 0.904	136.785 ± 0.962	-7.062 ± 3.839
	-5.262 ± 0.955	139.53 ± 0.834	-1.349 ± 3.511
	-6.586 ± 0.871	137.125 ± 1.136	-2.355 ± 2.825
0130:36/L	-12.068 ± 0.027	127.505 ± 0.019	-1.275 ± 0.058
0138:36/L	-7.916 ± 0.188	110.792 ± 0.176	0.277 ± 0.438
	-8.431 ± 0.239	111.494 ± 0.331	-1.893 ± 0.406
0142:23/M	-4.907 ± 0.198	112.820 ± 0.239	-2.248 ± 0.547
0150:23/M	-6.841 ± 0.204	113.835 ± 0.224	-2.430 ± 0.416

Table 3.3-2. SPECTRAL DATA

			Magnetic Coordinates (R_J)		B (GAMMA)		
TIME/MODE	S III LAT	S III LONG	R	Z	B_R	B_ϕ	B_z
063 0841:00/L	1.024	102.529	25.158	-0.225	-17.356	7.815	-12.355
1527:24/L	0.463	342.714	19.787	-2.430	-34.869	-3.577	-27.985
1535:24/L	0.449	347.412	19.662	-2.584	-39.318	-0.857	-28.537
1738:36/L	0.210	59.572	18.054	-2.334	-50.649	10.220	-38.310
1755:11/M	0.175	69.249	17.875	-1.973	-46.272	8.933	-39.415
1819:11/M	0.122	83.244	17.610	-1.368	-37.814	10.031	-39.993
1827:11/M	0.104	87.905	17.518	-1.151	-33.608	10.339	-40.374
1844:47/M	0.063	98.152	17.308	-0.658	-24.205	11.100	-43.040
1903:59/M	0.018	109.317	17.063	-0.112	-11.435	11.855	-46.270
1913:35/M	-0.006	114.895	16.934	0.157	-0.366	12.508	-47.137
1933:48/L	-0.056	126.633	16.648	0.702	18.900	11.258	-51.764
1934:23/M	-0.057	126.967	16.640	0.717	19.171	11.536	-52.188
1950:23/M	-0.098	136.243	16.402	1.114	31.231	10.588	-54.335
1956:47/M	-0.115	139.950	16.304	1.261	35.891	10.142	-57.064
2011:11/M	-0.153	148.285	16.082	1.567	43.912	9.017	-59.772
2033:35/M	-0.214	161.232	15.734	1.957	55.416	7.002	-65.682
2103:59/M	-0.299	178.435	15.271	2.292	65.885	2.967	-72.819
2148:47/M	-0.438	204.520	14.644	2.363	72.420	-5.169	-85.644
2223:24/L	-0.551	224.347	14.209	2.077	66.721	-11.197	-95.945
2233:35/M	-0.586	230.160	14.087	1.944	63.280	-13.219	-98.665
2236:12/M	-0.597	231.986	14.049	1.899	61.774	-13.929	-100.092
2244:47/M	-0.625	236.550	13.954	1.776	58.560	-15.977	-102.340
2255:59/M	-0.665	242.932	13.822	1.588	51.688	-16.828	-106.194
2308:47/M	-0.711	250.215	13.671	1.351	42.932	-19.785	-111.112
2311:59/M	-0.723	252.033	13.633	1.289	39.825	-21.143	-112.210
2323:11/M	-0.765	258.393	13.497	1.063	33.997	-22.288	-116.734
2324:47/M	-0.771	259.301	13.478	1.030	31.749	-22.032	-116.314

Table 3.3-2. SPECTRAL DATA (continued)

			Magnetic Coordinates (R_J)		B (GAMMA)		
TIME/MODE	S III LAT	S III LONG	R	Z	B_R	B_ϕ	B_z
063 2326:23/M	-0.777	260.209	13.458	0.996	30.385	-22.655	-116.488
2327:59/M	-0.783	261.116	13.439	0.936	27.054	-23.280	-117.443
2329:35/M	-0.789	262.023	13.419	0.929	24.813	-23.237	-118.060
2331:11/M	-0.795	262.930	13.399	0.895	24.273	-22.944	-118.269
2332:47/M	-0.802	263.837	13.379	0.861	23.120	-22.612	-119.303
2334:23/M	-0.808	264.743	13.359	0.827	22.508	-22.766	-119.585
2335:59/M	-0.814	265.650	13.339	0.792	20.767	-22.863	-119.630
2337:35/M	-0.820	266.556	13.319	0.758	19.493	-23.210	-119.607
2339:11/M	-0.826	267.463	13.299	0.723	17.920	-22.908	-120.583
2340:47/M	-0.833	268.368	13.279	0.688	17.559	-23.674	-121.434
064 0025:00/L	-1.014	293.321	12.682	-0.282	-26.092	-25.889	-140.884
0045:48/L	-1.105	304.996	12.377	-0.713	-47.741	-27.086	-152.745
0111:24/L	-1.223	319.306	11.984	-1.186	-74.548	-25.705	-168.035
0130:36/L	-1.315	329.992	11.683	-1.486	-101.963	-26.175	-186.999
0138:36/L	-1.355	334.433	11.556	-1.594	-115.579	-20.202	-191.308
0142:23/M	-1.374	336.526	11.497	-1.642	-119.003	-23.173	-193.180
0150:23/M	-1.415	340.955	11.371	-1.736	-122.521	-18.784	-196.808

and vertical distance above or below the magnetic equator) and, the magnetic field components (in Jovicentric cylindrical coordinates). The magnetic field data is from the magnetometer experiment on Voyager (N. Ness, Principal Investigator) and is measured in units of gammas where $1\ \gamma = 10^{-9}\ T = 10^{-5}\ G$.

There are two major results in the data of Table 3.3-1. First, is the reconfirmation (using the full response) that the plasma departs from strict corotation about Jupiter as one moves out from the planet. *McNutt et. al.* [1981] pointed out that the plasma started to depart from corotation once past the orbit of Io. This analysis used only the D-cup spectra from which a velocity component normal to the D-cup was obtained; this component was inconsistent with the rigid corotation of the plasma. At that time the magnitude of the non-azimuthal velocity component remained unknown. Utilizing the full response function, the second major result shows that there is a substantial non-azimuthal plasma flow component. Again, this feature had been speculated to exist [*McNutt et. al.*, 1981] but the magnitude of this velocity component had not been estimated. Given that 20.5 km/sec = 1 R_J /hr the table of velocities suggests that one cannot ignore the non-azimuthal velocity in considering magnetospheric dynamics.

There is one major drawback with presenting results in the format given in Tables 3.3-1 and 3.3-2: the choice of corrdinate systems. Since the plasma sheet lies, for the most part, in the plane of the magnetic equator, one would expect to find symmetries, or properties, of the plasma with respect to a frame of reference in which the magnetic dipole axis is one of the coordinate axes. With this in mind, the magnetic field values and the plasma bulk flow velocities were transformed from the Jovicentric cylindrical coordinate system to the tilted dipole cylindrical coordinate system based upon the dipole axis being tilted 9.615° to the rotation axis and located in longitude at $\lambda_{III} = 201.682°$. The results of the transformation on the magnetic field and plasma velocities is given in Table 3.3-3 along with the time and mode of each spectra. In this format all the flow patterns seen in Table 3.3-1, are still seen after the transformation. In fact, the non-azimuthal component of plasma flow is seen to be even more pronounced when viewed in this frame.

Table 3.3-3. B AND V IN TILTED DIPOLE COORDINATES

TIME/MODE	B_R	B_ϕ	B_z	|B|	V_R	V_ϕ	V_z	|V|
063 0841:00/L	-17.691	5.722	-13.009	22.693	-42.481	230.933	-61.049	242.614
1527:24/L	-38.236	-6.25	-23.439	44.853	-20.172	208.395	-13.091	209.778
1535:24/L	-42.875	1.825	-22.790	48.590	-9.245	204.181	-4.423	204.438
1738:36/L	-55.367	6.222	-32.144	64.323	-32.291	201.304	-17.876	204.659
1755:11/M	-50.508	3.993	-34.748	61.437	-4.749	201.113	-19.011	202.065
1819:11/M	-40.957	4.042	-37.897	55.946	4.778	205.117	-26.944	206.934
1827:11/M	-36.324	4.042	-39.124	53.539	15.092	198.375	-25.984	200.638
1844:47/M	-25.916	3.962	-43.292	50.612	12.150	194.863	-28.212	197.269
1903:59/M	-11.763	3.967	-47.520	49.114	12.382	193.204	-39.056	197.501
1913:35/M	-1.082	4.696	-48.302	48.542	1.869	181.881	-26.335	183.787
1933:48/L	21.162	2.752	-52.039	56.245	5.668	200.251	1.494	200.337
1934:23/M	21.502	2.972	-52.469	56.782	2.189	192.831	15.522	193.467
1950:23/M	34.997	2.203	-53.010	63.559	-1.827	185.268	22.649	186.656
1956:47/M	40.361	1.622	-54.915	68.171	8.273	184.316	19.148	185.493
2011:11/M	49.713	0.898	-55.768	74.715	-7.856	186.556	25.441	188.446
2033:35/M	63.362	-0.190	-58.475	86.221	-21.672	185.397	24.783	188.297
2103:59/M	76.286	-1.871	-61.881	98.246	-22.349	184.097	30.006	187.860
2148:47/M	85.699	-4.456	-72.402	112.278	-32.423	172.188	30.941	177.925
2223:24/L	80.790	-4.975	-85.034	117.399	-12.623	154.348	38.447	159.564
2233:35/M	77.185	-5.296	-89.041	117.957	-19.512	154.282	35.431	159.496
2236:12/M	75.676	-5.421	-90.952	118.442	-21.746	164.633	39.871	170.783
2244:47/M	72.172	-6.114	-94.403	118.988	-22.411	152.336	29.764	156.826
2255:59/M	64.760	-5.020	-100.065	119.298	-23.804	153.743	33.370	159.114
2308:47/M	55.127	-5.722	-107.279	120.750	-17.085	140.916	38.088	146.969
2311:59/M	51.737	-6.537	-109.108	120.930	-12.239	140.016	38.943	145.845
2323:11/M	44.725	-5.784	-115.089	123.610	-6.857	135.906	34.006	140.264
2324:47/M	42.190	-5.418	-114.948	122.566	-8.860	133.951	37.480	139.378

Table 3.3-3. B AND V IN TILTED DIPOLE COORDINATES (continued)

TIME/MODE	B_R	B_ϕ	B_z	|B|	V_R	V_ϕ	V_z	|V|
063 2326:23/M	40.594	-5.843	-115.429	122.499	-14.914	136.327	40.836	143.092
2327:59/M	37.100	-6.158	-116.843	122.747	-18.273	131.653	42.240	139.465
2329:35/M	34.650	-5.864	-117.723	122.857	-18.057	131.400	41.574	138.997
2331:11/M	33.853	-5.389	-118.017	122.895	-12.156	135.218	36.492	140.582
2332:47/M	32.506	-4.757	-119.163	123.608	-5.969	133.407	35.214	138.105
2334:23/M	31.638	-4.720	-119.592	123.796	-5.690	131.126	37.533	136.511
2335:59/M	29.623	-4.663	-119.859	123.553	-8.573	131.556	42.284	138.450
2337:35/M	28.067	-4.870	-120.054	123.388	-8.967	131.816	41.774	138.567
2339:11/M	26.274	-4.286	-121.151	124.041	-15.602	135.120	37.997	141.226
2340:47/M	25.679	-4.377	-122.136	124.883	-8.899	139.380	30.544	142.965
					-8.796	138.428	34.918	143.032
064 0025:00/L	-26.782	-1.924	-143.103	145.600	-8.754	121.554	25.407	124.489
0045:48/L	-53.678	-1.711	-153.165	162.308	-13.190	138.757	31.099	142.810
					-13.774	144.221	29.32	147.815
0111:24/L	-87.490	-0.200	-163.705	185.618	-5.888	136.337	13.851	137.166
					-3.306	138.196	19.726	139.636
					-4.738	135.971	18.481	137.303
0130:36/L	-120.969	-0.937	-177.245	214.593	-10.008	126.592	16.703	128.081
0138:36/L	-136.630	3.971	-177.494	224.422	-5.959	109.928	14.749	111.075
					-6.702	110.895	12.764	111.828
0142:23/M	-141.091	0.438	-179.194	228.073	-3.227	112.293	11.722	112.949
0150:23/M	-136.629	3.326	-181.848	227.480	-5.198	113.428	10.875	114.066

With the velocities and magnetic field given in the tilted dipole coordinate system, one can determine how much of the non-azimuthal flow is field-aligned and how much is cross-field flow. To make sure only the effect of the non-azimuthal flow is seen, a frame of reference which moves with the azimuthal flow component (i.e., $V_\phi = 0$) is chosen. The results of this velocity decomposition is given in Table 3.3-4. If $V_\parallel$ is positive the flow is in the direction of the magnetic field, while a negative value of $V_\parallel$ indicates bulk flow in the direction opposite to the magnetic field vector (i.e., anti field aligned). For cross-field flow, $V_\perp$ is positive for flow away from Jupiter, and negative for flow toward Jupiter. Comparing values of $V_\parallel$ and $V_\perp$ one notices that most of the non-azimuthal velocity is field-aligned flow. The most notable exceptions to this are the spectra from day 64 and the spectra during hour 18 on day 63. But even these spectra generally show a $V_\parallel$ component which is greater than the $V_\perp$ component. Except for the magnetic equator crossing just before day 64, the sign change on the parallel velocity magnitude seems to be a good indicator of the spacecraft crossing the magnetic equator. When Voyager is above the magnetic equator the flow is field-aligned flow, while below the magnetic equator $V_\parallel$ is anti-field aligned. This behavior of the field aligned portion of the bulk flow was first suggested by *McNutt et. al.* [1981] and seems to be born out here. More will be said about this in Chapter 4.

Radial transport of plasma through the magnetosphere can be inferred by looking at the radial component of the cross-field flow, $V_{\perp_R}$. The data show both inflow and outflow taking place. For the most part, spectra during day 63 exhibit outflow while during day 64 there is a substantial inflow. This seems to be a very interesting result since it is generally thought that the flow is always outward on the dayside magnetosphere. More on this will be said in Chapter 5.

Using the radial and axial components of the parallel and perpendicular flows from Table 3.3-4 (i.e. $V_{\parallel_R}$, $V_{\parallel_z}$, $V_{\perp_R}$, $V_{\perp_z}$), and the radial and axial components to the B-field (obtained from the magnetometer team at the Goddard Space Flight Center), from Table 3.3-3, Figure 3.3-6 was constructed. The squiggly line is a projection of the Voyager 1 spacecraft's trajectory

Table 3.3-4. $V_\perp$ AND $V_\parallel$ IN TILTED DIPOLE COORDINATES (V_ϕ frame of reference)

TIME/MODE	$V_{\parallel_R}$	$V_{\parallel_\phi}$	$V_{\parallel_z}$	$V_\parallel$	$V_{\perp_R}$	$V_{\perp_\phi}$	$V_{\perp_z}$	$\lvert V_\perp \rvert$
063 0841:00/L	-53.102	17.175	-39.048	68.116	10.621	-17.175	-22.001	29.864
1527:24/L	-20.491	-0.335	-12.561	24.037	0.319	0.335	-0.530	0.704
1535:24/L	-9.029	0.384	-4.799	10.232	-0.216	-0.384	0.376	0.579
1738:36/L	-31.614	3.553	-18.354	36.728	-0.677	-3.553	0.478	3.648
1755:11/M	-12.049	0.953	-8.289	14.656	7.300	-0.953	-10.722	13.006
1819:11/M	-10.801	1.066	-9.994	14.754	15.579	-1.066	-16.950	23.047
1827:11/M	-5.936	0.661	-6.393	8.749	21.028	-0.661	-19.591	28.747
1844:47/M	-9.171	1.402	-15.321	17.911	21.321	-1.402	-12.891	24.955
1903:59/M	-8.340	2.813	-33.693	34.823	20.722	-2.813	-5.363	21.589
1913:35/M	-0.583	2.531	-26.034	26.163	2.452	-2.531	-0.301	3.537
1933:48/L	0.286	0.037	-0.695	0.751	5.382	-0.037	-0.037	2.189
1934:23/M	-5.118	-0.707	12.488	-13.514	7.307	0.707	3.034	7.943
1950:23/M	-10.955	-0.690	16.594	-19.896	9.128	0.690	6.055	10.975
1956:47/M	-6.233	-0.251	8.480	-10.527	14.506	0.251	10.668	18.008
2011:11/M	-16.113	-0.291	18.075	-24.216	8.257	0.291	7.366	11.069
2033:35/M	-24.056	0.072	22.200	-32.734	2.384	-0.072	2.583	3.516
2103:59/M	-28.149	0.690	22.834	-36.252	5.800	-0.690	7.172	9.250
2148:47/M	-34.118	1.774	28.825	-44.700	1.695	-1.774	2.116	3.240
2223:24/L	-25.142	1.548	26.463	-36.535	12.519	-1.548	11.984	17.399
2233:35/M	-25.855	1.774	29.827	-39.513	6.343	-1.774	5.604	8.648
2236:12/M	-28.439	2.037	34.180	-44.511	6.693	-2.037	5.691	9.019
2244:47/M	-22.569	1.912	29.520	-37.208	0.158	-1.912	0.244	1.934
2255:59/M	-22.209	1.722	34.316	-40.912	-1.595	-1.722	-0.946	2.531
2308:47/M	-19.001	1.973	36.994	-41.639	1.916	-1.973	1.093	2.960
2311:59/M	-17.272	2.182	36.425	-40.372	5.033	-2.182	2.518	6.036
2323:11/M	-12.354	1.598	31.789	-34.143	5.497	-1.598	2.217	6.139
2324:47/M	-13.150	1.689	35.827	-38.201	4.290	-1.689	1.653	4.898

Table 3.3-4. $V_\perp$ AND $V_\parallel$ IN TILTED DIPOLE COORDINATES (continued)
(V_ϕ frame of reference)

TIME/MODE	$V_{\parallel_R}$	$V_{\parallel_\phi}$	$V_{\parallel_z}$	$V_\parallel$	$V_{\perp_R}$	$V_{\perp_\phi}$	$V_{\perp_z}$	$\lvert V_\perp \rvert$
063 2326:23/M	-14.389	2.071	40.916	-43.422	-0.525	-2.071	-0.080	2.138
2327:59/M	-13.822	2.294	43.532	-45.732	-4.451	-2.294	-1.292	5.171
2329:35/M	-12.672	2.144	43.051	-44.929	-5.385	-2.144	-1.477	5.981
2331:11/M	-10.576	1.684	36.868	-38.392	-1.580	-1.684	-0.376	2.340
2332:47/M	-9.340	1.367	34.240	-35.517	3.371	-1.367	0.974	3.766
2334:23/M	-9.638	1.438	36.432	-37.713	3.948	-1.438	1.101	4.344
2335:59/M	-10.328	1.626	41.787	-43.075	1.755	-1.626	0.497	2.444
2337:35/M	-9.710	1.685	41.532	-42.685	0.743	-1.685	0.242	1.857
2339:11/M	-8.561	1.396	39.474	-40.416	-7.041	-1.396	-1.477	7.328
2340:47/M	-6.518	1.111	31.001	-31.698	-2.381	-1.111	-0.457	2.667
	-7.391	1.260	35.153	-35.944	-1.355	-1.260	-0.235	1.865
064 0025:00/L	4.297	0.309	22.961	-23.361	-13.051	-0.309	2.446	13.282
0045:48/L	8.263	0.263	23.578	-24.985	-21.453	-0.263	7.521	22.735
	7.644	0.244	21.812	-23.114	-21.418	-0.244	7.508	22.687
0111:24/L	4.449	0.010	8.326	-9.440	-10.337	-0.010	5.525	11.721
	7.466	0.017	13.969	-15.839	-10.772	-0.017	5.757	12.214
	6.630	0.015	12.405	-14.066	-11.368	-0.015	6.076	12.890
0130:36/L	4.597	0.036	6.735	-8.154	-14.605	-0.036	9.968	17.682
0138:36/L	4.918	-0.143	6.407	-8.078	-10.877	0.143	8.352	13.714
	3.679	-0.107	4.793	-6.043	-10.381	0.107	7.971	13.089
0142:23/M	4.463	-0.014	5.668	-7.214	-7.690	0.014	6.054	9.787
0150:23/M	3.347	-0.018	4.454	-5.572	-8.545	0.081	6.421	10.689

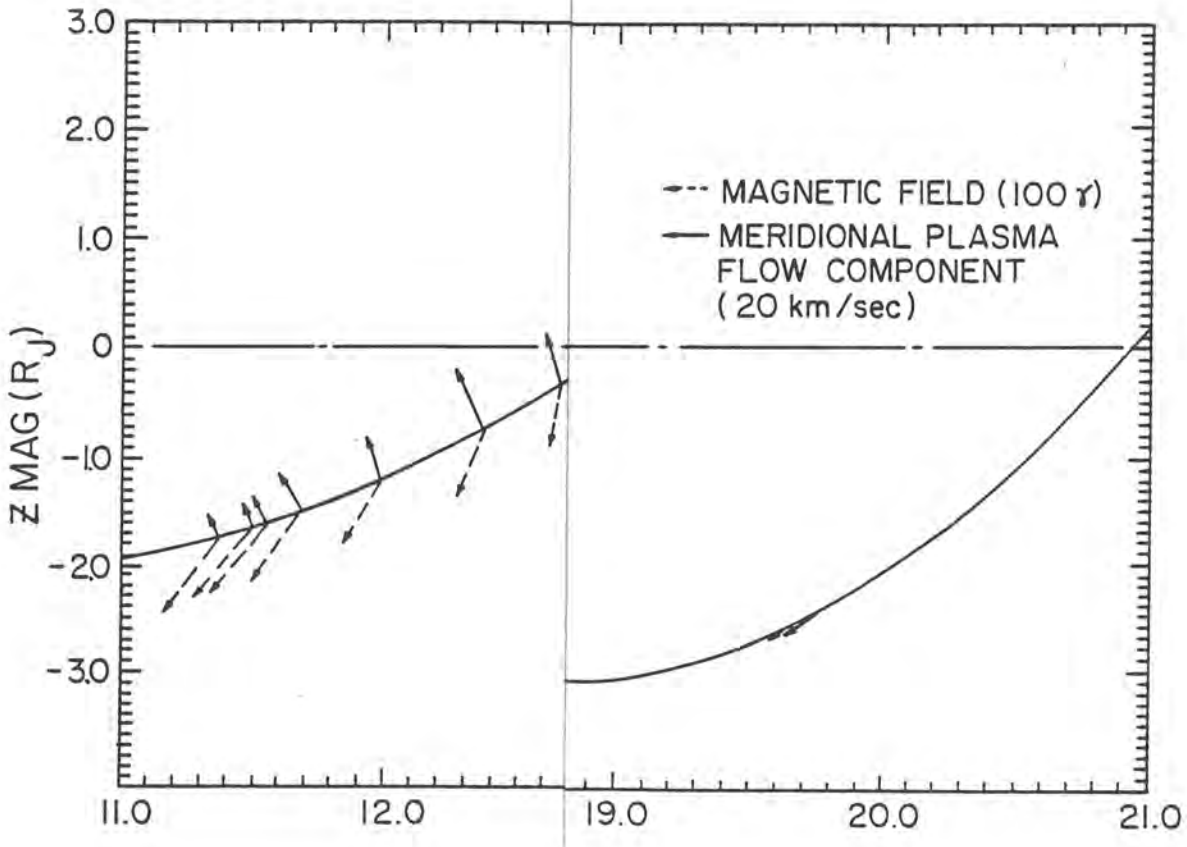
3.0
2.0
1.0
0
-1.0
-2.0
-3.0
Z MAG (R_J)
11.0
12.0
19.0
20.0
21.0
MAGNETIC FIELD (100 γ)
MERIDIONAL PLASMA FLOW COMPONENT (20 km/sec)

onto a magnetic meridional plane, with ZMAG being the distance above or below the magnetic equator and RMAG the cylindrical distance from the dipole axis; both distances are in units of Jovian radii. The poloidal (non-azimuthal) component of the magnetic field for each spectrum is represented by the dashed arrows. Solid arrows represent the non-azimuthal component of the bulk plasma flow obtained for each plasma spectral set. There are several important features of Figure 3.3-6 to note.

The first thing one may notice is the size of the field aligned (anti-aligned) portion of the flow. Every spectrum analyzed gave a flow which yielded a significant field-aligned (anti-aligned) component. The magnitude of this component ranged anywhere from about half the magnitude of the total non-azimuthal flow, to almost all of the non-azimuthal flow. This fact can be brought out more clearly in Figure 3.3-7. The plasma flow along the magnetic field is plotted against the total non-azimuthal flow. For reference, a dotted line has been drawn representing the locus of points where the magnitude of $V_{\parallel}$ equals the magnitude of the total non-azimuthal plasma velocity. The magnitude of this non-azimuthal flow reaches over 60 km/sec, which translates to approximately $3R_J$/hr or roughly one quarter the magnitude of the azimuthal velocity component for the appropriate spectrum. The ratio of the plasma flow along the magnetic field to the total non-azimuthal flow is plotted against cylindrical radius (tilted dipole coordinates), in Figure 3.3-8. Non-azimuthal (parallel, in particular) flow is seen to contribute significantly to the overall plasma flow (azimuthal plus non-azimuthal) throughout the middle magnetosphere. Ratios of 20% and over are apparently not uncommon. It would seem that a dynamical picture of the magnetosphere cannot ignore the non-azimuthal flow component.

A second observation is the direction of flow. From ~13 R_J to 25 R_J, the flow is away from the magnetic equator. If above (north of) the equator, flow is northerly while below the magnetic equator, flow is in the southern direction. However, inside of 13 R_J, while the flow is still away from the equator, the spacecraft is at northern magnetic latitudes; the flow is toward the equator when the spacecraft is at southern magnetic latitudes. This trend of flow away from the magnetic equator along with field-aligned flow is suggestive of solar wind influenced flow. More will be said about this in Chapter 4.

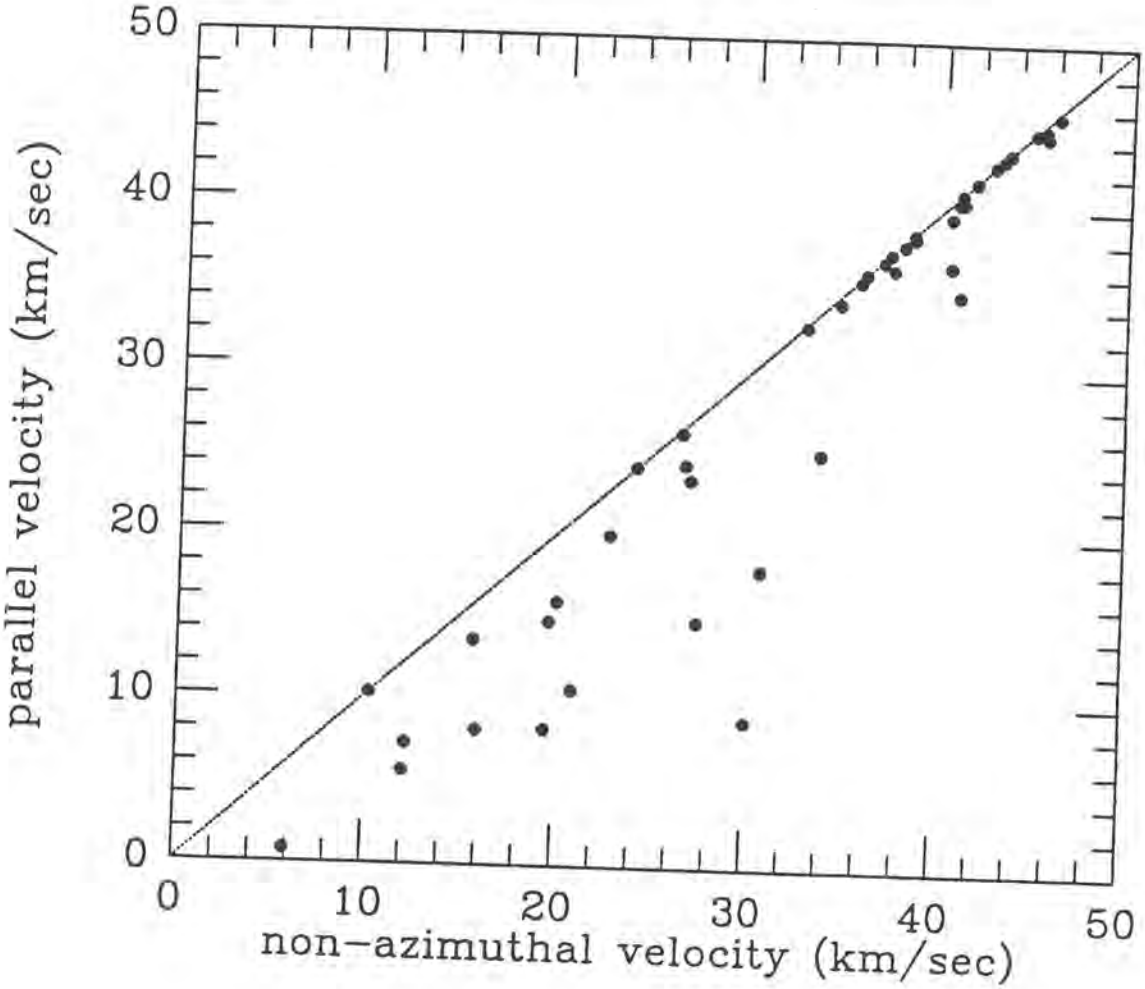

Figure 3.3-7. Plasma flow along the magnetic field is plotted vs. total non-azimuthal flow. Since parallel flow is contained within the non-azimuthal flow, $V_{\parallel}$ can never exceed the magnitude of the non-azimuthal flow component; the dotted line represents this cutoff.

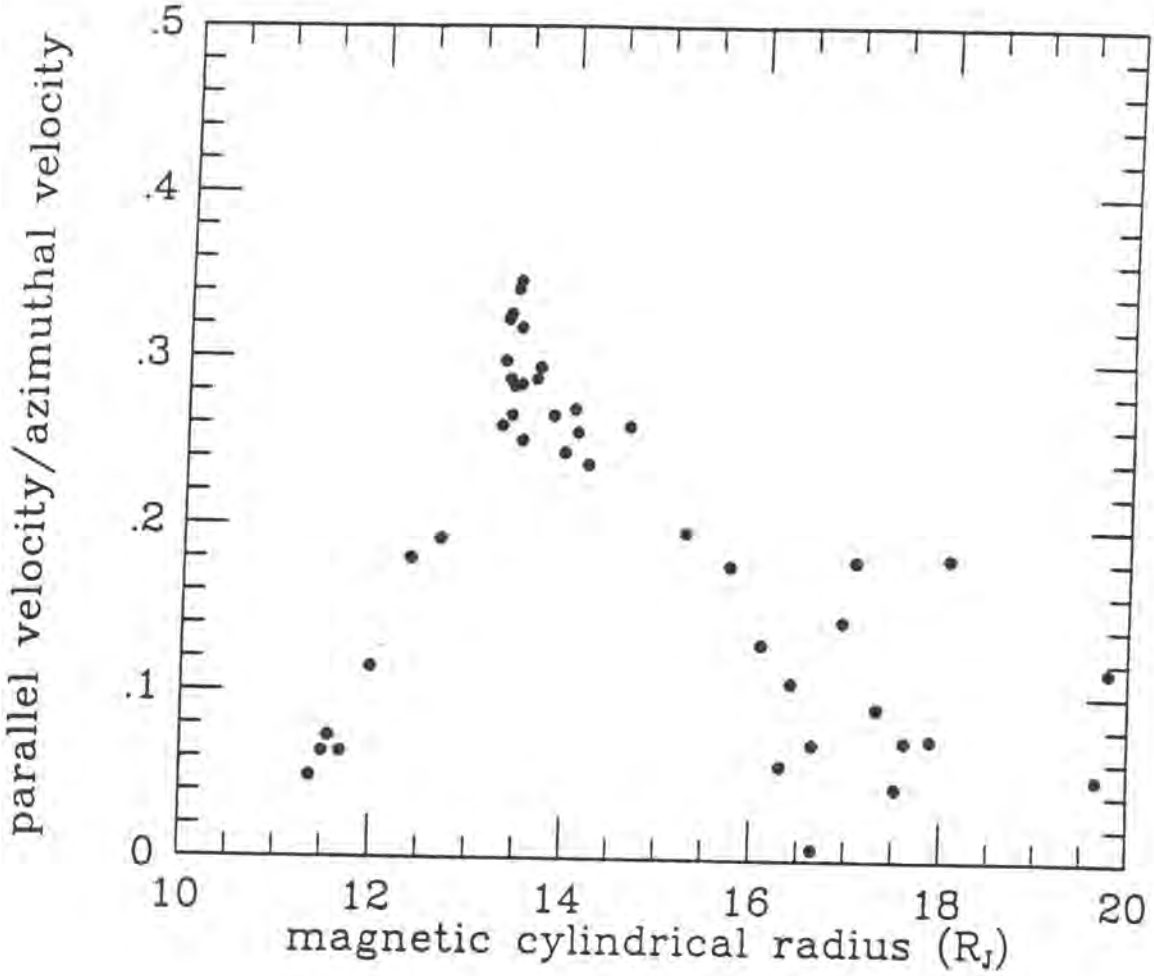

Figure 3.3-8. A plot of the ratio between parallel plasma flow and azimuthal flow vs. cylindrical radial distance.

If one looks at the cross-field component of the flow, another interesting observation can be made. From approximately 15 R_J to 25 R_J the cross-field flow direction is away from Jupiter while between 11 R_J and 13 R_J the direction is toward the planet. In the range 13 R_J to 15 R_J the cross-field flow is very small and oscillates back and forth between going away from Jupiter and moving inwards towards Jupiter. At the same System III longitude but different times, this cross-field flow has opposite signs. First, the direction of flow is away from the planet (the spacecraft is about 25 R_J out), then, at the next occurence of the same longitude (the spacecraft is approximately 12 R_J out), the cross-field flow is towards Jupiter. The significance of this fact will be made clear in Chapter 4.

Several other spectra were analyzed but not included in the tables of data because all three components of the plasma flow could not be determined. However, the fits still supplied useful information, the contents of which will now be discussed.

Further out on the dayside magnetosphere, another "pocket" of cold spectra was analyzed. Between about 40.5 R_J and 41 R_J several spectra had well resolved peaks in the D-cup. However, there was no signal in any of the other three cups, eliminating any chance of determining the full plasma velocity. Eventhough the non-azimuthal component to the flow could not be determined, only the D-cup is needed to obtain a good estimate of the azimuthal component of flow (the look direction of the side sensor faces almost directly into the direction of azimuthal flow). A typical spectrum in this region is shown in Figure 3.3-9 and was obtained on day 62 (March 3) at 1027 UT when Voyager was 40.8 R_J from Jupiter and 5.5 R_J below the magnetic equator (distance measured in magnetic cylindrical coordinates). The absence of an ion signiture in the main sensor is due to a cold ion temperature and a plasma flow velocity which is oblique to the instrument. An upper limit to the non-azimuthal flow component can be determined but is a tedious, time consuming task. With no coherrent signal for the analysis routine to simulate, only a trial and error method can be used. Pick a value of V_R or V_z, allow the analysis routine to calculate the currents, and see if any current shows up in either the B or C cups. If there is, the velocity components must be manually altered and the analysis rerun; there can be no signal in the main sensor. The opposite is also true, if the guess

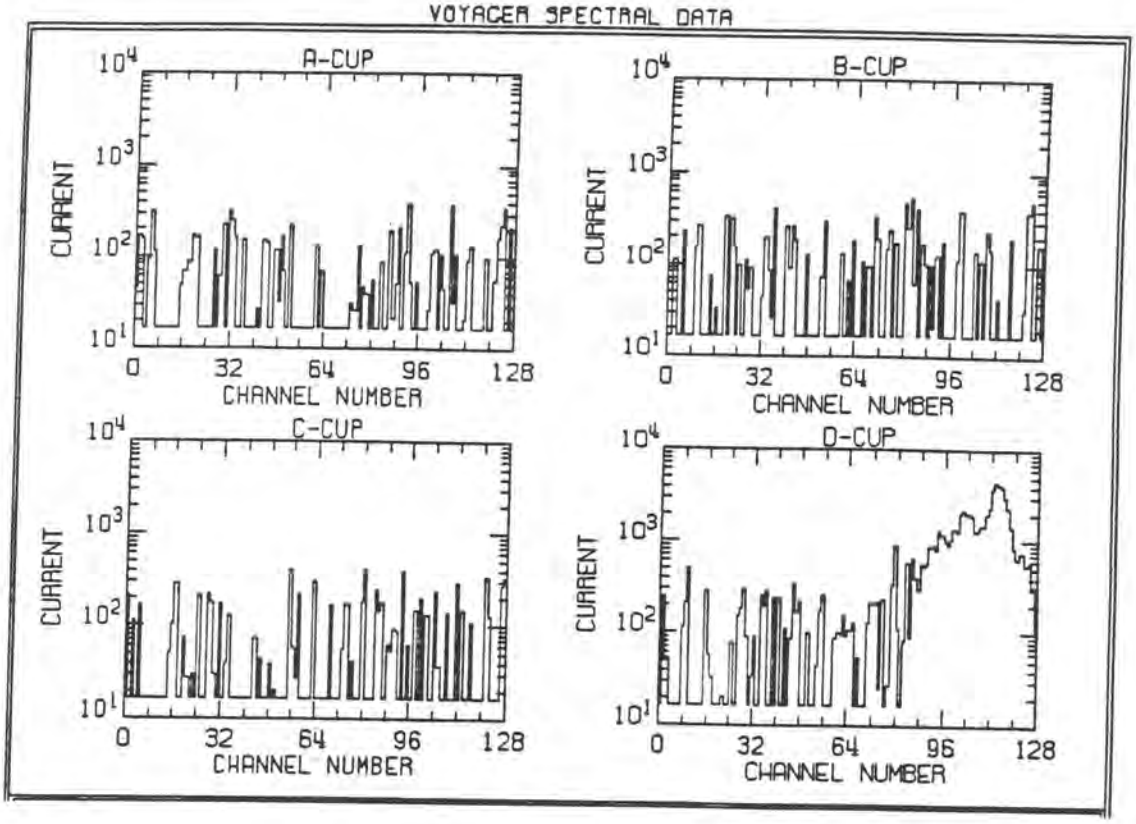

Figure 3.3-9. A spectrum obtained during the traversal of a "pocket" of cold plasma on the inbound portion of the Voyager 1 encounter with Jupiter. The spacecraft was approximately 41 R_J out from Jupiter.

results in no current in the B or C cups; a new guess must be made to see if currents appear. The best that can be achieved is to obtain a locus of possible velocities which would be consistant with the spectrum. It should be noted that V_ϕ too must be altered since changing V_R and V_z affects the position of the ion peaks in the D-cup.

Assuming the plasma flow to be purely azimuthal, the spectrum shown in Fig. 3.3-10 was analyzed with the best fit shown in Figure 3.3-10. Four ion species were used, O^{+2}, S^{+3}, O^{+}, and Na^{+}, all the densities were fit parameters (allowed to change independently), and the ions were assumed to be isothermal (the O^{+2} ion thermal speed was a fit parameter, all other ion thermal speeds were "tied" to the O^{+2} ion thermal speed by the square root of their mass ratio). The fit is very good, which is not surprising since the ion peaks are well resloved in energy-per-charge. Note that the value of V_ϕ obtained from the analysis (210 km/sec) is less than half the local corotation velocity of 517 km/sec. Since the V_R and V_z components were assumed zero, the value of V_ϕ is overestimated. Non-azimuthal velocity causes the current simulated in the D-cup (assuming only an azimuthal velocity) to be shifted down in energy-per-charge. However, ignoring the non-azimuthal flow component produces a decrease of less than 5% in the azimuthal velocity.

All the spectra analyzed in this region are listed in Table 3.3-5 along with the corresponding spacecraft position, in magnetic cylindrical coordinates. The local rigid corotation velocities and azimuthal velocities are also given. All the specta are consistant with V_ϕ nearly constant at 200 km/sec outside of 20 R_J [*McNutt et. al.*, 1981; and *Eviatar et. al.*, 1986].

Closer in to Jupiter, the second of two spacecraft manuvers was performed (called PLOMAN 2; PLasma Outflow MANeuver 2). At about 35 R_J from Jupiter a spacecraft yaw maneuver was performed in which the spacecraft was rotated 360° in a plane approximately parallel to Jupiter's equatorial plane. As the instrument was rotated signals from the flow appeared in the three cups of the main sensor, allowing a velocity measurements to be made. The maneuver began on day 62 (March 3) at 1823 UT and ended on day 62 at 1858 UT. The

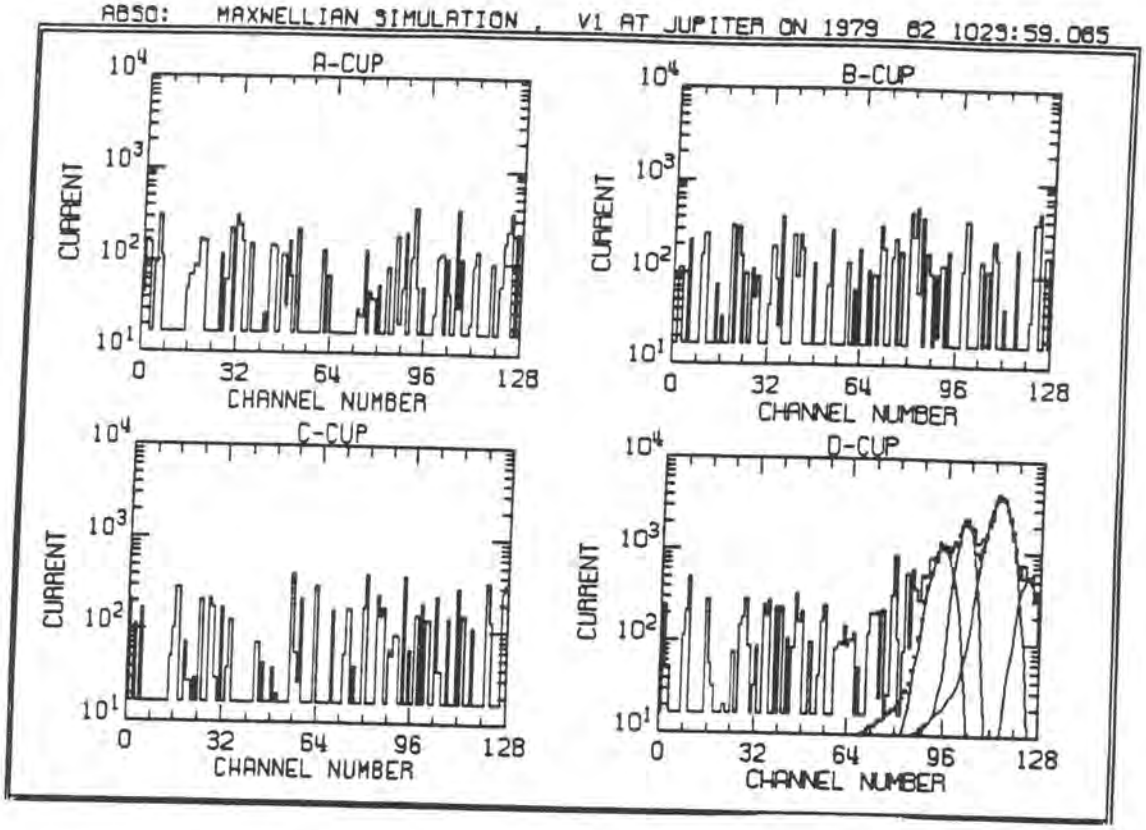

Figure 3.3-10. Results of a fit, assuming only azimuthal flow, to the spectrum in Fig. 3.3-9. The total simulated currents along with the individual ion currents (making up the total current), are superposed on the spectrum for comparison.

Table 3.3-5. PLASMA VELOCITIES (Assumed Azimuthal)

TIME/MODE	R_{MAG} (R_J)	Z_{MAG} (R_J)	Rigid Corotation (km/sec)	V_ϕ (km/sec)
62 1020:47/M	40.92	-5.55	518.01	209.03 ± 1.11
1023:59/M	40.88	-5.54	517.55	215.36 ± 0.46
1027:11/M	40.85	-5.53	517.08	210.02 ± 0.63
1030:23/M	40.81	-5.51	516.62	223.75 ± 0.59
1033:35/M	40.78	-5.48	516.15	232.27 ± 0.06
1036:47/M	40.75	-5.45	515.69	241.67 ± 1.08
1039:59/M	40.72	-5.40	515.22	241.85 ± 0.45
1046:23/M	40.66	-5.29	514.29	245.88 ± 0.71

maneuver was performed so that the PLS experiment could try and detect any outflowing plasma.

A typical spectrum during this maneuver is shown in Figure 3.3-11, obtained on day 62 (March 3) at 1844 UT when the spacecraft was at a cylindrical radius of 35.3 R_J from Jupiter and 2.1 R_J below the magnetic equator (in magnetic cylindrical coordinates). Low resolution modes were looked at because of their better signal-to-noise ratio. Because the ions were hot (large thermal speeds) individual ion peaks could not be identified. Ion species chosen for this analysis was based upon prior experience. All the spectral data seemed to consist of H^+, O^{+2}, S^{+3}, and O^+ ions, so these four were used in the analysis. The S^+ ion was not used because its peak occured above the highest energy-per-charge channel; only a portion of the feedthrough contribution could be seen which had no impact on the analysis. The best fit to this spectrum is illustrated in Figure 3.3-12, using all four ion densities, all three plasma velocity components, and the H^+ thermal speed as the fit parameters (a common thermal speed was assumed for all the ions).

None of the low energy-per-charge channels could be simulated in the main sensor, although the match was quite good in the rest of the channels. The biggest problem was the inability to get any current into the side sensor. A fit to the D-cup could only be achieved by increasing the thermal speeds of all the ions, resulting in the fit shown in Figure 3.3-13. By matching the current signiture in the D-cup, the currents simulated for the main sensor were orders of magnitude too high. This problem occured for every spectrum analyzed; the D-cup could not be simultaneously fit with the three cups of the main sensor. Trying to approximate the radial outflow was inconclusive at best. In fact, during the three minutes covered by the spectral data, which were analyzed, the plasma radial velocity covered the range from approximately $V_R = -2$ km/sec in one case, to $V_R = 61$ km/sec for the spectrum discussed here. Four spectral data sets could be analyzed during this maneuver with the results given in Table 3.3-6. The only firm conclusion which can be reached from the analysis of these spectra is that the plasma flow is primarly in the azimuthal direction and sub-corotational.

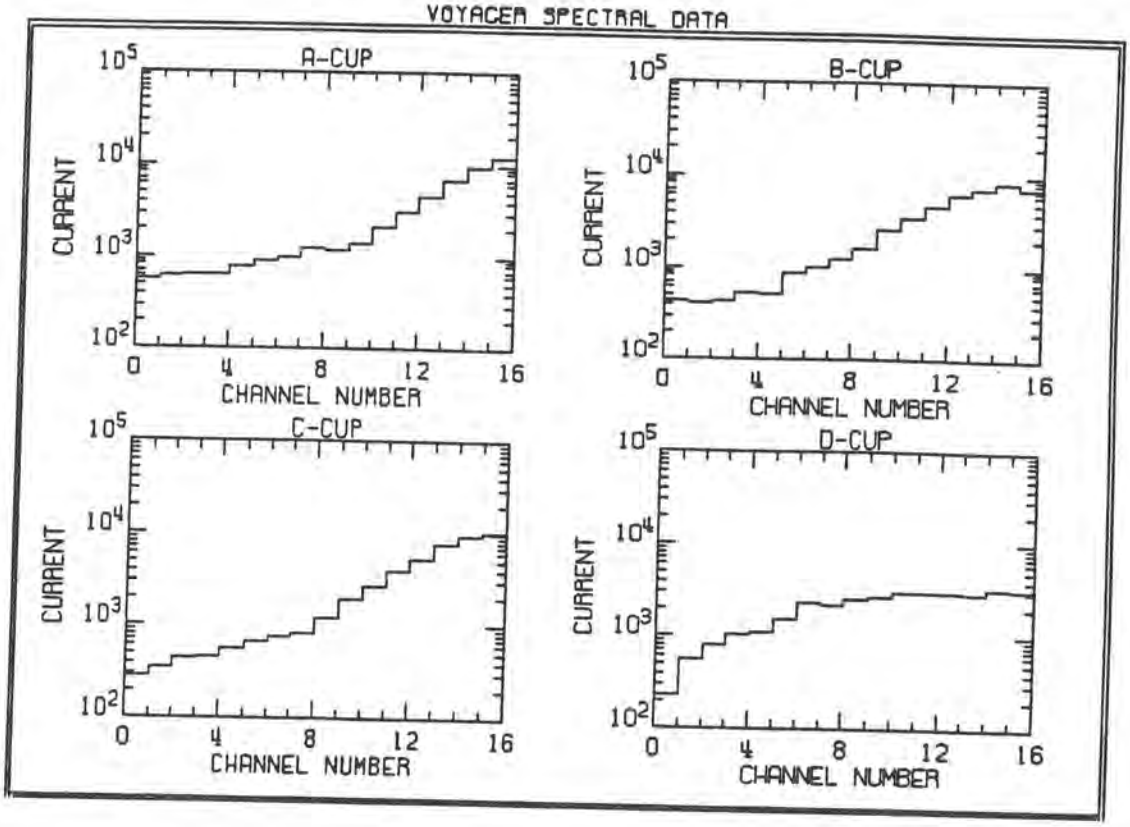

Figure 3.3-11. A spectrum obtained during the PLOMAN 2 maneuvar. The spacecraft was approximately 35 R_J out from Jupiter.

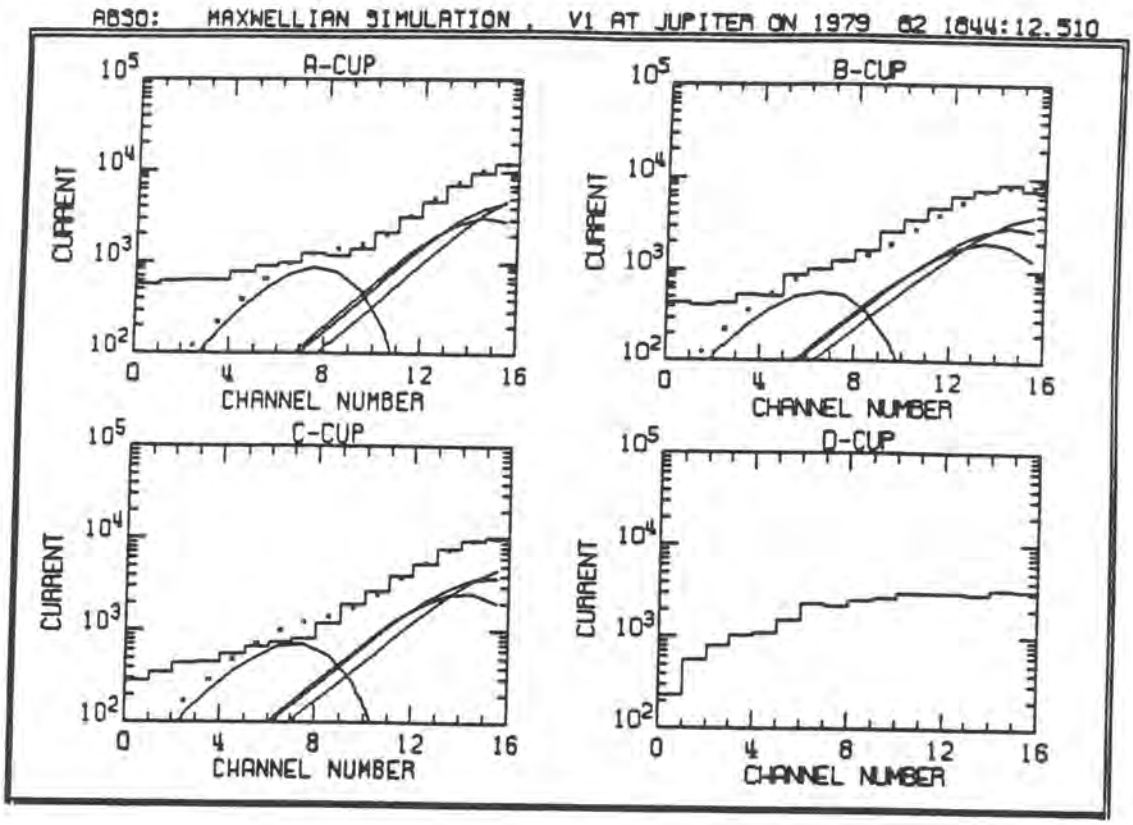

Figure 3.3-12. Results of a fit to the spectrum in Fig. 3.3-11. Performing the analysis revealed that only the current in the main sensor could be reproduced. Total, and individual ion currents are superposed on the spectrum.

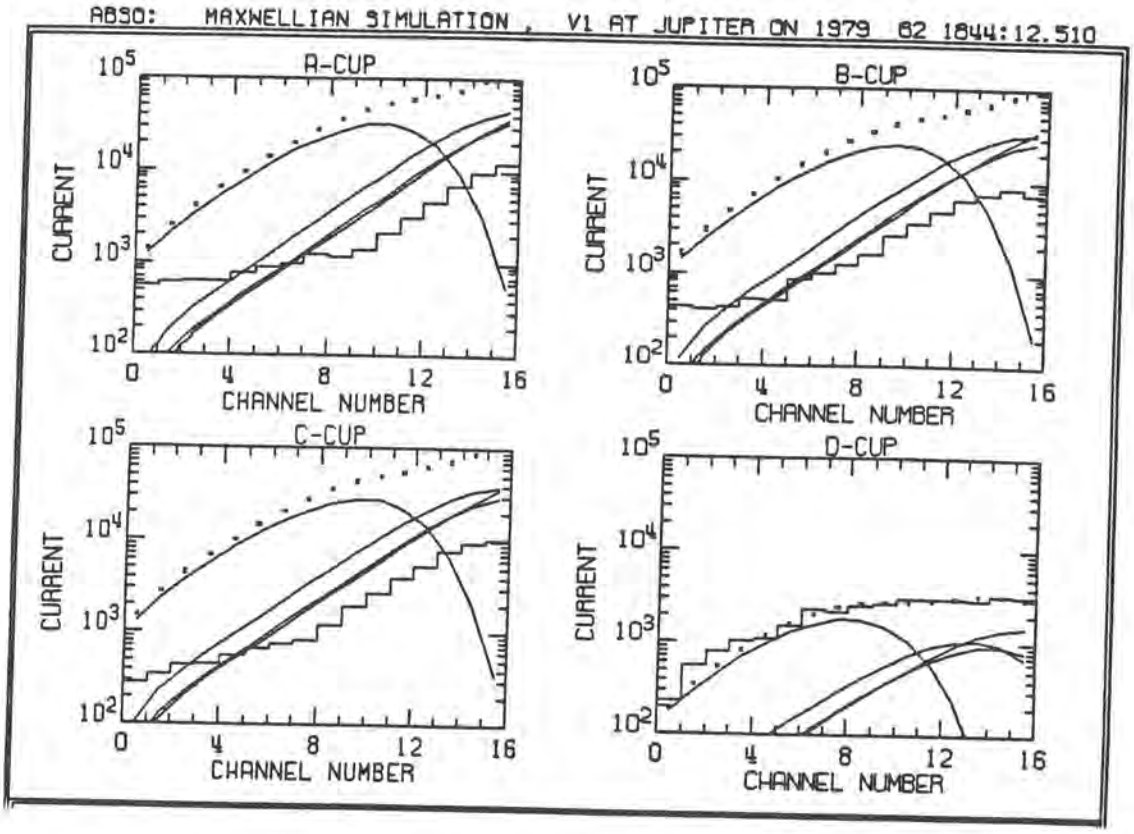

Figure 3.3-13. Results of a fit to the spectrum in Fig. 3.3-11 in which the D-cup signal is simulated. Total, and individual ion currents are superposed on the spectrum.

Table 3.3-6. PLASMA VELOCITIES DURING PLOMAN 2

TIME/MODE	R_{MAG} (R_J)	Z_{MAG} (R_J)	V_R (km/sec)	V_ϕ (km/sec)	V_z (km/sec)
062 1844:12/L	35.33	-2.06	61.85 ± 10.99	253.53 ± 10.56	-0.22 ± 3.31
1845:48/L	35.30	-2.14	0.62 ± 1.34	205.85 ± 10.51	-19.49 ± 8.67
1846:23/M	35.29	-2.17	36.98 ± 5.23	233.15 ± 2.95	42.93 ± 4.59
1847:24/L	35.28	-2.23	-1.13 ± 0.65	215.74 ± 1.29	41.42 ± 2.66

On the outbound leg of the Voyager trajectory only one spectrum was analyzed. This spectrum is shown in Figure 3.3-14 and was obtained on day 64 (March 5) at 1942 UT when Voyager was 9.3 R_J away from Jupiter and 0.28 R_J below the magnetic equator (distance measured in magnetic cylindrical coordinates). Analysis of this spectrum came out of a need for comparison of results given by *Hairston* [1986], the details of which are presented in Chapter 5.

Fitting this spectrum consisted of using eight ion species, five cold species (O^{+2}, S^{+3}, O^{+}, K^{+}, and Na^{+}) and three hot species (H^{+}, O^{+}, and Na^{+}). All the densities were allowed to vary independently, as well as all three velocity components. Cold ions were assumed to be isothermal with the O^{+2} ion thermal speed being the fit parameter, while the temperatures were allowed to vary independently for the hot ions. The fit obtained from the analysis is shown in Figure 3.3-15. The current in the main sensor (due to the hot ions) could not be totally reproduced, the calculated current tended to be too high in the low energy-per-charge channels and too low in the middle channels. Overall, the D-cup was simulated well except for the highest channels and lowest channels. The cold ion peaks were "smeared out" due to having thermal speeds which were slightly too large. However the structure of the cold ion peaks hint at being partially artifical (for example, note the squared off top of the highest peak in Fig. 3.3-14), which would cause problems for the analysis routine. Ignoring this possability, which would mostly affect density and thermal speed, the plasma velocity obtained was $\mathbf{V} = -7.4\hat{\mathbf{e}}_R + 115.3\hat{\mathbf{e}}_\phi + 8.6\hat{\mathbf{e}}_z$ km/sec. Fitting only the cold ions and assuming only azimuthal flow results in $V_\phi = 112.5$ km/sec. Both fits give an azimuthal velocity which is below the local corotation value of $V_\phi = 117.3$ km/sec. As a final note, when a convected bimaxwellian was assumed for the ion distribution function, no improvement was seen and the plasma flow was almost identical to the Maxwellian case.

3.4. Bimaxwellian Fits

To determine if the non-azimuthal component of plasma flow was due to a temperature anisotropy (or how an anisotopy would affect the velocity determination), spectra would have to

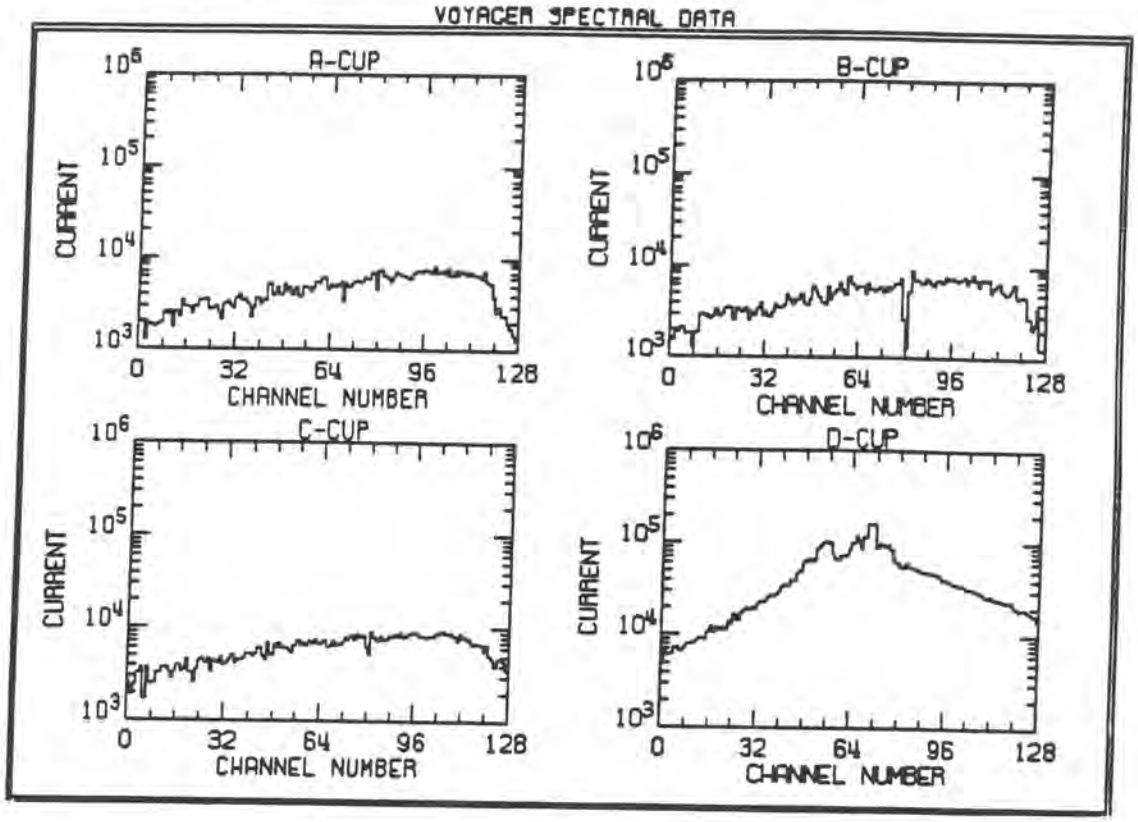

Figure 3.3-14. A spectrum obtained on the outbound leg of the Voyager 1 trajectory. The spacecraft was about 9 R_J past Jupiter.

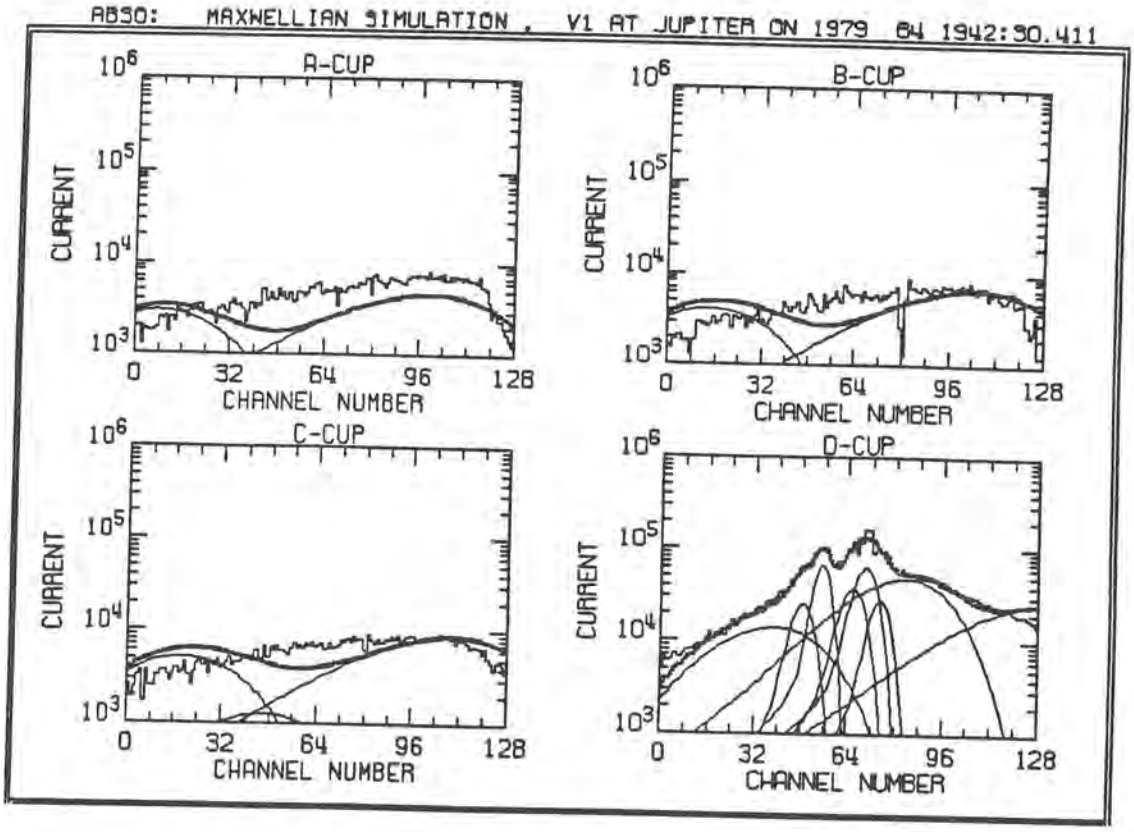

Figure 3.3-15. Results of a fit to the spectrum in Fig. 3.3-14. Both the "hot" ion background and "cold" ion peaks are simulated. Total, and individual ion currents are superposed on the spectrum.

be reanalyzed allowing the parallel and perpendicular thermal speeds to vary independently. Several spectra were analyzed assuming both a bimaxwellian and maxwellian distribution. One of these spectra is shown in Figure 3.3-2 (the Maxwellian simulation to this spectrum was presented in the previous section).

The spectrum is quite cold, the peaks representing the heavy positive ions can be picked out as well as the proton peak. As input to MJSANL, five positive ion species were used (H^+, O^{+2}, S^{+3}, O^+ (S^{+2}), and S^+) where $\mathbf{V}_R$, $\mathbf{V}_\phi$, $\mathbf{V}_z$, and the five ion densities were fit parameters. To check the affect of a temperature anisotropy on the determination of the plasma bulk flow, I reanalyzed the spectrum assuming $f(\mathbf{x}, \mathbf{v}, t)$ to be a convected bimaxwellian. Results of this fit are shown in Figure 3.4-1. The fit assuming a convected bimaxwellian falls right on top of the convected Maxwellian fit. The only differences show up in the last few channels of the B-cup and a slightly larger signal in the A-cup. Other spectra analyzed assuming both a Maxwellian and bimaxwellian ion distribution function gave similar results. This spectrum was shown because it had the largest deviation between the two cases and thus provided an upper limit to any possible temperature anisotropies in the middle magnetosphere. Because the hot ion background was not simulated, the parallel temperature was continually being increased to try and account for the signal in the upper channels. However, the current calculated in the A-cup served as a check to the maximum anisotropy allowed. A further increase in $T_\parallel$ caused the calculated current in the A-cup to overshoot the actual measured values, thus limiting the anisotropy. This "simulated" anisotropy gives an upper limit of the ratio $T_\parallel / T_\perp = 6.5$. The most important result was even with a temperature anisotropy greater than six, the calculated bulk plasma flow was practically identical to the Maxwellian case; for a convected bimaxwellian distribution, $\mathbf{V} = -4.9\hat{\mathbf{e}}_R + 140.1\hat{\mathbf{e}}_\phi + 16.9\hat{\mathbf{e}}_z$ km/sec.

Of all the spectra sent back by Voyagers 1 and 2 during the Jupiter encounter, only one spectrum has been found to exhibit a true temperature anisotropy. The spectrum shown in Figure 3.4-2 was obtained by Voyager 2 on July 9 (day 190), 1979 at 0720 UT (i.e., 1979 190 0720), where the spacecraft was 14.9 R_J from the dipole axis and 2.9 R_J below the magnetic

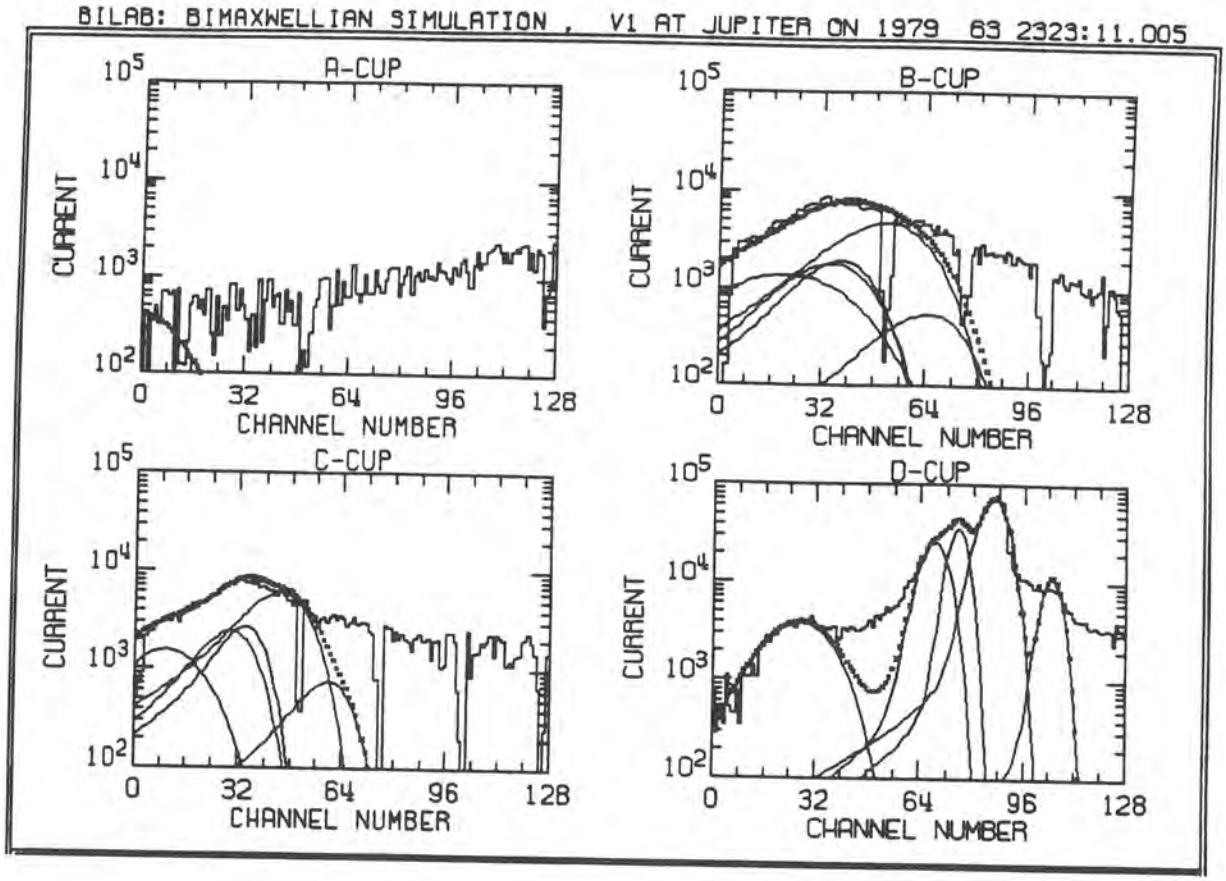

Figure 3.4-1. Results of a fit, assuming a bimaxwellian ion distribution function, to the spectrum in Fig. 3.3-2. There is very little difference between this fit and the fit assuming the ion distribution function to be Maxwellian (Fig. 3.3-4). Total, and individual ion currents are superposed on the spectrum.

equator. Because the spectrum was so hot, the individual peaks of the heavy ions all merged into one broad peak. The proton peak however, is still discernable in all four cups and could thus be used to yeild a bulk plasma flow. Fit parameters consisted of the proton density, thermal speed, and all three components of the bulk plasma flow. All four cups were used in the analysis since the proton signature is easily picked out in every cup. The best fit from the analysis, assuming a convected Maxwellian ion distribution, could not simulate the currents in all four cups simultaneously. For later comparison to the bimaxwellian case, results of this fit is shown in Figure 3.4-3. It was because of this inability to fit any cup which suggested a convected bimaxwellian distribution might do a better job. Using the same fit parameters as before but now allowing the parallel and perpendicular thermal speeds to vary independently gave the fit shown in Figure 3.4-4. The two fits are superimposed to show the difference in the results. Allowing the parallel and perpendicular temperatures to float independently greatly improved the fit in all four cups, giving an anisotropy of $T_{\parallel}/T_{\perp} = 3.08$. The bulk velocity was $\mathbf{V} = -44.2\hat{\mathbf{e}}_R + 151.4\hat{\mathbf{e}}_\phi - 48.1\hat{\mathbf{e}}_z$ km/sec which gave a non-azimuthal component of flow which was much larger than the maxwellian case.

Two important results came out of this analysis: the magnetospheric plasma is well approximated assuming a convected isotropic Maxwellian distribution for the ions, and the non-azimuthal flows obtained using a Maxwellian distribution are real and accurate. As a final note, even when spectra exhibit temperature anisotropies, the non-azimuthal flow component persists, giving further evidence that this component of the flow is real.

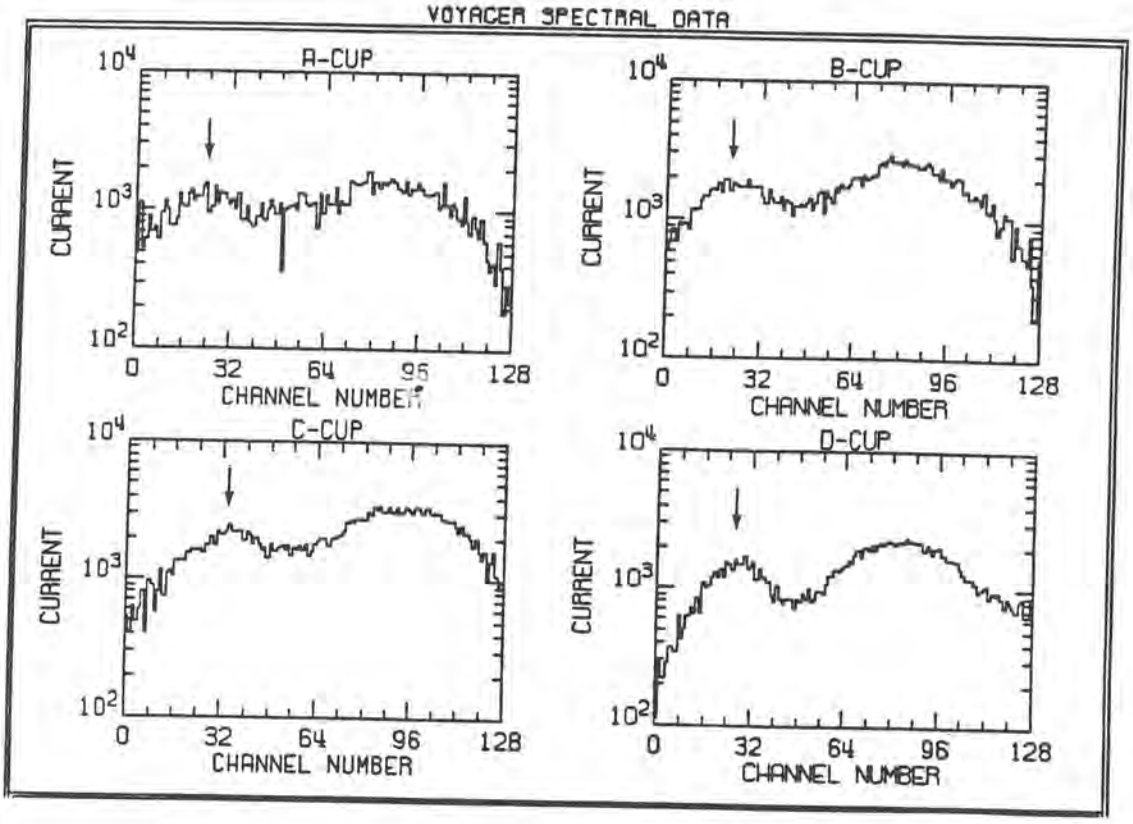

Figure 3.4-2. A spectrum obtained on the inbound portion of the Voyager 2 encounter with Jupiter. Voyager is about 15 R_J from Jupiter. Because the plasma temperature is high, only the proton peak is discernable in the four cups.

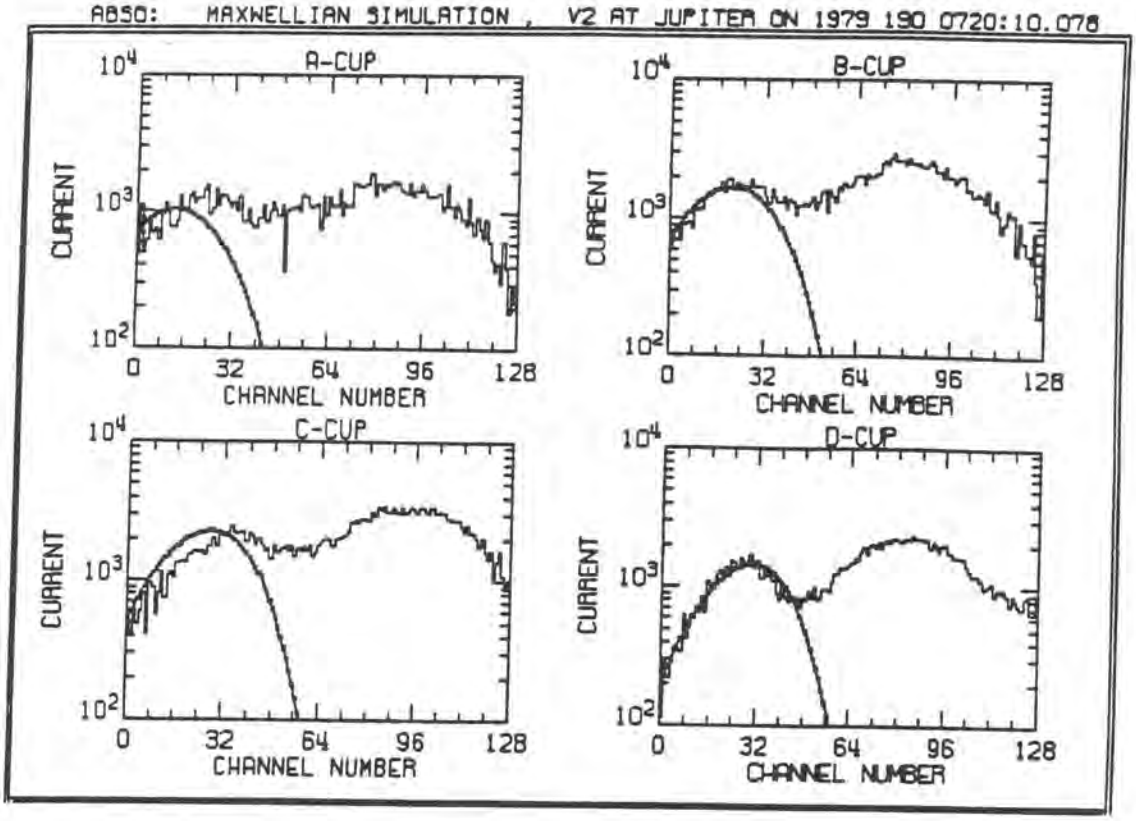

Figure 3.4-3. Results of a fit to the spectrum in Fig. 3.4-2, assuming a Maxwellian ion distribution function. The analysis is carried out for the protons only. Currents from all the cups could not be well simulated simultaneously.

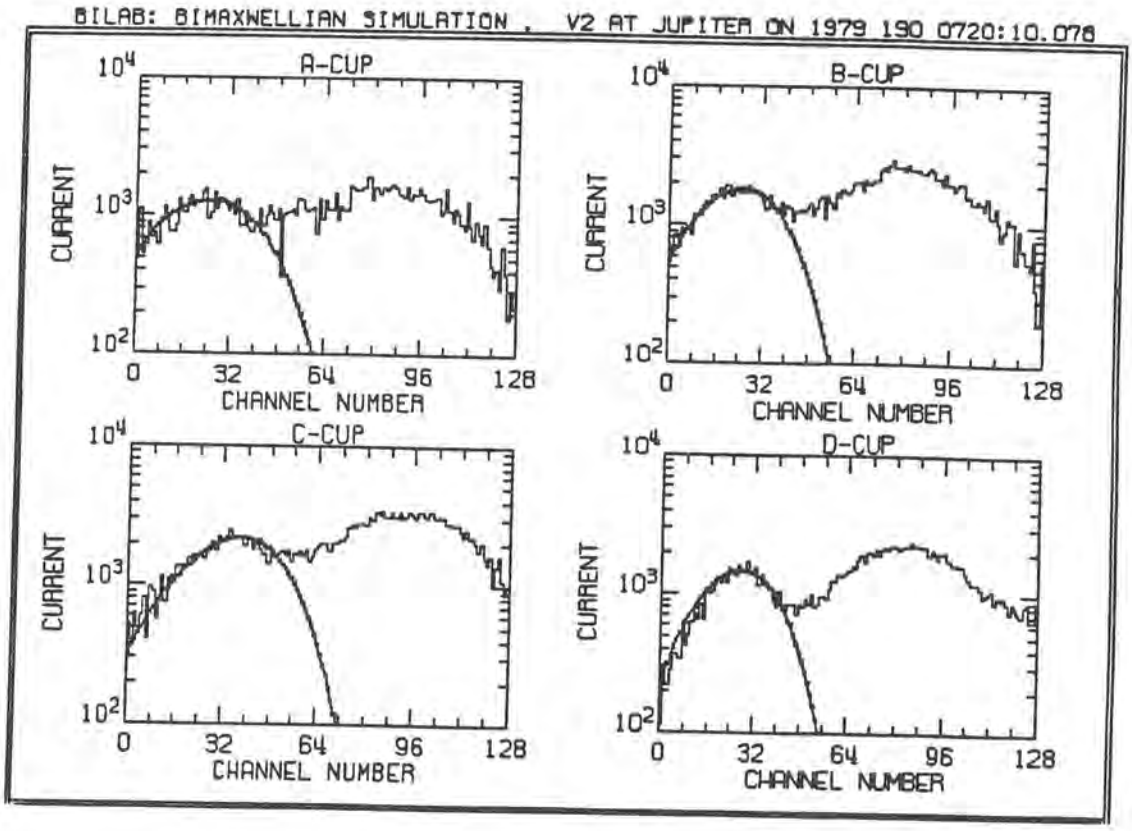

Figure 3.4-4. Results of a fit to the spectrum in Fig. 3.4-2, assuming a bimaxwellian ion distribution function. Only the protons are fit and the current from all four cups could be simulated.

CHAPTER 4

RESULTS

4.1. Magnetospheric Convection

Before discussing some consequences of the analysis performed in Chapter 3, new terminology must be introduced. The idea of magnetospheric convection was first developed by *Dungey* [1961], and *Axford et. al.*, [1965]. It is one of the most important concepts in magnetospheric physics; it is useful not only in the study of planetary magnetospheres, but also in astrophysics in the study of magnetospheres of pulsars, supernova remnant shells, binary star systems, and other phenomena. Only a brief description will be given here, a more detailed coverage of convection is given by *Hines* [1963], *Stern* [1977], *Vasyliunas* [1974], and references therein.

In space physics, a plasma can usually be considered as being collisionless (but only if high ion temperature and low density give a collisional scale length large compared to the dimensions of the system; for example, collisions are important in the Io torus), thus, transport of particles along **B** is unimpaired. This implies that the electrical conductivity, σ, parallel to the magnetic field, is infinite (although there typically can be anomolous effects), shorting out any parallel electric field (i.e., $E_{\|} = 0$), implying

$$\mathbf{E} \cdot \mathbf{B} = 0 \tag{4.1.1}$$

In steady state, the electric field can be expressed as the gradient of a scalar potential Φ,

$$\mathbf{E} = -\nabla\Phi \tag{4.1.2}$$

The result of substituting Eq. 4.1.2 into Eq. 4.1.1 implies that magnetic field lines are electric equipotentials. From ideal MHD, it is known that the component of **E** orthogonal to **B** causes the guiding center of a particle to drift with velocity

$$\mathbf{V} = \frac{c\mathbf{E} \times \mathbf{B}}{B^2} \tag{4.1.3}$$

Taking the dot product of Eq. 4.1.3 with $\mathbf{E}$ implies, from Eq. 4.1.2, that the plasma velocity, $\mathbf{V}$, also lies on surfaces of electric equipotentials.

For a planetary magnetosphere, convective motion results from the flow of the solar wind past the magnetosphere. Consider the planetary magnetic field lines which connect with the interplanetary magnetic field lines (i.e., "open" magnetosphere). Since the magnetic field lines are electric equipotentials, the solar wind electric field can be mapped down to the polar cap (region where the planetary and interplanetary field lines connect). Similarly, the plasma flow pattern can be mapped down along the field lines to the polar cap. Continuity then requires a return flow within the closed field line region of the magnetosphere (see Fig. 4.1-1). Mapping the return flow out into the equatorial plane of the magnetosphere gives rise to the convective circulation pattern shown in Fig. 4.1-2.

The discussion so far has neglected rotational affects of the planet. Convection over the polar cap represents a mapping of the external flow, and this is not directly affected by rotation. However, within the closed field line region the plasma flow, and associated electric field, will be modified by rotational affects.

Treating the planet (more properly the ionosphere of the planet) as an ohmic conductor, the electric field and current density are related by

$$\mathbf{E} + \frac{\mathbf{V}_s \times \mathbf{B}}{c} = \eta \cdot \mathbf{J} \tag{4.1.4}$$

where η is the resistivity tensor, and $\mathbf{V}_s$ is the bulk flow velocity of the neutral atmosphere at ionospheric heights. In the magnetosphere, $\mathbf{E}$ and $\mathbf{J}$ are governed by

$$\mathbf{E} + \frac{\mathbf{V} \times \mathbf{B}}{c} = 0 \tag{4.1.5}$$

$$\frac{\mathbf{J} \times \mathbf{B}}{c} = \rho \left[\frac{\partial}{\partial t} + \mathbf{V} \cdot \nabla \right] \mathbf{V} + \nabla \cdot \mathbf{P} \tag{4.1.6}$$

where $\mathbf{V}$ is the plasma bulk flow velocity and $\mathbf{P}$ represents the pressure tensor.

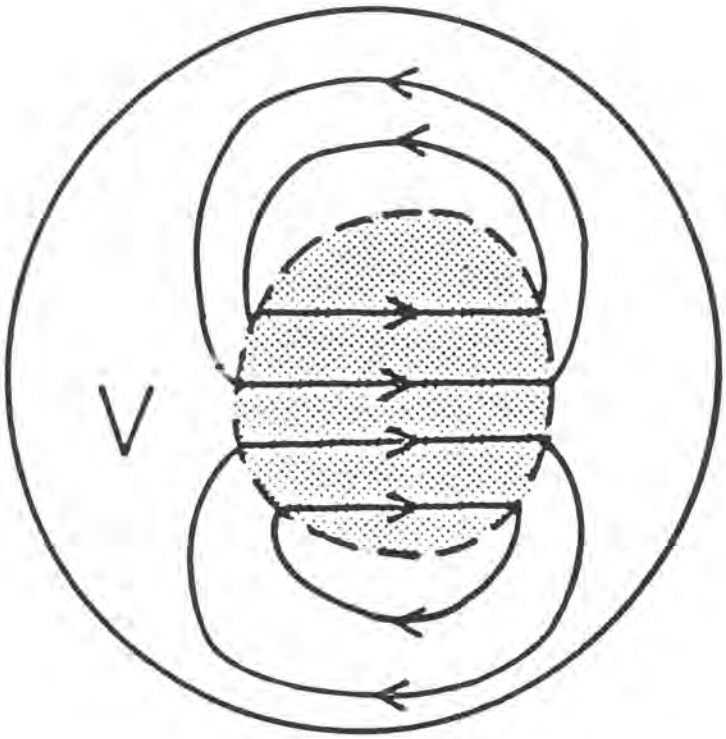

Figure 4.1-1. Streamlines of plasma flow mapped down along the magnetic field lines. Return flow occurs in closed field line region. The speckled region represents the polar cap.

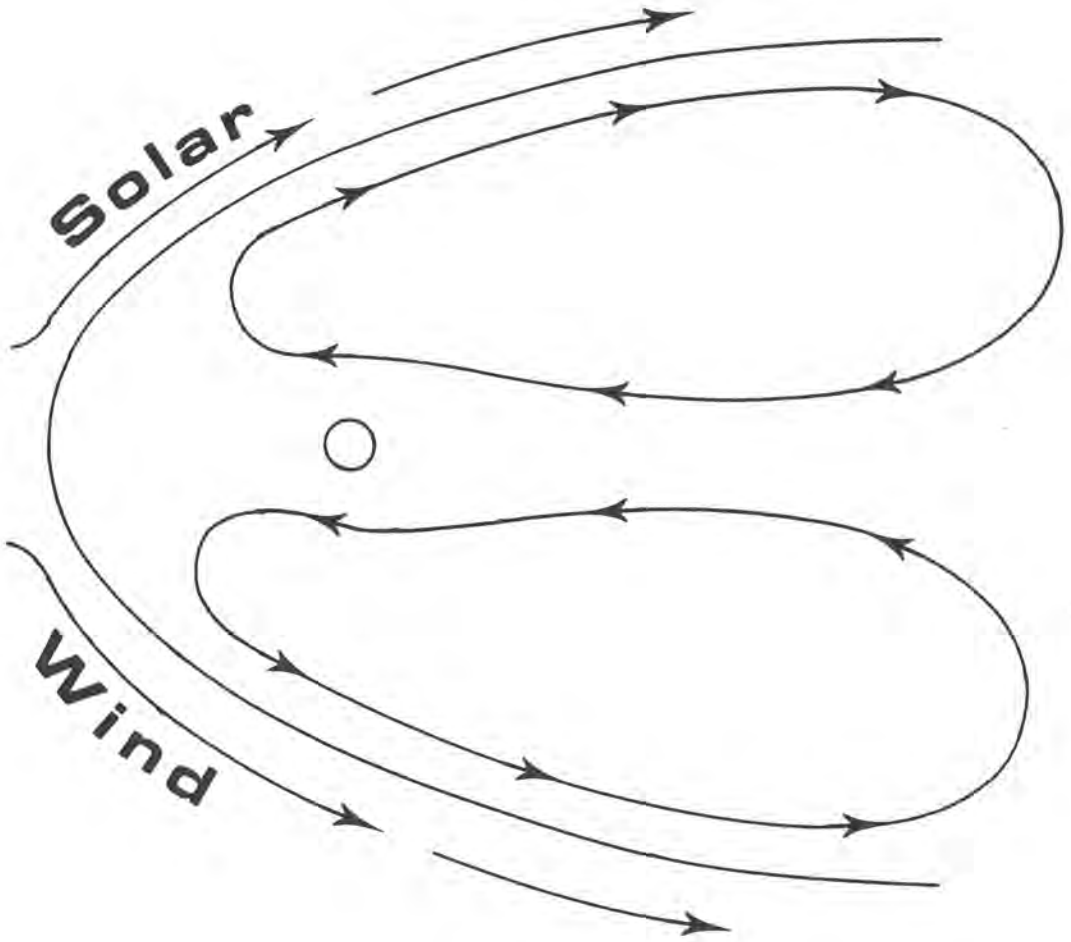

Figure 4.1-2. Return flow of Fig.4.1-1 mapped out into the equatorial plane of the magnetosphere. This is what is called the convective circulation pattern.

The neutral atmosphere of the planet provides a viscous transfer of momentum from the rotating planet to the ionosphere, spinning the ionosphere up to some velocity V. An electric field will be set up in the ionosphere according to

$$\mathbf{E} = -\frac{\mathbf{V} \times \mathbf{B}}{c} \tag{4.1.7}$$

Because the vertical scale height of the ionosphere is much smaller than the length scale of a planetary magnetosphere (typically the planetary radius), Eq. 4.1.7 can be substituted into Eq. 4.1.4 giving

$$\mathbf{E}^* \equiv \eta \cdot \mathbf{J} = \frac{(\mathbf{V}_s - \mathbf{V}) \times \mathbf{B}}{c} \tag{4.1.8}$$

where $\mathbf{E}^*$ is the electric field in the rest frame of the ionosphere. Thus, if $\mathbf{V} = \mathbf{V}_s$, there is no current in the frame of reference rotating with the planet (i.e., moving with velocity $\mathbf{V}_s$ in the ionosphere) and the magnetosphere is said to rigidly rotate or corotate with the planet. However, if $\mathbf{V} \neq \mathbf{V}_s$, a current is produced which is directed equatorward (see Fig. 4.1-3). To satisfy current continuity,

$$\nabla \cdot \mathbf{J} = 0 \tag{5.1.9}$$

currents must flow out along magnetic field lines at lower latitudes and in along magnetic field lines near the pole. These field-aligned currents are called Birkeland currents. Finally, the current loop must close somewhere in the magnetosphere, requiring the current to cross magnetic field lines. By mapping the electric field out along the magnetic field lines, the plasma bulk velocity can be determined using Eq. 4.1.3. The plasma flow lines (i.e., electric equipotentials) mapped back to the planet's surface are shown in Fig. 4.1-4.

Superposition of the convective motion and the rotational motion leads to the flow topology illustrated in Fig. 4.1-5. The heavy dot indicates the stagnation point, where the two flows cancel, and represents the plasmapause. This topology was put forward by *Nishida* [1966] and *Brice* [1967], who both identified the plasmasphere as the region bounded by the plasmapause. The plasmasphere lies outside the dot in the top figure (this corresponds to the

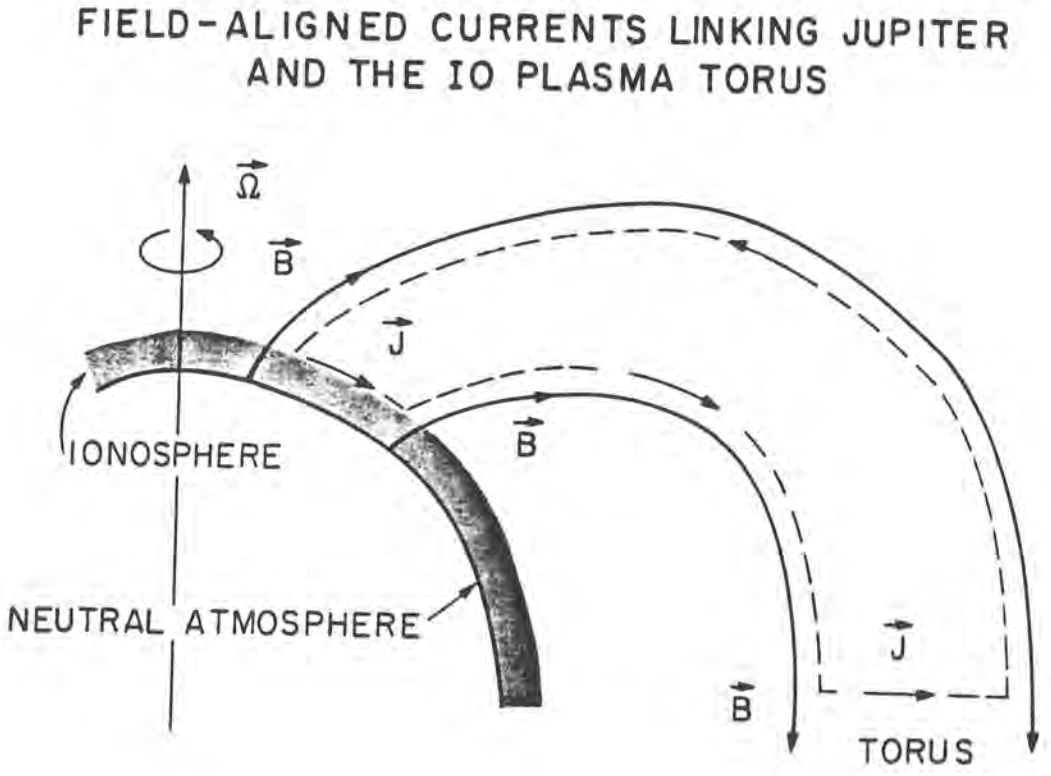

Figure 4.1-3. Current system set up between ionosphere and magnetosphere due to breakdown of rigid corotation. The field-aligned currents are called Birkland currents.

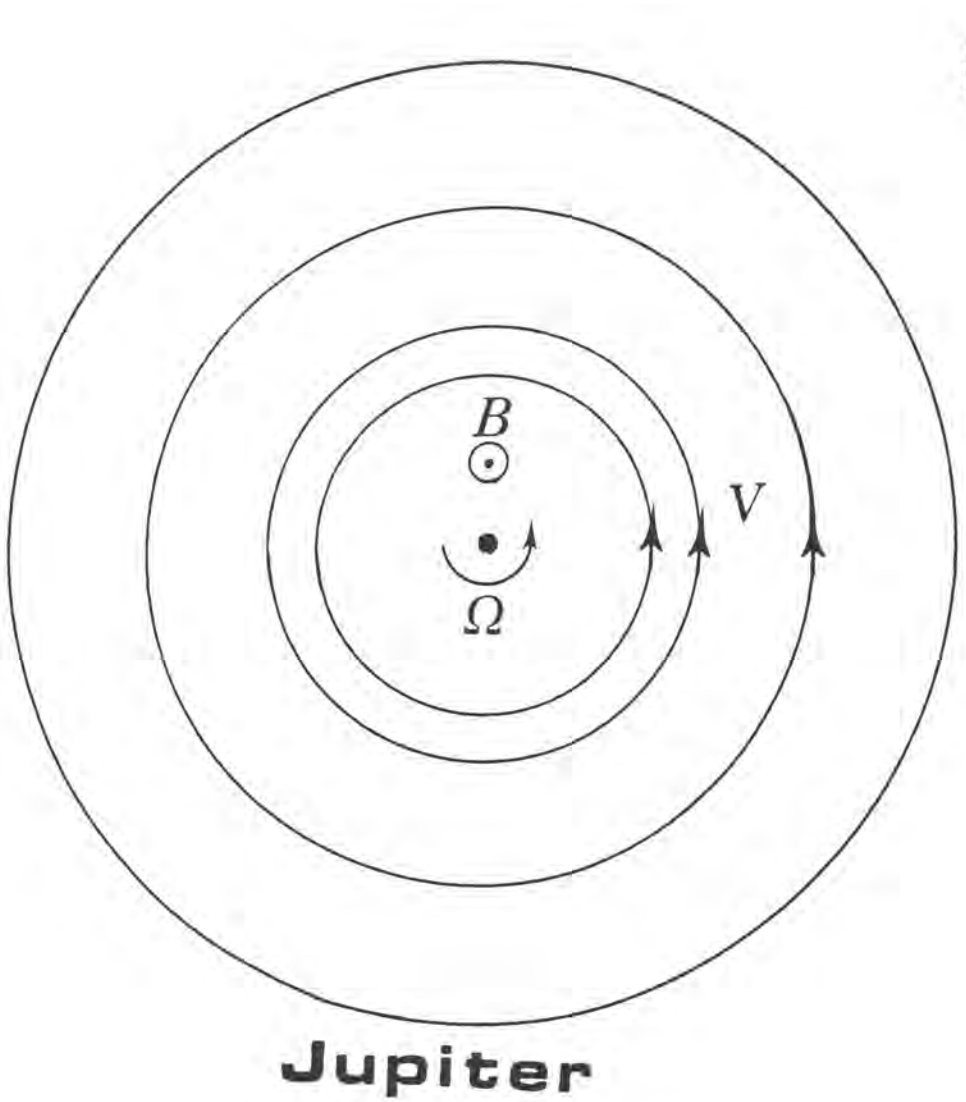

Figure 4.1-4. Plasma flow lines associated with the current system of Fig. 4.1-3. These flow lines are shown on the surface of the planet.

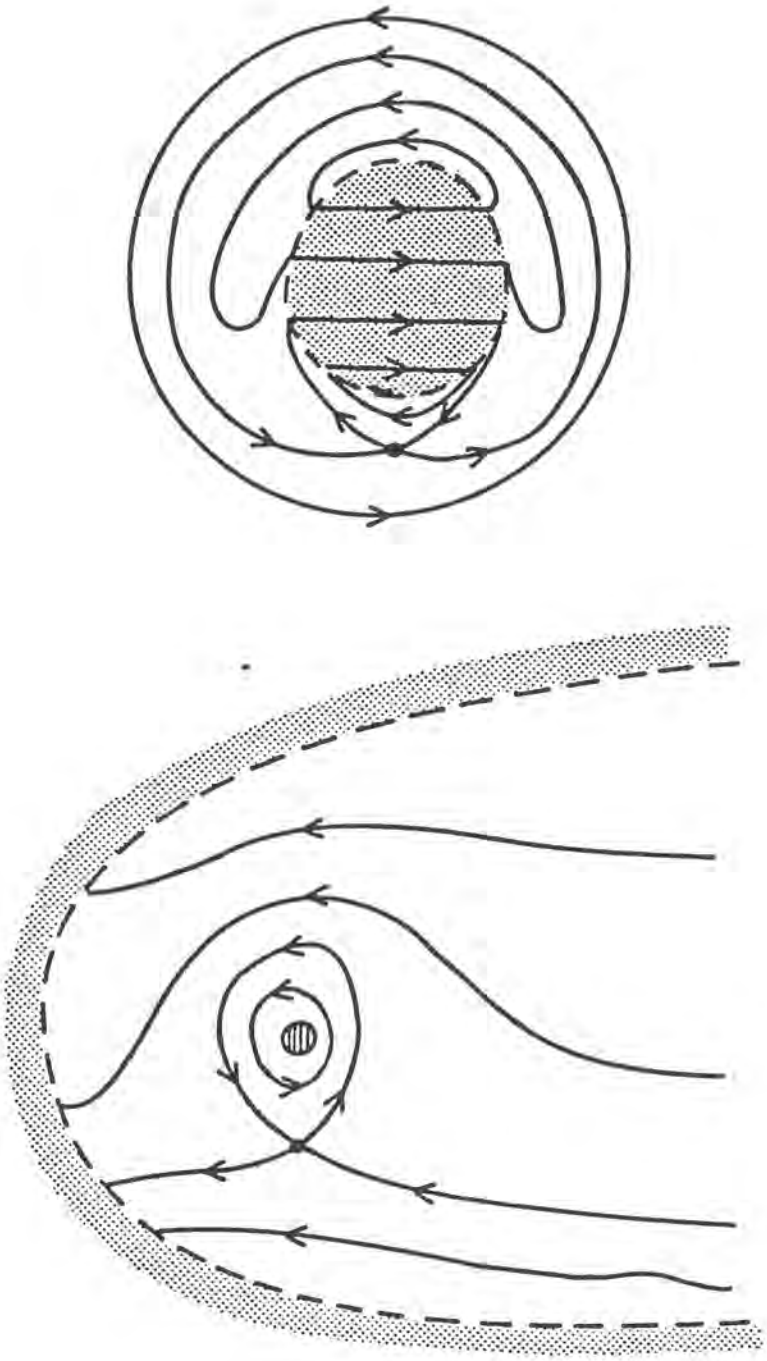

Figure 4.1-5. Superposing the convective motion of Fig. 5.1-1 with the rotational motion of Fig. 4.1-4 produces the flow topology shown here. The flow mapped to both the planet surface (top figure) and the magnetospheric equatorial plane (bottom figure) is shown. The heavy dot is the "stagnation" point (position where the sum of the two flows is zero). The speckled polar region of the top figure maps out to the speckled outer boundary of the lower figure. This is the topology for Earth. Reprinted from *Vasyliunas*, [1974].

inner region of closed circulating flow lines) since this region was likely to have a high plasma density. The region inside the dot corresponds to "open" flow lines, allowing the plasma to free stream out of the magnetosphere, thus producing a low density region. However, if the rotational motion is large enough, the stagnation point will fall within the polar cap region, where the superposition of convective and rotational motion does not apply. The resulting flow pattern will be characterized by Fig. 4.1-6; thus, the entire dayside magnetosphere will lie within the plasmapause. At Jupiter, were the rotational effects are large, the second case applies, whereas the first case describes the situation at Earth; the plasmapause falls inside of the magnetopause [*Brice and Ioannidis*, 1970; *Kennel and Coroniti*, 1975].

In addition to the convection system just discussed, at Jupiter another convection system has been proposed by *Hill et. al.* [1981] which would explain the Earth-based optical observations of a significant longitudinal asymmetry in the plasma torus surrounding Io. This asymmetry is in the form of enhanced collisionally excited emission lines of singly ionized sulfer [*Pilcher and Morgan*, 1980; *Trauger et. al.*, 1980]. This convection system hinges on the magnetic anomaly found at Jupiter. A magnetic anomaly is defined as a deviation of the surface magnetic field from that expected from the best fit displaced dipole. At Jupiter, the magnetic anomaly is a depressed field region in the northern hemisphere centered near the SIII longitude, $\lambda_{III} = 260°$ [*Acuna et. al.*, 1983], resulting from high-order multipoles in the internal magnetic field. *Dessler and Hill* [1975] proposed that this surface magnetic anomaly would cause a longitudinal asymmetry of the plasma sheet density; Fig. 4.1-7 shows how this is accomplished. The cross-sectional area of the foot of flux tube A, which is connected to the magnetic anomaly, is larger than the foot of flux tube B due to the lower magnetic field at the anomaly. For a given ionosphere escape flux, more ionospheric plasma will be transported to the equatorial plane by flux tube B. The region of the magnetosphere connected to this anomaly is known as the active sector, and spans about 100° in longitude centered near $\lambda_{III} = 225°$ [*Hill et. al.*, 1981].

Hill et. al. [1981] showed that this azimuthally asymmetric plasma mass distribution gives rise to a convection system with outward flow (away from Jupiter) in the longitude sector having greater-than-average plasma density, and inward return flow in the longitude sector

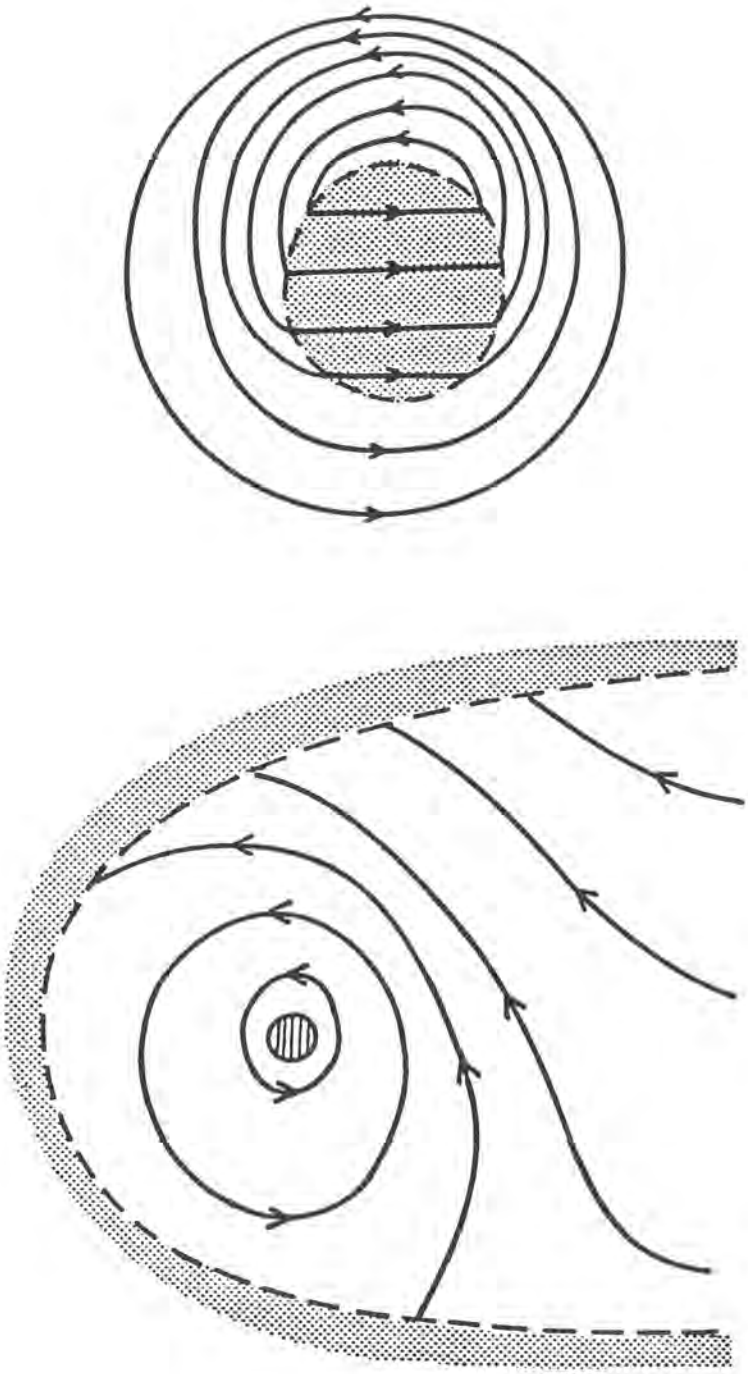

Figure 4.1-6. Topology corresponding to the situation where the rotational motion dominates over the convective motion. The stagnation point falls within the polar cap region. Thus, the entire dayside magnetosphere lies within the plasmapause. This is the topology for Jupiter. Reprinted from *Vasyliunas*, [1974].

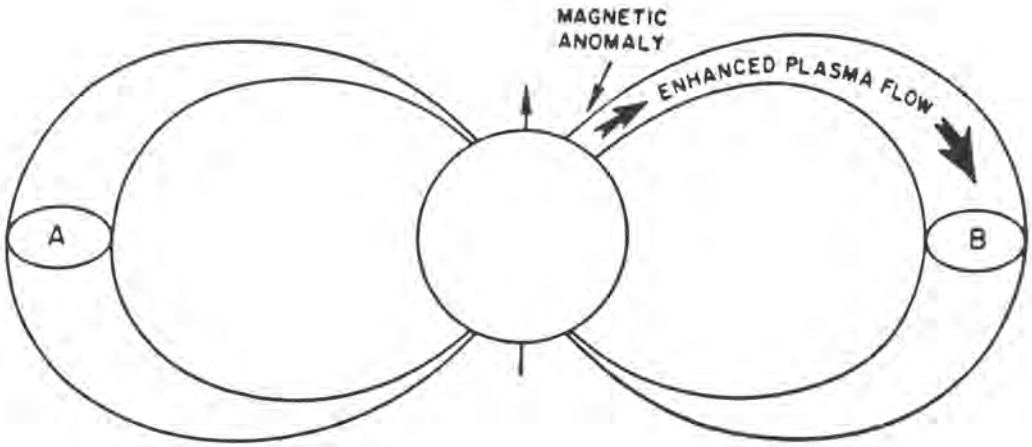

Figure 4.1-7. Schematic of haw a magnetic anomaly enhances the flow of ionospheric plasma into the Io torus and the magnetosphere. Flux tubes A and B have the same cross-sectional area at the equator. However, flux tube B, which enters a negative magnetic anomaly (a weak field region) in the northern hemisphere has a larger foot than either foot of flux tube A. Thus, for a given ionospheric escape flux, more ionospheric plasma will be transported to the equatorial plane by flux tube B. Reprinted from *Hill et. al.*, [1983].

having less-than-average mass density. This convection system would be fixed in the Jovian frame of reference (i.e., corotating convection system) since the magnetic anomaly, which drives the system, corotates with Jupiter. The current system associated with this outflow is illustrated in Fig. 4.1-8. Due to an increase in mass loading in the active sector, a current is developed which must produce Birkland currents and close in the ionosphere (so that current continuity is preserved). The ionospheric current produces an electric field (e.g., Eq. 4.1.4), which when mapped out along the field lines has the direction shown. From the $\mathbf{E} \times \mathbf{B}$ drift, the plasma flow is radially outward. For the rest of the magnetosphere where the mass loading is less-than-average, the sense of the current and electric field is reversed, providing radially inward flow. The anticipated flow pattern is shown in Fig. 4.1-9. As the plasma moves outward it deviates from purely radial flow due to mass loading of flux tubes further out. The ionosphere cannot supply the torque required to keep the feet of the flux tubes from slipping [*Hill*, 1979]. This slippage causes a breakdown in corotation, resulting in flow lines which spiral outward with a retrograde sense of rotation as viewed in Jupiter's frame of reference. The plasma sink represents the radially distant nightside of Jupiter where field lines open allowing plasma to free stream down the magnetotail. When the magnetic field lines reconnect, the remaining plasma flows in toward Jupiter over the remaining range of longitude. From momentum conservation, inward moving plasma is thought to attain velocities in excess of corotational speeds (i.e., supercorotational). One consequence of supercorotation would be the shown prograde spiral in the flow lines (i.e., magnetic field lines); a signature apparently found by *Hairston* [1986].

Using plasma velocities obtained through the analysis described in Chapter 3, the corotating convection model for plasma transport, can be directly tested. Table 3.2-4, which has a listing of the radial component of the plasma flow across the magnetic field, $V_{\perp R}$, covers a period of time during which the spacecraft went through the active sector twice. The first crossing of the active sector began shortly after the spectrum on day 63 at 0841 UT and ended before the spectrum on day 63 at 1527 UT. The second traversal covered the spectra from day 63 2103 UT to day 64 0025 UT. No definite conclusion can be made about the radial outflow during the time of the first active sector crossing, because no spectra were analyzed. Many

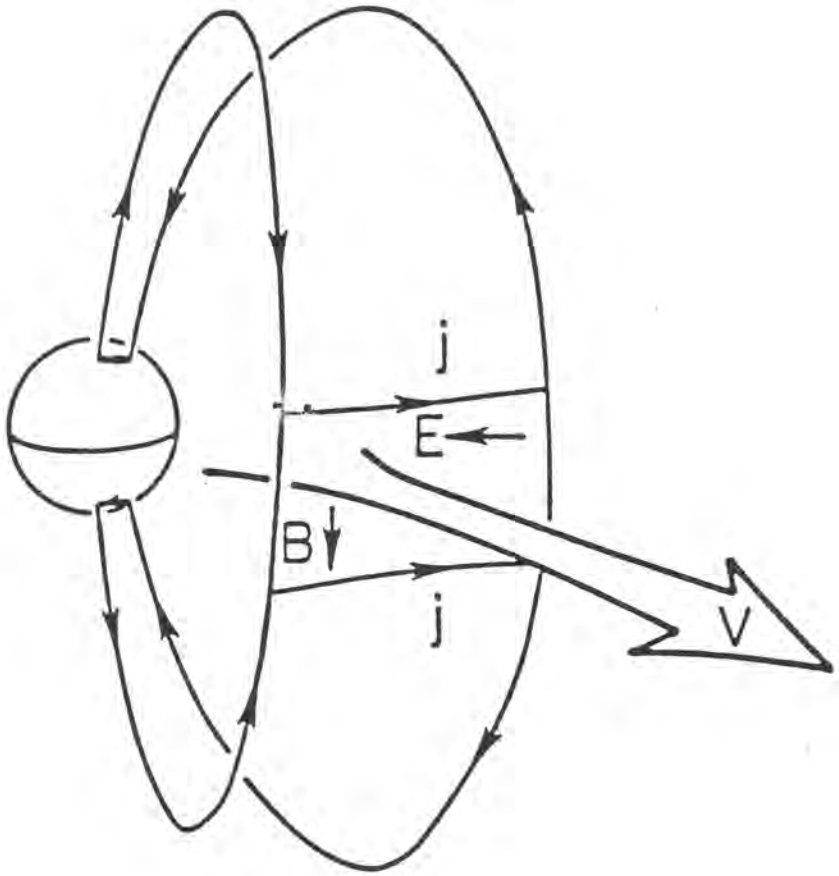

Figure 4.1-8. Current system associated with plasma outflow in the active sector. Increased plasma mass density sets up a current which must close in the ionosphere. Mapping back out the associated electric field gives an $\mathbf{E} \times \mathbf{B}$ drift in the direction shown by the arrow. Reprinted from *Hill et. al.*, [1981].

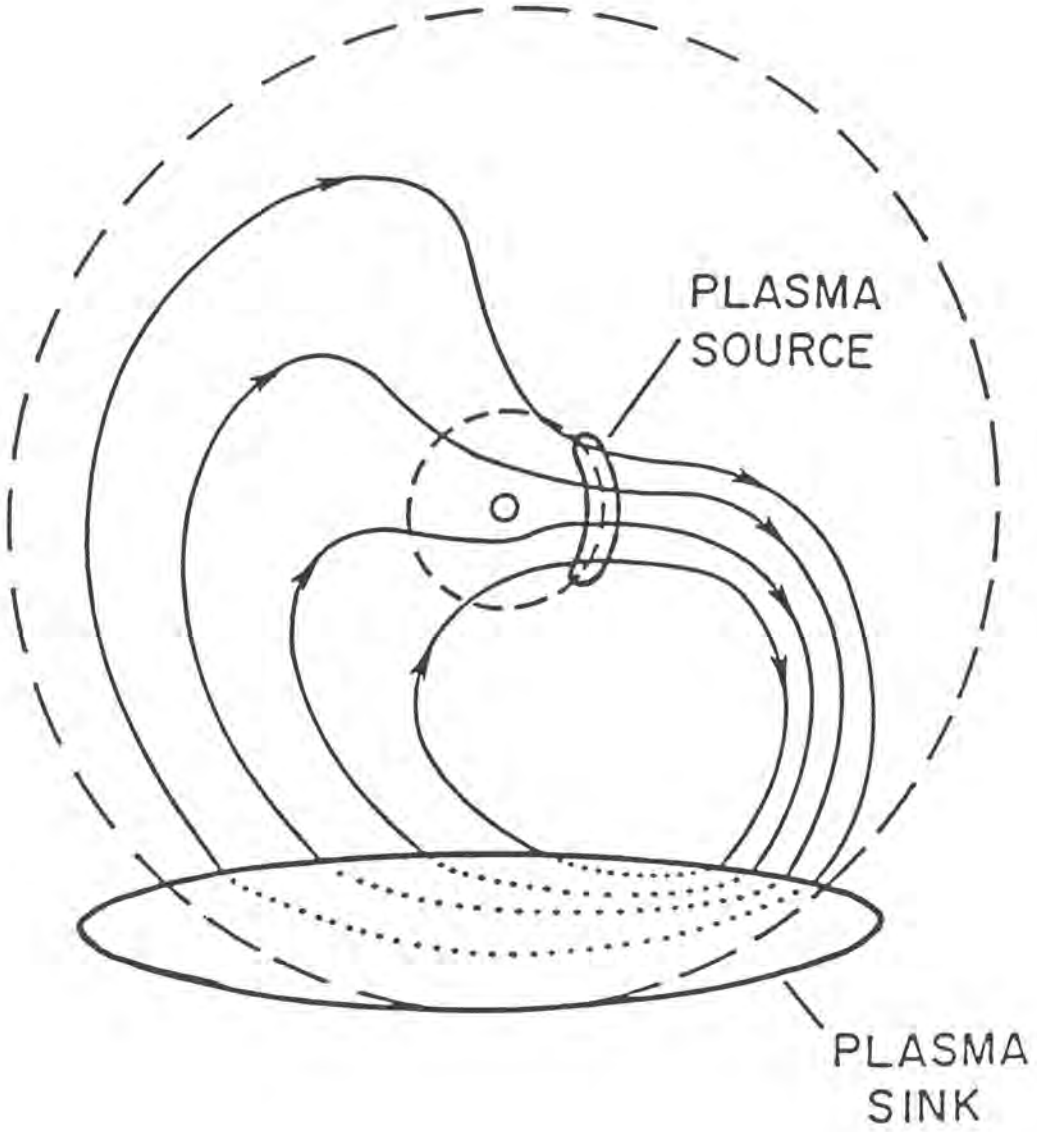

Figure 4.1-9. Anticipated plasma flow pattern, in the corotating frame of reference, due to the magnetic anomaly. The retrograde spiral in the flow pattern is due to corotational lag, whereas plasma compression causes the prograde spiral. The plasma sink represents the open field line region of the magnetotail. Reprinted from *Hill et. al.*, [1982].

spectra were analyzed during the second traversal of the active sector however, and a survey of the results show that not only was there outflow, but many spectra showed radial inflow. Also, the spectra with the largest radial outflow (between day 63 1819 UT and 1903 UT) do not lie within the active sector. These results seem to be diametrically opposed to those of *Hairston and Hill* [1985]. Looking at the same three inbound magnetic equatorial crossings covered by the data in Chapter 3, Hairston obtained estimates for the outward flowing plasma. The estimates were made by identifying the equator crossings and averaging the plasma data over a longitudinal range of $\pm$ 60 – 90 degrees from the crossings. A detailed discussion of how the velocity estimates are made is given by *Hairston* [1986]. Table 4.1-1 lists the radial plasma flows obtained by *Hairston* [1986] at each of the crossings, and the corresponding values determined from this thesis. Crossings A and C are in the active sector with the corresponding times listed. The sampling time interval for each crossing is also shown. The range of velocities obtained by Hairston are given in the parentheses while the perferred value is listed above them. For the two crossings inside the active sector, the flows are radially outward and larger than the value obtained at Crossing B (which is not within the active sector). Taking the values of $V_{\perp R}$ from Table 3.2-4 and averaging them over the same range for each crossing gave the results listed next to Hairston's.

During the outbound leg of the encounter *Hairston* [1986] expected to see an inflow of supercorotating plasma. Although most of the spectra outbound could not be fully analyzed, there was one spectrum from which a velocity could be obtained. This spectrum was obtained on day 64 at 1942 UT and is discussed in Chapter 3. There is an inward radial flow ($V_R = -7.4$ km/sec), however, the azimuthal velocity is less than the local corotational velocity. The analysis obtained an azimuthal velocity of $V_\phi = 115$ km/sec while the local corotational velocity is $V_\phi = 117$ km/sec.

Even a hybrid model proposed by *Hill et. al.* [1982] which combines corotating convection with radial diffusion, is not consistent with the observed velocities. In this case the net mass transport is outward at all longitudes but larger in the active sector, and the azimuthal flow is subcorotational everywhere. Even though the problem of supercorotation is solved, the

Table 4.1-1. COMPARISON OF RADIAL VELOCITIES

Crossing	Universal Time	Time Range	Hairston Velocity (km/sec)	Sands Velocity (km/sec)
A	64 0005	63 2154 to 64 0213	33.6 (22.5 – 47.9)	-2.04
B	63 1914	63 1754 to 63 2059	12.9 (9.1 – 15.0)	10.36
C	63 1408	63 1201 to 63 1633	26.4 (17.4 – 35.2)	3.56

problem of observed plasma inflow remains, both in the active sector and on the nightside.

The results of the analysis cast some doubt as to the validity of the corotating convection model, at least, as currently formulated. At best, it would seem that if the convection model is valid, it is not an important part of the overall dynamical picture of the Jovian magnetosphere.

4.2. Stress Balance

Because Jupiter is a rapid rotator, in a steady state situation, the momentum equation (Eq. 4.1.6) requires the inward Lorentz force to balance the outward component to the pressure gradient and centrifugal forces. *McNutt* [1982] found however that the stresses did not match up; the Lorentz force was much too large. The magnetic field model used was a tilted dipole plus current sheet. It assumes an azimuthal current of strength $J = I_0/R$ flowing in an annulus of inner radius a, outer radius b, and half thickness D [*Connerney et. al.*, 1981]. The dimensions of the annulus as well as I_0 are parameters which are adjusted by comparison with *in situ* magnetometer data. Using the assumption that the plasma flow, $\mathbf{V}$, was entirely in the azimuthal direction, $\mathbf{V} = \omega R\hat{\mathbf{e}}_\phi$, the outward centrigfugal force density had a magnitude of $\rho\omega^2 R$. Plasma mass density is given by ρ with R being the cylindrical radial distance from the symmetry axis of the system and ω the local angular speed of the plasma.

The centrifugal force results from the high density "cold" plasma (detected by the PLS experiment), whereas the pressure gradient results from the low density "hot" plasma (detected by the Low Energy Charged Particle, LECP, experiment). This is simply a consequence of the plasma β ($\equiv 8\pi p/B^2$), for the "cold" plasma, being only a few percent, while the "hot" plasma β is often greater than one.

One possible explanation for the lack of agreement between inward and outward stresses was the neglect of possible field-aligned flows [*McNutt*, 1982]. If field-aligned flow is assumed to exist, it will contribute to the outward stress in a manner similar to the centrifugal term. The force density due to this parallel flow, $\mathbf{V}_\parallel$, would be of the order $\rho V_\parallel^2/R_c$, where R_c is the radius of curvature of the magnetic field line. Since a parallel component to the plasma flow was found (see Chapter 3), the question of whether or not field-aligned flow played a role in the

cross-field stress balance, could be answered.

To calculate the radius of curvature, the magnetic field line curvature vector, κ, was calculated

$$\frac{1}{R_c} \equiv |\kappa| \equiv (\hat{\mathbf{b}} \cdot \nabla)\hat{\mathbf{b}} \tag{4.2.1}$$

where $\hat{\mathbf{b}}$ is the magnetic field unit vector. By explicitly writing the unit vector $\hat{\mathbf{b}} = \mathbf{B}/B$, and using vector identities, Eq. 4.2.1 can be cast into the following form,

$$\kappa = \frac{4\pi}{c} \frac{\mathbf{J} \times \mathbf{B}}{B^2} + \nabla_\perp(\ln B) \tag{4.2.2}$$

where, $\nabla_\perp \equiv \nabla - \hat{\mathbf{b}}(\hat{\mathbf{b}} \cdot \nabla)$. Using the current density profile obtained from the magnetic field model, the field curvature becomes

$$\kappa = \frac{4\pi I_0}{c} \frac{1}{RB^2}(B_z\hat{\mathbf{e}}_R - B_R\hat{\mathbf{e}}_z) + \nabla_\perp(\ln B) \tag{4.2.3}$$

The current density profile is valid for $|z| \leq 2.5\ R_J$ and $5\ R_J < R < 50\ R_J$. From *Connerney et. al.* [1981], a value of $\frac{4\pi I_0}{c} = 450\gamma$ gives the best simulation of the observed field, during the Voyager 1 encounter. Except for the $\nabla_\perp(\ln B)$ term and $\mathbf{J}$, all quantities are determined from *in situ* measurements. The perpendicular gradient term is small compared to the first term and can therefore be neglected. From Fig. 3.3-6, at about 17.5 R_J and 14 R_J, the spacecraft trajectory is seen to be approximately perpendicular to the magnetic field direction. Thus,

$$\nabla_\perp(\ln B) \approx \frac{\Delta \ln B}{\Delta s} = \frac{\ln B_1 - \ln B_2}{\Delta s} \tag{4.2.4}$$

where,

$$\Delta s^2 \equiv (R_1 - R_2)^2 + (z_1 - z_2)^2 \tag{4.2.5}$$

which allows one to estimate $\nabla_\perp(\ln B)$ at a point, by knowing the spacecraft position (in magnetic cylindrical coordinates) and magnetic field on both sides of that point. The perpendicular gradient term was estimated for ten spectra and added to the first term of Eq.

4.2.3, for calculating a radius of curvature. This value was then compared to the value of R_c which neglected the gradient contribution. For all cases, the effect of the $\nabla_\perp(\ln B)$ term was negligible. The largest contribution was for the spectrum at 1819 UT on day 63, where R_c = 2.18 R_J without the $\nabla_\perp(\ln B)$ piece, and R_c = 1.94 R_J with the added term (an 11% decrease in the size of R_c). All the other cases showed a decrease in the radius of curvature of less than one percent. Thus, neglecting $\nabla_\perp(\ln B)$ and substituting Eq. 4.2.3 into Eq. 4.2.1 gives,

$$R_c = \frac{1}{|\kappa|} = \frac{c}{4\pi I_0} RB \tag{4.2.6}$$

It has been assumed that $B^2 = B_R^2 + B_z^2$ (i.e., $B_\phi = 0$). With the radius of curvature known, the ratio of the curvature to the centrifugal stress can be calculated. Since the component of the centrifugal force, perpendicular to the field line is needed, its projection into the $-\hat{\kappa}$ direction must be found. From Fig. 4.2-1, the centrifugal force unit vector, $\hat{e}_c$, can be written as

$$\hat{e}_c = \frac{R}{r}\hat{e}_R + \frac{z}{r}\hat{e}_z$$

where $r^2 = R^2 + z^2$. Thus the ratio of the two stresses become

$$f = \frac{V_\parallel^2}{R_c} \frac{R}{\omega^2 R^2} \delta \tag{4.2.7}$$

where,

$$\delta \equiv \hat{e}_c \cdot -\hat{\kappa} \tag{4.2.8}$$

The quantity ωR is the local azimuthal velocity (defined as V_ϕ in the tables in Chapter 3), and δ is known since $\hat{\kappa}$ can be determined using Eqs. 4.2.3 and 4.2.4.

A plot of f vs. magnetic cylindrical radius is shown in Fig. 4.2-2 (the table of data used to produce this plot is given in Appendix D). The curvature stress generally contributes 20 – 50% to the total inertial stress. However, from *McNutt* [1982], the curvature term would have to be

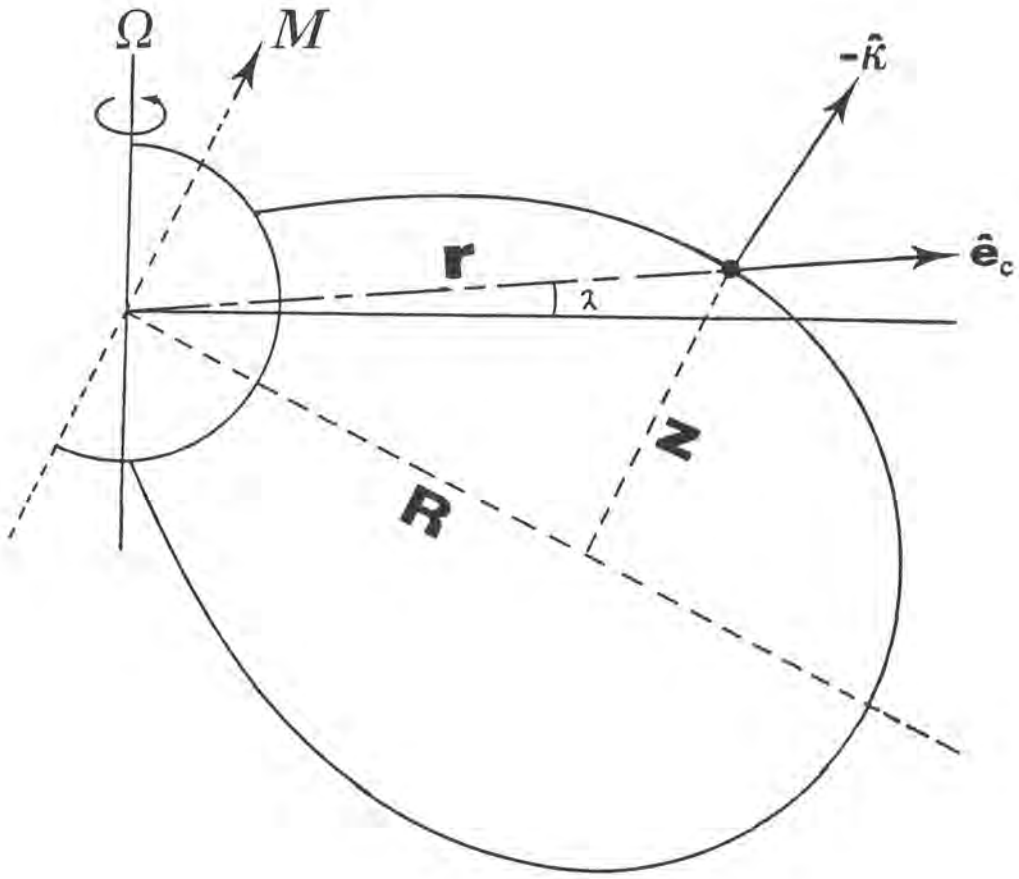

Figure 4.2-1. Geometry of the problem associated with calculating the component of the centrifugal force, in the direction of the curvature force.

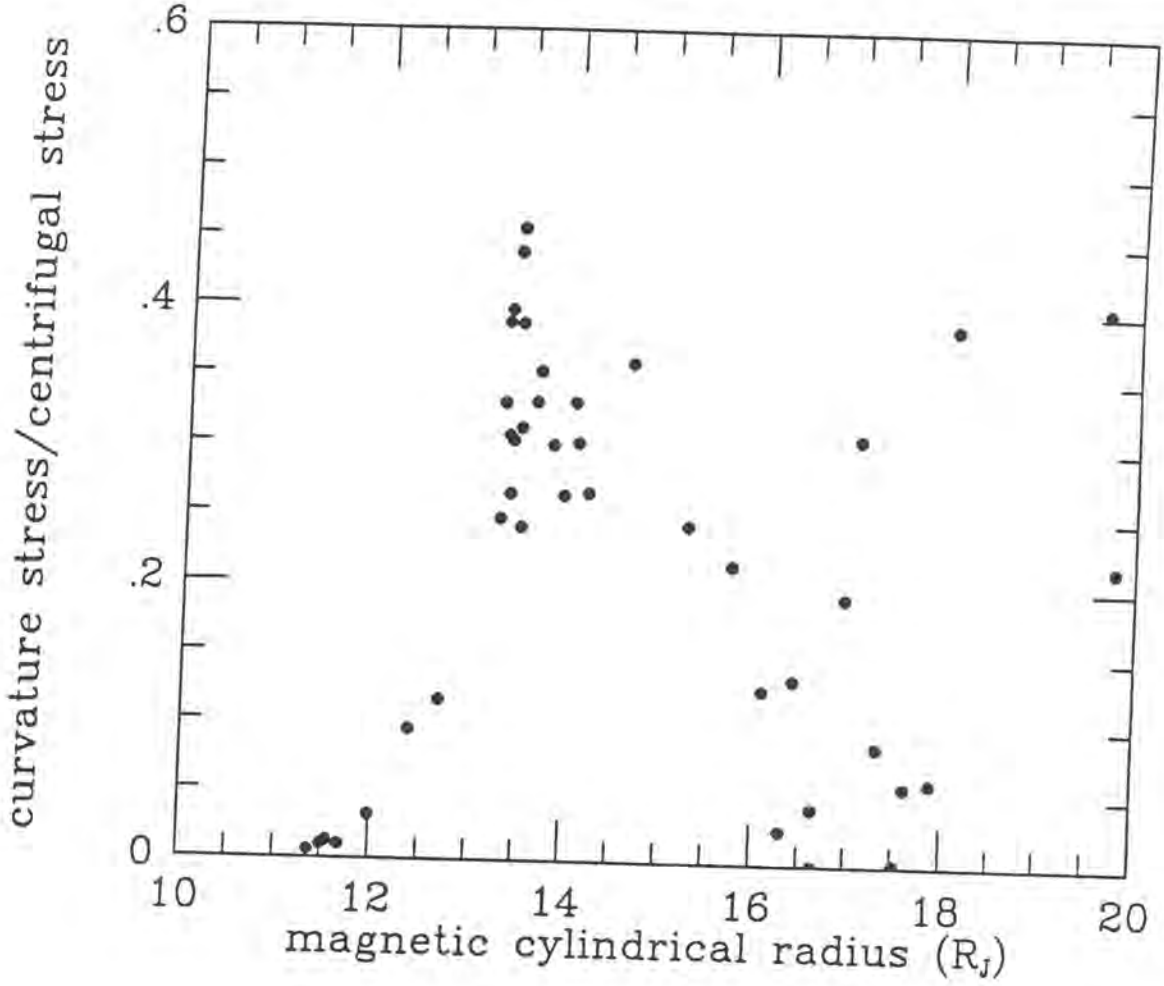

Figure 4.2-2. Ratio of curvature to centrifugal stress (i.e., *f*) is plotted vs. position. Curvature is seen to contribute roughly 30% to the total stress due to both centrifugal and curvature forces.

about ten times the centrifugal term in order for the Lorentz force to be balanced. It therefore appears that the outward stress due to field-aligned plasma flow cannot account for the discrepancy between inward and outward stresses.

CHAPTER 5

CONCLUSION

5.1. Summary of Results

An in depth study of the plasma data obtained from the Voyager 1 spacecraft encounter with Jupiter has been performed. Knowing the full response function (operating characteristics) of the Plasma Science experiment has made accurate determination of plasma parameters possible, in particular, plasma bulk flow velocities. The first result of this analysis was the reconfirmation of subcorotational plasma flow (less than the local rigid rotational speed), primarily in the azimuthal direction ($\hat{e}_\phi$ direction in cylindrical coordinates). However, the major result was the discovery of a substantial non-azimuthal piece to the plasma flow. The magnitude of this component, which has always been assumed small, has been found to be as large as almost 40% the local azimuthal speed, with 20% being a typical value. Transforming the non-azimuthal flow into its parallel and perpendicular (with respect to the magnetic field) constituents further showed that most of the flow was field-aligned (anti-field aligned). In fact, on the dayside magnetosphere (sunward facing side) plasma above (north of) the magnetic equator moved in an anti-field aligned direction, while below the equator, plasma moved in a field-aligned direction (i.e., plasma moved away from the magnetic equator).

To obtain the non-azimuthal flows, the analysis routine looks at the difference in current measured by the detectors making up the plasma experiment. Assuming the ion distribution function to be a convected Maxwellian, a plasma velocity is calculated which simulates the data. However, in theory, the difference in currents could also be an artifact of a plasma whose distribution is given by a convected bimaxwellian. To test this hypothesis, a current model was developed which used the full response function of the instrument and allowed the ion distribution function to be a convected bimaxwellian. Several spectra were then reanalyzed and

the results compared to the simulations assuming a Maxwellian distribution. It was found that the non-azimuthal flows were real; the difference in current was not due to a temperature anisotropy. In fact none of the spectra looked at, from the Voyager 1 encounter, showed any signs of an anisotropic plasma. A convected Maxwellian seemed to simulate the ion distribution quite well. Furthermore, the assumption of temperature anisotropies did not cause non-azimuthal flows to vanish. A spectrum from the Voyager 2 encounter with Jupiter was looked at assuming both a Maxwellian and a bimaxwellian ion distribution function. This spectrum could only be simulated if a convected bimaxwellian distribution was assumed for the ions. The non-azimuthal flow however, did not vanish as hypothesized, but persisted, and was actually larger than for the Maxwellian simulation. In the case of this spectrum, the temperature anisotropy was $T_{\parallel}/T_{\perp} = 3.08$.

Since the plasma velocities were shown to be real, they could now be used to investigate existing theories and problems concerning magnetospheric dynamics. A theory dealing with plasma transport and a problem associated with stress balance were investigated.

One model of plasma transport uses a localized depression of the surface magnetic field strength of Jupiter to enhance radially outward plasma flow. Because this magnetic anomaly rotates with the planet, the resulting plasma convection flow pattern is stationary in a corotating frame of reference (hence the name corotating convection model). The range in longitude over which this magnetic anomaly exists is called the active sector. The plasma data analyzed covered a period of time during which Voyager went through the active sector twice. Examination of the velocities showed no enhanced flow inside the active sector. In fact, during one traversal, most of the radial flow was inward, not outward (as required by this model). It was also suggested that this corotating convection system would produce supercorotational flow on the nightside. However, the spectrum from this region was consistant with flow which was subcorotational. The results of the analysis cast some doubt as to the validity of the corotating convection model, at least, as currently formulated. At best, it would seem that if the convection model is valid, it is not an important part of the overall dynamical picture of the Jovian magnetosphere.

Using the currently accepted magnetic field model of the Jovian magnetosphere, a stress balance analysis can be performed. Because the magnetosphere is in equilibrium, the sum total of the stresses should be zero. However, the inwardly directed $\mathbf{J} \times \mathbf{B}$ force is much larger than the outwardly directed centrifugal and pressure gradient forces. Because the plasma flow had a large field-aligned component, another term could be added to the stress balance; a stress due to magnetic field line curvature. By calculating the radius of curvature of the magnetic field (at the point of observation) and using $\mathbf{V}_{||}$, the relative importance of curvature stress, to the overall missing stress can be ascertained. Although, the curvature term could be as large as 50% of the centrifugal term, the additional outward stress was not enough to balance the Lorentz force. Thus, the nature of the missing outward stress is still a mystery.

5.2. Questions and Recommendations

As is usually the case, the answering of one question, brings forth new questions. In this case the plasma velocity was shown to have a substantial non-azimuthal (predominately field-aligned) flow component. However, the question arises, what produces this flow profile? Observations from Pioneer 10 and 11 and Voyager 1 and 2 indicate the solar wind as a possible cause. For example, the magnetosphere is known to undergo large compressions (reducing the extent of the dayside magnetosphere by a factor of two) regularly; there is a day/night asymmetry of the non-azimuthal flow (away from the magnetic equator on the dayside and toward the equator on the nightside), and field-aligned flow makes up most of the non-azimuthal plasma flow. All these observations suggest that the solar wind pressure, which causes the magnetospheric compression, results in the "squeezing" of magnetic flux tubes. This causes the plasma to stream out along the field lines (like squeezing a toothpaste tube) on the dayside. On the nightside the field lines are no longer compressed by the solar wind ram pressure, resulting in plasma falling back toward the magnetic equator (due to the centrifugal force). Whereas this is a qualitative picture of what might be driving the field-aligned flows, a quantitative theory must be worked out to prove this hypothesis (or possibly provide an alternative description).

One neccessary step to the development of this theory, or any other theory, is the acquisition of data. The results provided here represent the physical state of a small portion of the entire magnetosphere, during a small fraction of an encounter with Jupiter of one spacecraft, during a few hours of one particular day. What is obviously needed is a Jupiter orbiter, which would acquire data over an extended period of time, covering all areas of the magnetosphere. The Gallileo probe was one such mission, but it has been postponed (to a 1989 launch) after the Challanger accident (Gallileo was to be launched from a shuttle cargo bay). If not Gallileo, some other dedicated probe mission should be schedualed for a rendezvous with Jupiter. Its presence in the solar system allows us the unique oppertunity of making *in situ* observation and studies of plasma confined by a fast magnetic rotator, a subject of general and astrophysical interest.

APPENDIX A

PLS MODULATOR STEPING

A listing of the PLS modulator steps is given for both the low (L) and high (M) resolution modes. Along with the contiguous steps is a listing of the corresponding threshold voltage, peak voltage, average voltage, and voltage chage. For protons, an average speed and a range of speeds is given corresponding to each modulator step (i.e., voltage).

Table of nominal constants for MJS.

The delta values are the full width.

M.mode. K = 1.036633

MODULATOR STEP	THRESHOLD VOLTAGE	PEAK VOLTAGE	AVERAGE VOLTAGE	DELTA VOLTAGE
1	10.0000	12.1980	11.0990	2.19795
2	12.1980	14.4764	13.3372	2.27846
3	14.4764	16.8383	15.6574	2.36192
4	16.8383	19.2868	18.0626	2.44846
5	19.2868	21.8249	20.5559	2.53815
6	21.8249	24.4561	23.1405	2.63112
7	24.4561	27.1836	25.8198	2.72751
8	27.1836	30.0110	28.5973	2.82742
9	30.0110	32.9420	31.4765	2.93100
10	32.9420	35.9803	34.4612	3.03836
11	35.9803	39.1300	37.5552	3.14967
12	39.1300	42.3951	40.7625	3.26505
13	42.3951	45.7797	44.0874	3.38466
14	45.7797	49.2884	47.5340	3.50865
15	49.2884	52.9256	51.1070	3.63718
16	52.9256	56.6960	54.8108	3.77042

PROTONS

MODULATOR STEP	AVERAGE SPEED	DELTA SPEED
1	46.0847	4.57437
2	50.5341	4.32440
3	54.7646	4.13652
4	58.8298	3.99184
5	62.7640	3.87860
6	66.5979	3.78922
7	70.3517	3.71844
8	74.0422	3.66253
9	77.6828	3.61877
10	81.2848	3.58509
11	84.8573	3.55996
12	88.4083	3.54213
13	91.9447	3.53067
14	95.4725	3.52478
15	98.9968	3.52381
16	102.522	3.52729

Table of nominal constants for MJS.

The delta values are the full width.

M mode. K = 1.036633

MODULATOR STEP	THRESHOLD VOLTAGE	PEAK VOLTAGE	AVERAGE VOLTAGE	DELTA VOLTAGE
17	56.6960	60.6045	58.6502	3.90854
18	60.6045	64.6562	62.6304	4.05171
19	64.6562	68.8564	66.7563	4.20013
20	68.8564	73.2104	71.0334	4.35400
21	73.2104	77.7239	75.4671	4.51350
22	77.7239	82.4027	80.0633	4.67885
23	82.4027	87.2529	84.8278	4.85023
24	87.2529	92.2809	89.7669	5.02792
25	92.2809	97.4930	94.8869	5.21210
26	97.4930	102.896	100.194	5.40303
27	102.896	108.497	105.696	5.60097
28	108.497	114.303	111.400	5.80614
29	114.303	120.322	117.313	6.01883
30	120.322	126.561	123.442	6.23932
31	126.561	133.029	129.795	6.46788
32	133.029	139.734	136.381	6.70482

PROTONS

MODULATOR STEP	AVERAGE SPEED	DELTA SPEED
17	106.053	3.53475
18	109.594	3.54587
19	113.147	3.56033
20	116.716	3.57790
21	120.304	3.59835
22	123.914	3.62150
23	127.548	3.64719
24	131.209	3.67531
25	134.900	3.70569
26	138.622	3.73830
27	142.378	3.77303
28	146.169	3.80980
29	149.998	3.84853
30	153.867	3.88921
31	157.778	3.93175
32	161.731	3.97613

Table of nominal constants for MJS.

The delta values are the full width.

M mode. K = 1.036633

MODULATOR STEP	THRESHOLD VOLTAGE	PEAK VOLTAGE	AVERAGE VOLTAGE	DELTA VOLTAGE
33	139.734	146.684	143.209	6.95042
34	146.684	153.889	150.287	7.20505
35	153.889	161.358	157.624	7.46898
36	161.358	169.101	165.230	7.74258
37	169.101	177.127	173.114	8.02621
38	177.127	185.447	181.287	8.32024
39	185.447	194.072	189.760	8.62503
40	194.072	203.013	198.543	8.94098
41	203.013	212.282	207.648	9.26830
42	212.282	221.890	217.086	9.60791
43	221.890	231.850	226.870	9.95996
44	231.850	242.174	237.012	10.3247
45	242.174	252.877	247.526	10.7029
46	252.877	263.972	258.425	11.0950
47	263.972	275.474	269.723	11.5015
48	275.474	287.396	281.435	11.9229

PROTONS

MODULATOR STEP	AVERAGE SPEED	DELTA SPEED
33	165.731	4.02234
34	169.777	4.07030
35	173.872	4.12004
36	178.018	4.17149
37	182.216	4.22468
38	186.468	4.27957
39	190.776	4.33617
40	195.141	4.39446
41	199.566	4.45434
42	204.051	4.51605
43	208.599	4.57947
44	213.211	4.64449
45	217.889	4.71125
46	222.634	4.77977
47	227.449	4.84991
48	232.335	4.92197

Table of nominal constants for MJS.

The delta values are the full width.

M mode. K = 1.036633

MODULATOR STEP	THRESHOLD VOLTAGE	PEAK VOLTAGE	AVERAGE VOLTAGE	DELTA VOLTAGE
49	287.396	299.756	293.576	12.3596
50	299.756	312.568	306.162	12.8123
51	312.568	325.850	319.209	13.2817
52	325.850	339.618	332.734	13.7683
53	339.618	353.891	346.755	14.2727
54	353.891	368.687	361.289	14.7954
55	368.687	384.024	376.355	15.3374
56	384.024	399.923	391.973	15.8992
57	399.923	416.405	408.164	16.4817
58	416.405	433.490	424.948	17.0854
59	433.490	451.202	442.346	17.7114
60	451.202	469.562	460.382	18.3601
61	469.562	488.594	479.078	19.0327
62	488.594	508.324	498.459	19.7300
63	508.324	528.777	518.551	20.4526
64	528.777	549.979	539.378	21.2019

PROTONS

MODULATOR STEP	AVERAGE SPEED	DELTA SPEED
49	237.294	4.99552
50	242.327	5.07096
51	247.437	5.14831
52	252.624	5.22735
53	257.892	5.30808
54	263.241	5.39071
55	268.674	5.47504
56	274.193	5.56147
57	279.798	5.64981
58	285.493	5.73984
59	291.279	5.83177
60	297.158	5.92602
61	303.132	6.02197
62	309.203	6.12003
63	315.373	6.21999
64	321.644	6.32227

Table of nominal constants for MJS.

The delta values are the full widths.

M mode. K = 1.036633

MODULATOR STEP	THRESHOLD VOLTAGE	PEAK VOLTAGE	AVERAGE VOLTAGE	DELTA VOLTAGE
65	549.979	571.958	560.968	21.9785
66	571.958	594.741	583.349	22.7837
67	594.741	618.360	606.550	23.6184
68	618.360	642.843	630.601	24.4836
69	642.843	668.224	655.533	25.3804
70	668.224	694.534	681.379	26.3103
71	694.534	721.808	708.171	27.2739
72	721.808	750.081	735.944	28.2732
73	750.081	779.390	764.735	29.3088
74	779.390	809.772	794.581	30.3826
75	809.772	841.268	825.520	31.4956
76	841.268	873.917	857.593	32.6492
77	873.917	907.762	890.840	33.8452
78	907.762	942.848	925.305	35.0852
79	942.848	979.218	961.033	36.3704
80	979.218	1016.92	998.069	37.7026

PROTONS

MODULATOR STEP	AVERAGE SPEED	DELTA SPEED
65	328.018	6.42646
66	334.498	6.53276
67	341.085	6.64139
68	347.782	6.75213
69	354.590	6.86498
70	361.513	6.98037
71	368.552	7.09766
72	375.709	7.21749
73	382.988	7.33985
74	390.390	7.46432
85	397.918	7.59155
76	405.574	7.72088
77	413.361	7.85297
78	421.282	7.99780
79	429.338	8.12496
80	437.533	8.26465

Table of nominal constants for MJS.

The delta values are the full width.

M mode. K = 1.036633

MODULATOR STEP	THRESHOLD VOLTAGE	PEAK VOLTAGE	AVERAGE VOLTAGE	DELTA VOLTAGE
81	1016.92	1056.00	1036.46	39.0840
82	1056.00	1096.52	1076.26	40.5156
83	1096.52	1138.52	1117.52	41.9999
84	1138.52	1182.06	1160.29	43.5383
85	1182.06	1227.19	1204.62	45.1333
86	1227.19	1273.98	1250.58	46.7866
87	1273.98	1322.48	1298.23	48.5005
88	1322.48	1372.76	1347.62	50.2773
89	1372.76	1424.88	1398.82	52.1191
90	1424.88	1478.90	1451.89	54.0283
91	1478.90	1534.91	1506.91	56.0076
92	1534.91	1592.97	1563.94	58.0591
93	1592.97	1653.16	1623.06	60.1860
94	1653.16	1715.55	1684.35	62.3909
95	1715.55	1780.22	1747.89	64.6763
96	1780.22	1847.27	1813.75	67.0457

PROTONS

MODULATOR STEP	AVERAGE SPEED	DELTA SPEED
81	445.869	8.40751
82	454.349	8.55270
83	462.976	8.70063
84	471.752	8.85173
85	480.681	9.00559
86	489.764	9.16219
87	499.007	9.32216
88	508.410	9.48468
89	517.978	9.65058
90	527.713	9.81964
91	537.619	9.99188
92	547.698	10.1671
93	557.955	10.3459
94	568.391	10.5278
95	579.012	10.7134
96	589.820	10.9025

Table of nominal constants for MJS.

The delta values are the full widths.

M mode. K = 1.036633

MODULATOR STEP	THRESHOLD VOLTAGE	PEAK VOLTAGE	AVERAGE VOLTAGE	DELTA VOLTAGE
65	549.979	571.958	560.968	21.9785
66	571.958	594.741	583.349	22.7837
67	594.741	618.360	606.550	23.6184
68	618.360	642.843	630.601	24.4836
69	642.843	668.224	655.533	25.3804
70	668.224	694.534	681.379	26.3103
71	694.534	721.808	708.171	27.2739
72	721.808	750.081	735.944	28.2732
73	750.081	779.390	764.735	29.3088
74	779.390	809.772	794.581	30.3826
75	809.772	841.268	825.520	31.4956
76	841.268	873.917	857.593	32.6492
77	873.917	907.762	890.840	33.8452
78	907.762	942.848	925.305	35.0852
79	942.848	979.218	961.033	36.3704
80	979.218	1016.92	998.069	37.7026

PROTONS

MODULATOR STEP	AVERAGE SPEED	DELTA SPEED
65	328.018	6.42646
66	334.498	6.53276
67	341.085	6.64139
68	347.782	6.75213
69	354.590	6.86498
70	361.513	6.98037
71	368.552	7.09766
72	375.709	7.21749
73	382.988	7.33985
74	390.390	7.46432
85	397.918	7.59155
76	405.574	7.72088
77	413.361	7.85297
78	421.282	7.98780
79	429.338	8.12496
80	437.533	8.26465

Table of nominal constants for MJS.

The delta values are the full widths.

M mode. K = 1.036633

MODULATOR STEP	THRESHOLD VOLTAGE	PEAK VOLTAGE	AVERAGE VOLTAGE	DELTA VOLTAGE
113	3323.85	3447.44	3385.65	123.593
114	3447.44	3575.56	3511.50	128.120
115	3575.56	3708.38	3641.97	132.813
116	3708.38	3846.06	3777.22	137.679
117	3846.06	3988.78	3917.42	142.722
118	3988.78	4136.73	4062.75	147.948
119	4136.73	4290.09	4213.41	153.367
120	4290.09	4449.08	4369.59	158.988
121	4449.08	4613.89	4531.49	164.812
122	4613.89	4784.74	4699.32	170.848
123	4784.74	4961.85	4873.29	177.105
124	4961.85	5145.44	5053.64	183.594
125	5145.44	5335.76	5240.60	190.320
126	5335.76	5533.05	5434.41	197.293
127	5533.05	5737.57	5635.31	204.520
128	5737.57	5949.59	5843.58	212.012

PROTONS

MODULATOR STEP	AVERAGE SPEED	DELTA SPEED
113	805.847	14.7099
114	820.688	14.9730
115	835.795	15.2410
116	851.173	15.5139
117	866.825	15.7917
118	882.759	16.0743
119	898.977	16.3628
120	915.487	16.6565
121	932.293	16.9553
122	949.400	17.2594
123	966.814	17.5695
124	984.542	17.8852
125	1002.59	18.2066
126	1020.96	18.5342
127	1039.66	18.8675
128	1058.70	19.2069

Table of nominal constants for MJS.

The delta values are the full widths.

M mode. K = 1.036633

MODULATOR STEP	THRESHOLD VOLTAGE	PEAK VOLTAGE	AVERAGE VOLTAGE	DELTA VOLTAGE
97	1847.27	1916.77	1882.02	69.5017
98	1916.77	1988.82	1952.79	72.0476
99	1988.82	2063.51	2026.16	74.6870
100	2063.51	2140.93	2102.22	77.4229
101	2140.93	2221.19	2181.06	80.2590
102	2221.19	2304.39	2262.79	83.1992
103	2304.39	2390.63	2347.51	86.2471
104	2390.63	2480.04	2435.34	89.4065
105	2480.04	2572.72	2526.38	92.6816
106	2572.72	2668.80	2620.76	96.0769
107	2668.80	2768.40	2718.60	99.5964
108	2768.40	2871.64	2820.02	103.245
109	2871.64	2978.67	2925.15	107.027
110	2978.67	3089.61	3034.14	110.948
111	3089.61	3204.63	3147.12	115.012
112	3204.63	3323.85	3264.24	119.225

PROTONS

MODULATOR STEP	AVERAGE SPEED	DELTA SPEED
97	600.819	11.0948
98	612.011	11.2910
99	623.402	11.4907
100	634.995	11.6942
101	646.792	11.9013
102	658.799	12.1126
103	671.020	12.3275
104	683.457	12.5467
105	696.115	12.7697
106	709.998	12.9971
107	722.111	13.2285
108	735.457	13.4641
109	749.042	13.7044
110	762.868	13.9489
111	776.941	14.1979
112	791.266	14.4515

Table of nominal constants for MJS.

The delta values are the full width.

E_1 mode. K = 1.074608

MODULATOR STEP	THRESHOLD VOLTAGE	PEAK VOLTAGE	AVERAGE VOLTAGE	DELTA VOLTAGE
1	10.0000	14.4765	12.2382	4.47647
2	14.4765	19.2869	16.8817	4.81044
3	19.2869	24.4563	21.8716	5.16934
4	24.4563	30.0113	27.2337	5.55501
5	30.0113	35.9807	32.9960	5.96947
6	35.9807	42.3956	39.1881	6.41483
7	42.3956	49.2890	45.8423	6.89343
8	49.2890	56.6967	52.9928	7.40773
9	56.6967	64.6571	60.6769	7.96040
10	64.6571	73.2114	68.9343	8.55431
11	73.2114	82.4040	77.8077	9.19254
12	82.4040	92.2823	87.3431	9.87837
13	92.2823	102.898	97.5900	10.6154
14	102.898	114.305	108.601	11.4074
15	114.305	126.564	120.434	12.2584
16	126.564	139.737	133.150	13.1730

MODULATOR STEP	ELECTRONS AVERAGE SPEED	ELECTRONS DELTA SPEED
1	2067.48	381.335
2	2432.31	348.319
3	2770.76	328.585
4	3093.20	316.292
5	3405.69	308.703
6	3713.22	304.342
7	4015.56	302.344
8	4317.81	302.157
9	4620.60	303.422
10	4925.25	305.991
11	5232.89	309.388
12	5544.48	313.787
13	5860.87	318.995
14	6182.84	324.944
15	6511.10	331.582
16	6846.33	338.874

Table of nominal constants for MJS.

The delta values are the full widths.

L Mode. K = 1.33522

MODULATOR STEP	THRESHOLD VOLTAGE	PEAK VOLTAGE	AVERAGE VOLTAGE	DELTA VOLTAGE
1	10.0000	30.0113	20.0056	20.0113
2	30.0113	56.6968	43.3541	26.6855
3	56.6968	92.2825	74.4897	35.5857
4	92.2825	139.737	116.010	47.4543
5	139.737	203.018	171.377	63.2814
6	203.018	287.405	245.212	84.3870
7	287.405	399.937	343.671	112.532
8	399.937	550.001	474.969	150.064
9	550.001	750.114	650.058	200.113
10	750.114	1016.97	883.542	266.855
11	1016.97	1372.83	1194.90	355.858
12	1372.83	1847.37	1610.10	474.544
13	1847.37	2480.19	2163.78	632.815
14	2480.19	3324.06	2902.12	843.872
15	3324.06	4449.38	3886.72	1125.32
16	4449.38	5950.02	5199.70	1500.64

PROTON

MODULATOR STEP	AVERAGE SPEED	DELTA SPEED
1		
2	59.9357	32.0753
3	90.0903	29.4129
4	118.668	28.7616
5	148.385	30.6730
6	180.531	33.6197
7	216.070	37.4585
8	255.889	42.1787
9	300.895	47.8334
10	352.069	54.5151
11	410.501	62.3493
12	477.421	71.4897
13	554.227	82.1219
14	642.519	94.4626
15	744.134	108.767
16	861.181	125.329
	996.092	144.493

Table of nominal constants for MJS.

The delta values are the full widths.

E_2 Mode. K = 1.333522

MODULATOR STEP	THRESHOLD VOLTAGE	PEAK VOLTAGE	AVERAGE VOLTAGE	DELTA VOLTAGE
1	10.0000	30.0113	20.0056	20.0113
2	30.0113	56.6968	43.3541	26.6855
3	56.6968	92.2825	74.4897	35.5857
4	92.2825	139.737	116.010	47.4543
5	139.737	203.018	171.377	63.2814
6	203.018	287.405	245.212	84.3870
7	287.405	399.937	343.671	112.532
8	399.937	550.001	474.969	150.064
9	550.001	750.114	650.058	200.113
10	750.114	1016.97	883.542	266.855
11	1016.97	1372.83	1194.90	355.859
12	1372.83	1847.37	1610.10	474.544
13	1847.37	2480.19	2163.78	632.815
14	2480.19	3324.06	2902.12	843.872
15	3324.06	4449.38	3886.72	1125.32
16	4449.38	5950.02	5199.70	1500.64

MODULATOR STEP	ELECTRONS AVERAGE SPEED	DELTA SPEED
1		
2	2564.08	1374.53
3	3660.12	1217.55
4	5085.13	1232.49
5	6358.59	1314.40
6	7736.11	1440.67
7	9259.03	1605.17
8	10965.3	1807.44
9	12893.9	2049.76
10	15086.9	2336.09
11	17590.8	2671.79
12	20459.4	3063.48
13	23749.7	3519.09
14	27533.2	4047.91
15	31887.5	4660.86
16	36902.3	5370.59
	42688.5	6191.81

APPENDIX B

LABBI SOURCE CODE

This appendix contains the routine LABBI, discussed in Chapter 2. Currents can be calculated for positive ions having either a convected isotropic Maxwellian or convected bimaxwellian distribution function.

The main routine is similar to the one written by Alan Barnett (ABSO) which works only for convected isotropic Maxwellian-distributions. However, instead of a call to the subroutine XBAR (i.e., $\overline{X}$, see Chapter 2 or *Barnett*, [1984]), LABBI calls a subroutine XINT. This subroutine calculates the transverse velocity integrals using the analytical result of Chapter 2. Integration of the velocity component normal to the sensor is performed numerically.

labbi.f


```
C       06/26/86   16:41:29      06/26/86   16:40:43      $380300.MJS
      SUBROUTINE LABBI(DN,WPAR,WPER,U1,A,Z,MODE,NCHN,NCUP,BF,LDIST,DIST)
C
CC      THIS SUBROUTINE COMPUTES THE MAIN SENSOR RESPONSE OF THE
CC    VOYAGER PLS EXPERIMENT OPERATING IN EITHER THE M-MODE OR THE
CC    L-MODE TO A PLASMA WHOSE DISTRIBUTION FUNCTION CAN BE MODELED AS A
CC    CONVECTED BIMAXWELLIAN.  IT USES AN ALGORITHM IN WHICH THE
CC    INTEGRATIONS OVER THE COMPONENTS OF VELOCITY PERPENDICULAR TO
CC    THE CUP NORMAL ARE PERFORMED ANALYTICALLY, WHILE THE INTEGRATION
CC    OVER THE COMPONENT OF VELOCITY ALONG THE CUP NORMAL IS DONE
CC    NUMERICALLY.  THE ALGORITHM IS DESCRIBED IN DETAIL IN THE
CC    DOCTORAL THESIS OF MARK SANDS.
CC       FOR EACH MODULATOR STEP, THE INTEGRATION OVER THE CHANNEL
CC    WIDTH IS DONE USING SIMPSON'S RULE, WHILE A RECTANGULAR RULE
CC    IS USED FOR THE INTEGRATION OVER THE "TAIL".   THE CURRENT IN A
CC    GIVEN CHANNEL IS COMPUTED FROM THE DIFFERENCE BETWEEN THE
CC    INTEGRATED CURRENT FOR ADJACENT MODULATOR GRID STEPS.  THE VZ
CC    INTEGRATION IS CUT OFF AT A PREDETERMINED VALUE FOR EACH CHANNEL.
CC
CC    THE INPUT VARIABLES ARE:
CC       DN          DENSITY OF SPECIES  (NUMBER/CC)
CC       W           THERMAL SPEED (KM/SEC)
CC       U1          BULK FLOW VELOCITY IN CUP COORDINATES (KM/SEC)
CC       A           SPECIES MASS (AMU)
CC       Z           SPECIES CHARGE (PROTON CHARGES)
CC       MODE        1=L,2=M
CC       NCHN(2)     FIRST AND LAST CHANNEL TO BE SIMULATED
CC       LDIST       LOGICAL FLAG; T-RETURNS REDUCED DISTRIBUTION FCN
CC                                 F-RETURNS CURRENT
CC    THE OUTPUT VARIABLE IS
CC       DIST(128)   REDUCED DISTRIBUTION FUNCTION OR CURRENT
C
c     IMPLICIT REAL*4 (A-H,O-Z)
c     REAL*8 $$$DT(6) /'$$DATE$$','06/26/86','16:40:43',
c    |'    LABBI','  FORTRAN','MJS       '/
      LOGICAL*4 LDIST
      INTEGER*4 NFIRST,NCHN(2),NC1,NC2,NCHAN,MODE,MFIRST,NCUP
      INTEGER*4 NSTEP(129)
C
CC    THE INTEGER CONSTANTS HAVE THE FOLLOWING MEANING
CC       NSTEP(I)         NUMBER OF STEPS IN THE NUMERICAL INTEGRATION
CC                      BETWEEN THE THESHOLD VOLTAGES FOR CHANNEL I AND I+1
CC       NFIRST(I)        NUMBER OF THE FIRST ELEMENT OF TVZ INCLUDED
CC                      IN THE INTEGRATION OF THE NEAR TAIL FOR CHANNEL I
C
      REAL*4 BIT(2),ETA(2),AETA(2),BY(2),BETA(2,2),GAMMA(2)
      REAL*4 SIGMA(2),DELTA(2),ALPHA(2,4),XARG(2,2)
      REAL*4 AMA1,AMA2,AMC1,AMSFT,TVZ,TDVZ
      REAL*4 AAAVZ,AAVZ,AVZ,AAADVZ,AADVZ,ADVZ,DVOLT,DVOLTL
      REAL*4 U(3),U1(3),CC(2),SD,CCD,AAD,BF(3)
      REAL*4 VTINT(2,2),VINT(2,2,4),D(2,2),AC(2),CRR(129)
C     REAL*4 X(4)/-4.94E0,-1.10E0,1.10E0,4.94E0/
      REAL*4 Y(4),CRNT(129)
      REAL*4 R(4),T(4),ECHRGE
      REAL*4 PI
      REAL*4 DIST(128),BCUP(3)
C
CC    THE REAL CONSTANTS HAVE THE FOLLOWING MEANINGS
CC       X,Y         PARAMETERS FOR TRAPEZOIDAL APPROXIMATION TO SENSITIVE
CC                      AREA
C        R           NOMINAL APERTURE AREA
```

```
C         T          NOMINAL GRID TRANSPARENCY AT NORMAL INCIDENCE
C         ECHRGE     PROTON CHARGE  IN COULOMBS
C
      COMMON / ANSWER / ANS(150)
      COMMON / TRNPRD / AAD(100,129,2),CCD(100,129,2),SD(100,129)
      COMMON / TRNPAR / AMA1(100,129),AMA2(100,129),AMC1(100,129),
     ,  AMSFT(100,129)
      COMMON / VZ / AAAVZ(22,5),AAVZ(4,40),AVZ(2,84),AAADVZ(22,5),
     ,   AADVZ(4,40),ADVZ(2,84),DVOLT(128),NFIRST(129),MFIRST(129)
      COMMON / TAIL / TVZ(241),TDVZ(241)
      COMMON / LCOMP / DVOLTL(16),NM(129),NL(17)
      COMMON  JJ
      data       NSTEP       /22,16,10,6,41*4,84*2 /
      data     Y /-3.63,-2.02,0.048,2.29 /
      data     R / 3*100.,82.7 /,T / 3*.65,.6801 /,ECHRGE / 1.6E-19 /
      data     PI / 3.141592654 /
C
C     COMMON BLOCKS TRNPAR, VZ, TAIL, AND LCOMP ARE FILLED BY SUBROUTINE
C          CONRD, WHICH MUST BE CALLED BEFORE THE FIRST CALL TO LABCUR.
C          THE VARIABLES HAVE THE FOLLOWING MEANINGS
C          AMA1                          CONSTANTS
C          AMA2                    WHICH DESCRIBE THE CUP
C          AMC1                       TRANSPARENCY
C          AMSFT                   THE SHIFT FUNCTION
C     THE FIRST INDEX OF THE PRECEDING FOUR VARIABLES REFERS TO THE
C          STEP NUMBER IN THE VZ INTEGRATION;  THE SECOND INDEX
C          REFERS TO THE MODULATOR STEP NUMBER.
C
C          AAAVZ                  VALUES OF VZ FOR INTEGRATION ACROSS
C                                        CHANNELS 1-5
C          AAVZ                   VALUES OF VZ FOR INTEGRATION ACROSS
C                                        CHANNELS 6-45
C          AVZ                    VALUES OF VZ FOR INTEGRATION ACROSS
C                                        CHANNELS 46-129
C          AAADVZ                 WEIGHTS FOR SIMPSON INTEGRATION ACROSS
C                                        CHANNELS 1-5
C          AADVZ                  WEIGHTS FOR SIMPSON INTEGRATION ACROSS
C                                        CHANNELS 6-45
C          ADVZ                   WEIGHTS FOR SIMPSON INTEGRATION ACROSS
C                                        CHANNELS 46-129
C          DVOLT                   VOLTAGE WIDTHS OF THE M-MODE CHANNELS
C          DVOLTL                  VOLTAGE WIDTHS OF THE L-MODE CHANNELS
C          NM(I)                  NUMBER OF INTEGRATION STEPS INCLUDED
C                            WHEN STEP I IS UPPER THRESHOLD  (M-MODE)
C          NL(I)                NUMBER OF INTEGRATION STEPS INCLUDED
C                            WHEN STEP I IS UPPER THRESHOLD  (L-MODE)
C          TVZ                     TABLE OF VALUES OF VZ FOR INTEGRATION OF
C                                        THE TAIL
C          TDVZ                    TABLE OF WEIGHTS FOR NUMERICAL INTEGRATION
C                                        OF THE TAIL
C
C     DEFINE CONST AND COMPUTE NORMALIZED BULK VELOCITY
C
      IHERE=IHERE+1
      WRITE(6,678)IHERE
  678 FORMAT(2X,'I AM ENTERING LABBI',1X,I3)
      CONST=R(NCUP)*T(NCUP)*Z*ECHRGE*1.E20*DN / (2.0*PI*WPAR*(WPER**2))
      NC1=NCHN(1)
      NC2=NCHN(2)
      NC3=NC2+1
C
```

labbi.f


```
C     ENTER OUTER LOOP OVER MODULATOR STEPS
C
      DO 5000 NCN=NC1,NC3
      NCHAN=NCN
      IF(MODE .EQ. 1) NCHAN=1+8*(NCN-1)
C
C     INITIALIZE CURENT
C
      CURENT=0.E0
      DO 2600 JJ=1,100
C
C    LAST INTEGRATION POINT NOT NEEDED; SKIP LOOP IF APPROPRIATE
C
        if ( ncn .ne. nc3)  go to 18
        if (mode -2) 14,16,18
 14     if (jj .gt. nl(ncn)) go to 2599
        go to 18
 16     if (jj .gt. nm(ncn)) go to 2599
 18     continue
c      IF (NCN .EQ. NC3 .AND. JJ .GT. NL(NCN) .AND. MODE .EQ. 1)
c     +    GO TO 2600
c      IF (NCN .EQ. NC3 .AND. JJ .GT. NM(NCN) .AND. MODE .EQ. 2)
c     +    GO TO 2600
C
C     INITIALIZE G AND CHOOSE PROPER VALUE OF VZ, DVZ
C
      G=0.E0
      IF(NCHAN .GE. 6 .AND. NCHAN .LE. 45)GO TO 100
      IF(NCHAN .GE. 46)GO TO 200
      IF(JJ .GT. NSTEP(NCHAN)) GO TO 10
      VZ=DBLE(AAAVZ(JJ,NCHAN))*SQRT(Z/A)
      DVZ=DBLE(AAADVZ(JJ,NCHAN))*SQRT(Z/A)
      GO TO 1000
   10 N=JJ-NSTEP(NCHAN)+NFIRST(NCHAN)-1
      VZ=DBLE(TVZ(N))*SQRT(Z/A)
      DVZ=DBLE(TDVZ(N))*SQRT(Z/A)
      GO TO 1000
  100 IF(JJ .GT. 4) GO TO 110
      VZ=DBLE(AAVZ(JJ,NCHAN-5))*SQRT(Z/A)
      DVZ=DBLE(AADVZ(JJ,NCHAN-5))*SQRT(Z/A)
      GO TO 1000
  110 N=JJ-5+NFIRST(NCHAN)
      VZ=DBLE(TVZ(N))*SQRT(Z/A)
      DVZ=DBLE(TDVZ(N))*SQRT(Z/A)
      GO TO 1000
  200 IF(JJ .GT. 2) GO TO 210
      VZ=DBLE(AVZ(JJ,NCHAN-45))*SQRT(Z/A)
      DVZ=DBLE(ADVZ(JJ,NCHAN-45))*SQRT(Z/A)
      GO TO 1000
  210 N=JJ-3+NFIRST(NCHAN)
      VZ=DBLE(TVZ(N))*SQRT(Z/A)
      DVZ=DBLE(TDVZ(N))*SQRT(Z/A)
 1000 CONTINUE
C
      DO 3 I=1,3
         U(I)=U1(I)
    3 CONTINUE
C
C    DETERMINE B IN CUP COORDINATES, THEN DETERMINE ITS UNIT VECTOR,
C    AND LASTLY DOT IT INTO THE BULK VELOCITY.
C
      IF(ANS(5).NE.0.0)GO TO 69
      CALL VSCCP(BF(1),NCUP,BCUP)
      GO TO 68
```

```
   69    CALL VSCCP(ANS(5),NCUP,BCUP)
   68    CONTINUE
         CALL VECNOR(BCUP)
         UB=VECSCL(U,BCUP)
         Y1=(UB / WPAR)**2+(U(1)**2+U(2)**2+U(3)**2-UB**2) / (WPER**2)
C
C     ASSIGN VALUES OF RESPONSE PARAMETERS
C
         IF(NCUP.NE.4)GO TO 2018
         S=SD(JJ,NCHAN)
         CC(1)=CCD(JJ,NCHAN,1)
         AC(1)=AAD(JJ,NCHAN,1)
         AC(2)=AAD(JJ,NCHAN,2)
         GO TO 2019
 2018    S=AMSFT(JJ,NCHAN)
         CC(1)=AMC1(JJ,NCHAN)
         AC(1)=AMA1(JJ,NCHAN)
         AC(2)=AMA2(JJ,NCHAN)
 2019    CC(2)=1.0E0-CC(1)
         VTH=(1.0 / WPAR**2)-(1.0 / WPER**2)
         VTHBB=VTH*BCUP(1)*BCUP(2)
         BETAZ=1.0 / (WPER**2)+VTH*(BCUP(3)**2)
         GAMMAZ=U(3) / (WPER**2)+VTH*BCUP(3)*UB
         X1=-BETAZ*(VZ**2)+2.0*GAMMAZ*VZ
         Z1=X1-Y1
         DO 1 I=1,2
            BIT(I)=(1.0 / WPER**2)+(AC(I) / VZ**2)
            ETA(I)=BIT(I)+VTH*(BCUP(2)**2)
            AETA(I)=BIT(I)+VTH*(BCUP(1)**2)
            BY(I)=((VZ / S)**2)*ETA(I)
            GAMMA(I)=(VZ / S)*((U(1) / WPER**2)-VTH*BCUP(1)*(VZ*BCUP(3)-UB)-
     *                  VTHBB*((U(2) / WPER**2)-VTH*BCUP(2)*(VZ*BCUP(3)-UB)) /
     *                  ETA(I))
            SIGMA(I)=((VZ / S)**2*VTHBB) / SQRT(BY(I))
            DELTA(I)=(U(2) / (WPER**2)-VTH*BCUP(2)*(VZ*BCUP(3)-UB))**2 /
     *                  ETA(I)
            DO 2 L=1,4
               ALPHA(I,L)=SQRT(BY(I))*(Y(L)-(VZ / S)*(U(2) / (WPER**2)-VTH*
     *                     BCUP(2)*(VZ*BCUP(3)-UB)) / BY(I))
    2       CONTINUE
    1    CONTINUE
         DO 5 I=1,2
            DO 4 J=1,2
               BETA(I,J)=((VZ / S)**2)*(AETA(I)-(VTHBB**2 / ETA(J)))
               XARG(I,J)=DELTA(J)+((GAMMA(J)**2) / BETA(I,J))+Z1
    4       CONTINUE
    5    CONTINUE
C
         DO 6 I=1,2
            DO 7 J=1,2
               DO 8 L=1,4
                  CALL XINT(SIGMA(J),DELTA(J),ALPHA(J,L),XARG(I,J),
     *                     BETA(I,J),GAMMA(J),NCUP,Z1,XIT)
                  VINT(I,J,L)=XIT
    8          CONTINUE
    7       CONTINUE
    6    CONTINUE
C
C     SUM OVER TERMS IN GRID TRANSPARENCY APPROXIMATION
C
         DO 2500 I=1,2
            DO 2450 J=1,2
```

labbi.f


```
C
C     CALCULATE RESULT OF ANALYTICAL INTEGRATION OVER VY
C
                VTINT(I,J)=(VINT(I,J,4)-VINT(I,J,3)) / (Y(4)-Y(3))-
     *                     (VINT(I,J,1)-VINT(I,J,2)) / (Y(1)-Y(2))
                D(I,J)=CC(I)*CC(J) / BY(J)
C
C     ADD TO SUM FOR INTEGRAND (EXCEPT MAXWELLIAN FACTOR)
C
 50             G1=(VZ / S)**2*D(I,J)*VTINT(I,J)
 55             G=G1+G
2450        CONTINUE
2500   CONTINUE
C
C     ADD TO SUM OF CONTRIBUTIONS FOR NUMERICAL INTEGRATION OVER VZ
C                (INCLUDING MAXWELLIAN FACTOR)
C
        CURENT=CURENT+VZ*G*DVZ
C
C     FILL ARRAY FOR UPPER MODULATOR STEP INTEGRATION, IF APPROPRIATE
C
2590    if (mode - 2) 2591,2592,2595
2591    if  (jj .eq. nl(ncn)) crr(ncn) = curent*const
        go to 2595
2592    if ( jj .eq. nm(ncn)) crr(ncn) = curent*const
2595    continue
c 2590 IF (JJ .EQ. NL(NCN) AND. MODE .EQ. 1) CRR(NCN)=CURENT*CONST
c       IF (JJ .EQ. NM(NCN) AND. MODE .EQ. 2) CRR(NCN)=CURENT*CONST
2599    continue
2600   CONTINUE
C
C     FILL ARRAY FOR LOWER MODULATOR STEP INTEGRATION
C
        CRNT(NCN)=CURENT*CONST
5000   CONTINUE
C
C     COMPUTE CURRENTS BY TAKING DIFFERENCE BETWEEN ADJACENT MODULATOR
C          STEPS; IF LDIST= .TRUE., DIVIDE BY CHANNEL WIDTH
C
        DO 5110 JJ=NC1,NC2
        IF(MODE .EQ. 2) GO TO 5100
C
C     L-MODE, LDIST =  .TRUE.
C
        IF(LDIST)DIST(JJ)=(CRNT(JJ)-CRR(JJ+1)) / DVOLTL(JJ)
        GO TO 5110
C
C     M-MODE, LDIST =  .TRUE.
C
5100   IF(LDIST)DIST(JJ)=(CRNT(JJ)-CRR(JJ+1)) / DVOLT(JJ)
C
C     L- OR M-MODE, LDIST =  .FALSE.
C
5110   IF(.NOT. LDIST)DIST(JJ)=(CRNT(JJ)-CRR(JJ+1))
       WRITE(6,676)
676    FORMAT(2X,'I AM EXITING LABBI')
       RETURN
       END
       SUBROUTINE XINT(SIGMA,DELTA,ALPHA,XARG,BETA,GAMMA,NCUP,Z1,XIT)
C                                                                          XINT
       REAL*4 PC(4),XPHI(3),RHO(3),ARG(3),FAC(3),Z(3,4),ZHAT(4)
       REAL*4 CONST(3),KONST(3)
       REAL*4 SQRTPI, X(4),HAC(3)
       COMMON JJ
```

```
      data     CONST / 1.0,1.3,7.0 / ,KONST / 1.0,-0.6,-0.3 /
      data     SQRTPI / 1.772453851 /
C
C     DEFINING ALL NEEDED PARAMETERS USED IN THE VARIOUS
C     INTEGRAL EXPRESSIONS.
C
      X(1)=-4.94
      X(2)=-1.1
      X(3)=1.1
      X(4)=4.94
      IF(NCUP.NE.4)GO TO 55
      X(1)=-1.61
      X(2)=-0.106
      X(3)=0.106
      X(4)=1.61
 55   IF(XARG.GT.-140.0)GO TO 50
      GAC=0.0
      GO TO 25
 50   GAC=EXP(XARG)
 25   DO 10 K=1,3
        XPHI(K)=BETA+CONST(K)*(SIGMA**2)
        RHO(K)=(GAMMA-CONST(K)*ALPHA*SIGMA) / XPHI(K)
        ARG(K)=(RHO(K)**2)*XPHI(K)+DELTA-CONST(K)*(ALPHA**2)+Z1
        IF(ARG(K).GE.-140.0)GO TO 40
        FAC(K)=0.0
        GO TO 45
 40     FAC(K)=(KONST(K) / SQRT(XPHI(K)))*EXP(ARG(K))
 45     DO 20 M=1,4
          Z(K,M)=SQRT(XPHI(K))*(X(M)-RHO(K))
          IF(K.EQ.1)ZHAT(M)=SQRT(BETA)*(X(M)-GAMMA / BETA)
 20     CONTINUE
 10   CONTINUE
C
C     DETERMINE THE CRITICAL "X" VALUE FOR WHICH |Z|--> -Z.  ALSO
C     CALCULATE WHAT THE CORRESPONDING VALUE OF Z IS.
C
      IF(SIGMA.NE.0.0)GO TO 30
      IF(ALPHA)4,35,5
 35   WRITE(6,6)
 6    FORMAT(1X,1H ,'ALPHA EQUALS ZERO - CHECK LABBI FOR ERROR')
      RETURN
 30   XC=-ALPHA / SIGMA
      PC(1)=SQRT(BETA)*(XC-GAMMA / BETA)
      DO 15 I=2,3
        PC(I)=SQRT(XPHI(I))*(XC-RHO(I))
 15   CONTINUE
      DO 60 I=1,3
        IF(ABS(PC(I)).LT.12.0)GO TO 65
        HAC(I)=0.0
        GO TO 60
 65     HAC(I)=EXP(-(PC(I)**2))
 60   CONTINUE
      IF(XC.GT.X(1))GO TO 1
C
C     DETERMINATION OF INTEGRAL OVER TRANSVERSE VELOCITY COMPONENTS
C     UNDER THE CONDITION "XC < X(1)".
C
      IHERE=1
C     IF(NCUP.EQ.1 AND.JJ.EQ.1)WRITE(6,600)NCUP,XC,IHERE
 600  FORMAT(/ ,1X,1H ,'NCUP = ',I1,2X,'XC = ',F8.3,2X,'I AM AT ',I1)
 5    XI1=(SQRTPI*GAC / (2.0*SQRT(BETA)*(ZHAT(4)-ZHAT(3))))*
     *      ((0.5*SIGMA / SQRT(BETA))*(terf(ZHAT(2))+terf(ZHAT(3))-
     *      terf(ZHAT(1))-terf(ZHAT(4)))+(ALPHA+SIGMA*GAMMA / BETA)*
     *      (PHI(ZHAT(1))+PHI(ZHAT(4))-PHI(ZHAT(2))-PHI(ZHAT(3))))
```

labbi.f

...XINT

170

```
C
      XI2=(0.5*FAC(1) / (Z(1,4)-Z(1,3)))*(PHI(Z(1,1))+PHI(Z(1,4))-
     *     PHI(Z(1,2))-PHI(Z(1,3)))
C
      DO 100 I=2,3
        XXI=(0.5*SQRTPI*FAC(I) / (Z(I,4)-Z(I,3)))*(0.5*SIGMA /
     *       SQRT(XPHI(I))*(terf(Z(I,2))+terf(Z(I,3))-terf(Z(I,1))-
     *       terf(Z(I,4)))+(ALPHA+SIGMA*RHO(I))*(PHI(Z(I,1))+
     *       PHI(Z(I,4))-PHI(Z(I,2))-PHI(Z(I,3))))
        IF(I.EQ.2)XI3=XXI
        IF(I.EQ.3)XI4=XXI
100   CONTINUE
C
      XIT=XI1+XI2+XI3+XI4
      IF(SIGMA.LT.0.0)XIT=-XI1+XI2-XI3-XI4
      RETURN

1     IF(XC.GT.X(2))GO TO 2
C
C     DETERMINATION OF INTEGRAL OVER TRANSVERSE VELOCITY COMPONENTS
C     UNDER THE CONDITION  "X(1) < XC < X(2)".
C
      IHERE=2
C     IF(NCUP.EQ.1 AND.JJ.EQ.1)WRITE(6,600)NCUP,XC,IHERE
      XI1=(0.5*SQRTPI*GAC / (SQRT(BETA)*(ZHAT(4)-ZHAT(3))))*
     *     (0.5*SIGMA / SQRT(BETA)*(terf(ZHAT(1))+terf(ZHAT(2))+
     *     terf(ZHAT(3))-terf(ZHAT(4))-2.0*terf(PC(1))+4.0*(PC(1)-ZHAT(1)
     * )*    HAC(1) / SQRTPI)+(ALPHA+SIGMA*GAMMA / BETA)*
     *     (PHI(ZHAT(4))-PHI(ZHAT(1))-PHI(ZHAT(2))-PHI(ZHAT(3))+2.0*
     *     (ZHAT(1)*terf(PC(1))+HAC(1) / SQRTPI)))
      XI2=(0.5*FAC(1) / (Z(1,4)-Z(1,3)))*(PHI(Z(1,1))+PHI(Z(1,4))-
     *     PHI(Z(1,2))-PHI(Z(1,3)))
C
      DO 200 I=2,3
        XXI=(0.5*SQRTPI*FAC(I) / (Z(I,4)-Z(I,3)))*(0.5*SIGMA /
     *       SQRT(XPHI(I))*(terf(Z(I,1))+terf(Z(I,2))+terf(Z(I,3))-
     *       terf(Z(I,4))-2.0*terf(PC(I))+4.0*(PC(I)-Z(I,1))*
     *       HAC(I) / SQRTPI)+(ALPHA+SIGMA*RHO(I))*
     *       (PHI(Z(I,4))-PHI(Z(I,1))-PHI(Z(I,2))-PHI(Z(I,3))+2.0*
     *       (Z(I,1)*terf(PC(I))+HAC(I) / SQRTPI)))
        IF(I.EQ.2)XI3=XXI
        IF(I.EQ.3)XI4=XXI
200   CONTINUE
C
      XIT=XI1+XI2+XI3+XI4
      IF(SIGMA.LT.0.0)XIT=-XI1+XI2-XI3-XI4
      RETURN
C
2     IF(XC.GT.X(3))GO TO 3
C
C     DETERMINATION OF INTEGRAL OVER TRANSVERSE VELOCITY COMPONENTS
C     UNDER THE CONDITION  "X(2) < XC < X(3)".
C
      IHERE=3
C     IF(NCUP.EQ.1 AND.JJ.EQ.1)WRITE(6,600)NCUP,XC,IHERE
      XI1=(0.5*SQRTPI*GAC / (SQRT(BETA)*(ZHAT(4)-ZHAT(3))))*
     *     (0.5*SIGMA / SQRT(BETA)*(terf(ZHAT(1))+terf(ZHAT(3))-
     *     terf(ZHAT(2))-terf(ZHAT(4))+4.0*(ZHAT(4)-ZHAT(3))*
     *     HAC(1) / SQRTPI)+(ALPHA+SIGMA*GAMMA / BETA)*
     *     (PHI(ZHAT(2))+PHI(ZHAT(4))-PHI(ZHAT(1))-PHI(ZHAT(3))-
     *     2.0*(ZHAT(4)-ZHAT(3))*terf(PC(1))))
```

labbi.f


```
C
      XI2=(0.5*FAC(1) / (Z(1,4)-Z(1,3)))*(PHI(Z(1,1))+PHI(Z(1,4))-
     *     PHI(Z(1,2))-PHI(Z(1,3)))
C
      DO 300 I=2,3
        XXI=(0.5*SQRTPI*FAC(I) / (Z(I,4)-Z(I,3)))*(0.5*SIGMA /
     *       SQRT(XPHI(I))*(terf(Z(I,1))+terf(Z(I,3))-terf(Z(I,2))-
     *       terf(Z(I,4))+4.0*(Z(I,4)-Z(I,3))*HAC(I) /
     *       SQRTPI)+(ALPHA+SIGMA*RHO(I))*(PHI(Z(I,2))+PHI(Z(I,4))-
     *       PHI(Z(I,1))-PHI(Z(I,3))-2.0*(Z(I,4)-Z(I,3))*terf(PC(I))))
        IF(I.EQ.2)XI3=XXI
        IF(I.EQ.3)XI4=XXI
300   CONTINUE
C
      XIT=XI1+XI2+XI3+XI4
      IF(SIGMA.LT.0.0)XIT=-XI1+XI2-XI3-XI4
      RETURN
C
3     IF(XC.GT.X(4))GO TO 4
C
C     DETERMINATION OF INTEGRAL OVER TRANSVERSE VELOCITY COMPONENTS
C     UNDER THE CONDITION  "X(3) < XC < X(4)".
C
      IHERE=4
C     IF(NCUP.EQ.1 AND JJ.EQ.1)WRITE(6,600)NCUP,XC,IHERE
      XI1=(0.5*SQRTPI*GAC / (SQRT(BETA)*(ZHAT(4)-ZHAT(3))))*
     *     (0.5*SIGMA / SQRT(BETA)*(terf(ZHAT(1))-terf(ZHAT(2))-
     *     terf(ZHAT(3))-terf(ZHAT(4))+2.0*terf(PC(1))+4.0*(ZHAT(4)-
     *     PC(1))*HAC(1) / SQRTPI)+(ALPHA+SIGMA*GAMMA / BETA)*
     *     (PHI(ZHAT(2))+PHI(ZHAT(3))+PHI(ZHAT(4))-PHI(ZHAT(1))-2.0*
     *     (ZHAT(4)*terf(PC(1))+HAC(1) / SQRTPI)))
C
      XI2=(0.5*FAC(1) / (Z(1,4)-Z(1,3)))*(PHI(Z(1,1))+PHI(Z(1,4))-
     *     PHI(Z(1,2))-PHI(Z(1,3)))
C
      DO 400 I=2,3
        XXI=(0.5*SQRTPI*FAC(I) / (Z(I,4)-Z(I,3)))*(0.5*SIGMA /
     *       SQRT(XPHI(I))*(terf(Z(I,1))-terf(Z(I,2))-terf(Z(I,3))-
     *       terf(Z(I,4))+2.0*terf(PC(I))+4.0*(Z(I,4)-PC(I))*
     *       HAC(I) / SQRTPI)+(ALPHA+SIGMA*RHO(I))*
     *       (PHI(Z(I,2))+PHI(Z(I,3))+PHI(Z(I,4))-PHI(Z(I,1))-2.0*
     *       (Z(I,4)*terf(PC(I))+HAC(I) / SQRTPI)))
        IF(I.EQ.2)XI3=XXI
        IF(I.EQ.3)XI4=XXI
400   CONTINUE
C
      XIT=XI1+XI2+XI3+XI4
      IF(SIGMA.LT.0.0)XIT=-XI1+XI2-XI3-XI4
      RETURN
C
4     CONTINUE
C
C     DETERMINATION OF INTEGRAL OVER TRANSVERSE VELOCITY COMPONENTS
C     UNDER THE CONDITION  "X(4) < XC".
C
      IHERE=5
C     IF(NCUP.EQ.1 AND JJ.EQ.1)WRITE(6,600)NCUP,XC,IHERE
      XI1=-(0.5*SQRTPI*GAC / (SQRT(BETA)*(ZHAT(4)-ZHAT(3))))*
     *     (0.5*SIGMA / SQRT(BETA)*(terf(ZHAT(2))+terf(ZHAT(3))-
     *     terf(ZHAT(1))-terf(ZHAT(4)))+(ALPHA+SIGMA*GAMMA / BETA)*
     *     (PHI(ZHAT(1))+PHI(ZHAT(4))-PHI(ZHAT(2))-PHI(ZHAT(3))))
```

labbi.f


```
C
      XI2=(0.5*FAC(1) / (Z(1,4)-Z(1,3)))*(PHI(Z(1,1))+PHI(Z(1,4))-
     *     PHI(Z(1,2))-PHI(Z(1,3)))
C
      DO  500  I=2,3
          XXI=-(0.5*SQRTPI*FAC(I) / (Z(I,4)-Z(I,3)))*(0.5*SIGMA /
     *          SQRT(XPHI(I))*(terf(Z(I,2))+terf(Z(I,3))-terf(Z(I,1))-
     *          terf(Z(I,4)))+(ALPHA+SIGMA*RHO(I))*(PHI(Z(I,1))+
     *          PHI(Z(I,4))-PHI(Z(I,2))-PHI(Z(I,3))))
          IF(I.EQ.2)XI3=XXI
          IF(I.EQ.3)XI4=XXI
  500 CONTINUE
C
      XIT=XI1+XI2+XI3+XI4
      IF(SIGMA.LT.0.0)XIT=-XI1+XI2-XI3-XI4
      RETURN
      END
```

APPENDIX C

SAMPLE INPUT LISTING FOR MJSANL

A sample input listing for MJSANL is given. The input shown is for analyzing a spectrum from Voyager 1 on day 63 at 2323 UT, 1979 (see Chapter 3, Fig. 3.3-2). The analysis routine chosen is ABSO and five ion species are used to simulate the spectrum (H^+, O^{+2}, S^{+3}, O^+, and S^+). All five densities, the proton thermal speed (the plasma is assumed isothermal), and all three plasma bulk velocity components make up the fit parameters. The analysis is performed on energy-per-charge channels in the B, C, and D-cups. Once the initial guesses for the fit parameters are input into the analysis code, currents and the associated χ^2 (see Chapter 3) are calculated. At this point, the user has the option of either continuing with the analysis or terminating the analysis (outputing the results and ploting the calculated currents).

*** JUPITER DATA DISPLAY ***

SEDR DATA FILE COVERS:

V1 - 1979 062 0600 TO 1979 065 1200

SPECTRAL DATA FILE COVERS:

V1 - 1979 062 0600 TO 1979 065 1200

INPUT START TIME: IYR, IDAY, IHR, IMIN, ISEC, IMSEC

1979,63,23,23,11,5

TIME OF CURRENT SPECTRUM IS 1979 63 2323:11.005

CURRENT SPECTRUM IS AN M-MODE

PLOT DATA? 1=YES, 0=NO

1

THRESHOLD IS 1.6475e+01 FEMTOAMPS.

SATURATION IS 1.5893e+05 FEMTOAMPS.

MINIMUM AND MAXIMUM CURRENTS (IN FEMTOAMPS) ARE:

1.647e+01 2.447e+03 IN CUP 1

1.647e+01 8.621e+03 IN CUP 2

1.647e+01 8.317e+03 IN CUP 3

2.826e+02 8.023e+04 IN CUP 4

WRITE OUT ALL CURRENTS? 1=YES, 0=NO

0

THE SCALE STARTS AT 1.00e-01 FEMTOAMPS AND GOES UP 6 DECADES

CHANGE CURRENT SCALE FROM CURRENT VALUE? 1=YES 0=NO

1

YB (MUST BE A POWER OF 10),IDEC (NUMBER OF DECADES)

100,3

DO NONLINEAR LEAST SQUARES ANALYSIS WITH CURRENT SPECTRA?

1=YES 2=NO.

1

USE DOUBLE PRECISION ROUTINE? T OR F

f

```
 SELECT FITTING OPTION:
 0 ==> DO NOT DO FIT
 1 ==> FIT USING PMODEL
 3 ==> FIT USING XJC (UNITY RESPONCE)
 4 ==> FIT USING ABSO (L OR M MODES - LABCUR,LDCUR)
 5 ==> FIT USING ABSOM (M-MODE ONLY - ABCCUR,DCUR)
 6 ==> FIT USING ABSO (BIMAXWELLIAN VERSION)
 7 ==> FIT USING COLD BEAM (CUPINT,DCPINT)
 8 ==> FIT USING RECTANGULAR APPROX (XCUR)
 9 ==> FIT USING VERY COLD BEAM (CUPEXP)
 GT 10 ==> TERMINATE EXECUTION
 4

 ** PARAMETERS FOR USE IN ANALYSIS **


 INPUT NUMBER OF COMPONENTS TO FIT TO SPECTRA
 5

 DO YOU WISH TO HAVE DENSITY AS A FIT PARAMETER?  (T OR F)
 t

 INDICATE WHICH DENSITIES TO FIT (T OR F FOR EACH OF THE 5 SPECIES)
 t,t,t,t,t

 INPUT LOGICAL VARIABLES (T OR F ) TO SELECT FIT PARAMETERS

 FIT VR, VPHI, VZ FOR COMPONENT  1 ?
 t,t,t
 FIT THERMAL SPEED FOR THIS COMPONENT ?
```

t

INPUT MASS AND CHARGE STATE (INTEGERS) OF COMPONENT 1

1,1

INPUT LOGICAL VARIABLES (T OR F) TO SELECT FIT PARAMETERS

FIT VR, VPHI, VZ FOR COMPONENT 2 ?

f,f,f

FIT THERMAL SPEED FOR THIS COMPONENT ?

f

INPUT MASS AND CHARGE STATE (INTEGERS) OF COMPONENT 2

16,2

INPUT LOGICAL VARIABLES (T OR F) TO SELECT FIT PARAMETERS

FIT VR, VPHI, VZ FOR COMPONENT 3 ?

f,f,f

FIT THERMAL SPEED FOR THIS COMPONENT ?

f

INPUT MASS AND CHARGE STATE (INTEGERS) OF COMPONENT 3

32,3

INPUT LOGICAL VARIABLES (T OR F) TO SELECT FIT PARAMETERS

FIT VR, VPHI, VZ FOR COMPONENT 4 ?

f,f,f

FIT THERMAL SPEED FOR THIS COMPONENT ?

f

INPUT MASS AND CHARGE STATE (INTEGERS) OF COMPONENT 4

16,1

INPUT LOGICAL VARIABLES (T OR F) TO SELECT FIT PARAMETERS

FIT VR, VPHI, VZ FOR COMPONENT 5 ?

f,f,f

FIT THERMAL SPEED FOR THIS COMPONENT ?

f

INPUT MASS AND CHARGE STATE (INTEGERS) OF COMPONENT 5

32,1

USE ISOTROPIC MAXWELLIANS IN FIT ?

t

USE COMMON TEMPERATURE (ALL THERMAL SPEEDS ARE NOT FIT PARAMETERS) ?

t

NCOMP	CHARGE	MASS	FIT N	FIT VR	FIT VPHI	FIT VZ	FIT W
1	1	1	t	t	t	t	t
2	2	16	t	f	f	f	f
3	3	32	t	f	f	f	f
4	1	16	t	f	f	f	f

5 1 32 t f f f f

FLAM = 0.100 ALAM = 0.001

ISOTROPIC MAXWELLIAN t

SAME TEMPERATURE t

CHANGE FIT OPTIONS? 1=YES, 0=NO

0

HOW MANY CONTIGUOUS SETS OF CHANNELS FOR CUP 1?

0

HOW MANY CONTIGUOUS SETS OF CHANNELS FOR CUP 2?

4

INPUT LOWER AND UPPER CHANNELS FOR SET 1

4,48

INPUT LOWER AND UPPER CHANNELS FOR SET 2

55,72

INPUT LOWER AND UPPER CHANNELS FOR SET 3

79,97

INPUT LOWER AND UPPER CHANNELS FOR SET 4

105,118

HOW MANY CONTIGUOUS SETS OF CHANNELS FOR CUP 3?

4

INPUT LOWER AND UPPER CHANNELS FOR SET 1

4,48

INPUT LOWER AND UPPER CHANNELS FOR SET 2

54,73

INPUT LOWER AND UPPER CHANNELS FOR SET 3

78,97

INPUT LOWER AND UPPER CHANNELS FOR SET 4

105,124

HOW MANY CONTIGUOUS SETS OF CHANNELS FOR CUP 4?

1

INPUT LOWER AND UPPER CHANNELS FOR SET 1

4,128

VELOCITY IS INITIALIZED TO THAT OF RIGID COROTATION

THERMAL SPEEDS INITIALIZED ASSUMING MACH 3 FLOW

DENSITIES ESTIMATED FROM DATA IN CUP 4, DIVIDED BY "NCOMP"

NCOMP	VR	VPHI	VZ	W	DEN
1	0.000	169.909	0.000	56.636	2.607
2	0.000	169.909	0.000	56.636	2.607
3	0.000	169.909	0.000	56.636	2.607

4 0.000 169.909 0.000 56.636 2.607

5 0.000 169.909 0.000 56.636 2.607

HOW MANY SPECIES DO YOU WISH TO MODIFY FIT PARAMETERS OF? 0=NONE 9=ALL

9

INPUT LOGICAL VARIABLES (T OR F) FOR PARAMETERS YOU WISH CHANGED

CHANGE VR,VPHI,VZ,W,DEN FOR COMPONENT 1

t,t,t,t,t

INPUT NEW VALUES OF VR,VPHI,VZ,WPAR,DEN FOR COMPONENT 1

-4.5,139.7,16.7,55.8,1.22

INPUT LOGICAL VARIABLES (T OR F) FOR PARAMETERS YOU WISH CHANGED

CHANGE VR,VPHI,VZ,W,DEN FOR COMPONENT 2

t,t,t,t,t

INPUT NEW VALUES OF VR,VPHI,VZ,WPAR,DEN FOR COMPONENT 2

-4.5,139.7,16.7,13.9,1.46

INPUT LOGICAL VARIABLES (T OR F) FOR PARAMETERS YOU WISH CHANGED

CHANGE VR,VPHI,VZ,W,DEN FOR COMPONENT 3

t,t,t,t,t

INPUT NEW VALUES OF VR,VPHI,VZ,WPAR,DEN FOR COMPONENT 3

-4.5,139.7,16.7,9.9,.95

INPUT LOGICAL VARIABLES (T OR F) FOR PARAMETERS YOU WISH CHANGED

CHANGE VR,VPHI,VZ,W,DEN FOR COMPONENT 4

t,t,t,t,t

INPUT NEW VALUES OF VR,VPHI,VZ,WPAR,DEN FOR COMPONENT 4

-4.5,139.7,16.7,13.9,8.89

INPUT LOGICAL VARIABLES (T OR F) FOR PARAMETERS YOU WISH CHANGED

CHANGE VR,VPHI,VZ,W,DEN FOR COMPONENT 5

t,t,t,t,t

INPUT NEW VALUES OF VR,VPHI,VZ,WPAR,DEN FOR COMPONENT 5

-4.5,139.7,16.7,9.9,1.07

BELOW ARE THE CURRENT VALUES OF THE FIT PARAMETERS

NCOMP	VR	VPHI	VZ	W	DEN
1	-4.500	139.700	16.700	55.800	1.220
2	-4.500	139.700	16.700	13.900	1.460
3	-4.500	139.700	16.700	9.900	0.950
4	-4.500	139.700	16.700	13.900	8.890
5	-4.500	139.700	16.700	9.900	1.070

DO YOU WISH TO MAKE ANY FURTHER CHANGES? 1=YES 0=NO

0

NTERMS = 9

FIT IS TO CHANNELS BELOW. TOTAL AND NUMBER PER COLLECTOR 326 0 96105125

4 5 6 7 8 9 10 11 12 13 14 15 16 17 18 19

20 21 22 23 24 25 26 27 28 29 30 31 32 33 34 35

36 37 38 39 40 41 42 43 44 45 46 47 48 55 56 57

58 59 60 61 62 63 64 65 66 67 68 69 70 71 72 79

80 81 82 83 84 85 86 87 88 89 90 91 92 93 94 95

96 97 105 106 107 108 109 110 111 112 113 114 115 116 117 118

4 5 6 7 8 9 10 11 12 13 14 15 16 17 18 19

20 21 22 23 24 25 26 27 28 29 30 31 32 33 34 35

36 37 38 39 40 41 42 43 44 45 46 47 48 54 55 56

57 58 59 60 61 62 63 64 65 66 67 68 69 70 71 72

73 78 79 80 81 82 83 84 85 86 87 88 89 90 91 92

93 94 95 96 97 105 106 107 108 109 110 111 112 113 114 115

116 117 118 119 120 121 122 123 124 4 5 6 7 8 9 10
11 12 13 14 15 16 17 18 19 20 21 22 23 24 25 26
27 28 29 30 31 32 33 34 35 36 37 38 39 40 41 42
43 44 45 46 47 48 49 50 51 52 53 54 55 56 57 58
59 60 61 62 63 64 65 66 67 68 69 70 71 72 73 74
75 76 77 78 79 80 81 82 83 84 85 86 87 88 89 90
91 92 93 94 95 96 97 98 99 100 101 102 103 104 105 106
107 108 109 110 111 112 113 114 115 116 117 118 119 120 121 122
123 124 125 126 127 128

FIT ITERATIONS. FIT PARAMETERS ARE 11 0.100

REINITIALIZE FIT MATRICES FROM PREVIOUS SESSION? 1=YES, 0=NO

0

CALLING XFNCDV TO INITIALIZE FITTING RUN

INITIAL VALUES IN "A-ARRAY"

1.22 1.46 0.95 8.89 1.07 -4.50 139.70

16.70 55.80

REDUCED CHI SQUARE = 1.15726e+04

CPU TIME USED = 0.26142 MINUTES

TOTAL ELAPSED CPU TIME = 0.27611

THIS ITERATION COST 6.27 (PRIME TIME RATE)

DO YOU WISH TO CONTINUE? 1=YES, 0=NO

1

PLOT SIMULATED CURRENTS (IN XMJSFT) ? 1-4=YES, 0=NO

0

0.9468 0.89 0.57 6.53 0.85 -1.90 138.57

CPU TIME USED = 0.26042 MINUTES

TOTAL ELAPSED CPU TIME = 0.53819

THIS ITERATION COST 6.25 (PRIME TIME RATE)

CHI SQUARE HAS DECREASED. THIS IS SIMULATION NUMBER 2

DO YOU WISH TO CONTINUE? 1=YES, 0=NO

0

THE DATE IS 10/15/84 AND THE TIME IS 14:44:56

INFORMATION FROM MAXWELLIAN SIMULATION OF V1 AT JUPITER

ON 1979 63 2323:11.005

CUP CHANNELS USED IN FIT BY ABSOM

A-CUP: *** NO FIT PERFORMED ***

B-CUP: CHANNELS 4 - 48

CHANNELS 55 - 72

CHANNELS 79 - 97

CHANNELS 105 -118

C-CUP: CHANNELS 4 - 48

CHANNELS 54 - 73

CHANNELS 78 - 97

CHANNELS 105 -124

D-CUP: CHANNELS 4 -128

CHI SQUARE = 0.418e+04

PARAMETERS AND 1-SIGMA UNCERTAINTIES FROM FIT TO SPECTRUM AT 1979 63 2323:11.005

CURRENTS WERE GENERATED USING XJC(UR)

SINGLE PRECISION CODE WAS USED

MASS	NQ	DEN	XDEN	VR	XVR	VPHI	XVPHI	VZ
XVZ	W	XW						
1	1	0.9468	0.1990	-1.8986	0.5045	138.5711	0.3341	17.2417
0.4919	63.0971	4.3462						
16	2	0.8908	0.0774	-1.8986	0.5045	138.5711	0.3341	17.2417
1.4919	15.7743	1.0866						
32	3	0.5677	0.0442	-1.8986	0.5045	138.5711	0.3341	17.2417
1.4919	11.1541	0.7683						
16	1	6.5262	0.1757	-1.8986	0.5045	138.5711	0.3341	17.2417
1.4919	15.7743	1.0866						
32	1	0.8499	0.1230	-1.8986	0.5045	138.5711	0.3341	17.2417
1.4919	11.1541	0.7683						

PARTICLE VELOCITIES IN S/C COORDINATES (KM/SEC)

NCOMP	VX	VY	VZ
1	2.81	2.82	-19.03
2	2.81	2.82	-19.03
3	2.81	2.82	-19.03
4	2.81	2.82	-19.03
5	2.81	2.82	-19.03

PROJECTION OF FITTED VELOCITIES ALONG CUP NORMALS (KM/SEC)

NCOMP	VA	VB	VC	VD
1	-16.57	-18.24	-18.85	-4.64

```
2    -16.57   -18.24   -18.85    -4.64
3    -16.57   -18.24   -18.85    -4.64
4    -16.57   -18.24   -18.85    -4.64
5    -16.57   -18.24   -18.85    -4.64

PLOT FIT CURRENTS FROM BEST FIT ? 1-4=YES, 0=NO
1

THE SCALE STARTS AT 1.00e+02 FEMTOAMPS AND GOES UP 3 DECADES
CHANGE CURRENT SCALE FROM CURRENT VALUE? 1=YES 0=NO
0


IF A PLOT OF THE SIMULATED CURRENTS IS REQUESTED:
IPLT=1 ==> TOTAL CURRENT ONLY
IPLT=2 ==> TOTAL CURRENT AND DATA
IPLT=3 ==> TOTAL CURRENT AND INDIVIDUAL SPECIES
IPLT=4 ==> TOTAL CURRENT, DATA, AND INDIVIDUAL SPECIES
THE CURRENT VALUE OF IPLT IS    1
INPUT NEW VALUE
4
```

OUTPUT THIS FIT TO YOUR DISK? 1-9 = YES, 0,CR = NO

0

DO NONLINEAR LEAST SQUARES ANALYSIS WITH CURRENT SPECTRA?

0

READ NEXT SPECTRUM? 1=YES, 0=NO, 2=TERMINATE

2

APPENDIX D

TABLE OF DATA FOR STRESS BALANCE

The table of points used to make the plot of curvature stress/centrifugal stress vs. distance (Fig. 4.4-2) is presented. Along with the time and radius of curvature of each spectrum, the associated centrifugal and curvature acceleration is given. In calculating these quantities, the azimuthal component of the magnetic field ($\mathbf{B}_\phi$) is assumed zero. The parameter δ is defined by Eq. 4.2.8, while a_{curv} and a_{cent} are the curvature acceleration ($\frac{V_\parallel^2}{R_c}$), and the component of the centrifugal acceleration in the direction of the curvature force ($\frac{V_\phi^2}{r}\delta$), respectively.

Table D.1. DATA USED FOR FIG. 4.2-2

TIME/MODE	R_c (R_J)	δ	a_{cent} ($\times 10^{-2}$) (km/sec^2)	a_{curv} ($\times 10^{-3}$) (km/sec^2)
063 0841:00/L	1.228	0.6001	1.782	52.920
1527:24/L	1.973	0.6229	1.901	4.102
1535:24/L	2.123	0.5803	1.709	0.691
1738:36/L	2.565	0.6094	1.900	7.366
1755:11/M	2.436	0.6545	2.062	1.235
1819:11/M	2.184	0.7340	2.449	1.396
1827:11/M	2.078	0.7764	2.438	0.516
1844:47/M	1.940	0.8764	2.691	2.316
1903:59/M	1.856	0.9723	2.979	9.151
1913:35/M	1.818	0.9996	2.735	5.274
1933:48/M	2.078	0.9101	3.068	0.004
1934:23/M	2.098	0.9407	2.942	1.219
1950:23/M	1.632	0.8694	2.542	3.397
1956:47/M	2.470	0.8485	2.469	0.628
2011:11/M	2.669	0.8082	2.438	3.077
2033:35/M	3.013	0.7635	2.318	4.981
2103:59/M	3.333	0.7382	2.269	5.523
2148:47/M	3.651	0.7596	2.127	7.665
2223:24/L	3.701	0.8173	1.899	5.051
2233:35/M	3.683	0.8375	1.963	5.937
2236:12/M	3.696	0.8476	2.270	7.508
2244:47/M	3.679	0.8650	1.999	5.271
2255:59/M	3.668	0.8964	2.133	6.391
2308:47/M	3.659	0.9297	1.882	6.637
2311:59/M	3.659	0.9401	1.885	6.239
2323:11/M	3.698	0.9575	1.830	4.415
2324:47/M	3.667	0.9623	1.789	5.574
2326:23/M	3.655	0.9650	1.861	7.225
2327:59/M	3.664	0.9714	1.750	7.995
2329:35/M	3.662	0.9766	1.756	7.721
2331:11/M	3.657	0.9780	1.865	5.645
2332:47/M	3.667	0.9793	1.821	4.818
2334:23/M	3.674	0.9804	1.764	5.422
2335:59/M	3.662	0.9831	1.784	7.097
2337:35/M	3.648	0.9852	1.797	6.995
2339:11/M	3.660	0.9873	1.896	6.251
2340:47/M	3.679	0.9880	1.994	4.919

Table D.1. DATA USED FOR FIG. 4.2-2 (Continued)

TIME/MODE	R_c (R_J)	δ	a_{cent} ($\times 10^{-2}$) (km/sec^2)	a_{curv} ($\times 10^{-3}$) (km/sec^2)
064 0024:00/L	4.086	0.9848	1.607	1.871
0045:48/L	4.472	0.9610	2.090	1.955
0111:24/L	5.348	0.9244	2.053	0.657
0130:36/L	5.581	0.8905	1.697	0.167
0138:36/L	5.747	0.8692	1.261	0.159
0142:23/M	5.826	0.8660	1.317	0.125
0150:23/M	5.740	0.8797	1.378	0.076

APPENDIX E

DETERMINATION OF ERRORS

To determine the errors in the values of the fit parameters, the error associated with each measured current must be specified. As χ^2 is used as the criterion for determining the "best fit" to the plasma data, the problem reduces to choosing the proper statistical weights for the data in the fits. Sources of "error" include those due to the ambient plasma being sampled and the instrument itself. With respect to the ambient plasma, the presence of suprathermal tails in the distribution functions contributes to "error" because Maxwellian (or bimaxwellian) distribution functions are assumed as fitting functions. Time variability in the plasma on scales shorter than the time required to complete an energy-per-charge scan ("time aliasing") will also appear as a source of error. Acoustical noise and electrical interference from other spacecraft systems (both of which are known to be present but are not easily quantified) as well as penetrating radiation from high energy particles increase the instrument noise level.

Uncertainties also occur in the form of electrical noise and digitization error of the measured current. Because the logarithm of the measured currents is digitized, this error is constant and has a weight factor of $\sigma_i = 0.01058 I_i$, where I_i is the measured current of channel i. Thermal fluctuations in the instrument amplifiers are a source of electrical noise, producing fluctuations in the measured currents. The rms power associated with these fluctuations should be about the same in all the energy-per-charge channels. However this thermal noise is typically smaller than the unmodeled noise discussed above.

The formal error, σ_{a_j}, in the value of fit parameter a_j can be expressed in terms of the error matrix (covariance matrix) which is the inverse of the curvature matrix evaluated at the minimum value of χ^2 [*Bevington*, 1969]

$$\sigma_{a_j}^2 = \varepsilon_{jj}$$

where ε_{ij} are elements of the error matrix. The value of σ_{a_j} is the formal 1σ error for a "good

fit"; such a fit is characterized by a value of $\chi^2/\nu \approx 1$, where ν is the number of degrees of freedom (number of data points less the number of fit parameters). However, if only the thermal noise and digitization errors are included, values of $\chi^2/\nu \gg 1$ are found. In addition, the digitization error tends to weight smaller currents more heavily, giving increased weight to the non-Maxwellian tail in the measured spectra. The large values of χ^2/ν are presumably due to unmodeled sources of error, so this "true error" in the measurements is taken to be the same for each current (i.e., digitization is excluded) and is estimated from the variance of the best fit (see e.g. [*Bevington*, 1969]). The formal errors are then given by

$$\sigma_{a_j}^2 = \frac{\varepsilon_{jj}\chi^2}{\nu}$$

These formal errors associated with the plasma parameters, determined through the analysis, have been shown to give reliable estimates of the uncertainties in the fit parameters [*Barnett*, 1986; *Richardson*, 1986; and *Bagenal*, 1985]. The theoretical formulation of the instrument response function was shown by *Barnett and Olbert* [1986] to be accurate to within a few percent for all cases of interest. Using the response function, *Barnett* [1986] was able to analyze spectra containing unresolved peaks (from the Io torus region). From this data, he obtained a range of values of the Alfvén speed and compared them to two other independent calculations of the Alfvén speed in this same region. Values obtained from the magnetometer data and an Alfvén wave model [*Barnett*, 1986] were consistent with the Alfvén speeds obtained from analyzing the PLS data. *Bagenal* [1985] analyzed data from the Io torus and determined plasma velocities for spectra with well resolved peaks. Because the symmetry axis of the main sensor pointed almost directly into the corotating flow, the response function was assumed to be unity. With this assumption, the plasma velocities obtained through the analysis, were found to lie within 1% of the local corotation speed. Error bars for these velocities combined formal error and instrument error, with a typical value of 5%. In analyzing data from Saturn, *Richardson* [1986] found that high energy (non-Maxwellian) tails had a negligible influence on plasma flow velocity determination. Mocking up the high energy tail with a hot ion population, Richardson re-analyzed several spectra and found almost no difference in the

velocity components. All of these cross comparisons between the formal errors and analyses of the PLS data in the magnetospheres of Jupiter, Saturn, and Uranus (and in the solar wind) give a high level of confidence to the errors in the fit parameters quoted herein.

APPENDIX F

REFERENCES

Acuna, M. H., and N. F. Ness, Results from the GSFC fluxgate magnetometer on Pioneer 11, in *Jupiter*, ed. T. Gehrels, University of Arizona Press, Tucson, 830, 1976*a*.

Acuna, M. H., and N. F. Ness, The main magnetic field of Jupiter, *J. Geophys. Res.*, *81*, 2917, 1976*c*.

Acuna, M. H., K. W. Behannon, and J. E. P. Connerney, Jupiter's magnetic field and magnetosphere, in *Physics of the Jovian Magnetosphere*, ed. A. J. Dessler, Ch. 1, Cambridge University Press, New York, 1983.

Axford, W. I., H. E. Petschek, and G. L. Siscoe, Tail of the magnetosphere, *J. Geophys. Res.*, *70*, 1231, 1965.

Bagenal, F., Plasma conditions inside Io's orbit: Voyager measurements, *J. Geophys. Res.*, *90*, 311, 1985.

Bagenal, F., and J. D. Sullivan, Direct plasma measurements in the Io torus and inner magnetosphere of Jupiter, *J. Geophys. Res.*, *86*, 8447, 1981.

Barnett, A., In situ measurements of the plasma bulk velocity near the Io flux tube, *J. Geophys. Res.*, *91*, 3011, 1986.

Barnett, A., The response function of the Voyager plasma science experiment, M. I. T. Center for Space Research *Technical Report CSR-TR-84-1*, Cambridge, MA (1984).

Barnett, A., and S. Olbert, The response function of modulator grid Faraday cup plasma instruments, *Rev. Sci. Instr.*, *57(10)*, 2432, 1986.

Belcher, J. W., The low-energy plasma in the Jovian magnetosphere, in *Physics of the Jovian Magnetosphere*, ed. A. J. Dessler, Ch. 3, Cambridge University Press, New York, 1983.

Belcher, J. W., and R. L. McNutt, Jr., The dynamic expansion and contraction of the Jovian plasma sheet, *Nature*, *287*, 813, 1980.

Belcher, J. W., C. K. Goertz, and H. S. Bridge, The low energy plasma in the Jovian magnetosphere, *Geophys. Res. Lett.*, *7*, 17, 1980.

Brice, N. M., Bulk motion of the magnetosphere, *J. Geophys. Res.*, *72*, 5193, 1967.

Brice, N. M., and G. A. Ioannidis, The magnetospheres of Jupiter and Earth, *Icarus 13*, 173, 1970.

Bridge, H. S., J. W. Belcher, R. J. Butler, A. J. Lazarus, A. M. Mavretic, J. D. Sullivan, G. L. Siscoe, and V. M. Vasyliunas, The plasma experiment on the 1977 Voyager mission, *Space Sci. Rev.*, *21*, 259, 1977.

Bridge, H. S., J. W. Belcher, A. J. Lazarus, J. D. Sullivan, R. L. McNutt, Jr., F. Bagenal, J. D. Scudder, E. C. Sittler, G. L. Siscoe, V. M. Vasyliunas, C. K. Goertz, and C. M. Yeates, Plasma observations near Jupiter: Initial results from Voyager 1, *Science*, *204*, 987, 1979*a*.

Bridge, H. S., J. W. Belcher, A. J. Lazarus, J. D. Sullivan, F. Bagenal, R. L. McNutt, Jr., K. W. Ogilvie, J. D. Scudder, E. C. Sittler, V. M. Vasyliunas, and C. K. Goertz, Plasma observations near Jupiter: Initial results from Voyager 2, *Science*, *206*, 972, 1979*b*.

Brown, R. A., A model of Jupiter's sulfur nebula, *Astrophys. J. Lett.*, *206*, L179, 1976.

Brown, R. A., and F. H. Chaffee, Jr., High resolution spectra of sodium emission from Io, *Astrophys. J. Lett.*, *187*, L125, 1974.

Burke, B. F., and K. L. Franklin, Observations of a variable radio source associated with the planet Jupiter, *J. Geophys. Res.*, *60*, 213, 1955.

Connerney, J. E. P., M. H. Acuna, and N. F. Ness, Modeling the Jovian current sheet and inner magnetosphere, *J. Geophys. Res.*, *86*, 8370, 1981.

Davis, L., Jr., Stellar electromagnetic fields, *Phys. Rev.*, *72*, 632, 1947.

Davis, L., Jr., Stellar electromagnetic fields, *Phys. Rev.*, *73*, 536, 1948.

Divine, N., Evaluation of Jupiter longitudes in system III(1965), *JPL IOM3577-76-32*, 1976.

Dungey, J. W., Interplanetary magnetic field and the auroral zones, *Phys. Rev. Lett.*, *6*, 47, 1961.

Eviatar A., J. D. Richardson, and R. L. McNutt, Jr., Plasma corotation in the Jovian and Kronian magnetospheres, *Proceedings from conference on Comparative Magnetospheres, in France*, 1986.

Fillius, R. W., and C. E. McIlwain, Maesurements of the Jovian radiation belts, *J. Geophys. Res.*, *79*, 3589, 1974.

Frank, L. A., K. L. Ackerson, J. H. Wolfe, and J. D. Mihalov, Observations of plasmas in the Jovian magnetosphere, *J. Geophys. Res.*, *81*, 457, 1976.

Gledhill, J. A., Magnetosphere of Jupiter, *Nature*, *214*, 155, 1967*b*.

Goertz, C. K., The current sheet in Jupiter's magnetosphere, *J. Geophys. Res.*, *81*, 3368, 1976.

Goertz, C. K., D. E. Jones, B. A. Randall, E. J. Smith, and M. F. Thomsen, Evidence for open field lines in Jupiter's magnetopshere, *J. Geophys. Res.*, *81*, 3393, 1976.

Gold, T., Motions in the magnetosphere of the earth, *J. Geophys. Res.*, *64*, 1219, 1959.

Goldstein, H., Theory of the plasma sheet in the Jovian magnetosphere, *Planet. Space Sci.*, *25*, 673,1977.

Hairston, M. R., Ph.D. thesis, Dept. of Space Physics and Astronomy, Rice University, 1986.

Hairston, M. R. and T. W. Hill, Jovian ionospheric conductivity and magnetospheric plasma outflow: Voyager 1, *J. Geophys. Res.*, *90*, 9889, 1985.

Hill, T. W., Inertial limit on corotation, *J. Geophys. Res.*, *84*, 6554, 1979.

Hill, T. W., Corotation lag in Jupiter's magnetosphere: Comparison of observation and theory, *Science*, *207*, 301, 1980.

Hill, T. W., A. J. Dessler, and C. K. Goertz, Magnetospheric models, in *Physics of the Jovian Magnetosphere*, ed. A. J. Dessler, Ch. 10, Cambridge University Press, New York, 1983.

Hill, T. W., A. J. Dessler, and L. J. Maher, Corotating magnetospheric convection, *J. Geophys. Res.*, *86*, 9020, 1981.

Hill, T. W., A. J. Dessler, and F. C. Michel, Configuration of the Jovian magnetosphere, *Geophys. Res. Lett.*, *1*, 3, 1974*a*.

Hill, T. W., C. K. Goertz, and M. F. Thomsen, Some consequences of corotating magnetospheric convection, *J. Geophys. Res.*, *87*, 8311, 1982.

Hill, T. W., and F. C. Michel, Heavy ions from the Galilean satellites and the centrifugal distortion of the Jovian magnetosphere, *J. Geophys. Res., 81*, 4561, 1976.

Hines, C. O., Hydromagnetic motions in the magnetosphere, *Space Sci. Rev., 3*, 342, 1964.

Hones, E. W., Jr., and J. E. Bergeson, Electric field generated by a rotating magnetized sphere, *J. Geophys. Res., 70*, 4951, 1965.

Ioannidis, G. A., and N. M. Brice, Plasma densities in the Jovian magnetosphere: Plasma slingshot or Maxwell demon?, *Icarus 14*, 360, 1971.

Kennel, C. F., and F. V. Coroniti, Is Jupiter's magnetosphere like a pulsar's or earth's?, *Space Sci. Rev., 17*, 857, 1975.

Kupo, I., Y. Mekler, and A. Eviatar, Deteaction of ionized sulfur in the Jovian magnetosphere, *Astrophys. J. Lett., 205*, L51, 1976.

McDonald, F. B., A. W. Schardt, and J. H. Trainor, Energetic protons in the Jovian magnetosphere, *J. Geophys. Res., 84*, 2579, 1979.

McNutt, R. L., Jr., The dynamics of the low energy plasma in the Jovian magnetosphere, Ph. D. thesis, Dep. of Phys., Mass. Inst. of Technol., Cambridge, July 1980.

McNutt, R. L., Jr., J. W. Belcher, and H. S. Bridge, Positive ion observations in the middle magnetosphere of Jupiter, *J. Geophys. Res., 86*, 8319, 1981.

McNutt, R. L., Jr., J. W. Belcher, J. D. Sullivan, F. Bagenal, and H. S. Bridge, Departure from rigid corotation of plasma in Jupiter's dayside magnetosphere, *Nature, 280*, 803, 1979.

McNutt, R. L., Jr., P. S. Coppi, R. S. Selesnick, and B. Coppi, Plasma depletions in the Jovian magnetosphere: evidence of transport and solar wind interaction, *J. Geophys. Res., in print*, 1987.

Mead, G. D., Magnetic coordinates for the pioneer 10 Jupiter encounter, *J. Geophys. Res., 79*, 3514, 1974.

Melrose, D. B., Rotational effects on the distribution of thermal plasma in the magnetosphere of Jupiter, *Planet. Space Sci., 15*, 381, 1966.

Mihalov, J. D., H. R. Collard, D. D. McKibben, J. H. Wolfe, and D. S. Intriligator, Pioneer 11 encounter: Preliminary results from the Ames Research Center plasma analyzer experiment, *Science, 188,* 448, 1975.

Nishida, A., Formation of plasmapause, or magnetospheric plasma knee, by the combined action of magnetospheric convection and plasma escape from the tail, *J. Geophys. Res., 71,* 5669, 1966.

Northrop, T. G., T. J. Birmingham, and A. W. Schardt, Anisotropies in the fluxes of Pioneer 10 protons, *J. Geophys. Res., 84,* 47, 1979.

Northrop, T. G., C. K. Goertz, and M. F. Thomsen, The magnetosphere of Jupiter as observed with Pioneer 10, 2. Nonrigid rotation of the magnetodisc, *J. Geophys. Res., 79,* 3579, 1974.

Pilcher, C. B., and J. S. Morgan, The distribution of [SII] emission around Jupiter, *Astrophys. J., 238,* 375, 1980. Pontius, D. H. Jr., T. W. Hill, and M. E. Rassbach, Steady state plasma transport in a corotation dominated magnetosphere, *Geophys. Res. Lett., 11,* 1097, 1986.

Richardson, J. D., Thermal ions at Saturn: Plasma parameters and implications, *J. Geophys. Res., 91,* 1381, 1986.

Richardson, J. D. and R. L. McNutt, Jr., Observational constraints on interchange models at Jupiter, *Geophys. Res. Lett., 14,* 64, 1987.

Richardson, J. D. and G. L. Siscoe, The problem of cooling the cold Io tours, *J. Geophys. Res., 88,* 2001, 1983.

Richardson, J. D., G. L. Siscoe, F. Bagenal, and J. D. Sullivan, Time dependent plasma injection by Io, *Geophys. Res. Lett., 7,* 37, 1980.

Sands, M. R., Field aligned flows in Jupiter's dayside middle magnetosphere, *EOS, 65,* 1038, 1984.

Sands, M. R. and R. L. McNutt, Jr., Plasma flow velocities in the magnetosphere of Jupiter, *Proceedings from Second Neil Brice Memorial Symposium on magnetospheres of the outer planets,* 4, 1986.

Scudder, J. D., E. C. Sittler, Jr., and H. S. Bridge, A survey of the plasma electron environment of Jupiter: A view from Vohager, *J. Geophys. Res., 86,* 8157, 1981.

Simpson, J. A., D. Hamilton, G. Lentz, R. B. McKibben, A. Mogro-Campero, M. Perkins, K. R. Pyle, A. J. Tuzzolino, and J. J. O'Gallagher, Protons and electrons in Jupiter's magnetic field: Results from the University of Chicago experiment on Pioneer 10, *Science, 183,* 306, 1974.

Siscoe, G. L., and D. Summers, Centrifugally driven diffusion of Iogenic plasma, *J. Geophys. Res., 86,* 8471, 1981.

Smith, E. J., L. Davis, Jr., D. E. Jones, P. J. Coleman, Jr., D. S. Colburn, P. Dyal, C. P. Sonett, and A. M. A. Frandsen, The planetary magnetic field and magnetosphere of Jupiter: Pioneer 10, *J. Geophys. Res., 79,* 3501,1974.

Smith, E. J., L. Davis, Jr., D. E. Jones, P. J. Coleman, Jr., D. S. Colburn, P. Dyal, and C. P. Sonett, Jupiter's magnetic field, magnetosphere, and interaction with the solar wind: Pioneer 11, *Science, 188,* 451, 1975.

Smith, E. J., R. W. Fillius, and J. H. Wolfe, Compression of Jupiter's magnetosphere by the solar wind, *J. Geophys. Res., 83,* 4733, 1978.

Stern, D. P., Large-scale electric fields in the Earth's magnetosphere, *Rev. Geophys. Space Phys., 15,* 156, 1977.

Summers, D. and G. L. Siscoe, Wave modes of the Io plasma torus, *Astrophys. J., 295,* 678, 1985.

Trainor, J. H., F. B. McDonald, B. J. Teegarden, W. R. Webber, and E. C. Roelof, Energetic particles in the Jovian magnetosphere, *J. Geophys. Res., 79,* 3600, 1974.

Trauger, J. T., G. Munch, and F. L. Roesler, A study of the Jovian [SII] nebula at high spectral resolution, *Astrophys. J., 236,* 1035, 1980.

Van Allen, J. A., D. N. Baker, B. A. Randall, and D. D. Sentman, The magnetosphere of Jupiter as observed with Pioneer 10, 1. Instrument and principle findings, *J. Geophys. Res., 79,* 3559, 1974.

Van Allen, J. A., D. N. Baker, B. A. Randall, M. F. Thomsen, D. D. Sentman, and H. R. Flindt, Energetic electrons in the magnetosphere of Jupiter, *Science, 183,* 309, 1974*a*.

Vasyliunas, V. M., Plasma distribution and flow, Ch. 11 in *Physics of the Jovian Magnetosphere*, A. J. Dessler, ed., Cambridge Univ. Press, New York, 1983.

Vasyliunas, V. M., Concepts of magnetospheric convection, *Tech. Rep. CSR-P-74-129*, M. I. T. Center for Space Research, Cambridge, 1974.

Vasyliunas, V. M., *Particles and Fields in the Magnetosphere*, ed. B. M. McCormac, Reidel Publishing Co., Dordrecht-Holland,1970.

Vlasov A. A. and F. Kh. Khakimov, Steady-state properties fo the completely ionized plasma surrounding the earth, *Sovi. Phys. Dokl., 8,* 785, 1964.

Wolfe, J. H., J. D. Mihalov, H. R. Collard, D. D. McKibben, L. A. Frank, and D. S. Intriligator, Pioneer 10 observations of the solar wind interaction with Jupiter, *J. Geophys. Res., 79,* 3489, 1974.